Methodology and optimisation of neutron-gamma pulse shape discrimination through specifically engineered scintillators coupled to Silicon Photomultipliers

---

Luca Malinverno

XXXII Ph.D. Student Class, 2016 - 2019
Version: Final

Università degli Studi dell'Insubria

Department of Science and High Technology

PSD

Methodology and optimisation of neutron-gamma pulse shape discrimination through specifically engineered scintillators coupled to Silicon Photomultipliers

Luca Malinverno

XXXII Ph.D. Student Class, 2016 - 2019

A mio padre Claudio dedico la vetta più alta di questa mia avventura. A lui che mi ha sempre insegnato ad arrivare, ogni giorno, sempre un po' più su, sempre un po' più lontano.

Contents

Introduction

The International Atomic Energy Agency (IAEA) brought attention to a new threat arising from the misuse of radioactive sources at the International IAEA Board conference held in London in 2005: nowadays seems that illicit trafficking of radioactive sources is mostly linked to malicious use in terroristic attacks rather than to a violation of the Non-Proliferation Treaty [1]. The terroristic attack to the Twin Towers on September 11^{th} 2001 revealed that non-state actors have no qualm in using the most brutal means to spread panic in their attacks against the population. Since the use of radioactive sources is nowadays applied in all fields of technology as well as medicine, well logging, γ radiography for pipeline structures and damage control, it is mandatory to build a strong control structure to prevent sources from being stolen or illicitly dismissed since those are the ones that may enter the black market. The awareness about this risk pushed companies, researchers and policymakers to study different solutions, concerning the standard fixed checkpoints at borders used to detect illicit trafficked sources. The solution commonly believed to be the most promising is a diffuse monitoring system made out of many small detectors configured as a smart grid. In this scenario, detectors are placed in fixed points next to sensitive objectives or given to police officers, taxi and bus drivers, letter carriers, to move those detectors around the city continuously. This approach results in the creation of a smart grid of sensors capable of detecting small quantities of radioactive material and lessening the possibility for a smuggler to avoid a checkpoint. The main challenge is to build small devices which maintain sensitivity to the radiation of interest, either γ or neutron. On the market, existing tools that are based on two detectors, specific for each kind radiation, to meet the sensitivity criteria outlined by the IAEA, European and ANSI standards. In the last decades, the interest for novel engineered scintillators that are sensitive to both γ and neutron radiation has increased, as outlined in the European Commission document about the novel technology that will help as countermeasures for nuclear risks [2]. In particular scintillators sensitive to γ and neutrons with pulse shape that depends on ionisation density, thus on the interacting particle, are of particular interest since they will allow increasing the performances of small detectors by increasing their active volume without changing the detector dimension, a feature

particularly useful in the case of neutron detection. However, any new detector must be capable of performing on-line discrimination of the impinging particle to be compliant with the IAEA prescriptions.

The main goal of the thesis was the understanding of how an instrument affects the reconstruction of the signal shape. It will be shown how the efficiency in light collection as well as the Silicon Photomultiplier and electronic readout transfer function affects the capability of γ neutron discrimination capable scintillator.

Silicon Photomultipliers are state of the art light detectors, with single-photon sensitivity, high dynamic range, robustness, low cost and low power consumption. These sensors have a low bias voltage, below 100V, that make them suitable for a small and portable battery-operated detector. However, Silicon Photomultipliers generally have a large capacitance that strongly impacts the signal shape, and so far their successful use in Pulse Shape Discrimination has never been apparent. Indeed whole acquisition chain must preserve the information contained in the scintillating light profile and, for a field-usable instrument, the signal processing has to be done on-line for particle discrimination and subsequent alarm triggering.

The thesis is the results of two joint research projects: a first one aimed to engineer an instrument for diffuse monitoring based on a digital signal processing, and a second one aimed to characterise an Application Specific Integrated Circuit (ASIC) for nuclear security applications.

The whole study about the impact of digital electronics was part of the joint research project with a UK based company called Atomic Weapons Establishment (AWE). The main deliverable of the project was the customisation of an instrument for the diffuse monitoring. In order to deliver such instrument required by the project committee, research focused on discrimination capabilities of a digital electronics system that led to the customisation of the I-Spector, a device designed by Nuclear Instruments Srl and commercialised by CAEN spa. The custom version of the devices embeds a digitiser and a Field Programmable Gate Array (FPGA) that performs the on-line particle identification. Control software that allows to calibrate the system and set alarms if the radiation level overcomes a certain threshold was commissioned as part of the research. In particular, the performances in terms of discrimination capabilities of the on-line procedure were tested against a standard and well settled off-line analysis procedure. In the thesis, procedures to define minimum requirements, tests on the systems, including the commissioning of the final deliverable, will be presented.

On the other hand, a joint research project with Kromek Group plc was the framework in which the analogue pulse shape discrimination was studied and compared to the

digital approach. The focus of this project was the characterisation of ASIC called APOLLO, produced by Kromek. The ASIC was characterised and tested for on-line Pulse Shape Discrimination using an evaluation board that allows accessing to all the channels and the functionality of the ASIC.

The thesis is structured to give, in its initial chapters, common basis about law and scientific frameworks for nuclear security. After the analysis of the bibliography, the scientific work moves towards the understanding of the mechanism underneath different Pulse Shape Discrimination Algorithms. As a results new algorithm, that better performs with SiPM concerning the standard techniques practised with Photomultipliers tubes, have been defined. Moreover, a full chapter (Chapter 3) is dedicated to a review of the Silicon Photomultipliers technology. A significant portion of the thesis (Chapter 4 and 5) have been dedicated to the analysis of noise and light collection impact in Pulse Shape Discrimination. By the end of this sections, it will result clear why the new algorithm for pulse shape discrimination, defined as the ratio between the integral of the falling edge of the signal and the signal amplitude, better performed with respect the standard ones. In these Chapters, both experiments and numerical simulation were used to understand the measured phenomena. Indeed, the last two chapters of the thesis (Chapters 7 and 8) are focused on measurements edit to understand how either a digital or an analogue signal processing circuit performs in on-line pulse shape discrimination. A set of preliminary measurements were aimed to quantify the effect of signal shaping, bit resolution and different sampling rate impact on discrimination in order to set the minimum requirement for the digital system, in particular, the ADC bit resolution and sampling frequency concerning the shaping of the Front End Electronics. Performances of the analogue pulse shape discrimination circuits were investigated using the APOLLO ASIC by Kromek. The ASIC has 16 input channels, and it embeds both an analogue integrator and a "peak and hold" circuits, that allows implementing Pulse Shape Discrimination algorithm on-line. It was initially characterised, from a test board that gives full access to the 16 channels, in its linearity and working range. From the qualification board, however, it was only possible to dump the measured quantity to build up the discrimination parameters. The discrimination was performed off-line, but a near-real-time procedure implemented on actual instruments that make use of APOLLO ASIC should not behave differently from the presented results.

1 Nuclear Security

After its discovery, and an initial usage without regulations, radioactivity posed severe concerns to health while used for industrial, military or medical applications. The first concerns arose after the X-ray discovery, since some patients showed the symptoms of Radiation-Induced Diseases (RIDs). Even though the discovery of Radium self-activity and the possibility to split a Uranium atom to allow a self-sustained chain reaction opened the way to new technologies, like nuclear reactors, the awareness about the risk of those technologies increased at last. The belief that a peaceful and regulated use of radioactivity would be more than beneficial was stronger and stronger due to the proved benefits as, for example, cancer treatment. After the terrible events inC Hiroshima and Nagasaki the "Cold War", as George Orwell defined the arms race between USA and USSR, led to the signature of the Non-Proliferation Treaty (NPT). NPT was sponsored by the International Atomic Energy Agency (IAEA) the international organisation that aims to promote the peaceful use of atoms and atomic energy.

The events of 9/11 started a new era of nuclear threats since non-state actors or terrorist organisations, like Al-Qaeda, actively tried to acquire nuclear or radioactive material for a wilful malicious act[3]. In this chapter, after a brief historical recall of milestones in radioprotection, a focus on the risk scenarios recognised by International Atomic Energy Agency (IAEA) and relevant regulatory laws that are in use worldwide will be outlined. The analysis of the IAEA documents containing a review of the major accidents and threats will guide the discussion toward the definition of instruments and procedure for the detection of illicit activity related to nuclear or radioactive material (NRM).

1.1 The roots of Nuclear Security

In late 1895 W.K. Röntgen discovered the X-Rays. The potentiality of its discovery, well above the curiosity-driven breakthrough, was promptly evident in the medical field, indeed yet from 1896 X-Ray machines have been used in hospitals to get internal images of injured body, helping in diagnosing and surgery processes [4]. Just one year after X-Rays, A. H. Becquerel discovered the radioactivity in Uranium (1896) while Elihu Thomson conducted experiments to understand better whether

there was any damage caused by the use of X-Ray. People that used Röntgen rays daily suffered from burns, hair loss and other side effects [5]. The γ rays discovered by Pierre and Marie Curie while studying Radium in 1898 was proved to be more penetrating than X-Rays in 1900 by P. U. Villard. The next year, 1901 while Roentgen was awarded the Nobel Prize, it was confirmed by W.H. Rolling that the X-Rays were lethal to mammals, and a few years later, when Becquerel and the Curies won their Nobel Prize (1903), it was proven that X and γ rays could induce damage into the body [6, 7]. However, in the very same year, a study was published by G. Perthes that confirmed X-Rays inhibit the tumorous cell multiplication [8]. In the following years, medical and industrial breakthroughs were indisputable, as much as the proofs that radiation can cause leukaemia, cancers or other possibly lethal side effects, for example, the death of a patient treated with ^{226}Ra injection, who suffered from Arthritis. In 1915 the British Röntgen Society proposed a regulation for the protection of those workers that used radioactive in their daily activity. The regulatory action was still in its larval stage, that is why, in 1922, the first worker (a woman called Amelia Maggia) died after prolonged exposure to ^{226}Ra in radioactive painting for dials. A few years later, in 1930, C. Lauritsen proposed its first radiotherapy machine. Despite the benefits that radiation was bringing into the world, poor knowledge of its side-effects caused many deaths; to remember the 169 physicians and technician that died from radiation-induced diseases who sacrificed their lives for the knowledge and the benefit of the humankind, in 1936 the city of Hamburg placed the first memorial [9].

With a jump of more than ten years, while in Los Alamos scientist involved in the Manhattan project were trying to build the Nuclear Weapon after the discovery of the mechanism for the self-sustained chain reaction in Uranium (1938 by Otto Hahn), the U.S. Committee on X-Ray protection published the first regulation in terms of radiation protection. This regulation limited the Radium quantity for body injection at 0.1 μCi, and a note posted by L.S. Taylor recommended to use "*less than 0.02 Roentgen/day of X-ray radiation to lower the probability of RID*".

In 1942, while Fermi operated the first nuclear reactor in Chichago, it was shown that a dose of 4 Roentgen/day was lethal to humans, and a year later the toxicology study on Uranium was started [9]. The terrible explosion of *Little Boy* and *Fat Man*, the two atomic weapons dropped on Hiroshima e Nagasaki on 6^{th} and 9^{th} of August 1945 triggered not only a profound shock for the consciousness of all humankind but also the research on the biological effect of large scale radiation exposure after an explosion or a fallout. Indeed, as the years go by, the American Public Health Association pointed out in a report dated back to 1956 that the primary concern for the citizens would have been the pacific use of radioactivity since those applications would have generated more chemicals and radioactive waste dispersion in the environment proven to be a significant hazard for the heath.

In the 1960s USA and USSR begun a negotiation about the nuclear weapons, to reduce the amount of objects[1] retained by both countries since the cost of the army race and maintenance cost was not worth to increase the security level [11]. The Non-Proliferation Treaty (NPT), was open for signature from 1968, and its incipit and the ratio underneath the treaty:

> *"Considering the devastation that would be visited upon all humankind by a nuclear war and the consequent need to make every effort to avert the danger of such a war and to take measures to safeguard the security of peoples, Believing that the proliferation of nuclear weapons would seriously enhance the danger of nuclear war, In conformity with resolutions of the United Nations General Assembly calling for the conclusion of an agreement on the prevention of wider dissemination of nuclear weapons, Undertaking to co-operate in facilitating the application of International Atomic Energy Agency safeguards on peaceful nuclear activities [The Signing States agrees that]"*
>
> **Non Proliferation Treaty, 1968**

After NPT was signed only the five countries that developed a nuclear weapon before 1970, namely USA, USSR, UK, France and the Popular Republic of China, could maintain the nuclear weapons, but they were forced to reduce the total number. Several other treaties were signed after that first one, like the STAR I and START II aimed to reduce the ability to fire nuclear bombs all over the world hoping to increase the security across the globe.

Since its foundation, IAEA not only was the institution in charge of control the decommissioning of nukes but also promoted the peaceful use of atomic energy and defines the procedure to reduce risks that come from the misuse of radioactive sources.

Along with the unaware exposure of citizens due to the source illicitly abandoned or dismissed, the so-called orphan sources, after the terrorist attack to the Twin Towers in New York, 9/11 2001, IAEA registered an increased risk linked to the will of non-state actors in the acquisition of nuclear or radioactive source for a malicious act. The warning was, and still is, entirely factual since Al-Qaeda proved to be not afraid in using most disrupting arms to damage and spread panic [12]. Since the illicit trafficking, theft, sale, delivery, usage, disposal, transfer or possession of nuclear material could lead not only to proliferation of atomic weapons but also to the construction of devices to spread radioactivity in terroristic attacks, nowadays instruments, protocols and international regulatory regimes are adopted to guarantee the highest level of security [12, 13].

[1] Nuclear weapons are often called, in official documents "*nuke*" or "*object*" or "*gadget*" [10]

1.2 Incident with nuclear and radioactive material

The technology advancement that we experienced in the last century did not leave behind the use of Radioactive sources in the most different fields. Military, as well as civil application, have been exploited since the scientific discoveries made the use of radioactive source safer. However, if not appropriately controlled, such materials could represent a significant source of risk, so far not only nuclear but also radioactive materials undergo a Regulatory Control by IAEA, called Safeguards. Safeguards consist in procedures, instruments, tools and periodic controls to certify nature and use of such material to be pacific and safe, and that quantity of such material, useful for a malicious act, is not theft or loss. The word "incident", in the IAEA standards, does not refer to explosions or fallout, but to the discovery of illicit trafficking, theft lost of orphan sources [14].

In nuclear security, there is a clear difference between radioactive and nuclear material [15].

Radioactive materials are all those isotopes that emit ionising radiation. This class is comprehensive of all radioactive source used in civil and military application. To this class belong, for example, ^{137}Cs, ^{22}Na, ^{131}I, ^{60}Co, ^{90}Sr to cite the most used ones [13, 15].

The nuclear material is a special class of radioactive material. In particular, it is referred to any special fissile material, like ^{239}Pu,^{233}U and Uranium enriched with the isotope ^{235}U and ^{233}U, or other materials that may trigger a self-sustained decay chain. Nuclear power plans or nuclear weapons make use of those sources. Those materials are also called Highly Enriched Uranium or Weapon Grade Plutonium (HEU/WGP). For example, the difference between occurring natural Uranium and HEU is the percentage of isotope ^{235}U, that naturally occurs in the more stable ^{238}U only as 1/140. At the same time, it is enriched to more than 20% in the nuclear weapon useful material [10]. The actual composition of nukes in terms of Uranium or Plutonium isotope enrichment, tamper and construction details are, of course, classified. Still, some models exist, and they can be used to guess the energy and flux of expected neutron and γ spectra and activity [16].

- **HEU** : ^{234}U 1%, ^{235}U 93%, ^{238}U 6%;
- **WGP** : ^{239}Pu 93%, ^{240}Pu 6%.

Special nuclear material isotope composition according to the model reported in [16]

1.2.1 IAEA source classification

Sources are classified according to the threat level they poses. IAEA summarise this information in quantity called activity ratio A/D. It takes into account not only the intrinsic source activity, but its size to determine the actual risk they can pose to population.

The activity of a radioactive source, A, is defined as the number of decay per second and it does not account for the kind and multiplicity of particle or radiation emitted by the decaying nuclei. Activity is measured either in **Becquerel** (Bq), namely the total number of disintegration per second in a given sample, or in Curie (Ci), namely the equivalent activity of 1g of ^{226}Ra; the conversion between **Ci** and **Bq** is expressed in(1.1).

$$1Ci = 37GBq \tag{1.1}$$

The normalised activity D is a value that established for each radioisotope representing a threshold of danger, which takes into account the typer and the energy of the emitted radiation. In this sense, the quantity called Activity Ratio A/D acts as a quantitative parameter to assess sources based upon the level of risk they trigger. The IAEA source classification, reported in Table 1.1 is based on this quantity [17].

Category	A/D	Source Usage
1	≥ 1000	Radioisotope thermoelectric generators (RTGs) Irradiators Tele-therapy sources Fixed, multi-beam teletherapy (gamma knife) sources
2	$[10, 1000]$	Industrial gamma radiography sources High/medium dose rate brachytherapy sources
3	$[1, 10]$	Fixed industrial gauges that incorporate high activity sources Well logging gauges
4	$[0.01, 1]$	Low dose rate brachytherapy sources Low activity industrial gauges Bones densitometers Static Eliminator
5	≤ 0.01	Permanent low dose rate medical sources X ray fluorescence (XRF) devices Electron capture devices Mossbauer spectrometry sources Positron emission tomography (PET) check sources

Tab. 1.1: IAEA classification of radioactive source based on the normalised activity ratio A/D as reported in [17].

1.2.2 Incident and Trafficking Database

The planning of countermeasures to contain the nuclear risk is based on the research and tracking of significant incidents related to the trafficking and the discovery of sources that should be under the regulatory control as reported by member states. Records of those events are collected in the Incident and Trafficking Database (ITDB) that helps in the definition of the threats to be addressed in the Nuclear Security Plans from 1995. The full record of events is not accessible since the confidentiality of the shared information act both as an incentive to the cooperation of member states and as a preventive measure against leakage of critical information to pursue the non-proliferation of nuclear weapons. However, it is clear from the documents that intelligence services most likely control the non-proliferation of atomic weapons by a member state. The events collected in the database, from the fact-sheet where aggregated data are disseminated as informative service to the population and policymakers, shows that in the last 20 years the focus should be more on the misuse of radioactivity by non-state actors rather than an institutional one. Indeed only a few incidents are reported as linked to the quantity of HEU or WGP that could be used to build a nuclear weapon. Most of the events are related to other criminal offences that would have exposed population to radiation if not detected.

In the ITDB the events are classified according to these groups:

- ***Group I***: Events connected, or very likely connected, to the trafficking of radioactive and nuclear material for malicious use.

- ***Group II***: Events of trafficking whose final use is unknown. It may be both a malicious use or the unlawful disposal of sources.

- ***Group III***: Events that are not, at least very unlikely, linked with terrorist purposes even though they caused an unjustified exposure of subjects (worker, or citizens) to radiation.

The ITDB records incidents that happened since 1993: a total of 3497 entries were reported as of 31^{th} of December 2018, 253 of which in the sole 2018 among 49 States, indicating that the unauthorised activities involving trafficking and malicious use are far from unlikely to happen [14]. A total of 285 events, since 1993, were in the group I, indeed proven after police investigation to be linked with the wilful terrorist-driven malicious act. Almost 1000 recorded events were recorded with too few information to determine whether they were addressed to terrorism, and more than 2200 cases were related to unlawful disposal of nuclear material or other non-terrorist purposes.

Even though the events in the *Group I* never exceed the 20 occurrences per year (Figure 1.1), the number is enough to justify the security procedure at borders to look for the radioactive source and international cooperation of Intelligence Agencies. In this group, scam and fraud are reported as well, since their first buyers are on the black market are terrorist organisations.

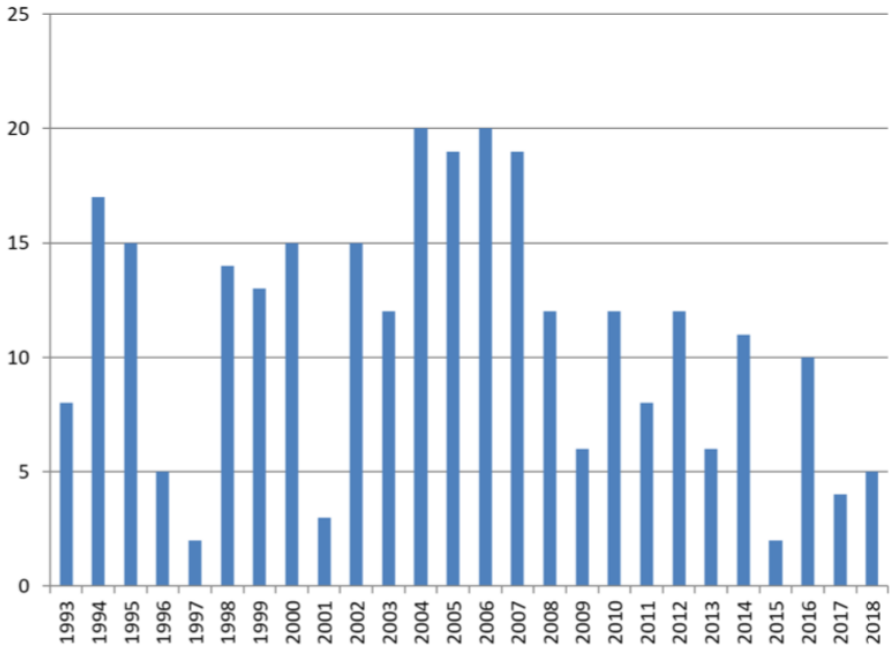

Fig. 1.1: Number of reported incident per year since 1993 up to 2018 in *Group I*, from [14]

Luckily only a few of them, the ITDB fact sheet does not report the exact number, involved significant quantity, in the order of 25 kilograms for HEU and of 8 kilograms for WGP (Figure 1.2) [15]. However, from the few information obtained by the ITDB or other available disclosed sources, the number of successful transaction of nuclear materials on the black market is not known. Most of the illicit trafficking is discovered at borders where the detection pass trough the Radiation Portal Monitors (RPM). The RPMs are big detectors used to scan lorries and containers at major commercial hubs and border. Working principle of the RMS will be discussed later on in Section 1.3.2.

Group II: to this group belongs all that incidents that includes stole or missing material for which no enough information is available to determine the end-use of the missing material. Those events are of great importance in the Nuclear Security Plan since they highlight vulnerability in the nuclear or radioactive material storage or the transport procedure. A small number of events in this group regard the discovery of illicit possession of radioactive material from the industrial users that bypassed controls to reduce the management cost of sources; those are high-risk events since sources outside the regulatory control or illicitly possessed are most likely to be trafficked on the black market after the disposal. To contain the number

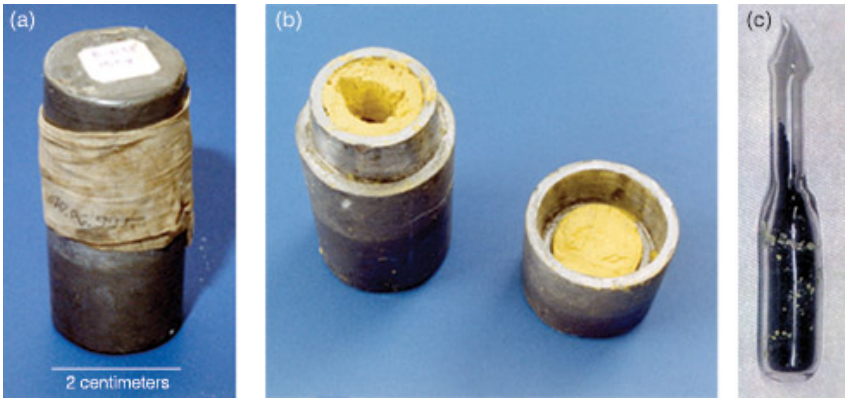

Fig. 1.2: An example of HEU source found in 1999 in Bulgaria in routines border controls [15]. In (a) is the package as it was found, (b) is a detail of the moderator and shielding and the (c) is the HEU source itself.

of those incidents, mostly constant in the past 20 years as shown in Figure 1.3, most of the security relies on procedures and protocols to make more and more complicated the operation outside safeguards and Agency controls.

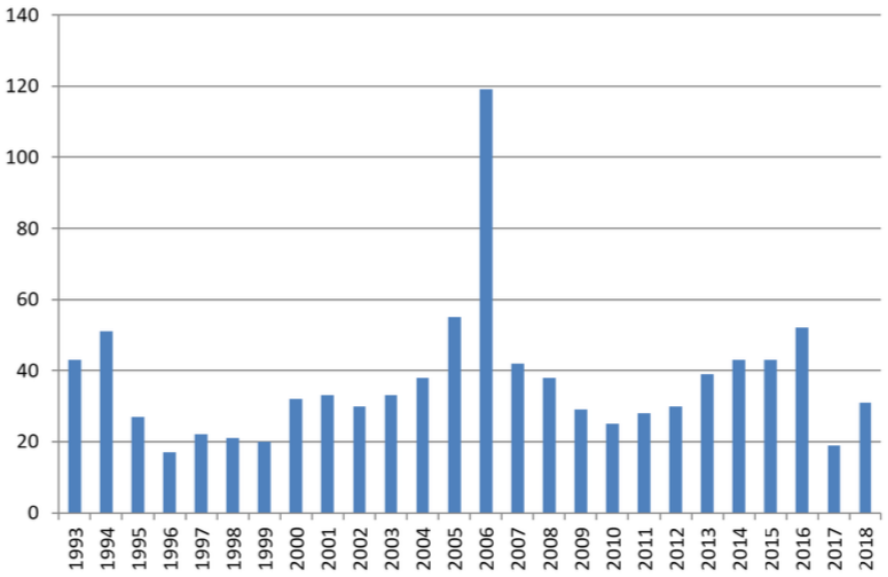

Fig. 1.3: Number of reported incident per year since 1993 up to 2018 in *Group II*, from [14]. The spike in 2006 is due to a change in reporting procedure, and do not represent a real increase of incident linked to that year.

Primary trafficked sources come from industrial applications where they are used for non-destructive test or medical imaging since those sources are perceived as of great value on the black market. These groups also include highly enriched Uranium and plutonium, and plutonium neutron sources. Sources up to the Category 2 of the IAEA source classification (Section 1.2.1) enter this group, with significant attention to sources in the Category 2-3, that has a dedicated follow-up procedure to guarantee that the missing sources are found and then disposed within the safeguards prescription. Sources in the category 4-5 do not represent significant

hazard, so they do not undergo a dedicated follow-up procedure. Most of them are related to short-living radioisotopes that will not cause harm even if released in the environment.

The *Group III* comprises all incidents that are not linked to any malicious act. Those events regard both unauthorised detection of material for industrial application or the discovery of sources illicitly disposed and released in the environment, the so-called orphan sources. Another not negligible amount of incidents regard the unaware shipment of a radioactive source, mainly within metal scrap. Events of this kind are again an indication of an ineffective procedure to control the radioactive sources. The diffusion of RPM after the 9/11 events, not only at border but also at metal scrap working facilities gates causes an increase of the detected contaminated scrap or unaware shipmen, as indicated in Figure 1.4 by the increase of such incidents after 2001.

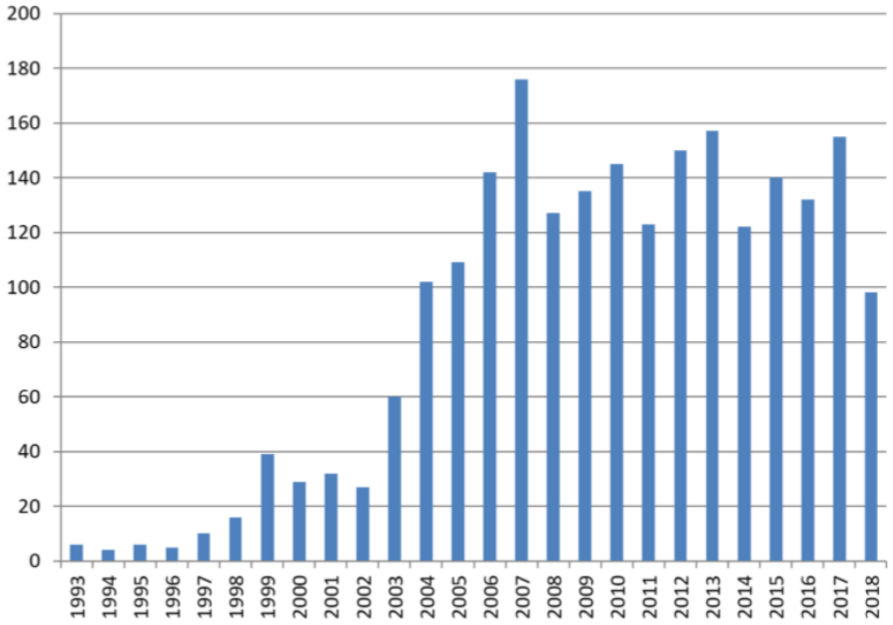

Fig. 1.4: Number of reported incident per year since 1993 up to 2018 in *Group III*, from [14]

Those incidents are linked to the unnecessary or unaware exposure of citizens and worker to radiation, more than to the risk for a malicious act. The harm is not negligible even in Italy: from a report by Agenzia Regionale per la Protezione Ambientale - ARPA, the Italian regional environmental protection agency, recorded more than 260 records of contaminated scrap from 150 firms between 1997 and 2000 in just a province of Lombardy, Brescia, but they were not all recorded in ITDB since they involved sources in Category 5 [18]. Those pieces of information are any way useful to understand the weak point in the safeguards chain, and help in the definition of more strict countermeasures.

Another useful source of information to evaluate the danger and the effects of actual incidents caused by the misuse of radioactive and nuclear material or by failure in security systems is the Johnston Archive [19]. It is a website, cited among the other by the Bulletin of the Atomic Scientist [20], that collects data about the injury and fatalities directly caused by radiation incidents. Apart from the war use at the end of World War II, and from incident directly involving nuclear power reactors, the total number of fatalities is more than 200 with more than 1500 people directly injured from 1986 to 2008 in the significant reported events.

1.3 Malicious Act: Threats and countermeasures

It was possible to evaluate the major threats the world could face due to a malicious act of non-state actors in possession of nuclear or radioactive material thanks to the information gathered from the ITDB. The risks reported in the document produced by The International Conference of London, held by the IAEA board in 2005 [1]:

"The threats involve criminal or terrorist acquiring and using for malicious purposes:

(a) nuclear explosive device;

(b) nuclear material to build an improvised nuclear explosive device IND;

(C) radioactive material to construct a radiation dispersal device (RDD); and/or

(d) the dispersal of radioactivity trough sabotage or installation in which nuclear and other radioactive material can be found or of such material in transport."

From the reports outlined in that conference appears clear how, if the non-proliferation is mostly guarantee by deterrence and intelligence to control if independent states do not violate the treaty, a significant risk from the population comes from non-state actors that would move small quantity of radioactive material with the main goal to spread terror instead of an efficient damage. The approach to the various threats should take into consideration the different type of radionuclide and technology and in which measure they are accessible to different criminals and criminal organisations. In the last decade IAEA recognised that:

Advanced in information technology and the availability of radioactive material have increased the likelihood that a terrorist or other criminal organisation could obtain not

only the necessary material but also the components and the expertise to construct an IND or RDD [15]

Apart from sabotage, that would require a physical, possibly military, protection [21], RDD and improvised nuclear bombs are the most substantial threats. The most effective RDD called "*Dirty Bombs*" would combine nuclear or radioactive material, mainly sources outside regulatory control (orphan source, lost or thief material), with conventional explosive that, when detonated, contaminates persons, properties and environment. Non-explosive means can also be used to spread radiation, for example just leaving a source on a means of public transport or by sabotage of water pipelines. Effective countermeasures against RDD should focus on sources capable of long-lasting damage or contamination. Luckily, even if a lot of different radioactive materials are used in for an industrial, medical and civil application, only a few of them would cause serious prompt damage or a long-lasting contamination [13].

Nuclear weapons, on the other hand, are addressed to a different purpose. Although there were only two usages of nuclear bombs against the population, August 1945 in Japan, the direct threat is caused by the proliferation of such devices other than the mass killing. Illicit use of nuclear material for nuclear weapons occurs when a state acquires nuclear material to build proper nuclear weapons outside the NPT like North Korea did in last few years, but also because non-state actors try to build the so-called Improvised Nuclear Devices. The risk of the first scenario is a war at global level, but the discovery of such threat is, in most of the case, directly disclosed from the country who de-legitimate the treaty, since the possession of a nuclear weapon would place the country on a higher level on the political chessboard. It is however unlikely that such country would use for real such weapon. In the second case, the risk for the population is more factual: if the terrorist does not appropriately treat the Nuclear Material, it may cause exposure and damage of population while the bomb is in construction, not to mention the damage caused by an unforeseen or wilful explosion [15] that a non-state actor would purse since a different motivation aims it.

States signed several multilateral treaties that impose technological, regulatory laws, code of conduct for exporters or buyers of nuclear material at a national level in order to contain those risks.

1.3.1 International Treaties

Nuclear security is, of course, a matter of national law, but all the governments agree that the effectiveness of the implemented countermeasures is beneficial only if shared and adopted by the broadest possible number of countries [15]. The

international treaty does not only deal with nuclear non-proliferation, but also with radiation protection, physical and military protection of sites and power plants, transportation of nuclear and radioactive material and emergency assistance. On the non-proliferation side, treaties define commercial relationships among the states to facilitate pacific use of atomic energy and to discourage the proliferation of nuclear weapons trough controls and sanctions, establishing rights and duty on many aspects related to the commercialisation of nuclear material and knowledge. The IAEA published a comprehensive manual of the in-force international law: *Handbook on Nuclear Law* [22]. It is worth to mention that enormous effort has been pursued by the States to achieve and effectively adopt the following multilateral initiative:

1. Non Proliferation Treaty - 1970 [23];
2. NPT Exporters Committee - Zangger Committee Guidelines [24];
3. Nuclear Suppliers Group Guidelines [25];
4. Regional Nuclear Non-Proliferation and arms control Treaties[26, 27, 28, 29];
5. IAEA safeguards agreement and protocols [30, 31];
6. Convention on Physical Protection of Nuclear Materials (CPPNM) 1980[32, 33];
7. Convention on Early Notification of a Nuclear Accident (CENNA) 1986 [34];
8. Europool Convention 1999 [35];
9. Convention on suppress AcT of Nuclear Terrorism 2005 [36];
10. Code of Conduct on the Safety and Security of Radioactive Sources [37];
11. Guidance on the import and export of radioactive sources [38];
12. United Nation Security Council Resolutions (UNSCRs) 1540 and 1373[39, 40].

Among those, the most important is the Non-Proliferation Treaty (NPT). It was open for signature in 1968, and 1970 it became effective. In 1995 all the Signing States agreed to extend it indefinitely. The main features of the NPT are stated in the first three articles. In ***Article I*** the five countries that possessed a nuclear weapon at the time of treaty signature, namely USA, USSR, UK, France and the Popular Republic

of China, agree to not transfer or sell any nuclear weapon to any other country. In ***Article II***, on the other side, the non-nuclear states agree not to receive or try to buy any nuclear warhead, nor to invest in research and development of nuclear weapons. In ***Article III*** all the countries necessarily agrees with the safeguard regime imposed by the IAEA. To reinforce this treaty, the Zangger Committee Guidelines and the Nuclear Suppliers Group Guidelines imposes other strict conditions to the nuclear and radioactive material producer about the export and the selling strategies. Even from the multilateral initiative history, it is possible to see how the states moved from the stop of nuclear proliferation to measures that would guarantee the protection of radioactive sources to inhibit acts of Nuclear Terrorism, as outlined in the IAEA London Conference held in 2005.

Following this trend, the main topic of this thesis would focus on the study of materials and method that could be of interest for source identification and illicit trafficking control field.

1.3.2 Radiation Detectors for Nuclear Security

In the IAEA guidelines for the tools against the illicit trafficking and usage of nuclear or radioactive material in Radiological Dispersal Devices identifies two classes of instruments: Radiation Portal Monitors (RPMs) addressed to fixed checkpoints and hand-held or personal instruments for patrols and officer, like Personal Radiation Detectors (PRDs), Hand-held γ and neutron search detectors (GSDs and NSDs) and Hand Held Radio-Isotopes Identification Devices (RIIDs) [15]. More sophisticated laboratory equipment that would be used in the forensics or the academic research is not of interest since it requires specific training and competences to be used successfully, and they do not give real-time alarms. At the same time, the mentioned devices can be operated with just a little training of the operators to obtain real-time alarms. The instruments for the detection of illicit material are not only intended to prevent any injury or damage to people, properties and environment but also they are used to assay the source to use the gathered information in the legal proceeding against who was committing the criminal offence. Nuclear material differs from NORMS in the typical γ and neutron fluence, being more intense in one with respect to the other. It is common for illicit traffickers to mask N.R. material with other NORM. All the detectors must take in account the environment radiation background, so they are usually calibrated to trigger an alarm only of the radiation level is higher than four standard deviations with respect to the background [15, 41, 42]. This general prescription for the threshold is then adjusted to reduce the false alarm due to background fluctuation, but still, one alarm per day can be anticipated. All the instruments must meet some sensibility criteria. For the γ it is required that at 0.2 μSv/h background, a dose rate increase of 0.1 μSv/h is detected within 1 second. For

neutron detectors, a general prescription reported in [43] states that "*It is required that a neutron detector for homeland security application not produce any neutron alarm when exposed to a* $10mR/H$ γ*-ray exposure rate during* 10^6 *measurements, while still meeting the neutron detection requirements*"; anyhow this is of little use when it comes to the validation of an instrument. The general rule expressed in [43] comes from an analysis of the ANSI-N42.34 and ANSI 42.35. In those standard documents, the prescription is translated into operational tests to measure if the detector meets the sensibility criteria. In the same paper from the U.S. Department of Energy (PNNL-18903), procedures and measurable quantities, that can help to asses if the general prescription is met, are reported. Measurable neutron sensitivity and γ insensitivity quantity for neutron detectors are:

- absolute neutron detection efficiency ϵ_{abs-n};
- Intrinsic γ-neutron detection efficiency $\epsilon_{int_\gamma - n}$;
- Gamma absolute rejection ratio for neutrons, $GARRn$.

ϵ_{abs-n} is measured in the absence of γ sources. It is the ratio between the neutron emitted from a source of ^{252}Cf (37ng, $\approx 20\mu Ci$) at 2m distance from the detector when the neutron source is moderated by 5mm of lead and 25mm of polyethene. The number of detected neutrons in this condition shall be more abundant than 2.5 per second. The $\epsilon_{int_\gamma - n}$ is the net number of event tagged as "neutron" with respect to the total number of γ hitting the detector when the detector is exposed to a $10mR/h$ of a γ source (usually ^{192}Ir,^{137Cs} or ^{60}Co) in absence of neutron source. $\epsilon_{int_\gamma - n} < 10^{-6}$ is the minimum value that ensure to fulfil the general prescription. $GARRn$ is defined as in Equation (1.2) as the absolute neutron detection efficiency in presence of both sources ($\epsilon_{abs-n\gamma}$) divided by the absolute neutron detection efficiency of the detector (ϵ_{abs-n}). If γ source would have no impact the $GARRn$ would be 1, however, a $GARRn$ between 0.9 and 1.1 at $10mR/h$ γ exposure is accepted and would allow fitting the general prescription.

$$GARRn = \frac{\epsilon_{abs-n\gamma}}{\epsilon_{abs-n}} \tag{1.2}$$

The details of the instruments and its minimum requirements have been settled by IAEA in collaboration with Europool and Interpool and collected in the *IAEA-TECDOC 1312* and the *IAEA-NSS1:Technical and Functional Specification for Border Radiation Monitoring Equipment* [41, 42].

Radiation Portal Monitors and Personal or Hand-held radiation detection devices must fulfil the criteria as mentioned above, and by operational means, they have to guarantee a limited number of false alarm per operation period not to halt the border procedure. The procedures that measure whether those criteria are met are reported in the IEC 62244 and ANSI 34.35 standards, for what it concerns the RPMs, and into the IEC 62327 and ANSI 34.34 standards for what it concerns the RIIDs.

1.3.3 Radiation Portal Monitors

Radiation Portals Monitors (RPMs) are pass-through monitors, made usually by two pillars, each of them containing a γ and a neutron detector. For those kinds of instruments, the neutron and the gamma alarms must be differentiated to identify better the source and the procedure that should be adopted. RPMs are designed to be used at checkpoints and are very useful in the scan of the flow of vehicles, people, luggage and goods without interfering with their flow. RPMs are equipped with an occupancy sensor, so when the scanned area is not occupied, it measures the background radiation, and it automatically adjusts the alarm threshold level. RPMs are installed in the so-called choke points, where the flow can be forced to pass, that is why RPMs are particularly useful at borders, customs, airports or international train stations. They are meant to alert the authorities about the presence of nuclear or radioactive material.

Fig. 1.5: Example of veicles RPMs at border.

γ detectors are large area plastic scintillators, due to intrinsic low cost, or sodium-iodide (NaI) or caesium-iodide (CsI) inorganic scintillators, while neutron detectors could be based on ^{3}He, ^{4}He tubes or plastic scintillators. RPM detectors should be

Fig. 1.6: Example of pedestrian RPMs at airport border.

calibrated periodically to guarantee that they still have the sensitivity required by IAEA [41].

The control procedure requires that when an alarm is triggered, the suspicious cargo should pass again trough the portal and, if the alarm is repeated, the vehicle or pedestrian has to be out-flowed and checked with specific hand-held instrumentation to localise and possibly identify the source.

ANSI standard 42.34 set the threshold for the response to γ and neutron radiation. In particular, for the γ sensitivity it is required that at a background level of not more than $20\mu R/h$ an alarm shall be triggered when exposure rate is increased due to one of the sources reported in the Table 1.2 with their required activity. The source shall be placed in between the two pillars of the RPM, and it has to be moved at $8km/h$ in case of vehicle RPM, or $1.2m/s$ in case of pedestrian one. The probability of detecting the source should be higher than 90% with 95% confidence. This means that alarms have to be triggered at least 59 times in 60 passages. The sources listed in Table 1.2 tests the sensitivity in an energy range that ranges from $60keV$ to $2.6MeV$. The neutron source, a ^{252}Cf source with a neutron flux of $2 \cdot 10^4 n/s \pm 20\%$, shall be detected with the same probability, i.e. in 59 passages out of 60. The neutron source has to be detected even in the presence of a γ background up to $100\mu R/h$. The RPMs shall not trigger false alarms above one on 1000 passages at a background level not less than $5\mu R/h$.

1.3.4 Radiation Detectors and Hand-held Radioisotope Identification Detectors

Personal radiation detectors (PRDs) are light, small, high sensitivity and battery-operated devices. They are about the size of a mobile phone to be easily worn at the belt or carried around in the pocket (Figure 1.7). They allow for a hands-free scan providing alarms if a suspicious level of radiation is detected. They are mainly used for personal protection of officers involved in nuclear security scenarios. Those instruments, based on scintillator detectors[2] like the CsI or the NaI, are factory calibrated, and they guarantee 400h of operation. The false alarm should not occur more than once per hour since any alarm has to be verified, moving the PRDs close to the source or person suspected to have triggered the alarm. The PDRs emits audible, luminous or vibrating signal whose intensity is proportional to the radiation field, in this sense when the PRD is closer to the source it will emit higher signal, allowing for a localisation of the source; this kind of scan should be performed no farther than 15 cm from the surfaces of the pack suspected to contain a source [15, 41, 42].

Fig. 1.7: Example of Personal Radiation Detectors [15].

There also exists **Hand-held devices** with a radioisotope identification capability (RIIDs). Even if they do not allow for hands-free operation, Hand-held RIIDs are very flexible instruments since they can be used as primary detector search for radioactive sources when there is no forced flux of people, good or vehicles trough a choke point or to confirm alarms from RPMs. Those instruments are inherently more complicated, and the operators have to follow the training since the human factor in non-fixed radiation detectors is of vital importance. When they are used as a secondary detector to confirm the alarm from an RPM, the instrument should be kept

[2] Other Geiger-muller or gas proportional counter detectors are commercialised, but they do not meet the latest European and ANSI standards.

at few centimetres from the package surface and moved slowly. If the alarm level is constant all around the package, it is most probably a NORM that triggered the alarm since an RDD o SNM would appear as a localised source. More information can be obtained if the detector is capable of identifying the source by analysis of the energy spectrum.

Fig. 1.8: Example of Hand-held Gamma or Neutron Search Detector and Radiation Identifier Detectors [15].

The preferred γ detectors are based on NaI or CsI. Since it is not possible in general to distinguish between the neutron and the γ alarms using plastic scintillators, they are rarely used in RIIDs, and an additional detector is used for the neutrons, typically a ^{3}He tube. NaI/CsI detectors are more often used since they allow to identify the radionuclide better. Hand-held instruments usually measure on a time scale of about 0.5 seconds, that is also the required time to trigger an alarm. Sometimes those instruments can have a α/β probe to check if any surface contamination occurred. To be qualified as a RIID a hand-held instruments must:

- measure the γ spectra over a range that covers energy from 30 keV to 3 MeV;
- process the spectrum to determine the energy and the area of the spectrum lines, as well as the overall spectrum shape;
- embed a decision logic to compare the spectrum lines and shape with lookup tables;

- use decision making filters to assign the energy to the correspondent radionuclide, especially in case of shielding with a heavy box or within other licit radioactive material to mask the line of the smuggled source.

With RIIDs not only radionuclide have to be identified, but also the instrument should clearly state the category at which they belong: Nuclear Material, Medical Radionuclides, Industrial Radionuclide or NORMS as specified in Section 10 of IAEA Reference Manual for Illicit Trafficking prevention at Borders[15].

Small neutron detectors are, instead, less sensitive and not suitable to correctly identify a weak neutron source in a short time. Indeed to obtain reliable information, mainly when weak neutron field is expected, they can be operated to measure neutrons flux on a larger time scale.

According to the ANSI 42.35 standard, RIIDs are required to trigger an alarm, in 1 second, when an immediate increase of 50$\mu R/h$ from a ^{137}Cs source to the background occurs. Within 5 seconds, the instrument shall indicate the new dose rate with a maximum error of 50%. When the radiation field returns to its original values the decrease shall be indicated in 1 second, and in 5 seconds the instrument has to indicate the new level of radiation with a maximum error of 50%. The relative intrinsic error in the response od the instruments to a ^{137}Cs dose shall not exceed the 30%. In order to test this specification the measurement procedure requires that when a threshold for an alarm is set at 1 mR/h dose rate, an instrument exposed to a 2 mR/h radiation field from a ^{137}Cs source, an alarm shall be triggered within 3 seconds. When exposed to an unmoderated 0.01μg ^{252}Cf source at about 25 cm from the detector, the neutron alarms shall be activated within 2 seconds. The radionuclide identification requires that, when exposed to a 50$\mu R/h$ dose rate, the detector identifies the source and the category in 8 runs on ten consecutive trials. The instruments shall be able to identify, with this confidence level, at least two sources at the same time. This test is usually performed with a ^{241}Am and a ^{232}Th sources. These requirements shall be met even in the presence of a γ radiation from a strong β shielded source (bremsstrahlung, x-rays photons etc...). The false alarm rate is tested in a 10 $\mu R/h$ radiation field, and the instrument must not identify any radionuclide in 8 out of 10 consecutive trials. The only radionuclide accepted is the NORM ^{40}K, and if it can not be removed or shielded the instruments must identify only this radionuclide. Those tests are repeated placing a steel plate between the source and the detector, in order to test whether the instruments are capable of radionuclide identification even in the presence of surrounding material that may alter the energy spectrum.

The neutron alarm, on the other side, shall be tested under ^{60}Co radiation field up to the maximum dose rate specified by the manufacturer, the neutron alarm shall be activated only in the presence of a neutron source, and not by the high γ dose rate.

Radionuclide	Activity
^{57}Co	$93\mu Ci(3.5\ MBq)$
^{133}Ba	$23\mu Ci(0.85MBq)$
^{137}Cs	$16\mu Ci(0.6MBq)$
^{60}Co	$4\mu Ci(0.15MBq)$
^{228}Th	$7\mu Ci(0.26MBq)$
^{241}Am	$462\mu Ci(17MBq)$
Neutron ^{252}Cf	$2 \cdot 10^4 n/s \pm 20\%$

Tab. 1.2: Activity of the sources used in standard tests shall be within 20% of the values reported in the table

1.3.5 Diffuse Monitoring

In the last few years, an increasing attention in the field of nuclear security have been focused on the security in towns or in at the so-called Major Public Events as defined by IAEA, like the Beijing Olympics Game, the Youth Days in Panama, big musical festival or International Politics Meeting (G8, G20 etcetera) [44]. In those situations, the typical security measures should be further integrated by a novel concept called *diffuse monitoring*. The concept behind the diffuse monitoring is to create a network of detector that can measure the radiation level on a large area. For this reason, small and portable detectors are appealing for this specific application since they can be mounted on drones, distributed to bus and taxi drivers, letter carriers, police officers, security staff, or placed in fixed point (like a traffic light) around the most sensitive target. Each of the RIIDs used in a diffuse monitoring application should be connected to a central hub where it can send information, geo-tagged and time-tagged, about the radiation levels measured. The resulting grid of detector, whose information are aggregated and centrally analysed, allows moving the paradigm of nuclear security from fixed checkpoints to continuous and capillary monitoring.

An example of those detectors is the one commercialised by Kromek Group: the DS3-Net [45]. Each unit consists of a RIID (Figure 1.9) that connects via Bluetooth to a smartphone.

A dedicated application sends the measurements results and the GPS data to a central unit that process the data and eventually send to the app an alarm. The diffusion of the instruments and the central processing of all the information allow them to build up a map of the measured level of background in a wide area. A

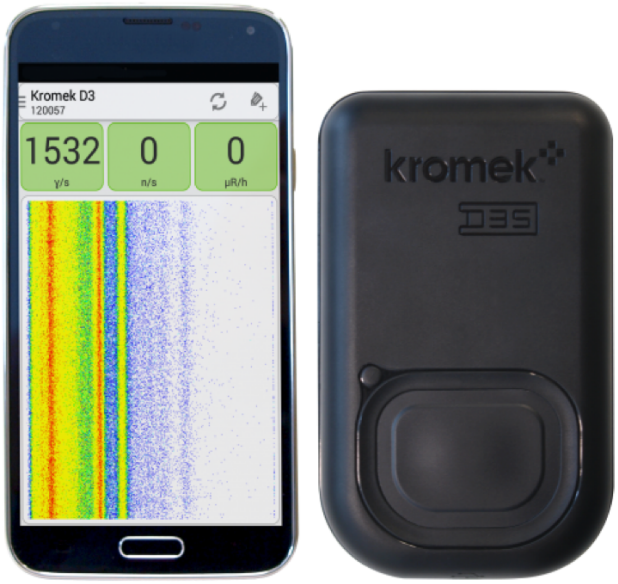

Fig. 1.9: D3S Detector commercialised by Kromek Group plc [45].

system like that can be easily embedded in a drone to increase the area that can be monitored [46].

Figure 1.10 shows the background radiation level changes as a function of position within the city. This is related to the amount of people, goods and buildings populating the area. This highlight the need for an alarm threshold level that is, again, a function of the position. In case of Diffuse Monitoring, the threshold is computed by the central computational unit while in case of the RPMs, PRDs and RIIDs it is now clear why the background evaluation is so important to meet the failure rate required by IAEA.

At the current stage, all the instruments considered by the standard procedures and protocols are based on two different detectors for γ and neutron radiation to meet the sensitivity criteria for γ and neutron radiation. However, in the last two decades, the advancement in detectors technology allows building detectors that are not only sensitive to both radiations but also capable to discriminate the detected one. This feature could be of great interest since it would allow increasing the detector volume within the same dimensions of the market-ready detectors nowadays in use. This thesis will focus on the study of those materials, and in particular features that, in the signal acquisition chan, would impact the most on discrimination capability, since, in a mixed γ and neutron field, good discrimination would make possible to meet the IAEA sensitivity criteria.

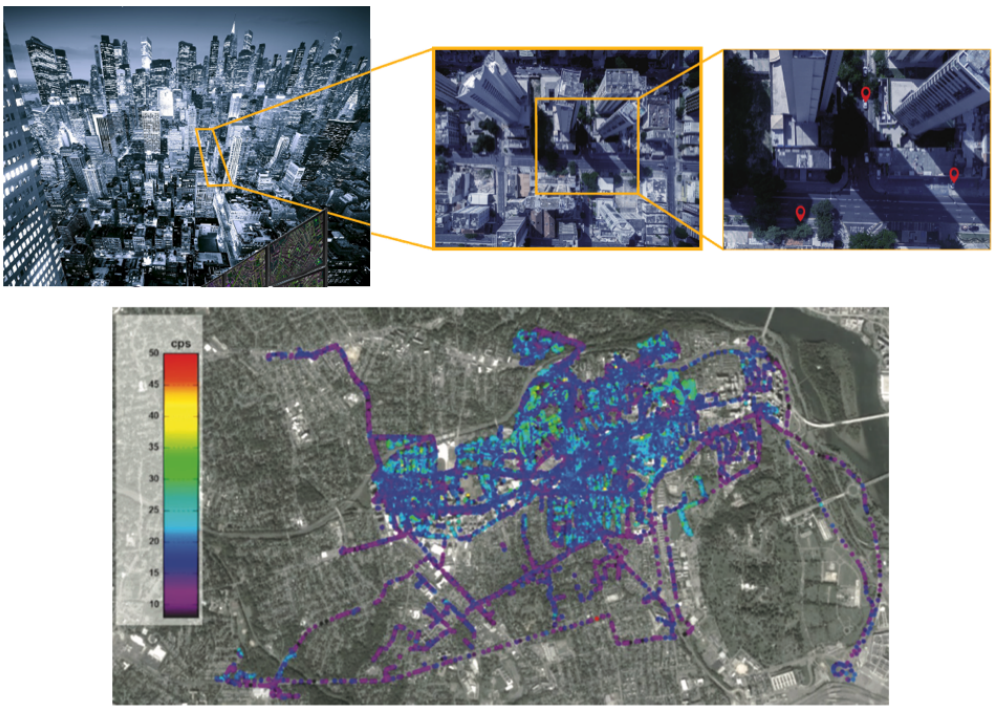

Fig. 1.10: Image of the reconstructed map of background radioactivity in a city with the D3S-Net instrument [45].

2 Novel approach to γ-Neutron discrimination

State of the art portable radiation detector can be based on two different strategies to be effective and meet the sensitivity criteria and the $GARR$ level required by the standards mentioned in the previous chapter. On the one hand, the use of two different detectors for γs and neutrons, on the other hand, a single active volume sensitive to both radiations at the same time can be used. In the first case volumes, threshold and signal processing strategies are different and optimised independently for the two detectors embedded in a single instrument. In the second case, discrimination techniques should be optimised in order to make the particle identification good enough to avoid misidentification that would worsen the $GARRn$. This chapter will start with a review of the techniques for neutron detection when two separate detectors are used, while in the second part of the chapter I will review the solution for a combined γ and neutron detection. The combined detection is based on those novel scintillators capable of distinguishing particles according to the different light temporal development they trigger in the scintillators, called Pulse Shape Discrimination (PSD) capable scintillators. Several algorithms exist to distinguish particles according to the signal shape in PSD scintillators. In this chapter it will be presented digital PSD algorithms that could be easily implemented in a portable, battery-operated and low computational power instrument. The discrimination qualifier will also be introduced along with the leading results found in literature about the measured performances of Pulse Shape Discrimination capable scintillator coupled with SiPMs.

Introduction to radiation detection

Scintillators as γ detectors are the preferred one because the energies of interest (between 60 and 1400 keV) are detected with a lower cost with respect to other solutions, and with the benefit of well-established production technology. Scintillators are an optimal solution since they can measure the dose and allow for a Radiation Identification by analysing the energy spectrum obtained from a high Z scintillator (in RIID the most used are NaI and CsI).

On the other hand, neutron detection is not straightforward since the energies of interests does not allow for uniques detection techniques. Indeed, in Nuclear

Security scenario, both slow and fast neutrons are expected, and this requires a priori detection strategy to be defined. In case of separate neutrons and γ detection, the neutron detection strategy will not interfere with the γ detection one, while in the combined detection, a choice of a strategy for neutron detection that depends on energy, has an impact on the γ detection capabilities.

2.1 Neutron Detection

Neutrons are classified as a function of their energy: the so-called *slow* neutrons have energy below 0.5 eV, and they are called *thermal* if they are in thermal equilibrium with the environment. Neutron in thermal equilibrium at room temperature (25^o) corresponds to neutrons with a Maxwellian energy distribution with mean value 0.025 eV. Neutrons with energy greater than 0.5 eV up to several MeV are called *fast*. Sources of concerns in a nuclear security scenario emit fast neutron, but in order to be transported safely smugglers shield the source; the effect of the shielding is to reduce neutron energy down to the slow or thermal energy. A key point in this energy classification is that the interaction between neutron and detector strongly depends on the neutron energy, and so far it does the kind of detector that can be used to identify one or another neutron energy class. Slow neutron detection would allow detecting the sources in the majority of the case as reported in the ITDB. However, fast neutron detection suffers less from background contamination, and fast neutrons, however, emerge from the shield. Most of the neutron detectors produce a response even to γ rays, but with lower efficiency. So far in most of the neutron detector is possible to ignore the response to the γ since they are however capable of meeting the gamma insensitivity criteria expressed in the Chapter 1. It is anyhow essential to understand the working principle of the most used detectors embedded in small and portable instruments. The neutron interaction with matters happens mainly via head-on collision with atomic nuclei, and they can result in a recoiling nucleus, mainly in fast neutron interaction, or in fission fragments, mainly due to the slow ones [47]. The cross-section and the subsequent detection probability strongly depends on the neutron energy, as reported in Figure 2.1 for the three most used converters in neutron detectors.

2.1.1 Slow Neutron Detection

Table 2.1 reports the reaction of the most used converters for slow neutron detection. Those converters are widely used since their reactions with neutrons have high Q-values. Thus they create easy to detect heavy charged particles or high energy γ ray. Slow Neutron detectors are mainly based on proportional counters or scintillators. The use of silicon detector is not prevalent in this field since they are expensive, and

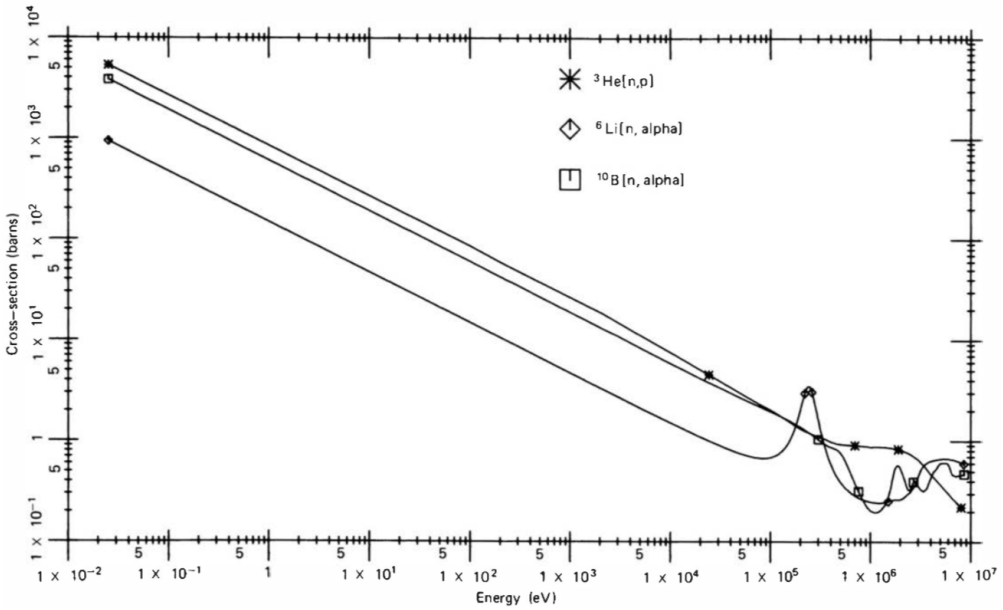

Fig. 2.1: Neutron capture cross section for ^{10}B[n,α], ^{6}Li[n,α] and ^{3}He[n,p] reactions, as reported from [47]

they work at low temperature in a controlled environment; nevertheless, they are widely used for neutron imaging or spectrometry in scientific research [48, 49].

In principle detectors for thermal neutron detection should show as response a spectrum with a single peak of the full energy (Q-value) from the reaction product. Due to the high Q-Value in most detectors, especially the gas-based, discrimination versus γ rays can be performed by the sole pulse amplitude. However, boundary effects and active volume size may introduce features in the spectrum that would require accurate post-processing in order to obtain the correct neutron measurement.

n +	Product	Q Value	Final State	$\frac{d\sigma}{d\Omega}$ barns	Natural Abundance
^{10}B	^{7}Li + α	2.792 MeV	Ground	230	20%
^{10}B	^{7}Li* + α	2.310 MeV	Excited	3610	20%
^{6}Li	^{3}H + α	4.78 MeV	Ground	940	7%
^{3}He	^{3}H + p	0.764 MeV	Ground	5330	0%
^{113}Cd	γ cascade	9 MeV	Excited	20000	12%
^{156}Gd	γ cascade	8 MeV	Excited	61000	15%
^{157}Gd	γ cascade	8 MeV	Excited	260000	16%

Tab. 2.1: Main Neutron Capture reaction for slow neutrons. The total cross section for neutron capture by boron is 3840 bars, 6% of the events left the lithium product in the ground state, while the remaining 94% events leave the lithium in the excited state. Capture from Lithium and Helium always gives product in the ground state [47, 2].

2.1.2 Proportional Counters

^{3}**He** based detectors are proportional counters that are considered standard detectors for nuclear detection in many fields. Their intrinsic insensitivity to γ rays fulfils the prescription of the [43] and makes them suitable for their use in Radiation Portal Monitors, where the dimensions of detectors are not an issue. The shortage of ^{3}He, since it is a by-product of nuclear weapons production process, increased its price, and it is not possible to build a ^{3}He tube suitable for a small hand-held pager-size portable device as the one presented in Section 1.3.5.

Boron Based Proportional Counters are a BF_3 gas tube that can be used in place of ^{3}He. However, the BF_3 gas is toxic, and it suffers from poor discrimination in case of high γ ray flux [47]. In fact, in those proportional counter, the possibility that one of the two fission fragments escape the tube is non-negligible because the gas pressure should not exceed 1 atm [47]. This is the cause of the so-called wall effect, a distortion of the fission fragment energy spectrum that may introduce a misidentification of γ as neutrons, altering the $GAARn$. An exemplary spectrum is reported in Figure 2.2. Both high gamma flux and small dimensions of the active volume can reduce the gap between the pulses of the γ and the pulses of the neutron resulting in an overlap of the γ and neutron regions.

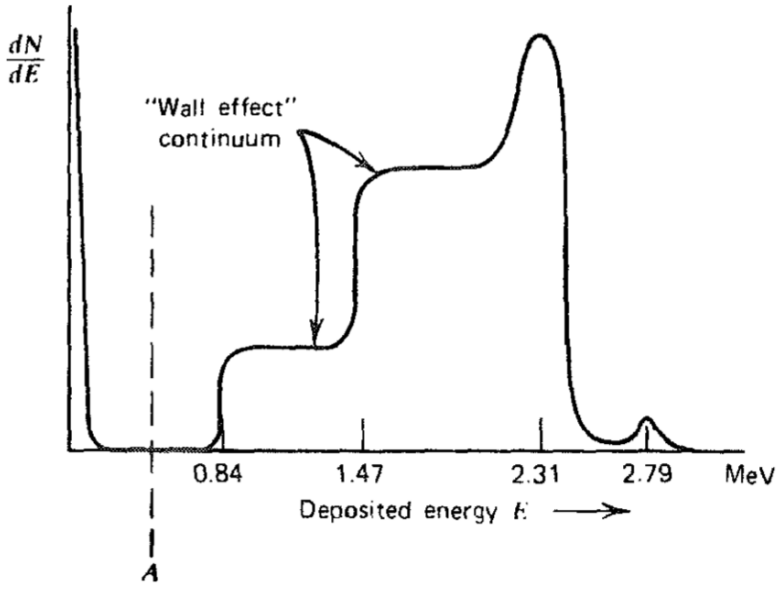

Fig. 2.2: BF_3 proportional counter spectrum: line represent the $gamma$ threshold above which the detected events are tagged as neutrons

To partially overcome the toxicity and the non-ideal properties of the BF_3 as proportional counters, it is also possible to coat with ^{10}B the inner side of a standard proportional counter detector. In this case, to allow the fragments to reach the active volume, a tiny layer of ^{10}B should be deposited, affecting the neutron capture

efficiency and the γ discrimination. Other solutions based on the suspension of nano-particles of B_4C, whose diameter is less than the range of the disintegration fragments are currently under study. Those solutions can be useful for the RPM, but the technology is still not mature enough since the nano-particles tend to fix to chamber walls with consequent reduction of detection efficiency over time [2].

2.1.3 Scintillators

Thermal neutrons can be detected with standard scintillator materials doped or covered with a converter, most likely the Lithium or the Boron. ZnS can be mixed with LiF with 95% enriched ^{6}Li or with ^{10}B. ZnS can produce up to 160000 photons per neutron converted by the ^{6}Li capture reaction. It is not very translucent to its our scintillating light, and effective light collection can be achieved if the scintillator is thinner than 1 mm [50], reducing neutron efficiency. Moreover, the enrichment of LiF is a costly procedure. However, companies like Scintacor, Eljen and Saint-Gobain produce ^{6}Li/ZnS screens for neutron detection [51, 52, 53]. Boron mixed with ZnS scintillator are also available and manufactured by Bridgeport Instruments [54]. This scintillator is less performing than the ^{6}Li based one since even though the neutron capture cross-section for the Boron is higher even at the natural isotopic composition, the Q-value of the reaction is lower.

Another very used option is to load liquid organic scintillators with ^{6}Li, ^{10}B, Gadolinium or Cadmium. The liquid scintillators act as moderator, as a converter and as charged particle detectors but, in the case of Lithium or Boron loading, they result in a poor light yield for neutron absorption, equivalent less than a 400 keV electron. Therefore is necessary the use of Pulse Shape Discrimination methods, algorithms that allow for the determination of the nature of impinging particle (γ or neutron) based on the analysis of the full waveform acquired with a fast Data Acquisition system. Gadolinium and Cadmium, on the other side, produce a cascade of γ rays whose total energy is 8-9 MeV; so far a detector with a volume large enough to absorb all the γs in necessary to achieve good discrimination based on pulse amplitude. An advantage of liquid scintillators is their intrinsic sensitivity to fast neutron, but they are not widely used in nuclear security application for concerns raised by the toxicity and flammability of the scintillator itself. Liquid scintillators are, on the other hand, widely used in neutron and neutrino research where large volume and affordable detectors are the preferred solution [2].

Solid plastic scintillators loaded with ^{6}Li or ^{10}B are not commercially available even if they are not toxic nor flammable and can be manufactured in different shape and sizes. They generally have a lower light yield requiring a pulse shape analysis to discriminate γ from neutrons [55, 56].

Arktis commercialise a gas scintillator tube lined with ^{6}Li, based on ^{4}He as scintillating gas [57]. This solution, however, suffers from the same drawbacks of the Boron-based proportional counters in terms of Lithium coating thickness and consequent thermal neutron detection efficiency [2].

Scintacor and Saint-Gobain commercialise the used for decades ^{6}Li based glass scintillators. Those detectors are a well-established technology in neutron detection. However, they are not suitable for nuclear security for two reasons. On the one hand, neutron capture events have the same amplitude of a 1.5 MeV γ ray due to quenching mechanism inside the glass. On the other hand, the pulse shape of a γ or a neutron-induced pulse are almost identical, so nor amplitude nor pulse shape analysis can be used to efficiently for particle discrimination [50].

2.1.4 Fast Neutron Detectors

Nuclear reaction with ^{3}He, ^{6}Li or ^{10}B can be used as well to detect fast neutron, but they have a low cross-section, and those reactions may not guarantee the neutron sensitivity for fast neutron in small detectors required by the standards. Indeed since the cross-section for high energy neutrons is fewer than 10 barns (Figure 2.3), a detector 100 times larger would be required in order to meet the same efficiency [47] of slow neutron detection even for fast neutron. However, the direct detection of fast neutrons is possible, and it opens up the possibility to determine the direction of the incoming neutron. This information can be used both to determine the localisation of the source better and to reduce the background. The energy alone can not reduce the background since the cosmic neutrons are in the fast neutron energy range. In addition to that, the possibility to retain the energy information is of great importance in the determination of the source type and eventually the shielding, not to mention that the lack of moderator allow to build the very compact detector, pretty useful for the diffuse monitoring application [2]

Fast neutron detectors rely on the scattering of neutrons with the Hydrogen. The cross section of the fast neutron detection depends only on the scattering cross section σ_s, so that the detection efficiency (ϵ) goes as an exponential function for the single interacting material:

$$\epsilon = 1 - e^{-N\sigma_s d} \tag{2.1}$$

Where the N is the density of target nuclei, and d is the pathway through the material. In most cases, like plastic scintillators used for fast neutron detection, the

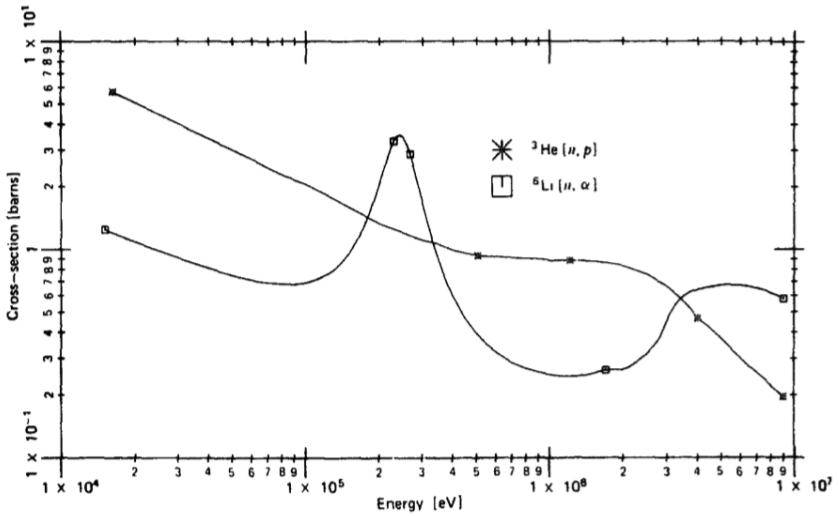

Fig. 2.3: Cross section for nuclear reaction $^3He(n,p)^3H$ and $^6Li(n,\alpha)^3H$ induced by fast neutron as reported in [47].

most probable scattering is against hydrogen and carbon nuclei. Equation (2.1) should be then modified as in (2.2).

$$\epsilon = \frac{N_h \sigma_H}{N_H \sigma_H d + N_C \sigma_C} \left(1 - e^{-(N_H \sigma_H d + N_C \sigma_C) d}\right) \tag{2.2}$$

Even if it does not exist an analytical expression for the scattering cross-section, an empirical fit of the form in Equation (2.3) was proposed by Marion and Young [58, 47].

$$\sigma_s(E_n) = \frac{4.83}{\sqrt{E_n}} - 0.578 barns \tag{2.3}$$

Non-relativistic neutrons have energy below 939 MeV, that is the case in a nuclear security application, and the energy transferred to the recoiling nucleus can be estimated by imposing the momentum and energy conservation. The energy of the recoil nucleus E_R with mass A depends on its recoil angle θ and the incoming energy neutron E_n as in Equation (2.4). The interaction mechanism is sketched in Figure 2.4 for a laboratory coordinate reference system[47].

$$E_R = \frac{2A}{(1+A)^2} cos^2\theta E_n \tag{2.4}$$

The only case in which the neutron energy can be transferred entirely to the nucleus is in the case $A = 1$ and $\theta = 0$, namely for the neutron backscatter by a hydrogen atom. Angles other than 0^o give rise to a continuum in the distribution down to 0. In all the other cases, only a fraction of the neutron energy is transferred. It is possible, thanks to unfolding techniques, to recover the energy spectra of the neutrons to identify the source and possible shielding [59].

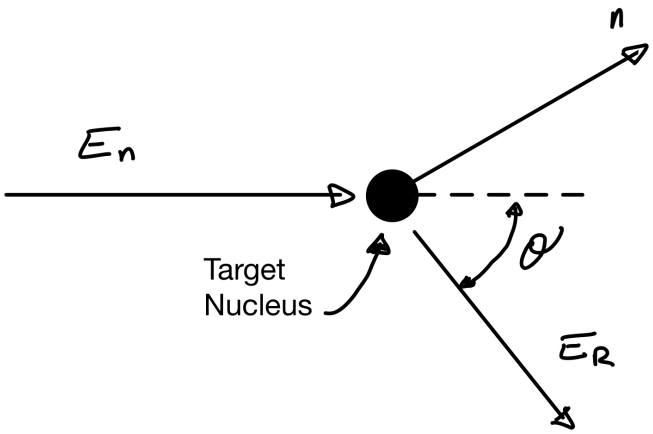

Fig. 2.4: Neutron scattering in laboratory reference system

These scintillators are intrinsically sensitive to γ rays, so far it is mandatory to have techniques to distinguish the two particles. Time of Flight measurements to separate γ from neutrons is the preferred and the most robust techniques, but it can not be used in a portable detector [47].

2.2 Pulse Shape Discrimination scintillators

A PSD scintillator sensitive to all neutron energy of interest does not exist. Moreover, the choice of the energy of interest for neutron detection in PSD scintillators defines even the γ interaction, so far the radio-nuclide identification capability. The two most used varieties of PSD scintillators are the inorganic and the plastic scintillators with enhanced pulse shape discrimination capabilities. Inorganic elpasolite scintillators are high Z materials doped with ^{6}Li. The ^{6}Li dopant makes those scintillators sensitive to thermal neutrons via nuclear capture reactions, and the high Z allows for the photo-peak absorption of γ rays in the energy of interest (60 keV - 1.4 MeV) allowing for a radionuclide identification via peak spectrum analysis. On the other hand, organic scintillators detectors allow for fast neutron scattering on hydrogen or carbon nuclei. They have a low Z, so far the most probable γ interaction for the energy of interest is the Compton scattering, not allowing for the radionuclide identification but only for the dose evaluation. Other solutions, like composite

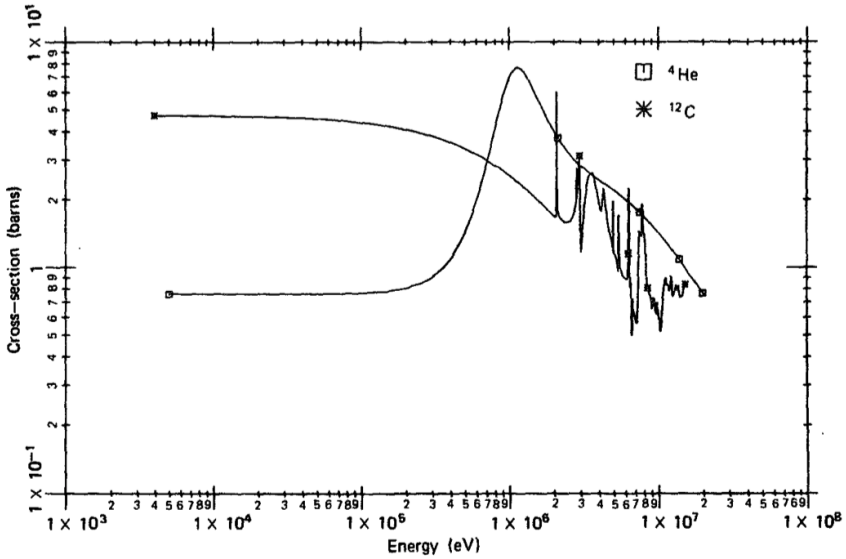

(a)

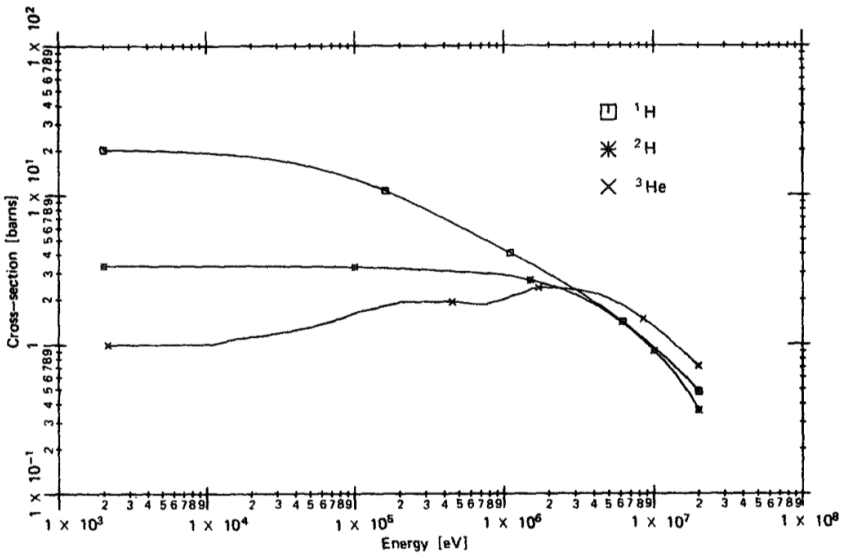

(b)

Fig. 2.5: Elastic Scattering cross section $\sigma_s(E_n)$ for Hydrogen, Deuterium, Helium (in the isotopes ^{4}He and ^{4}He) and for carbon as reported in [47].

scintillators obtained by coupling plastic and ZnS/^{6}Li scintillator, can be engineered, but they are not widely used so they will not be treated in this dissertation [60].

2.2.1 Elpasolite scintillators

A key element in elpasolite scintillators is the presence of Lithium, that enriched in ^{6}Li at 95% guarantees a good thermal neutron detection efficiency without altering the scintillation properties of those material thanks to the well-established growth methodology [61]. Cerium used as a dopant in elpasolite has a strong influence in the light temporal distribution since it affects the lifetime of excited states at the base of light generation [62]. Temperature influences as well not only the light output but also the pulse shape differences [63, 64]. Another drawback is that those scintillators are highly hygroscopic, so dedicated housing is required in on-field use. Detection of the alpha particle generated by the neutron-induced reaction ^{6}Li(n,α)^{3}H, produces the same amount of light of a γ ray between 3 and 3.5 MeV and it is possible to achieve neutron-gamma discrimination based on sole pulse amplitude [65]. To further improve the purity of neutrons detected events, additional discrimination can be achieved with pulse-shape discrimination techniques [66].

One of the most used elpasolite is the **CLYC**, whose chemical formula reads $Cs_2LiYCl_6(Ce)$. It has a capture efficiency slightly above 10% and an energy resolution of 662 γ ray from ^{137}Cs of 5% as measured in [67]. The different pulse shape depends on the difference in excited levels of the crystal energy levels according to the ionising density. Light is emitted with 3 decay time constant τ_1, τ_2 and τ_3. For the CLYC in particular low ionising density associated to the electron detection from γ ray absorption excites the valence electron giving rise to the so-called Core Valence Light (τ_1) that presents typical decay time in the order of $1ns$. This light is associated with the transition from the 5p level of the Cs^+ core band to the 3p level of Cl^- valence band. Scintillating photons may be absorbed by the dopant and re-emitted with a typical time constant of 30ns. Due to the so-called deep-trapping mechanism, the charge carrier could be trapped in an excited state of Ce^+ and released with a time constant τ_2 of $1\mu s$ as reported in [68].

The third component of the scintillating light arises from an exciton-Ce^+ interaction and its typical light time decay time τ_3 lies between 1 and 6 μs according to the percentage of the dopant. Core Valence Light is present only under γ excitation, while the processes that give rise to the $\tau_{2,3}$ components of scintillation light are always present. CLYC can be used not only for thermal neutron detection. Indeed, if it is enriched in ^{7}Li, it showed neutron spectroscopy capability [70]. However, the poor resolution for fast neutron spectroscopy and the reduced thermal neutron efficiency limits the diffusion of this solution.

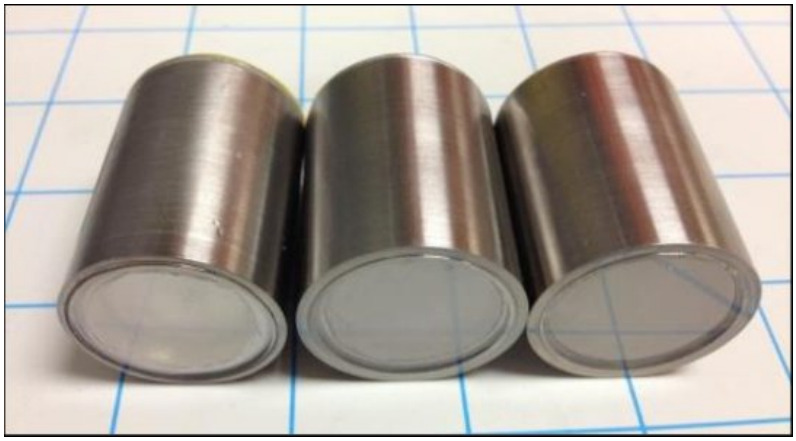

Fig. 2.6: Images of the CLLC scintillators from [69]

CLLC is similar to the CLYC, but with Lanthanum instead of Yttrium, since it is a little brighter it presents a 662 γ ray resolution of 3.5%, but it suffers from internal activity due to the presence of Lanthanum. **CLLB** and **CLLB-C**, with chemical formula $Cs_2LiLaBr_6(Ce)$ presents a higher light yield that results in an energy resolution of the 662 keV peak below 3%, but it presents internal activity due to the Lanthanum a slightly worst pulse shape discrimination capability [62].

2.2.2 Plastic PSD scintillators

Pulse shape difference in plastic scintillators is obtained by means of optimisation of scintillating primary and secondary dye ratio in the plastic matrix. Emitted photons can be up to a factor 2 in some components, making relatively easy the particle tagging. The effect of different % of dye was studied mainly since in some concentration the ageing effect is not negligible, making the scintillators no longer suitable for nuclear security purposes [47]. Nowadays, the Polyphenol oxidase (PPO) dye concentration can be higher than 20% and up to 36%. The secondary dye can be a POPOP benzene scintillator used as a light wavelength shifter. 7-diethylamino-4-methyl coumarin secondary dye used in place of POPOP can enhance both the light output and the PSD capability as reported in [71].

The addition of divinylbenzene (DVB) was tested to contain the ageing at different concentration of secondary dye (PPO) as reported in [71]. Moreover, post-treatment techniques of scintillators with ethanol (EtOH) allowed recovering the surface detriment when PPO concentration exceeds 30%.

To further reduce ageing, the use of non-aromatic molecules (like PMMA) as a medium to solve aromatic Lithium salt has experimented, but it resulted in a reduced light output that makes difficult the discrimination of γ and neutron [72]. Higher

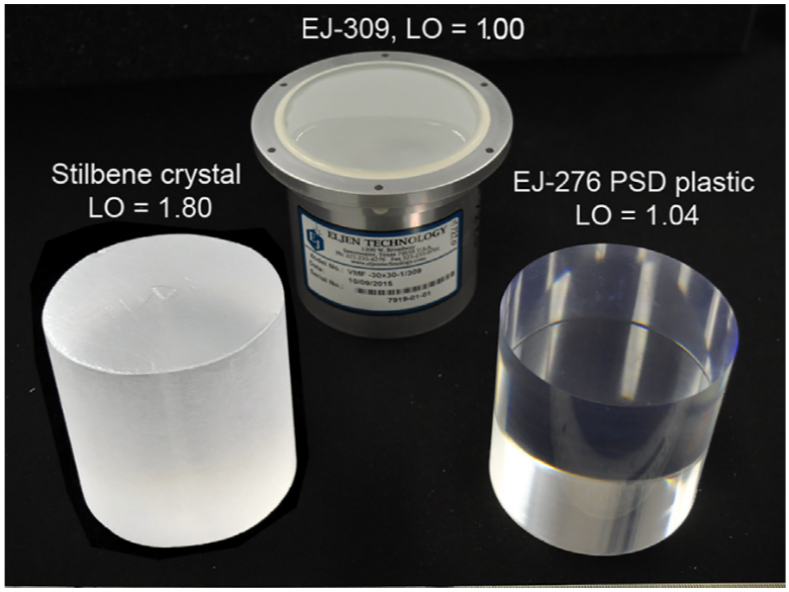

Fig. 2.7: Images of Plastic Scintillators with PSD capability scintillators with relative Light Output (LO) from [71]

it is the solubility of the Lithium salt, more probable is the light quenching from the PPO; on the other side, increasing the number of rings to reduce the solubility produces a red-shift in the generated light that reduces, even more, the total light output.

2.2.3 Pulse Shape Discrimination scintillators for Nuclear Security

The main characteristics of the scintillators in use in nuclear security with pulse shape discrimination capable scintillators are reported in Table 2.2. A comparison of γ spectroscopy capability with standard scintillators for γ spectroscopy is reported in Figure 2.9. In particular, the materials reported in this subsection are the ones used in the literature summarised in the Section 2.5.

In this dissertation, the crystal used in order to compare and to evaluate the two detection strategies are the CLLB and the EJ-276 since their emission light wavelength matches the maximum efficiency of the Silicon Multipliers used.

2.3 Pulse Discrimination Algorithms

Several algorithms have been proposed to distinguish particles according to the signal shape from PSD scintillators. The discrimination algorithm used, may be

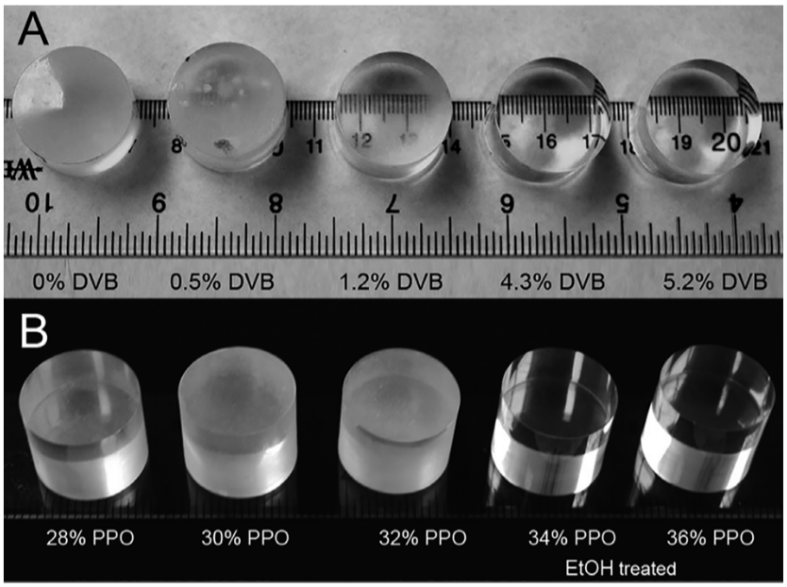

Fig. 2.8: Images of one year old PSD plastic scintillator developed at Lawrence Livermore National Laboratory with different concentration of PPO, DVB tested to reduce the ageing effect [71]

either the computation of a single observable that, according to a threshold value, determines if a signal is most likely be produced by a neutron or a γ or more complicated discrimination scheme based on the analysis of the pulse shape by a neutral network in machine learning or artificial intelligence application. The discrimination techniques of interest for this thesis are the one requiring low computational power, so far the Neural Network is not detailed. Exemplary results of a machine learning discrimination algorithm will be presented at the end of the chapter. The temporal distribution of photons mostly differs in the long decay component, and an observable that could enhance and measure this difference is the core of the majority of pulse shape discrimination algorithms. In analogue electronics, the algorithms for particle identification were the Zero-Crossing and the Charge Comparison. These

	g/cm^2	**ph/MeV**	λ_{peak} **[nm]**	$\frac{\Delta E}{E}_{662keV}$	τ_γ **[ns]**	τ_n **[ns]**
CLLB	4.2	40000	420	$\leq 4\%$	180(61%) 1080(39%)	180(50%) 1080(50%)
CLYC	3.31	20000	370	$\leq 5\%$	1 50 1000	N.A. 50 1000
EJ-276	1.096	8600	425	N.A.	13 35 270	13 59 460
Stilbene	1.15	10700	390	N.A.	5 21 135	5 27 255

Tab. 2.2: Main characteristic of the most used plastic and inorganic scintillators suitable for Nuclear Security Applications as reported from produced data-sheets [73, 74, 75, 76]

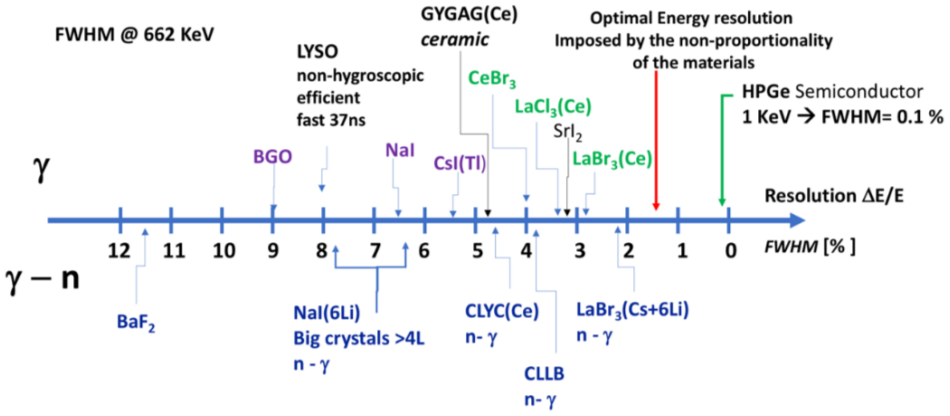

Fig. 2.9: Different γ detection performances of PSD scintillators compared to standard γ scintillator detectors [2]

two discrimination schemes were implemented in an analogue circuit configuration. The first one consists in a filter that transforms the detected signal into a bipolar pulse: the time between the trigger and the zero-crossing is retained as discrimination parameter [77] since it was longer for the particle with the long decay component. The Analogue Charge Comparison (CCA) is an algorithm that retains as discrimination parameter the ratio between the integral of the signal and the charge integrated into the tail via a combination of different RC circuits, as described in [78]. With the advent of the digital era, those algorithms were implemented in digital circuits. The zero-crossing that was the most promising one in the analogue implementation failed to be as effective in the digital implementation due to the finite resolution with which was possible to implement the digital filter. Charge Comparison, on the other hand, proved to be more fruitful, but also other algorithm born due to the potentiality opened up by the digital signal treatment. The general approach was to compare:

- the charge in the tail
- a point in the signal falling edge

with respect to:

- the total charge in the signal
- the signal amplitude

The algorithms presented in the following section is then the possible combination of these quantities as they are easy to be computed with digital circuits, so far usable in a real case scenario.

2.3.1 Digital PSD algorithms

The digital version of the CCA showed better performances concerning the digital implementation of the zero-crossing time method since the digital filter that shapes the signal is not as effective as the analogue one in discriminating particles [79].

2.3.2 Algorithm for on-line discrimination

Among the one found in literature, four algorithms for pulse shape discrimination were compared, since they are the one most suitable to purse on-line discrimination in a small device with low computational power.

- *Constant Time:* The Constant Time (CT) algorithm discriminates based on the value of the signal $S(t)$, at time t concerning the onset, normalised to the total signal area [80]

$$PSD = \frac{S(\bar{t}_{CT})}{\int S(t)dt} \tag{2.5}$$

  Where $\bar{t}_{CT}$ is the time-lapse since the onset of the signal.

- *Pulse Gradient Analysis:* The Pulse Gradient Analysis (PGA) algorithm discriminates the pulses on the basis of the value of the signal $S(t)$, at time t with respect to the onset, normalised to the peak [81].

$$PSD = \frac{S(\bar{t}_{PGA})}{max\{S(t)\}} \tag{2.6}$$

  where, as above, the $\bar{t}_{PGA}$ is the time lapse since the onset of the signal.

- *Charge comparison:* The Charge Comparison algorithm (PSD_{CC}) discriminates the pulses on the basis of the ratio between the integral of the signal tail and the total signal area. [82]

$$PSD = \frac{\int_{t_{delay}}^{t_{int}} S(t)dt}{\int S(t)dt} \tag{2.7}$$

  where t_{delay} is the time lapse since the onset of the signal from where the integration window, that last t_{int}, starts.

- *Peak - Tail:* The Peak-Tail algorithm (PSD_{PT}) is a new proposed algorithm in which discrimination is obtained by normalising the signal to the peak value rather than the total area, and considers the integral value in the tail.

$$PSD = \frac{\int_{t_{delay}}^{t_{int}} S(t)dt}{max(S(t))} \tag{2.8}$$

where t_{delay} and t_{int} are defined as for the CC algorithm.

2.4 γ-neutron discrimination qualifiers

In order to tag the detected particle, a threshold is set on PSD parameter value in order to determine which was the impinging particle nature. The standard qualifier to quantify the discrimination power is the Figure of Merit ($F.o.M.$) defined as the distance between the centroids of the γ and neutron related PSD distributions, divided the sum of their Full-Width Half Maximum (FWHM), as in Equation (2.9)

$$F.o.M. = \frac{\Delta_{PSD}}{FWHM_{\gamma_s} + FWHM_{neutrons}} \tag{2.9}$$

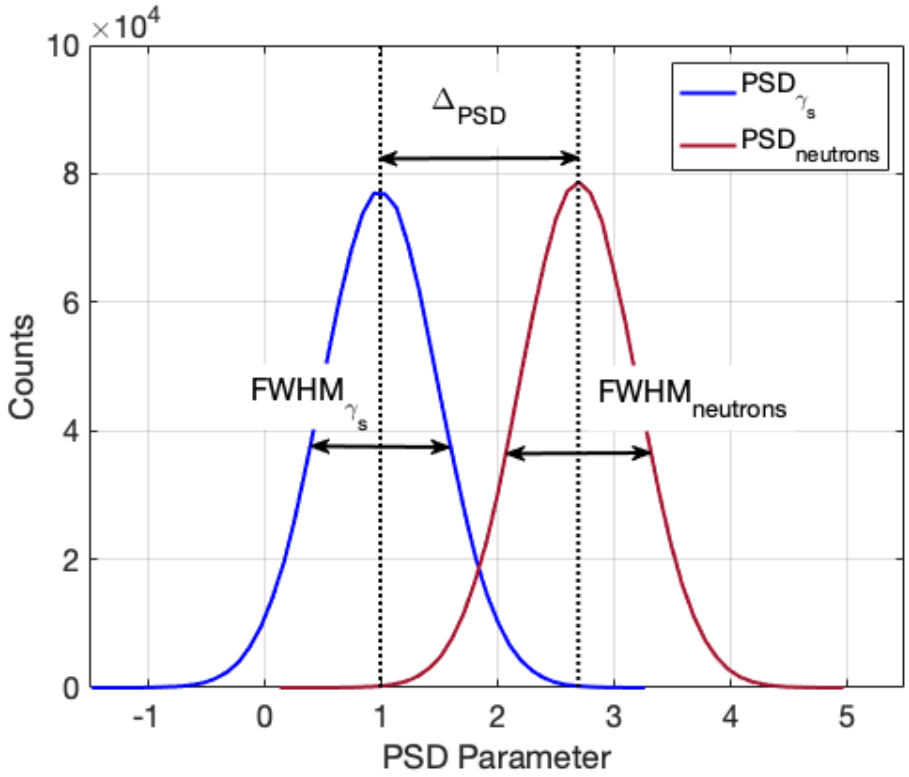

Fig. 2.10: Arbitrary Gaussian distributions showing the meaning of $F.o.M.$'s main parameters by graphic means.

If the two PSD are Gaussian distributed, the meaning of the $F.o.M.$can be linked to the σ of the distribution, as from Equations (2.11), since the Δ_{PSD} and the two $FWHM$s can be written as a function of σ.

$$F.o.M. = \frac{\Delta_{PSD}}{FWHM_{\gamma_s} + FWHM_{neutrons}} \tag{2.10}$$

$$= \frac{\kappa \cdot (\sigma_\gamma + \sigma_{neutrons})}{2.355 \cdot (\sigma_\gamma + \sigma_{neutrons})} \tag{2.11}$$

$$\kappa = 2.355 \cdot F.o.M. \tag{2.12}$$

where κ is the distance of PSD distribution in units of σ. $F.o.M.$values greater than 2.2 mean that two distributions are distant more than $5\sigma_s$, being σ the root square of the distribution's variance. The 3σ limit corresponds to a $F.o.M.$of 1.27. The $F.o.M.$is evaluated for a reference energy window of particular interest for the specific application to compare the performances of different detectors or algorithms.

In detectors used for fast neutron detection, it was observed that $F.o.M.$is a function of energy. When the detectors are calibrated using a γ source, the energy is expressed in eVee, electron-volt electron equivalent. A keVee correspond to the amount of light generated from one keV energy released by γ ray. Indeed, for fast neutron detector, the minimum energy $E_{min}[eVee]$ that guarantees a $F.o.M.(E)> 1.27$ can be used as another qualifier of the goodness of discrimination.

$$E_{min} \ : \ F.o.M(E_{min}) \geq 1.27. \tag{2.13}$$

2.5 State of Art in PSD

The comparison of different pulse shape discrimination systems was the main topic of several publications. In particular, the comparison of different scintillators, light detection systems or algorithms showed that the use of SiPM is a viable solution, but with some caveat. So far, is interesting to compare not only the Stilbene with other materials like the Eljen EJ-299-34 (that was the same scintillator as the EJ 276-34 but with more reduced mechanical properties) in order to qualify those new materials concerning a reference standard, but also to test how and if the use of SiPM affects the discrimination capabilities. In addition to that, elpasolite crystals were tested with different temperature conditions, as scintillation light profile (light yield and temporal profile) depends on temperature.

The first relevant study is the one conducted by Ruck Flaska and Pozzi [83] that investigated discrimination capability of a stilbene scintillator coupled with SiPMs. In that work results from a stilbene crystal 6x6x10mm^3 coupled to a PMT, and two different SiPMs from SensL (Figure 2.11), a B and a C series, were compared [84]. The main difference between those two SiPMs is the PDE and the total sensor capacitance, affecting the electronic signal shape. The output signal has been digitised with a CAEN DT5730 digitiser, 500 Msps, 14 bits and 2V of input dynamic range. Discrimination was based on the (2.7), so far, the area was chosen as normalisation.

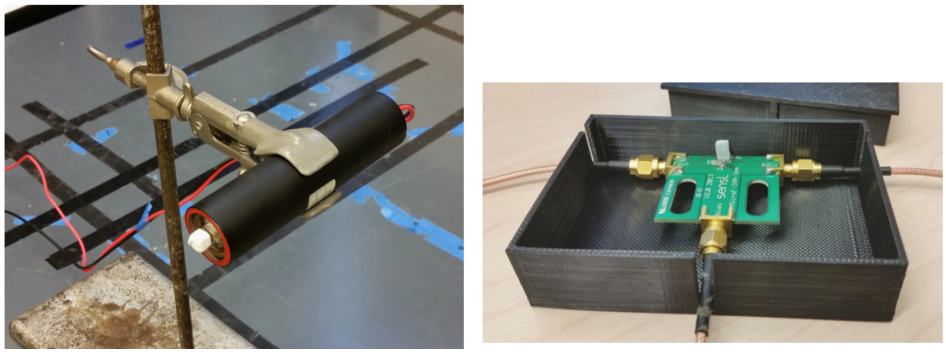

(a) (b)

Fig. 2.11: Experimental set-up for the Stilbene readout by a PMT (Fig. a) and for a SiPM (Fig. b) as reported in [83]

A ^{252}Cf source has been used as γ and neutron source; in Figure 2.12 the traces from a typical neutron and γ pulse are reported;

In this paper, it is shown that the performances of SiPMs are comparable to the ones of the PMT. In the energy range between 100 and 200 keVee, the FOM is reported in Table 2.3. In Figure 2.13 the PSD value as a function of pulse energy for the C-Series SiPM and the histogram of the PSD_{CCA} for the three configurations in the energy window between 100 and 200 keVee is reported.

Sensor	$F.o.M.(E)$, $E \in [100; 200] keV$
PMT	1.93
B-Serie SiPM	1.37
C-Serie SiPM	2.13

Tab. 2.3: $F.o.M.$as reported in [**SilbeneSiPM**]

A second relevant study compared how different algorithms affect the EJ-299/34 capabilities [85]. The signal from the scintillators that is the first production of the actual EJ-276 but with more inferior mechanical properties whose dimensions are

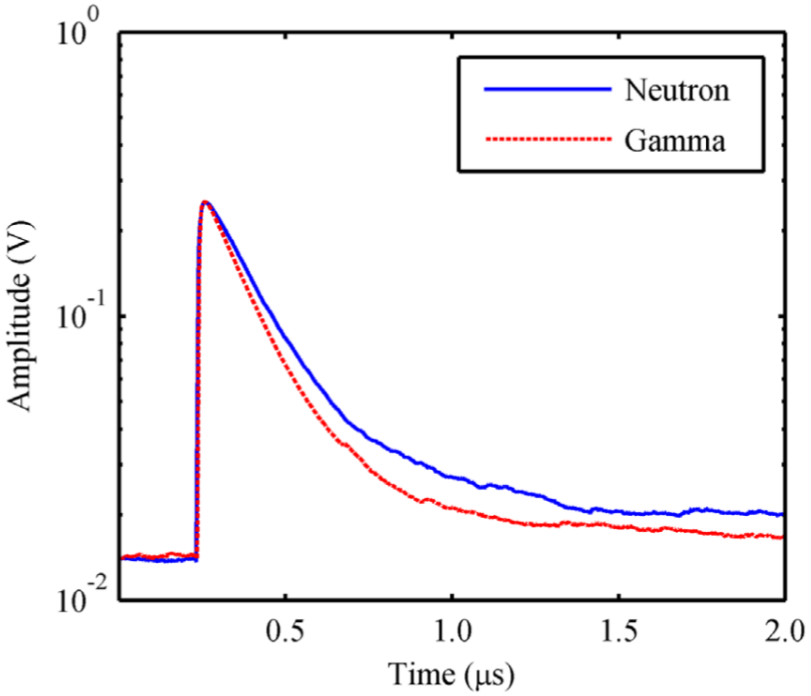

Fig. 2.12: Digitised 1 MeVee neutron and γ ray pulse measured with the stilbene crystal coupled to a B-Series SiPM [83]

10x10x50mm^3, was digitised and tested with two different algorithms: the digital charge comparison method (2.7) and a genetic algorithm. The $F.o.M.(E)$is reported in Figure 2.14 for two different algorithms and three light detectors: an XP2262 PMT, an FB60035 SiPM from FBK and an s10985-50c SiPM from Hamamatsu Photonic (HPK).

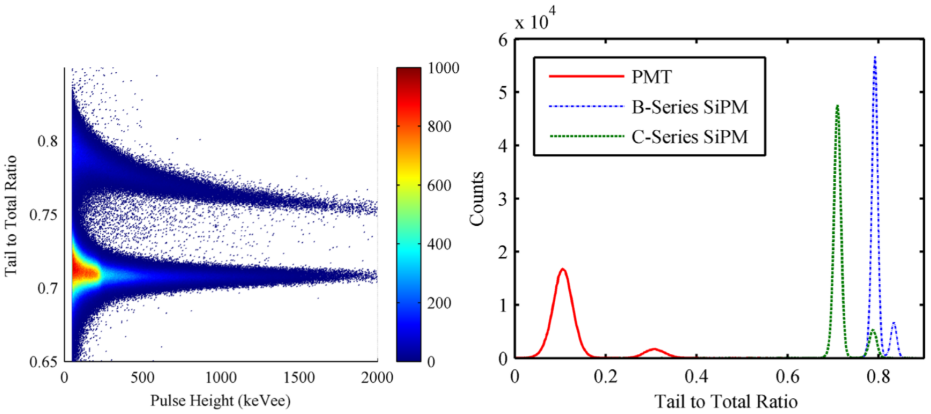

Fig. 2.13: In Figure (a) PSD distribution vs the energy and in Figure (b) the histogram of PSD_{CCM} in the energy windows 100-,200 keVee [83]

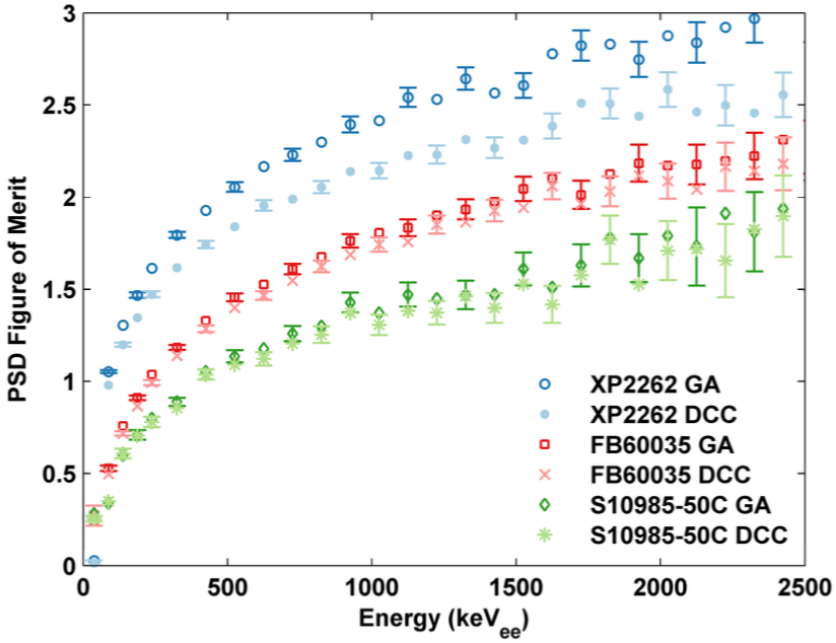

Fig. 2.14: $F.o.M.(E)$measured with the EJ-299/34 detector. Only every second point has $\pm 2\sigma$ error bar.

While the genetic algorithm, (GA) and the digital Charge Comparison (DCC, as it is referred to in [85]) method give similar results with a bias towards the GA, even in this study, it is confirmed that the light sensor strongly influences PSD. $F.o.M.$between 2.5 and 3 for signals higher than 1500 keVee is obtained for the measurement performed with the PMT, while with the SiPM $F.o.M.$does not exceed 2.

An exemplary study carried out with a CLYC crystal compared the discrimination obtained with two different SiPM arrays. The array is made out by 16 channels, each

of them with an active area of 6x6mm^2 in the case of C-Series, and a 64 channel of 3x3mm^2 array manufactured by Hamamatsu (C11206-0808FA(X)) [86], both of them arranged in a square. $F.o.M.$of 1.5 is achieved when the scintillating light is read out by the HPK SiPM array. In Figure 2.15, it is clear that with the SensL array the discrimination is worst as it can be seen in the figure where the slow neutron and the γ PSD-distribution are overlapped. In this case, the PSD was measured in an energy interval centred around 3MeV, that is the γ equivalent energy deposited by the α particle generated by the detection of a neutron.

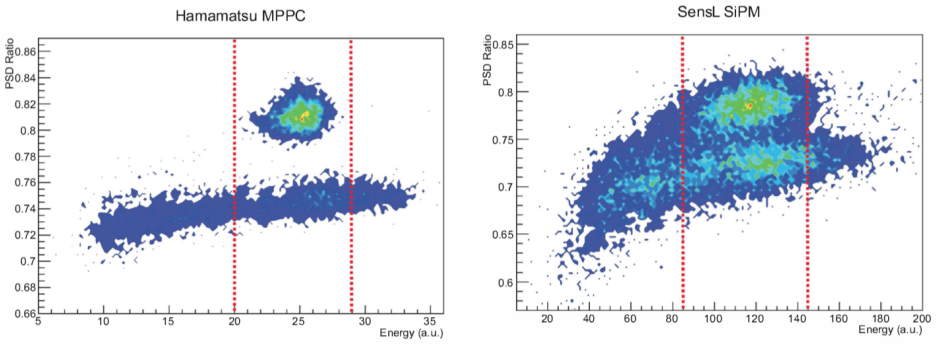

(a) (b)

Fig. 2.15: PSD vs the energy distribution obtained reading the CLYC crystal with an Hamamatsu array C11206-0808FA (a) or a SensL C-Series array (b)

Temperature dependence of the response of such scintillators has also been studied in [87]. The $F.o.M.$decreases, for all the tested algorithm, as temperature increases. $F.o.M.$higher than 2, in the reference energy interval, is expected at room temperature, falling below 1 at 50^{o}C, as reported in Figure 2.16. At high temperature, the light output of those scintillators is degraded, and the decay time constants change their proportions making the discrimination more difficult.

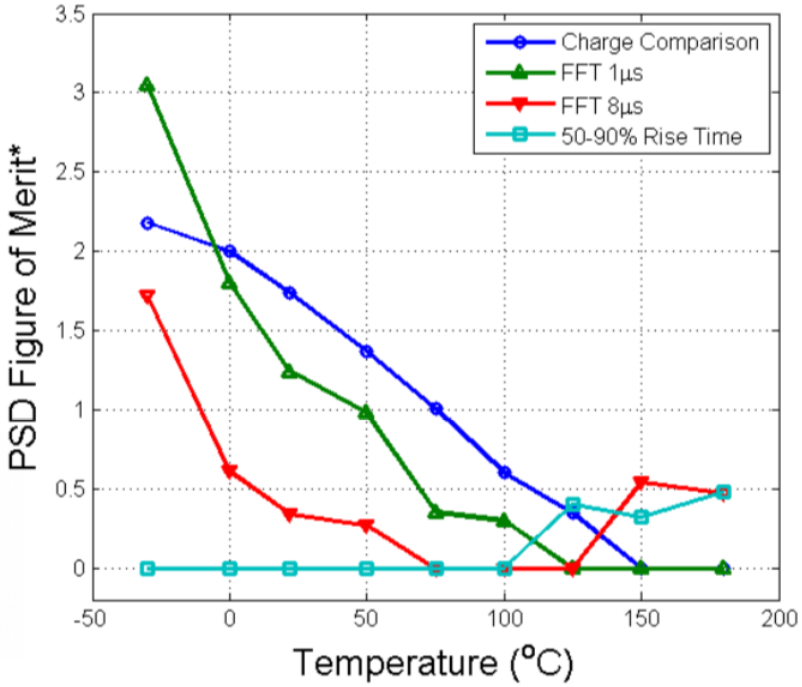

Fig. 2.16: Temperature dependence of $F.o.M.$for a CLYC crystal as reported in [87]

2.5.1 Comments on PSD results

From the results reported above, there are two main factors that seems to have an influence in discrimination capability [83, 85]:

- the light sensor and electronics signal shaping
- the discrimination algorithm.

In addition to that, the above mentioned studies suggested that the amount of light itself may have e crucial role in the discrimination. Even if the all the resulted obtained so far showed promising good discrimination, there are no systematic study of all those effects on the PSD performances at one. This is a reason why this thesis proposes a study that will tackle all the effects that may influence the PSD capabilities.

3 Silicon Photomultipliers

The scintillating light from novel PSD scintillators in this work was read out by Silicon Photomultipliers. In the last two decades Silicon Photomultipliers (SiPM) became the cutting-edge light sensors with unprecedented single-photon detection sensitivity, remarkable photon detection efficiency, unprecedented photon number resolving capability, excellent time resolution and extended dynamic range. Their features, like the compactness, robustness, insensitivity to magnetic fields and low operating voltages make them suitable for a class of applications that ranges from fundamental and applied science to automotive, consumer devices for distance measurements, and industry. Those advantages, in addition to the design flexibility and low-cost mass production, allowed SiPM to became the first choice for many different fields of applications, including the nuclear security one. However, SiPM has a high intrinsic capacitance, that could actively shape the output signal usually when arrays of SiPM are built up.

3.1 Working Principle of SiPM

The exploitation of the solid-state silicon technology opened up the possibility to build a class of Avalanche Photo-diodes sensitive to a single photon, called Geiger-mode Avalanche Photo-diodes (GM-APDs) or Single Photon Avalanche Diodes (SPADs). The SPAD is a reverse-biased p-n junction that operates in Geiger-Muller regime. So far, the response of the SPAD to a light stimulus can not be proportional to the incoming light field. For application in which single-photon detection is required, SPADs are excellent detectors, but they are useless in applications where a response proportional to the incoming light field is critical.

To overcome the single SPAD limits, matrices of SPADs with density up to 10^4 diodes per mm^2, on a common substrate, with output combined in parallel to a single output, were manufactured. Thanks to this configuration, the output is proportional to the number of fired SPADs, being thus proportional to the incoming light field. Those matrices are called Silicon Photomultipliers [88]. Each cell in a SiPM is a diode operated at a voltage exceeding breakdown(25-100V depending on the producer) by few volts. The primary avalanche in each cell can be generated either by a photon of by a charge carrier freed by thermal excitation or tunnelling effect in silicon. In

Figure 3.1 an artist's view of SiPM as a collection of cells is reported along with the one of a photon that generates a charge carrier that initiates an avalanche.

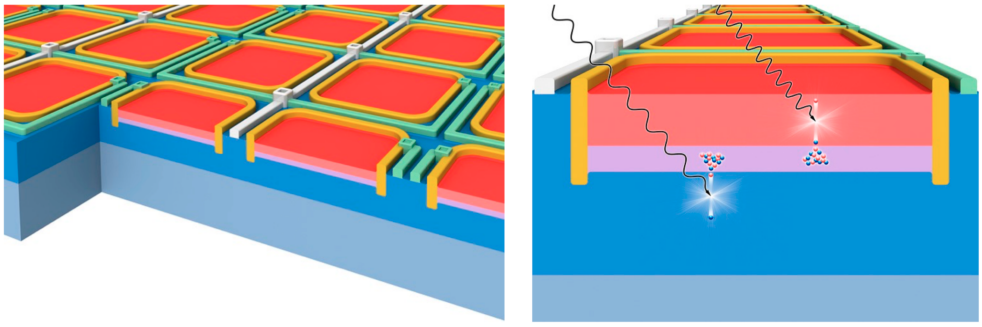

Fig. 3.1: Artist's view of the SiPM as collection of SPAD on a single substrate.

Each SPAD in a SiPM is an abrupt n/p junction whose structure is sketched in Figure 3.2, from reference [89]. The Figure refers to an n+/p configuration, with a low dopant concentration layer (π) and an enrichment box (p) that realise in silicon the electric field sketched in Figure 3.2 when the voltage is applied ad diode terminals.

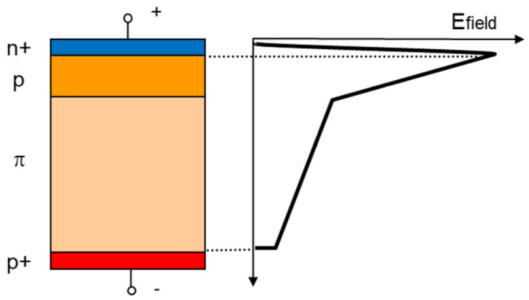

Fig. 3.2: n+/p junction scheme of single SPAD, as reported in [89]

When a photon is absorbed an electron/hole pair is generated: if the photon is absorbed above the high electric field region, the holes are drifted towards the high electric field region, while if absorbed below the electrons are drifted toward the high electric field. The absorption depth depends on the wavelength of the incident photon, while the trigger probability depends on the mobility of electrons or holes, that may trigger with different probability a self-sustained multiplication process. The electron avalanche needs to be quenched through a resistor placed within the single cell to prevent the destruction of the cell itself. The current generated by the avalanche flows through the resistor and causes a voltage drop; when the electric field is too low to sustain the multiplication process, the avalanche stops, and the operating voltage is restored in a time proportional to the resistance and capacitance of the single-cell [89, 90, 91, 92].

The integration of more than one SPAD in a single substrate requires some isolation between the cells from the electrical and optical point of view. As shown in Figure 3.3

a guard ring surrounds the high field region, to help a smooth and fast transition to low values of the electric field; along with the isolation structure that separates each cell from an electrical point of view to reduce cross-talk effect from photons generated by the multiplication process, as explained in section 3.4.2, optical trenches can also be implanted.

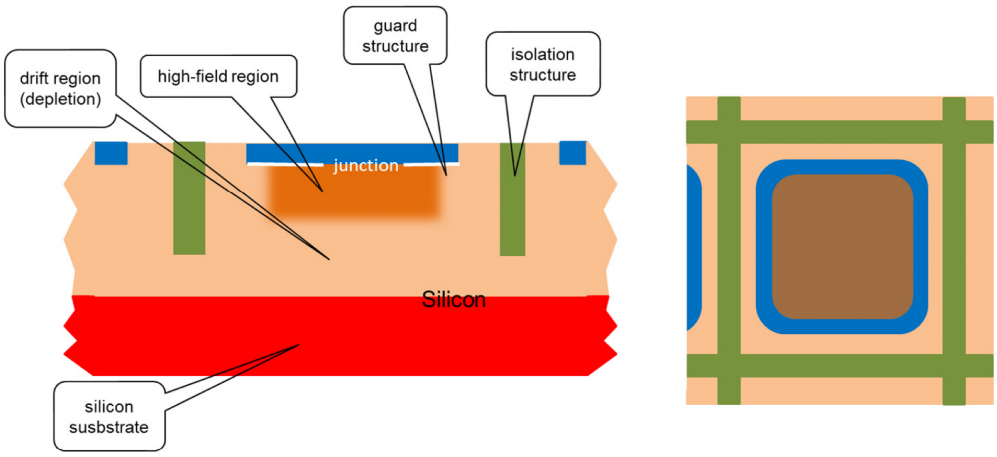

Fig. 3.3: Cross-section and top view of a single cell in SiPM as reported in [89]

SiPMs have photosensitive areas that range from $1 \times 1\,mm^2$ to $6 \times 6\,mm^2$. The single cells are binary detectors (fired/not fired), but the output obtained as the sum of all the fired cell signals gives information proportional to the light field at the SiPM surface. In Figure 3.4(a) a typical trace plot of a SiPM response to a light pulse emitted by a LED is shown. Each trace corresponds to a different number of fired cells and, since the noise band is small concerning single cell high gain, SiPMs allows for photon number resolved detection. By integrating the traces, it is possible to obtain a frequency histogram of the collected charge (Figure 3.4.b) where each peak corresponds to a different number of fired cell, and the peak distance (Δ_{pp}) is proportional to the charge developed in a single avalanche.

The spread of the first 0-photon peak measures to the system noise, while σ_1, that is slightly larger than the pure electronic noise, reflects non-uniformities of cells. Despite the high-quality silicon process that allows obtaining unprecedented cells uniformity, the photon number resolving capability in SiPM is spoiled by that so-called cell-to-cell gain variation ($\sigma_{cell-to-cell}$) that can be up to 10%. Peak width increases with the number of fired cell N_{fired} following a $\sqrt{N_{fired}}$ law, limiting the maximum number *M* of peaks that is possible to resolve. The Sparrow criterion was suggested to identify the limits in resolving power: it states that two peaks are no longer resolved if the half-way dip is no longer visible. The quantitative limit is based on the Resolution parameter R, defined in Equation (3.1), as the ratio between the peak separation Δ_{pp} and the $\sigma_{cell-to-cell} = \sqrt{\sigma_1 - \sigma_0}$. According to the Sparrow

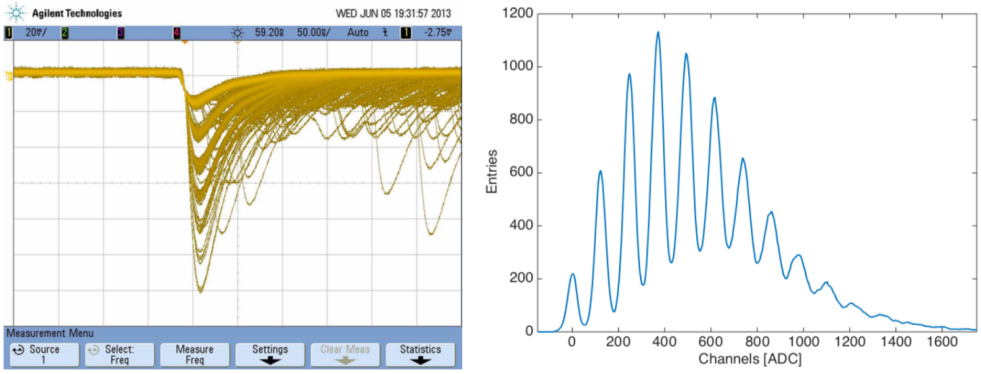

(a) (b)

Fig. 3.4: Typical trace plot from an SiPM response to pulsed LED light, and frequency histogram of collected charge proportional to the number of fired cells, as reported in [93]

Criterion, it is possible to estimate the number M of distinguishable peaks as in (3.2) [94, 95].

$$R = \frac{\Delta_{pp}}{\sigma_{gain}} \tag{3.1}$$

$$M = \frac{R^2}{4} \tag{3.2}$$

3.1.1 Electrical Model of SiPM

Electrical model of SiPM can be found in [96, 97, 89, 98]. Despite small differences among them, the essence of the model for the single cell is the one reported in Figure 3.5(a) according to [96]. In this scheme photo-diode is modelled as a capacitor C_D, charged by an excess voltage V_{ov} defined as the difference between the biasing voltage V_{bias} and the breakdown voltage V_{bd}. The steady-ready condition is represented by an open switch and the capacitor fully charged. The switch closure models the primary free charge carrier that trigger an avalanche: in this occurrence, C_D discharges until the voltage at capacitor terminals equals to V_{bd} making $V_{ov} = 0$. During the discharge current flows through the junction's intrinsic resistance R_D and reaches the quenching resistor R_Q (usually $R_Q \approx 10^2\Omega$); current asymptotic value is $\Delta_V/(R_D + R_Q)$. The whole process follows an exponential curve with a time constant of $\tau_D = C_D R_D$. At the end of avalanche quenching the switch goes back to the "OPEN" position, the V_{ov} is restored, and the cell capacitance is recharged with a typical time constant of $\tau_{recovery} = R_Q C_D$. The current signal generated by the process is sketched in 3.5(b).

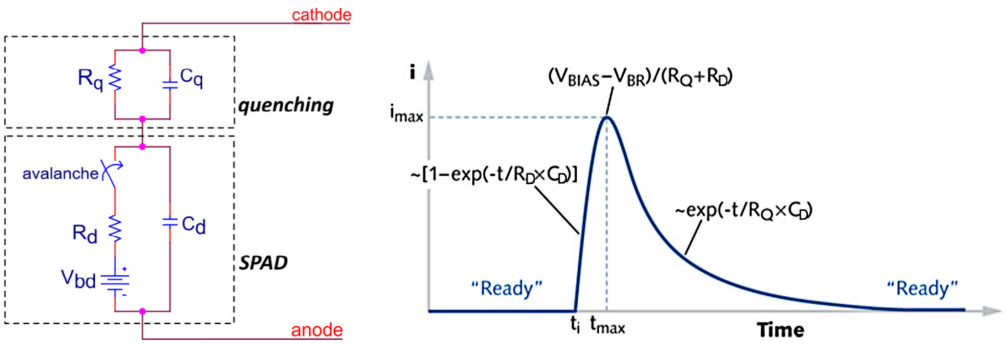

(a) (b)

Fig. 3.5: (a) Electronic model of a single cell as reported in [96] and (b) the single-cell Current development in time

The single cell model does not, however, consider the effect of the passive cells (the not fired ones). It is possible to extend the model considering N_{fired} fired cell (box "Active" in 3.6), $N_{tot} - N_{fired}$ passive cells (box "Passive" in 3.6) and the parasitic capacitance, resistance and inductance due to the electrical connections (box "Parasitic" in 3.6). This extended model is useful in simulations that are meant to engineer front end electronics since it allows us to consider all the SiPMs electrical features. Time characteristic of the signal in this model is not altered concerning the one of the single-cell since the parallel connection between the cell allows the increased capacitance ($C_{firedcell} = N_{fired} \cdot C_D$) to be counterbalanced by the parallel of the resistors R_D.

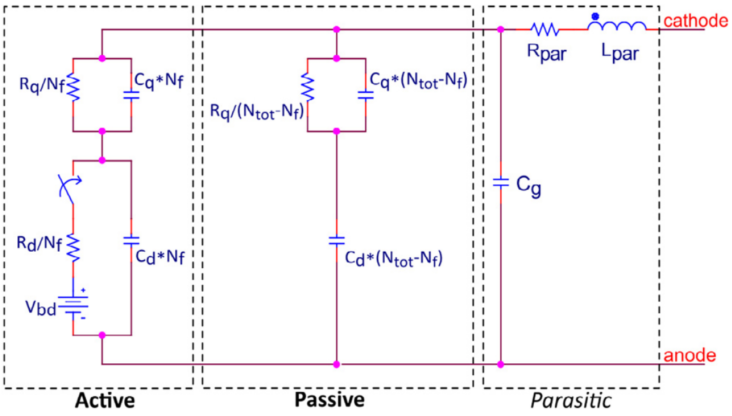

Fig. 3.6: Electronic model of the whole SiPM where N_f cell have been fired and $N_{tot} - N_f$ cell that act as passive components

3.1.2 Breakdown Voltage

The breakdown voltage V_{bd} defines the minimum bias at which the SPAD has to be operated to work in Geiger-Muller regime. It depends on construction technology and the temperature. Above the breakdown voltage, the generated free charge carrier produces a secondary charge with a different probability according to its

electron or hole nature [89]. Impact ionisation rate for electrons or holes, α_e and α_h respectively, are the rate of the secondary pair generated per unit distance travelled by a primary free charge carrier and they are a function of the electric field in the so-called "local approximation" [99]. Electron-hole pair generation rate (GR) can be expressed as in (3.3) as the sum of the product of the impact rate and the current density for electrons and holes.

$$GR = \alpha_e |J_e| + \alpha_h |J_h| \tag{3.3}$$

Conditions for which GR diverges guarantee self-sustained avalanches, so far the Geiger-Muller avalanche process. Impact ionisation rate for holes and electrons can be used to evaluate the depth of the high field region W that lead to a divergent process.

$$I = \int_0^W \alpha_h \cdot e^{-\int_0^x (\alpha_h - \alpha_e) dx'} dx \tag{3.4}$$

Values of W for which integral in Equation (3.4) equals to one is the width of the high field region, given the impact ionisation rates [100].

Breakdown voltage is strongly depended on the temperature. Indeed, V_{bd} increase with temperature because higher temperature enhances the probability of collision between the free charge carrier and the crystal lattice, reducing the mean free path [96] and therefore the energy when the free charge carrier hits the lattice. A higher electric field can compensate energy loss due to a shorter mean free path, so far a higher V_{bd} will be required to satisfy the Equation 3.4. In fact large V_{bd} are expected with less thick depletion region. It is crucial to notice how it has been measured that SiPMs with the deeper depleted region have a stronger dependence of the V_{bd} on temperature. On the other hand, the cell to cell gain variation is lower with the deeper depleted region. Usually, lower cell to cell gain variation is preferred against the temperature variation stability, since it is possible to compensate for the T variation by acting on the bias voltage. At the same time, it is not possible to counterbalance the natural cell-to-cell variations [89].

3.2 Gain

The capacitance of the junction defines SiPM gain, and it depends on the over-voltage V_{ov} as in Equation (3.5)

$$G = \frac{(C_D + C_q) \cdot V_{ov}}{q} \tag{3.5}$$

Where $q = 1.6 \cdot 10^{-19} C$ is the electron charge, and C_q is the parasitic capacitance of the quenching resistor. The single-cell capacitance varies with its area, being higher for SiPM with larger pitch. A typical value of gain ranges from 10^5 to 10^7, producing a signal well above the noise band, allowing for the photon counting capability shown in Figure 3.4. Typical dependence of the gain on V_{ov} can be seen in Figure 3.7, where the reported gain for a $40\mu m$ and $25\mu m$ cell pitch comes from a TCAD simulation [96].

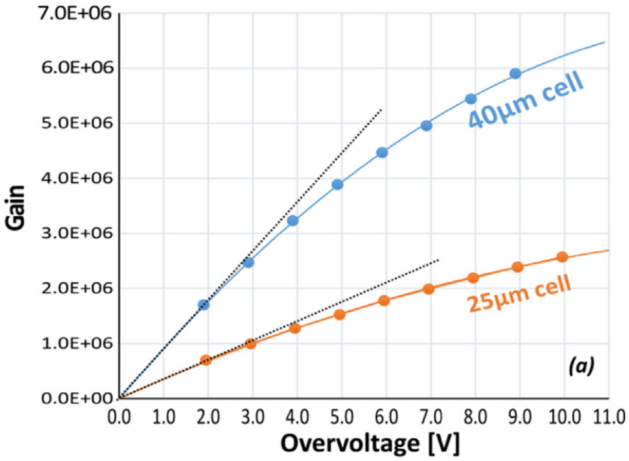

Fig. 3.7: SiPM Gain vs V_{ov} as reported in [96]

3.3 Photon Detection Efficiency

The probability of detecting a photon, Photon Detection Efficiency (PDE) defined as the product of the Quantum Efficiency (QE), the Trigger Probability (P_T) and the Geometrical Fill Factor (FF) as defined in Equation (3.6); those factors depend on the over-voltage and thus on temperature or physical proprieties as such as the λ of incoming photons of the electronics placement of the quenching resistor on the cell that may fade a portion of the active cell area.

$$PDE(V_{ov}(T), \lambda) = QE(\lambda) \cdot P_T(V_{ov}(T), \lambda) \cdot FF \tag{3.6}$$

The SiPM quantum efficiency depends on the wavelength of the impinging photon and the absorption region thickness (Figure 3.10). QE is a function of two factors: the probability that a photon crosses the anti-reflective coating (ARC) layer on top of the sensor and the one that a photon generates an electron-hole pair. The probability

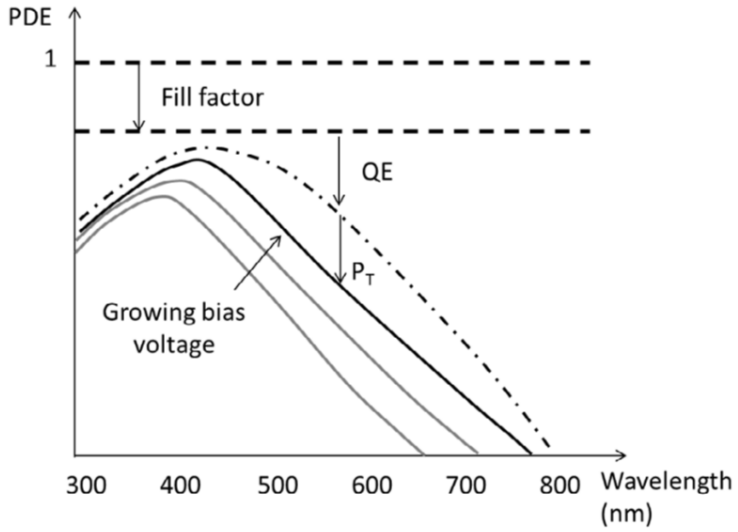

Fig. 3.8: Effective fired cells as a function of the number of photons per pulse on the active SiPM surface (full and zoom) for Hamamatsu S10362-050C type, 250 ns gate length.

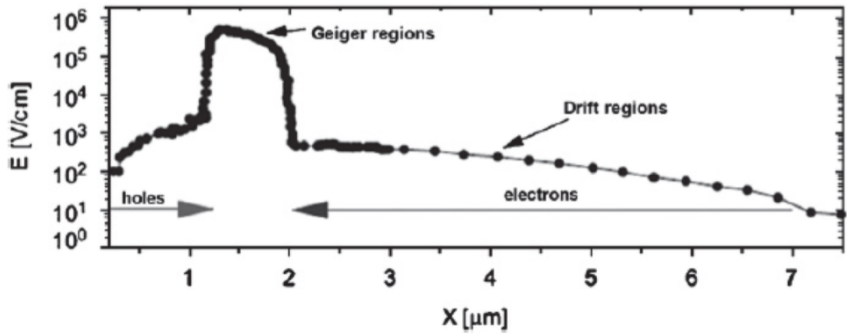

Fig. 3.9: The electric field outside the Geiger-Muller regime slowly decrease up to be almost zero in the substrate.

of generating an *eh* pair is a sole function of the incoming wavelength. Then the probability of triggering an avalanche is a function of the temperature and the wavelength, is related to the absorption depth of photons in silicon, that grows with the wavelength from $\geq$10 nm range for the UV/blue light, up to tens of microns for the near-infrared light. In particular, it is being absorbed above or below the junction influences the probability to reach the active region before the free charge carrier recombines.

Figure 3.9 shows the hole/electron drifting in a *n on p* junction. The charges above the junction have a higher probability of reaching the high field region, so far a photon with a wavelength such that this region is the most probable for the absorption will most likely trigger an avalanche. That is why it is fundamental to tune the active region thickness according to the specific wavelength is required to be detected.

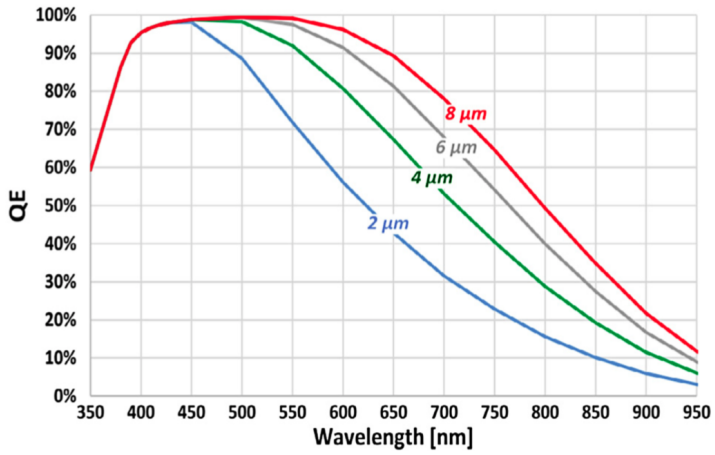

Fig. 3.10: Estimated internal QE vs the wavelength of incident photon for different effective epitaxial layer thickness.

In particular, considering an n+/p junction, short wavelengths photons features a small absorption depth. The eh pairs are mainly photo-generated above the junction, and only holes are drifted towards the avalanche region. In this case, a proper design of that layer allows better carriers diffusion and minimise the recombination. Indeed, the visible light is absorbed above and below the high field region, and both carriers can trigger the avalanche but with a not flat probability due to the different mobility of the free charge carrier. Finally, NIR photons generate mostly electrons below the junction.

The FF represents the fraction of the active area that is not shaded by the quenching resistor, and it increases with the pitch. In Figure 3.11(a) SiPM single cells with different pitch are shown. From the picture, it is possible to see that smaller is the cell pitch the smaller is the FF as the passive components cover a higher area fraction (Figure 3.11(a)).

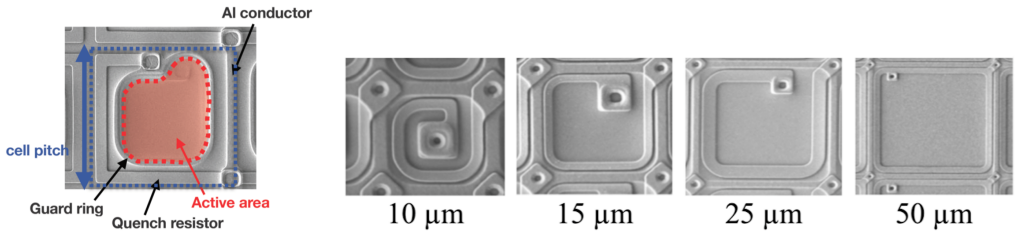

(a) Details of SiPM cell structure as reported in [93]

(b) Different SiPM cells with different pitch

The PDE tends to it asymptotic value increasing the V_{ov}, suggesting that higher the V_{ov} better it would be, as reported in Figure 3.11 for different SiPM manufacturer. However, with V_{ov} the noise increase and this could spoil the measurements. A balance between the cell pitch (so the number of available cells) and the V_{ov} is

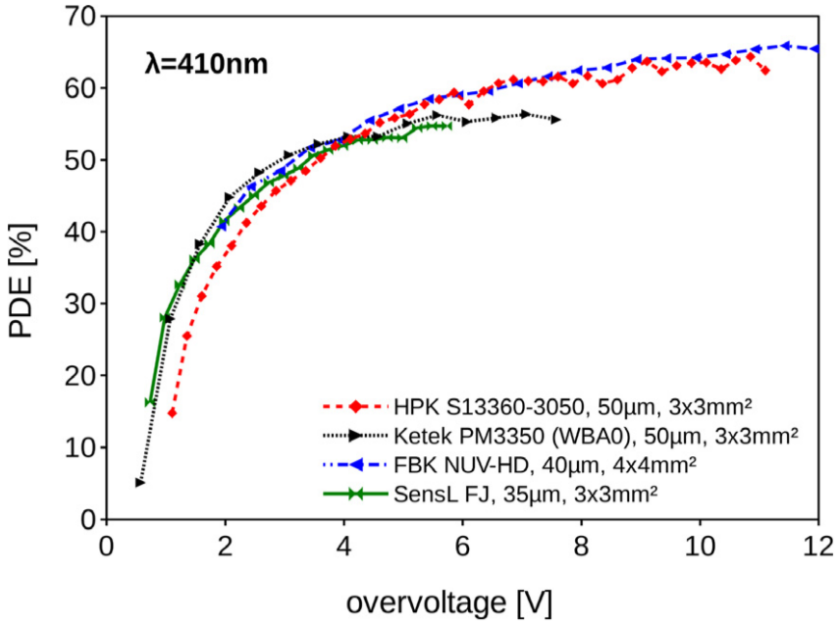

Fig. 3.11: Measure of the PDE as function of voltage as reported in [96]

usually found for every specific application. In γ spectroscopy, the use of SiPM with a smaller pitch, even if the PDE would be lower, is envisaged. Saturation limit is then moved to a higher number of photons impinging on the sensor, preventing the high number of photons produced by the scintillator to spoil the measurement.

3.3.1 Non linearities in SiPMs

The limited number of cell in SiPM limits the dynamic range of the SiPM, and it introduces intrinsic non-linearity. It happens because of the single-cell works in Geiger-Muller regime. It is reflected in a response that is linear with the number of incident photos only if the probability for two photons to enter the same cell is low. Considering the number of photoelectron as the total number of photons incident on the sensor multiplied by the PDE ($N_{ph.e.} = N_p \cdot PDE$), it is possible to estimate the number of fired cell N_{fired} considering the well known problem of putting n balls in m boxes as the one to put $N_{photons}$ in N_{tot} available cells. The expected number of boxes expected to contain one or more ball is $N = m[1 - (1 - m^{-1})^n]$. Equation (3.7) express the statistical problem with the notation used for the fired cells and emitted photons.

$$N_{fired} = N_{tot}\left[1 - \left(1 - \frac{1}{N_{tot}}\right)^{N_{ph.e.}}\right] \tag{3.7}$$

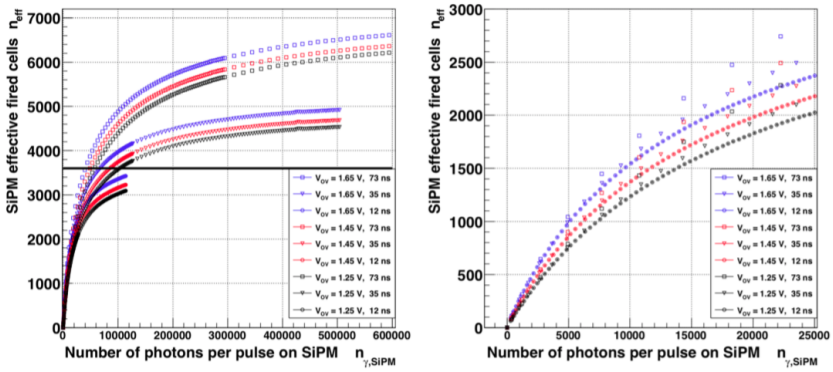

Fig. 3.12: Fit of Equation (3.8) to data acquired with a 1 by 1 mm^2 SiPM as reported in [98]

In the statistical problems of balls placing, when the number of boxes is higher than ~ 100 it is possible to consider the normal approximation. In the same way, the number of actual fired cell when $N_{ph.ee} \to \infty$, and $N_{ph.e.}/N_{tot}$ is finite can be evaluated by means of Equation (3.8), the limits for $N_{ph.ee} \to \infty$ of Equation (3.7) that provides a statistical correction to the measured number of photoelectrons [98].

$$N_{fired} = N_{tot} \cdot \left(1 - e^{-\frac{N_{ph.e.} \cdot PDE}{N_{tot}}}\right) \tag{3.8}$$

It should be noticed that this is an approximation since it applies in the ideal circumstances of no pulse recovery effect, and no noise is considered. When the occupancy, namely the ratio of the fired cell, is below 10% it was shown that no deviation from linearity could be appreciated [98].

3.4 SiPM noise evaluation

The noise figures in SiPM can be divided into Primary and Correlated noise [90, 91, 96]. Primary noise identifies all the avalanche initiated by a carrier that was not generated by light interaction with the SiPM but from thermal agitation or tunnelling effect. At room temperature, the first effect gives the main contribution to the so-called Dark Event, while at cryogenic temperatures tunnelling effect becomes dominant. On the other hand, secondary avalanches generated due to some physical effects in the primary avalanche are called correlated noise. Secondary and correlated avalanche can be after-pulsing or optical cross-talk. The firsts occur in the same cell of the primary avalanche due to later release of electrons trapped in impurities, and it produces pulses with amplitude lower than the single-cell amplitude, while the second one happens in a neighbour cell due to photons generated during the

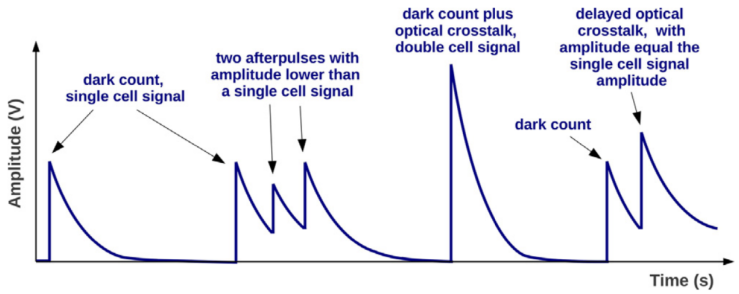

Fig. 3.13: Primary and Correlated noise signal shape as reported in [96]

primary avalanche. An exemplary illustration of how those effects appear in a typical pulse shape is reported in Figure 3.13 [96].

From the analysis of the waveform of SiPM signal output when no light stimulus is sent to the SiPM, it is possible to identify the features of a different kind of noise. The main differences are in the time distance of correlated noise concerning the primary event (a dark pulse in this case since no photons impinges on the sensor). The analysis of those pulses allows to evaluate the noise figure for the SiPM, but when it is not possible to digitise and analyse the whole waveform, Klanner et al. [101] proposed a method to measure noise based on the difference in reconstructed photon statistics, to the expected one from the light source.

3.4.1 Primary Noise

Primary-Noise rate, or Dark Counts Rate (DCR), is mainly determined by the SiPM manufacturing. At room temperature, the Shockley-Read-Hall (SHR) generation process is the main contribution to the trigger of spontaneous avalanches [99]. SRH effects occur when electrons, or holes, pass from the valence to conduct band, and vice versa, due to the thermal process. The mean lifetime of the SHR electrons τ_{SHR} depends on the flaws and impurities of the epitaxial layer of the SiPM, so far higher the number of impurities shorter is the τ_{SHR}, so far the free charge carrier jumps occur more often. Moreover, DCR depends on the thickness of the depleted region, being higher in SiPM with thicker active volume. In addition to that, another mechanism like the Pole-Frankel and thermal-enhanced trap-assisted tunnelling, related to the electric field characteristics inside the p-n junction, have the net effect of a shorter τ_{SHR}, since they increase the frequency at which free charge carrier can jump to the conduction band [102, 103]. In a given SiPM DCR thus depends directly on the cell pitch, on the temperature, doubling every $+10$ degree variation, and on the V_{ov}. In fact, higher PDE, given by V_{ov} variation to the temperature, makes more probable the trigger of an avalanche from a free charge-carrier. In addition to

that, an higher electric field enhances the SRH process and the thermal-enhanced trap-assisted tunnelling effects as shown in 3.14.

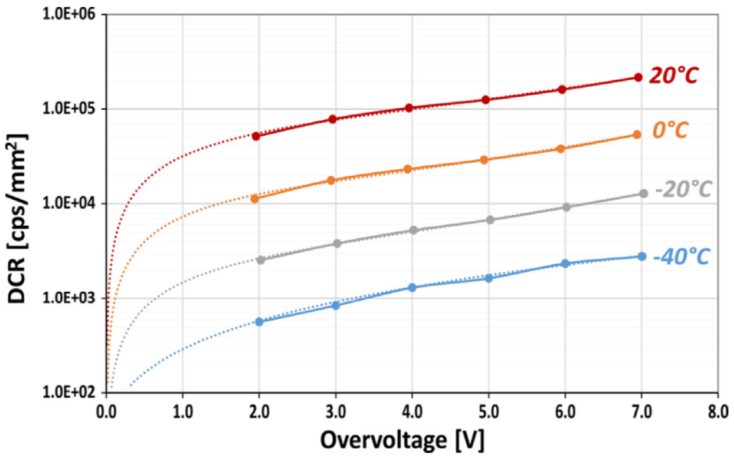

Fig. 3.14: Exemplary plot of DCR vs V_{ov} at different temperature as measured in [96]

The DCR then increases with the SiPM total area, and the number of cells, and for latest SiPM commercially available it is in the order of dozens of kHz at room temperature.

3.4.2 Optical Cross Talk

It has been demonstrated that during an avalanche in a SPAD the electrons with energy close to the silicon bandgap of $1.14eV$, namely the hot electrons, emit photons in the visible range with a probability of $\approx 2.9 \cdot 10^{-5}$ [93]. It means that within a SiPM with a gain of $\approx 10^6$, on average, 30 photons per avalanche are emitted, and eventually detected by neighbourhood cells. The absorption of photons generated due to an avalanche is called Optical Cross-Talk (OCT). OCT that occurs as sketched in Figure 3.15, also called Prompt Cross Talk (pCT) are indistinguishable from a situation where two or more cells fires simultaneously and independently. Direct cross talk can spoil measurements for which the photon number resolving capability have to be pushed to the limit, for example in Quantum Optics measurements [104, 105].

The delayed absorption of secondary avalanche photons is called Delay Cross-Talk (DeCT). DeCT may happen due to two different physical phenomena: the photon can be absorbed in the epi-layer of the SiPM, where residual low electric field slowly drift the photoelectron into the avalanche region, or they can be reflected at SiPM surface and re-enter the SiPM as shown schematically in Figure 3.16.

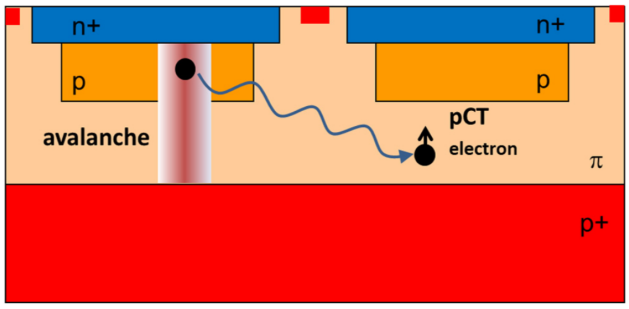

Fig. 3.15: Sketch of prompt optical cross-talk mechanism.

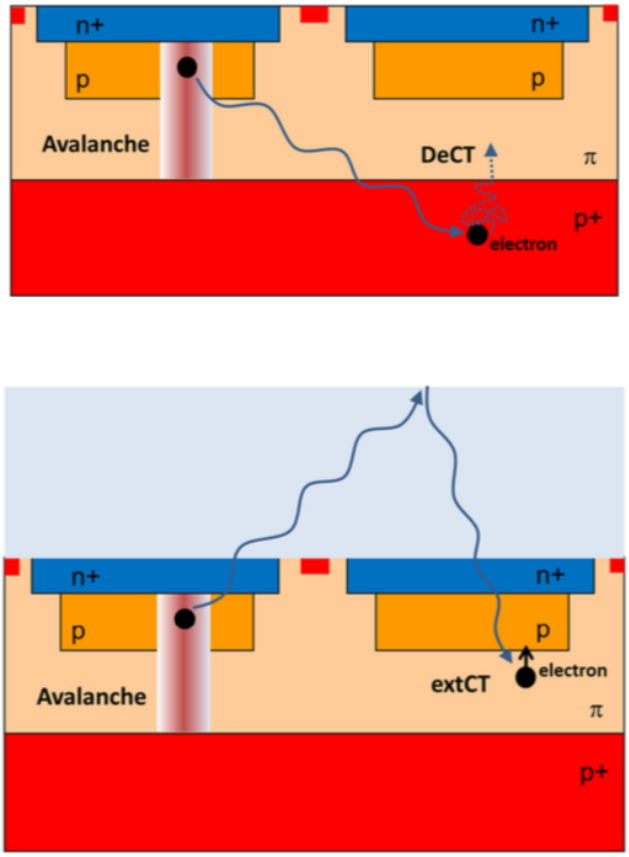

Fig. 3.16: Sketch of the two delayed cross-talk mechanism: in the upper figure the absorption in the epi-layer while in the bottom one the back reflection of the anti-reflective coating.

OCT probability increases with the V_{ov} since both the higher gain increase the number of photons generated by hot electrons, and the higher PDE being P_T dependent on the over-voltage. Optical trenches are implanted between the cells to stop photons that escape the cell reducing the pCT. Moreover, the OCT probability increases with the cell size according to the gain variation with the cell capacitance. The measurement of the OCT probability can be performed looking at the ratio of the rate of Dark pulses that presents an amplitude corresponding to more than one fired

cell to the primary event rate. It can be quickly done retaining the event rate at the increasing threshold as in Figure 3.17 and through Equation (3.9) measuring the OTC probability known frequency for the threshold amplitude that corresponds to 0.5 and 1.5 fired cell amplitude. This method is reliable since the probability to have two simultaneous DCR ($\Delta t_{DCR-DCR} < 1ns$) is less than 10^{-4} for 100 kHz DCR under the assumption that an avalanche may trigger at least a second avalanche in a neighbourhood cell.

$$OCT = \frac{\nu_{1.5ph.e}}{\nu_{0.5ph}} \tag{3.9}$$

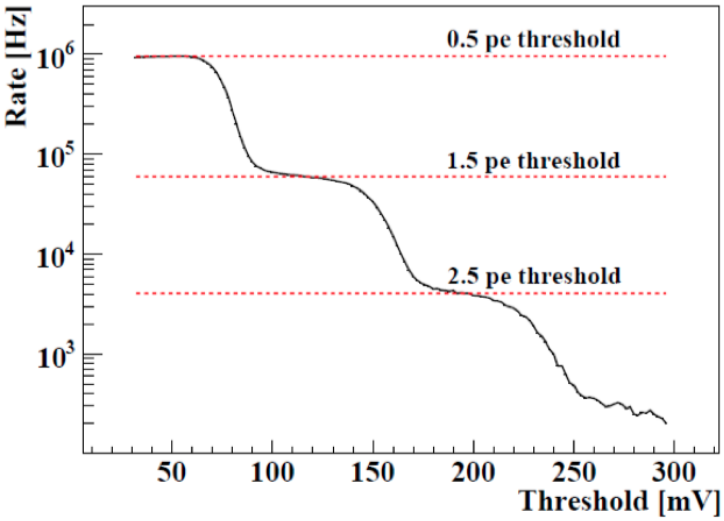

Fig. 3.17: Threshold scan of SiPM performed at room temperature with no impinging light as in [106].

3.4.3 After Pulse

Due to trapping centres caused by impurities in the p-n junction, some of the electrons generated during the avalanche can be trapped and then re-emitted triggering a second avalanche within the very same cell (Figure 3.18). This phenomenon is a source of another correlated noise called After-Pulsing (AP). APs are signals with a lower gain to the primary event since the V_{ov} is not fully restored when the AP takes place. Indeed, V_{ov} depends on time, according to the model presented in Section 3.1.1. The same happens to gain according to Equation (3.5). The time distribution of the AP follows an exponential law, and the Equation (3.10) gives the charge of an AP event that takes place at time t_{AP}.

$$Q_{AP}(t) = G \cdot \left(1 - e^{\frac{t_{AP}}{\tau_{AP}}}\right) \tag{3.10}$$

Equation (3.10) accounts for the fact that at time t_{AP} the cell V_{ov} is not fully recovered, so it detects the photons with a lower over-voltage and gain. The amplitude dependence of the AP events is shown in Figure 3.19. It is essential to notice that if an AP event occurs with time higher than the recovery time of the cell ($t_{AP} \geq 5\tau_{recovery}$) the AP is indistinguishable from primary events. Indeed the later avalanche may also occur if an electron was trapped outside the depletion layer, so it takes time longer than $\tau_{recovery}$ to enter the depleted region and thus trigger a second avalanche. On the other hand, if it occurs with a shorter time, it is possible to distinguish AP from DeCT looking at the amplitude distribution of subsequent events, expected to be lower than one photoelectron for AP events. For those reasons the after-pulse probability is modelled with a double exponential function as in Equation (3.11), wherein the expression μ_{AP_f} and μ_{AP_s} are the mean number of after-Pulses event per unit time accounting for the fast and slow process that gives rise to AP.

$$n_{ap}(\Delta t) = \mu_{AP_f} \cdot e^{-\frac{\Delta t}{\tau_{AP_f}}} + \mu_{AP_s} \cdot e^{-\frac{\Delta t}{\tau_{AP_s}}} \tag{3.11}$$

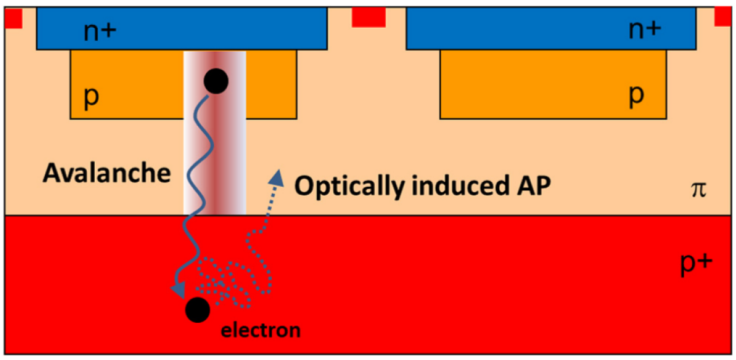

Fig. 3.18: Mechanism of After Pulsing.

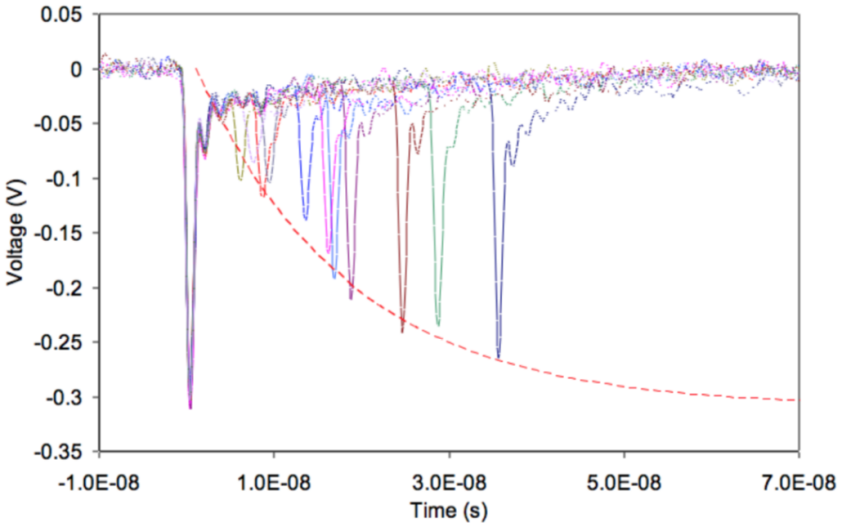

Fig. 3.19: After-pulse amplitude as function of time delay with respect to the primary event.

A first simple but yet robust method to evaluate the After-Pulsing is to evaluate the excess of charge, over the charge from dark pulses, after a light stimulus. The procedure, explained in [107], is based on the Central Limit Theorem and consists in measuring the excess of charge, but it can account only for the slow component of the after-pulsing τ_{AP_s}. Another procedure has been developed and reported in [108]. A waveform analysis was performed to tag events that present OCT or AP and by analysing the temporal distribution of inter-arrival time and amplitude. This procedure allows to overcome the experimental limits of 40ns for the AP measurement of the CTL procedure, below which the tag of a pulse after the primary one cannot be well identified, enhancing thus the sensibility and allowing for a correct measurement of both the time constant typical of after-pulsing events.

3.4.4 Excess Noise Factor

The presence of Optical Cross Talk and After-pulsing modifies the probability distribution of the detected photons for the probability distribution of the generated light. It can be measured as the degradation of the SNR of the input signal (SNR_{in}) to one of the output signal (SNR_{out}) (Equation (3.12)).

$$ENF = \left(\frac{SRN_{in}}{SRN_{out}}\right)^2 \tag{3.12}$$

The measurement can be conducted using a light source with a Poisson featuring few photons as mean value ($\approx\leq 10$). In this case, the ENF can be evaluated as in Equation (3.13) [101]. SNR_{in} is the ratio between the mean number of photon and

its variance, for the Poisson distribution μ and $\sqrt{\mu}$, while the SNR_{out} refers to the measured distribution of photoelectrons.

$$ENF = \frac{\sigma_{ph.e.}/\mu^2_{ph.e}}{\sigma_{Poisson}/\mu^2_{Poisson}} = \mu_{Poisson} \cdot \left(\frac{\sigma_{Poisson}}{\mu^2_{Poisson}} \right). \tag{3.13}$$

Where the notation $ph.e.$ refers to the photoelectron distribution while the $Poisson$ refers to the light distribution. The mean value of the light distribution can be estimated trough the probability of detecting no photons, as in Equations (3.14),(3.15), and the $\sigma_{ph.e.}$, and $\mu_{ph.d.}$ are evaluated from the distribution without any model assumption. Moreover, the photon detection has to be synchronous with the light emission.

$$P(0\ p.e.) = e^{-\mu} \tag{3.14}$$

$$\mu_{ZP} = -ln(P(0\ p.e.)) = -ln(\frac{\#_0}{\#_{tot}}) \tag{3.15}$$

where $\#_i$ are the number of detected photons.

4 Comparison of Pulse Shape Discrimination algorithms

In the previous chapter, several PSD algorithms were presented, and the results in the last section were referred only to the Charge Comparison algorithm. A complete study on the Pulse Shape Discrimination can not leave out the comparison of the discriminating performances of different algorithms on the same datasets and in different conditions. Such a comparison will also set the ground to compare fairly the different front end electronics, set-ups and detectors relying on the best performing discrimination technique. PSD algorithms performances comparison was obtained using the most performing set-up according to outcomes of Chapter 7. The detection unit is the outcome of a research project in collaboration with the Atomic Weapon Establishment (AWE) in which the need for a summing circuit in order to increase the photosensitive area by collecting light using multiple photomultipliers met the need to preserve as much as possible the temporal development of electronics signal shape. The detection unit used in this chapter is the outcome of a joint research project with AWE held in 2015, having the goal to provide a sizeable sensitive area Silicon Photomultiplier (up to 1 inch) preserving the time development of the signal as of the scintillator characteristics.

4.1 Experimental Set-up

The detecting unit (Figure 4.1) consists in a bar of EJ 299-34 plastic scintillator coupled to an array of 16 SiPMs. Each SiPM in the array has a dimension of $3 \times 3mm^2$ with the main characteristics reported in Table 4.1. A custom front-end electronics module supplies the bias to the sensor, sums-up the output from the SiPM array elements and amplifies the total signal, feeding a waveform digitiser. The summing circuits has been engineered in such a way all the channels are electrically decoupled to avoid unbalancing in SiPM characteristics to affect the signal. The output from the array has been digitised with a CAEN DT5720 module, sampling the signal at 250 MS/s with 12-bit resolution. The reported analysis is performed off-line on samples of recorded events.

The electronic circuit to sum the 16 channels is based on a scheme that will be detailed in Chapter 7. To summarise, it is a current summing scheme where all the

channels are appropriately decoupled to avoid impedance mismatch influence on signal quality.

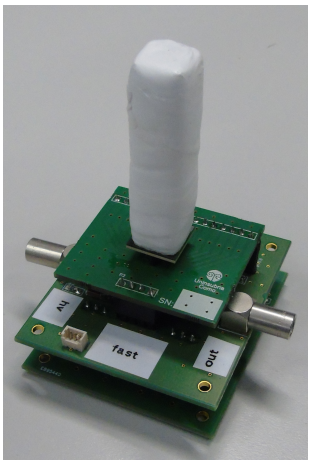

Fig. 4.1: The experimental set-up based on the EJ 299-34 coupled with the Hamamatsu s13361-3050AE-04 MPPC Array. The Hamamatsu C11204-01 supplies for the bias voltage.

The EJ 299-34 is a plastic scintillator produced by Eljen Technologies sensitive to fast neutrons and γs, with pulse shape discrimination capability. The temporal development of the light generated by a γ interaction is a sum of 3 decaying exponential curves with decay times of 15, 35 and 270 ns; the neutron interaction, i.e. scattering with hydrogen nuclei, produces light with decay times of 15, 50 and 450 ns as reported on the data-sheet. The light yield is 7000 photons per MeVee. The scintillator used for the present work has dimensions of $10 \times 10 \times 50 mm^3$ and was wrapped with Teflon tape to improve the light collection.

Hamamatsu S13361-3050AE - 04		
Number of SiPMs	16	-
Single SiPM Size	3 x 3	mm^2
Pixel Pitch	50	μm
V_{BD}	50	V
V_{op}	V_{BD} + 5	V
Gain	$1.7 \cdot 10^6$	-
DCR	0.5	Mcps
Cross-Talk	<5	%
PDE_{MAX}	40	%
Fill factor*	74	%
Dead Area**	0.2	mm

Tab. 4.1: Main characteristics of the SiPM array used for this analysis. * Fill Factor referred to a single SiPM. ** Dead area between two neighbouring SiPMs.

4.2 Pulse Shape Discrimination algorithm comparison

4.2.1 Energy Calibration

The radionuclides of interests emit γs with energies that predominantly interact through the Compton Scattering [47] as the EJ 299-34 has a low atomic number. The maximum deposited energy (Equation 4.1) for the Compton scattering interaction [47] was used as a reference point to provide a reliable energy calibration in each spectrum.

$$E_{max} = \frac{2E_{\gamma}^2}{2E_{\gamma} + m_e c^2} \tag{4.1}$$

Since the analytical form of the Compton Edge presents a sharp edge at the maximum deposited energy value [47], it has been modelled as a stepwise function ($\Theta(x)$). The resolution assumed to be Gaussian is convoluted with the $\Theta(x)$ to give a complementary Gaussian error function, as shown in Eqn (4.4).

$$\Theta(\eta) \otimes G(\eta) = \int_{-\infty}^{+\infty} \Theta(\eta - \tau) G(\tau) d\tau \tag{4.2}$$

$$\int_{-\infty}^{\eta} \Theta(\eta - \tau) G(\tau) d\tau = 0 \tag{4.3}$$

$$\Theta(\eta) \otimes G(\eta) = \int_{\eta}^{\infty} G(\tau) d\tau = \int_{\eta}^{\infty} e^{-\eta^2} d\eta = erfc(\eta) \tag{4.4}$$

When η is written as in Equation (4.5), x_0 results to be the ADC channel corresponding to the maximum deposited energy.

$$\eta = \frac{x - x_0}{\sigma\sqrt{2}} \tag{4.5}$$

In order to verify the reliability of the Compton edge fit, the procedure was tested with a CsI ($10 \times 10 \times 15 mm^3$) crystal, for which both the Compton scattering and the photo-peak absorption interaction have non-negligible cross-sections. Along with the calibration points obtained from the photo-peak energy, based on Gaussian fit (red line in Figure 4.2), the channels corresponding to the maximum deposited

energy were obtained after the erfc(x) fit (green line in Figure 4.2) as shown in Figure 4.2. The R^2 for the photo-peak calibration points is 0.9999. When the maximum deposited energy channels are considered along with the photo-peak calibration points the R^2 decrease to 0.9997. The good agreement between the maximum deposited energy points, and the calibration curve validates the procedure. Moreover, it is appreciable the high dynamic range allowed by this experimental set-up and summing scheme. Indeed it is possible to see in the ^{137}Cs Spectrum how the 30 keV line is well separated from the noise left over.

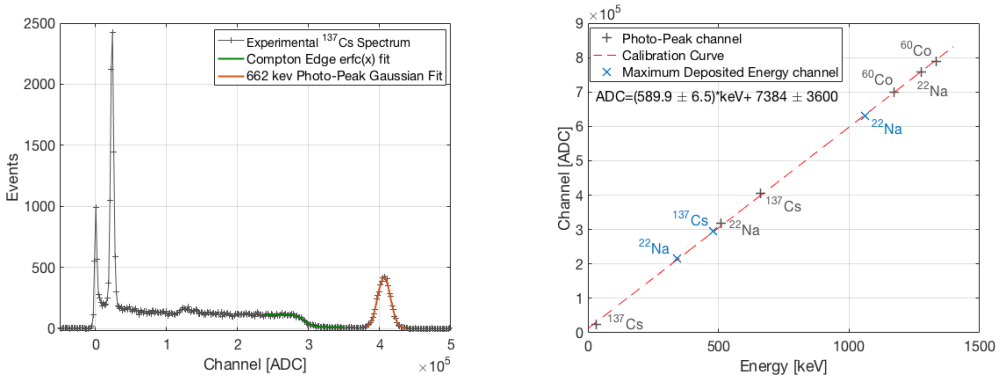

Fig. 4.2: On the left hand side is reported the ^{137}Cs spectra obtained with the CsI crystal. On the right hand side the calibration curve calculated with the use of the photo-peak position (grey points). The maximum deposited energy points (blue points) hold to the same calibration curve.

In Figure 4.3 Compton edge fit on ^{137}Cs spectrum obtained with the EJ 299-34 is reported along with the calibration curve for this plastic scintillator. The ^{60}Co point in fig. 4.3 refers to the average energy of the two maximum deposited energy related to the 1.3 MeV and 1.1 MeV γs.

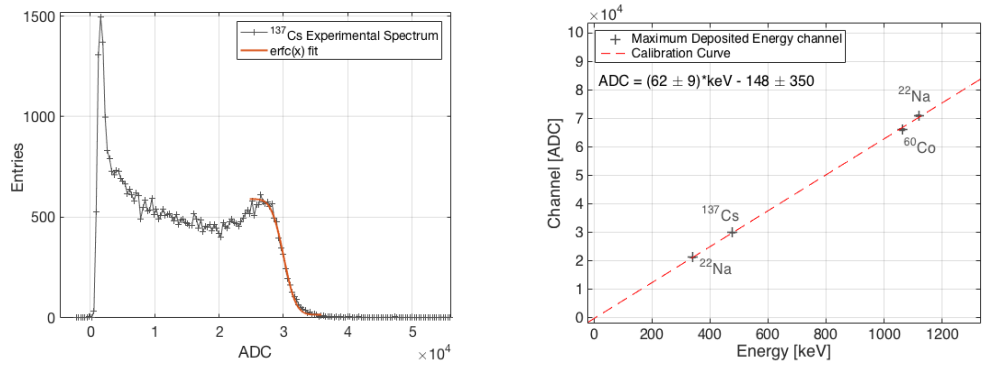

Fig. 4.3: On the left hand side the spectrum of the Compton edge of a ^{137}Cs source collected with the EJ 299-34. On the right hand side the calibration curve is reported.

4.2.2 Optimisation procedure

Optimisation procedure involves the selection of the parameters that maximise the $F.o.M.$of the neutron-γ discrimination in the energy window between 1-1.5 MeV. The $F.o.M.$was calculated, through automatic scan and fitting of PSD distributions, over a set of parameters to find the ones maximising $F.o.M.$. The output of optimisation scan for PT and CC algorithms is shown in Figure 4.4; the value of $F.o.M.$is reported accordingly to the colour legend, where X and Y axis are parameters t_{delay} and t_{int} values corresponding to reported $F.o.M.$.

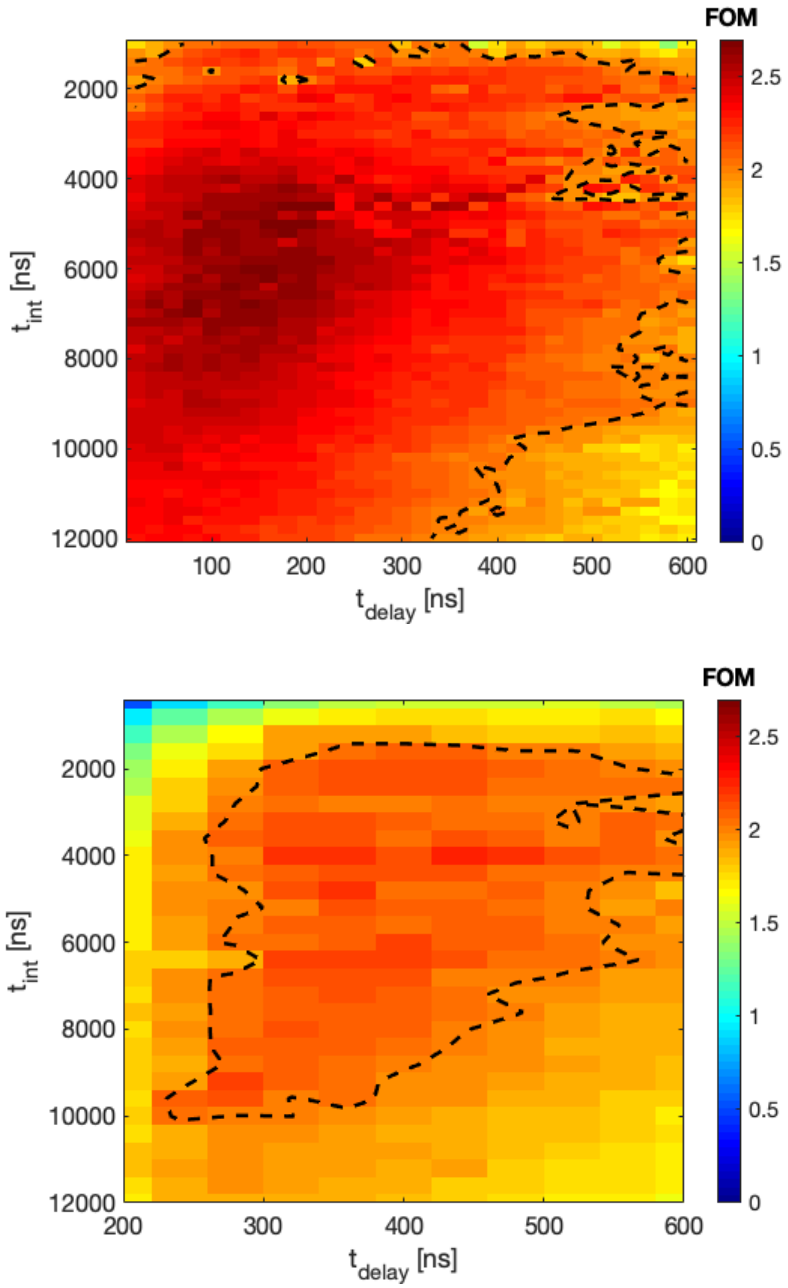

Fig. 4.4: The top figure reports the output for the optimisation procedure applied to the PT algorithm, while the bottom one reports the result for the CC algorithm. The area in the parameters space where FOM is > 2 (black dashed line) is $\approx 4000\ \mu s^2$ for the PT and $\approx 2150\ \mu s^2$ for the CC.

The PT algorithm applied using $t_{delay} = 160ns$ and $t_{int} = 6400ns$ returns PSD values in function of energy as plotted in Figure 8.15. Along with the ^{252}Cf source results for the ^{60}Co and for the ^{137}Cs were also plotted. The distribution of the PSD in the energy range 1 - 1.5 MeV is reported in Figure 4.5 where the FOM of 2.49 ± 0.02 was calculated on the ^{252}Cf data.

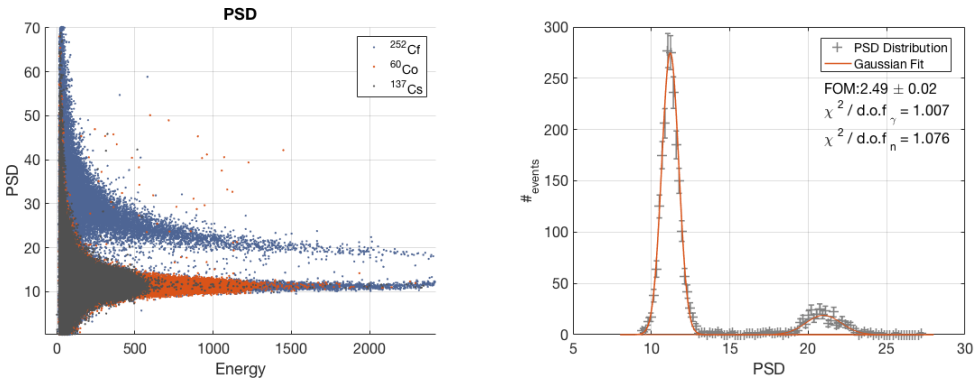

(a) (b)

Fig. 4.5: The distribution of the PSD is shown as a function of energy for the ^{252}Cf, the ^{60}Co and for the ^{137}Cs (a). Non-linearity and saturation effects, due to the non-linear region of the amplifier, occurs for energy greater than 2.5 MeV. Distribution of the PSD in the energy interval 1 - 1.5 MeV with superimposed two Gaussian fits (b).

Algorithms were compared on the base of the $F.o.M.$in different energy windows and on the energy value for a $F.o.M.= 1.27$, namely the minimum energy for an acceptable gamma/n discrimination. The comparison is reported in Figure 4.6 while the E_{min} is reported in Table 4.2 together with the $F.o.M.(E)$with $E \in [1; 1.5]MeV$.

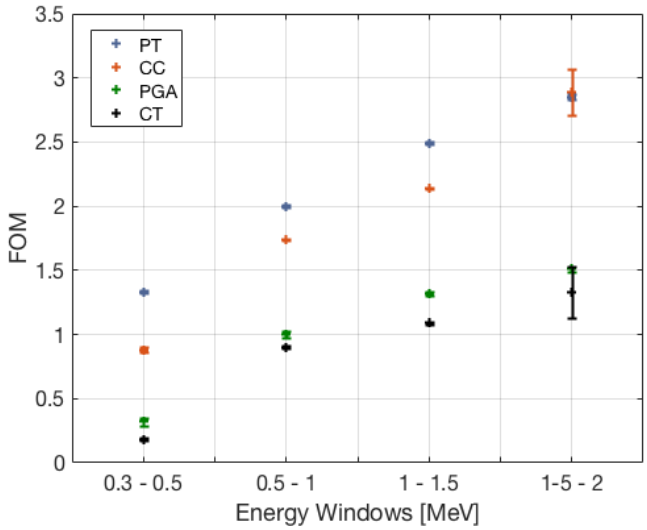

Fig. 4.6: FOM in different energy windows for the compared algorithms.

	PT	CC	PGA	CT
FOM	2.49 ± 0.02	2.14 ± 0.01	1.32 ± 0.01	1.09 ± 0.02
min Energy	200 keV	300 keV	1 MeV	1.5 MeV

Tab. 4.2: FOM in the energy window 1-1.5 MeV and the minimum energy that allows for a FOM greater than 1.3

The comparison outlines that the Peak - Tail algorithm results in better discrimination and improved stability. Figure 4.4 shows the optimisation output for the PT and CC algorithm; from these plots, it is possible to see that the first guarantees optimal performance over a more extensive set of parameter values. As observable that measure $F.o.M.$stability it was chosen the area in the parameters space where the $F.o.M.$is above 2. With an area that exceeds $4000\mu s^2$, the PSD_{PT} algorithm shows better stability with respect to the $2150\mu s^2$ area measured for the PSD_{CC} algorithm. The reason for these results is not apparent, and it is, moreover, counterintuitive. So far, numerical simulations were used to investigate more profoundly this result.

4.3 Simulation of a PSD scintillator

In order to understand the phenomenology that makes the Peak-Tail algorithm the best performing among the ones compared in the previous section, a Matlab simulation was used to simulate the scintillation light profile of the EJ-299/34 read out by a SiPM. The simulation also accounts for signal shaping by Front End Electronics. The core of the simulation is based on the code presented in [108, 93] and it accounts for the SiPM response to a burst of light plus SiPM's stochastic effects. The simulation parameters are SiPM dimension and the single-cell pitch (from where the total number of cell N_{cells} is calculated), the DCR, the Cross-Talk probability ϵ_{xt} and the after-pulsing probability ϵ_{AP} and τ_{AP}. The simulation is based on the following steps:

- generate $N_{p.e.}$ photons from a Poisson distribution with a mean number of photons $\mu_{p.e.}$;
- uniformly Distribute $N_{p.e.}$ photons on a square grid (SiPM sensor size) with N_{tot} cells available;
- for each cell a cross-talk event is generated in the neighbour cells with a probability ϵ_{xt};
- for each fired cell (primary + cross talk) an after pulse is generated with probability ϵ_{ap}.

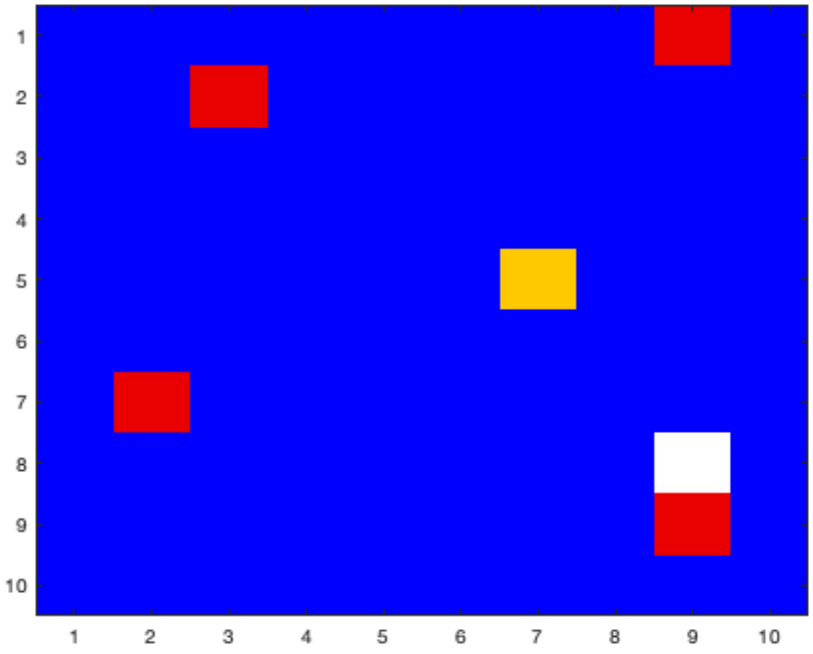

Fig. 4.7: Example of SiPM with 100 cells and 6 fired cell, of which red ones are primary event, the yellow one is a primary event plus an After Pulse and the white one is a Cross-Talk event.

- for each fired cell corresponding to a primary event or a cross-talk, a single electron response function is generated at time $t = 0$.

- every after pulse event is generated with a delay time (t_{AP}), with respect the primary event following an exponential distribution with characteristic time τ_{ap}, a single electron response with a amplitude $A(t_{AP}) = (1 - e^{-\frac{t_{AP}}{\tau_{ap}}})$), that is a fraction of the primary event charge.

- all the signals are summed together, and the output response of the SiPM is produced.

The result of a single iteration is shown in Figure 4.7, and the process is repeated N_{ev} times to generate a full dataset comprising N_{ev} events.

The single electron response is an analytical function of the form reported in Equation 4.6, and the simulation was modified, introducing a temporal distribution on the photon arrival time to simulate the scintillation light profile. The transfer function of the front end electronics was not analytically derived but was simulated instead through a digital band-pass FIR filter with custom cut-frequency. When this module is added to the simulation, the cut frequency represents an additional used-defined

parameter for the simulation. Simulation has been furthermore modified to consider the delayed cross talks probability separately from the prompt one. The simulation is quite flexible since it allows to simulate the light time profile with more than one-time component and to simulate the response of different front end by considering the bandwidth.

4.3.1 SiPM and Front End Electronics

The single-cell response was modelled as the sum of 3 exponential functions accounting for the rising edge and for the two falling edges (Equation (4.6)) time constants. The parameters chosen for the simulation are reported in Table 4.3. They were chosen to be close to the measurement of the single electron response of an s13360 series SiPM by Hamamatsu.

$$S(t) = G \cdot \left(P_R \cdot e^{-\frac{t}{\tau_{rise}}} - P_1 \cdot e^{-\frac{t}{\tau_{fall_1}}} - P_2 \cdot e^{-\frac{t}{\tau_{fall_2}}} \right) \tag{4.6}$$

Parameter used for simulation						
Parameter	P_R	P_1	P_2	τ_{rise}	τ_{fall_1}	τ_{fall_2}
Value	1	1	0.2	$0.2ns$	$0.3ns$	$30ns$
	DCR		CrossTalk (prompt/delayed)		Afterpulses	
	100 kHz		3%/7%		2%	

Tab. 4.3: Values of the parameters of the (4.6), and level of SiPM spurious effects.

Figure 4.8 shows the comparison between the simulate signal Single Electron Response and pulse acquired with the DT5720 digitiser. The digital filter used was an FIR filter with 40MHz bandwidth and a cut at 50MHz, similar to the summing circuit characteristics. The signal was evaluated on a time scale with a granularity of 10 picoseconds and then resampled to obtain the same sampling rate of the digitiser (250MHz).

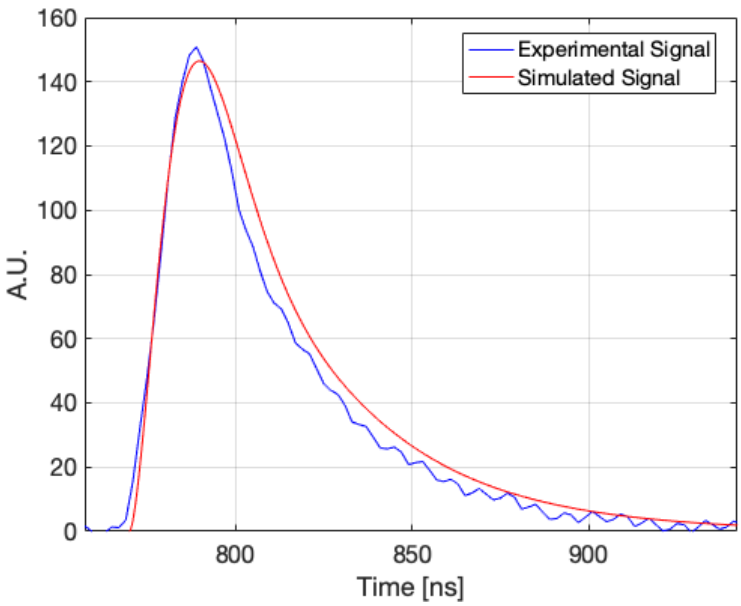

Fig. 4.8: Comparison of a simulated signal with a real signal of a single photo-electron.

4.3.2 Neutron-γ simulated signals

The photon distribution in time has been simulated with two decay constants (35 (γ) and 50 (neutron) plus a second decay time of 276 or 470 ns respectively), and the temporal distribution of the photons was tuned to simulate a response similar to the one of the EJ-276. However, to better understood the effect of the different ration of prompt and delayed component, signals with different time component ratio were simulated. Signals showed in Figure 4.9 were simulated with a 95% of the fast component and a 5% of the slow one.

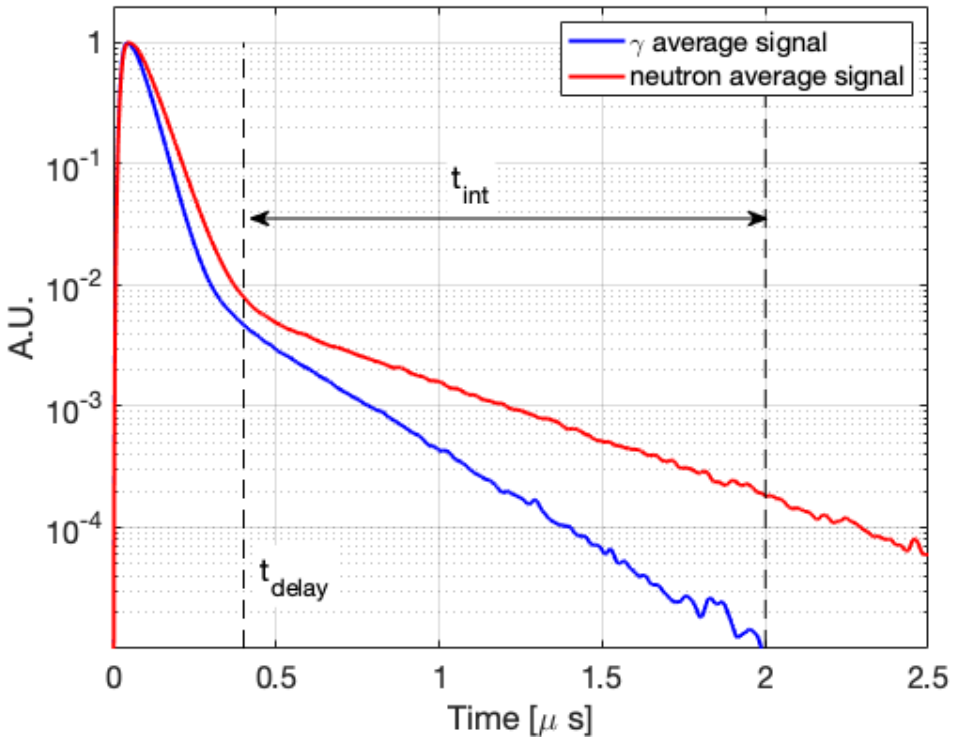

Fig. 4.9: Simulated signal of a γ and neutron induced pulse at the end of acquisition chain.

4.3.3 Algorithm Comparison

1000 γ and 1000 neutron pulses were simulated, with 2500 photoelectrons per each pulse. This number was chosen assuming that the light from 1 $MeVee$ deposited energy suffers from a 10% of light loss from the scintillator surface and considering the nominal SiPM PDE of 40%, as reported in the data-sheet.

The Kolmogorov Smirnov Test (KS) was used as a qualifier to compare the difference in signals when the area or peak amplitude normalisation is applied. KS measures the maximum difference in the cumulative of two distributions. The distribution considered are the simulated signal for γ and neutron interaction. A higher value of the KS test indicates a more considerable difference between the two signals, suggesting that the normalisation with the highest KS may allow for the better $F.o.M.$. The test was applied with different ratios of prompt/delayed components. In all simulations, the KS indicates the peak-amplitude normalisation as the one enhancing the difference in the two signals. Figure 4.10(b) and Figure 4.10(a) report the cumulative sum of a neutron signal (blue line) and a γ signal (red line) along with the KS result for two opposite scenario: the 5/95% and the 95/%5 ratio.

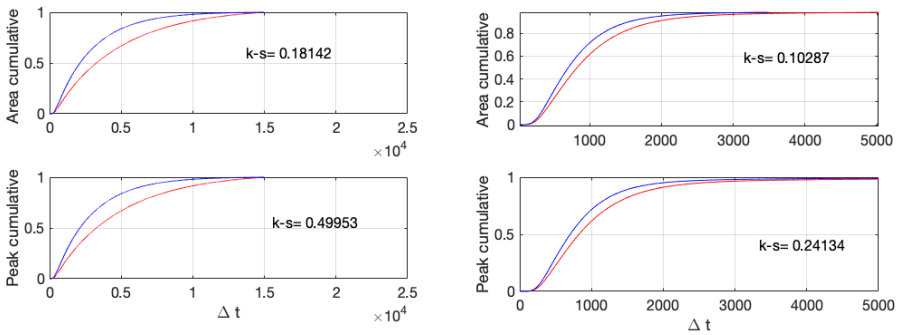

(a) (b)

Fig. 4.10: K-S test for a simulated signal where (a) the delay component predominates and (b) the prompt one does.

The two PSD algorithms were applied to the dataset, setting integration limits for the tail integration starts about 5 prompt τs after peak and lasts up to 5 delayed component τs ($t_{delay} = 300ns$ and $t_{int} = 1500ns$) as shown in Figure 4.9. In Figure 4.11(a) and Figure 4.11(b) the distribution of the PSD parameters evaluated according to (2.7) and (2.8) are reported. Mean value and $FWHMs$ for the two distribution have been calculated after a Gaussian fit.

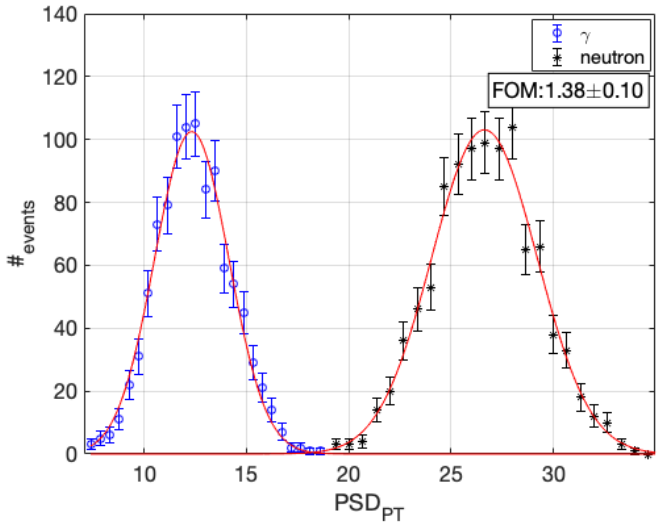

(a)

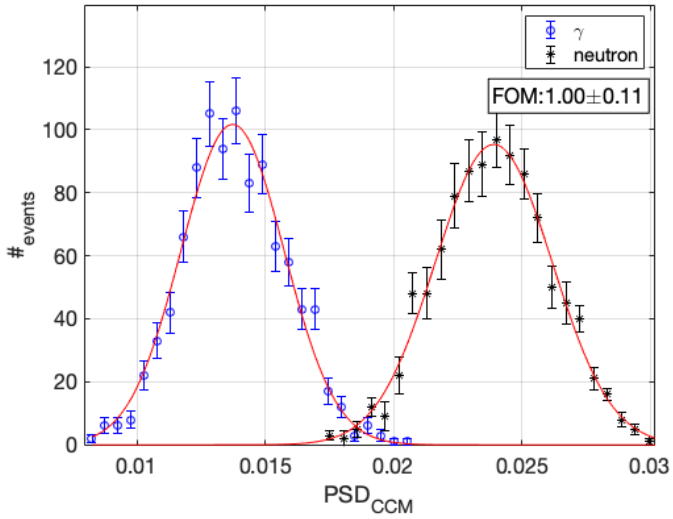

(b)

Fig. 4.11: PSD distribution for the PSD_{PT} (a) and PSD_{CCM} (b) parameter in simulated signals with 95%/5% component ratio.

The $F.o.M.$indicates that peak normalisation shows better separation ($F.o.M.$of 1.38 ± 0.1) with respect to area normalisation ($F.o.M.$of 1.00 ± 0.11). The result is in accord with the expectation of the Kolmogorov-Smirnov test. The $F.o.M.$, in favour of the PSD_{PT} algorithm, decreases as the ratio of two light components changes, leading to a better $F.o.M.$when the long light component prevails. In Figure 4.12 the $F.o.M.$are reported for both algorithm in case of 05%/95% component ratio with a $F.o.M.$of 4.45 ± 0.54 for the integral normalisation vs a $3.31.0.35$ $F.o.M.$for the peak amplitude normalisation.

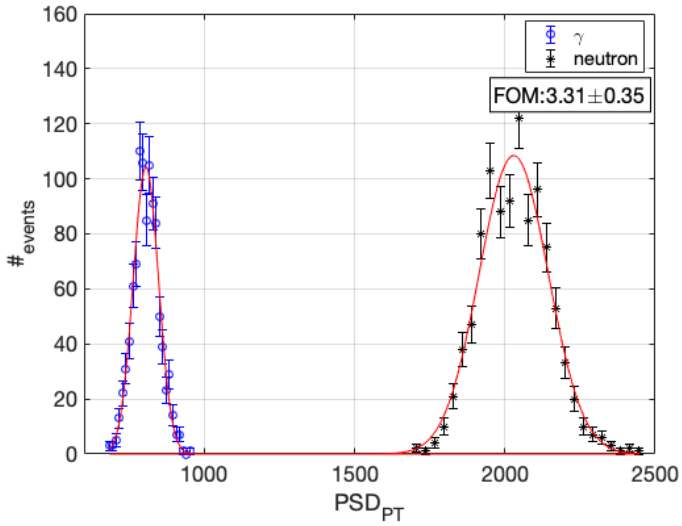

(a)

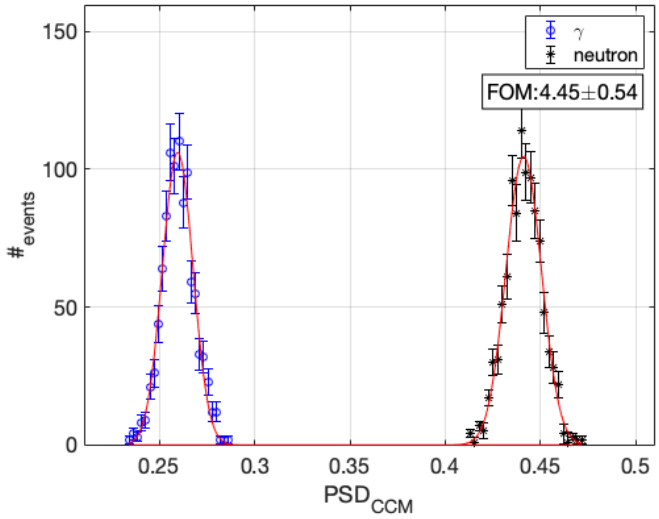

(b)

Fig. 4.12: PSD distribution for the PSD_{CCM} (a) and PSD_{PT} (b) parameter in simulated signals with 05%/95%component ratio.

$F.o.M.$has been evaluated for both algorithm at different light ratios, and the results are reported in Figure 4.13 where the errors bar are estimated propagating the error given by the fit procedure. PSD_{PT} results in a better $F.o.M.$as long as the prompt light component dominates over the long one. Once this condition no longer holds, the area normalisation results in better discrimination. The reason for the better discrimination, in some conditions, after the peak normalisation, is yet to be understood. The hypothesis that will be tested in the next chapter are the followings:

- the peak amplitude suffers less from the noise, so far the information brought by the peak is less affected by noise with respect to the integral

- the delayed components (that brings the information about the particle nature) are tested against the prompt components given that the peak is built-up mainly by the prompt photons.

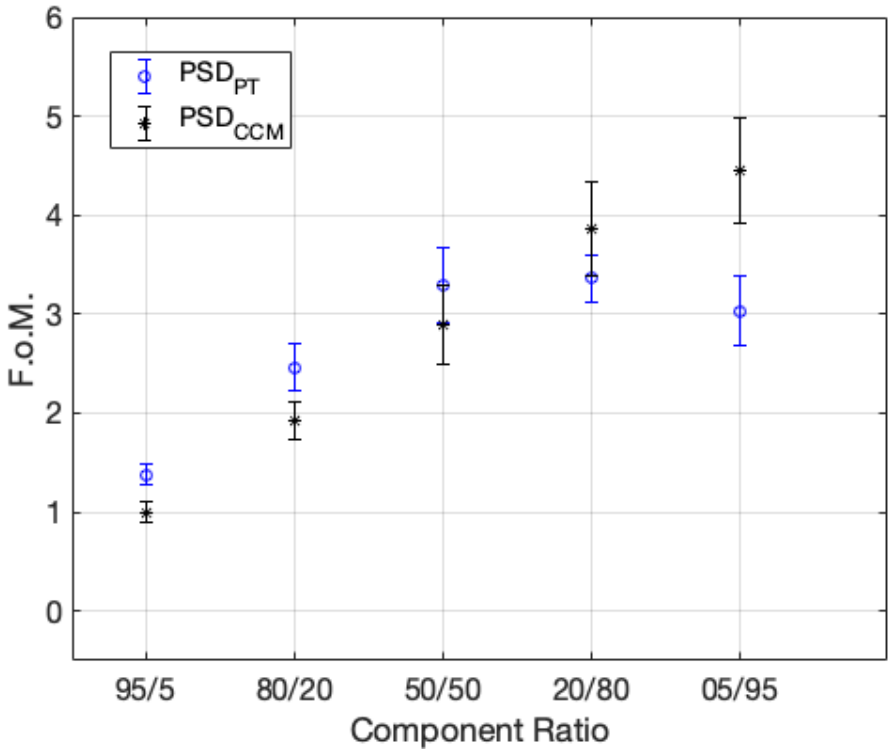

Fig. 4.13: $F.o.M.$as function of prompt/long ratio for both the PSD_{CCM} and PSD_{PT} discrimination parameters.

5 Noise estimation in Peak Amplitude or Charge Collection

Chapter 4 suggested that the use of peak amplitude instead of the integral could improve the pulse shape discrimination. The hypothesis is that the peak height can be used to measure the fast component, expected to be equal for a γ and a neutron with the same deposited energy, so far such a normalisation will enhance the difference in the tail of the scintillation signal.

Ina first place, through low light signals (less than 50 photons from a pulsed LED source, sensibly less than the scintillator Light Yeld) it had been qualified the electronic noise associated with the peak amplitude or with the charge integral. With the same light amount, the statistic fluctuations related to the different procedures have been qualified. This procedure was carried out to disentangle the effects of the scintillators and the detector. Indeed, beyond the noise figures, the comparison between the information conveyed by the use of the peak value of the signal and the integrated charge/pulse was based on the resolution power, namely the maximum number of different peaks in a multi-photon spectrum recorded with a 1.3x1.3mm^2 SiPM in above-mentioned low light condition.

The final step of the investigation involved the measurement in case a Scintillator is used. A reliable figure of merit can arise from the comparison of gamma spectra taken in different conditions. The SiPM in use was changed to a 6x6mm^2 sensor, interfaced to CsI(Tl) and LYSO scintillating crystals. Spectra were recorded using a ^{137}Cs nuclide and the assessment based on the resolution of the photo-peak at 662 keV. Measurements were performed with the slow CsI(Tl) scintillator and a fast LYSO (decay time 40ns), to account for the effects related to fast and slow components of the PSD scintillators.

Through numerical simulations, the impact of the time distribution of the emitted photons on the peak value build-up was measured and used to reinforce the understanding of experimental results about peak-tail algorithm performances.

5.1 Material and Methods

The analysis was conducted with SiPMs produced by HAMAMATSU Photonics, with the main features reported in Table 5.1. Small area sensors (1.3x1.3mm^2, s13360-1350) were used for detecting light pulses emitted by a LED source and conveyed on the surface of the sensor by an optical fibre. Larger area sensor (6x6mm^2, s13360-6050) was interfaced to scintillating crystals and used for γ ray detection. The scintillating crystals used were a CsI(Tl) and an LYSO with a volume of 6x6x15mm^3.

	S13360-1350CS	S13360-6050CS	
Cell pitch	50	50	μm
V_{BD}	53	53	V
V_{op}	V_{BD}+3	V_{BD}+3	V
Gain	$1.7 \cdot 10^6$	$1.7 \cdot 10^6$	-
Terminal Capacitance	60	1280	pF
DCR	90	2000	kcps
Cross-Talk	3	3	%
After Pulse	N.A.	N.A.	%
PDE$_{max}$	40	40	%

Tab. 5.1: Main figures of the sensors in use, as of the vendor's specifications. V_{bd} identifies the breakdown voltage and V_{op} the suggested operational voltage. The reported PDE corresponds to the peak value ($\lambda = 450nm$). Figures refer to an operating temperature T=25°C

A custom-designed circuit amplified the SiPM signal with twin amplification at 12/34 dB gain and 37 MHz bandwidth. A CR-RC circuit shaped the signal with time constants of $25ns$ and $17ns$ respectively for the differentiating and integrating circuits. The amplified signal was sampled using a CAEN DT5730 digitiser with 500 Msps sampling frequency, 250 MHz bandwidth and 14-bit digitisation over a 2V input range.

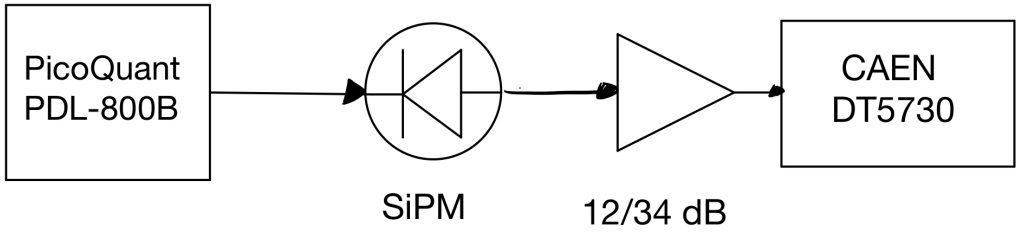

Fig. 5.1: Block scheme of the Experimental Set-Up.

Light pulses were generated at 1 MHz frequency by a PicoQuant PDL-800B module driving a blue LED, emitting bursts of photons with a sub-ns duration not exceeding twenty photons per shot in the used configuration.

5.2 Low Light Measurement

The impact of SiPM's stochastic effects, namely DCR, Cross-Talks and Afterpulses, was measured with a procedure that accounts for the different contribution independently with respect of the cell-to-cell gain variation. The sensor is exposed to a blue light from an LED conveyed to the SiPM (1.3x1.3mm^2, s13360-1350) by an optical fibre. A multi-photon spectrum was recorded by collecting the charge corresponding to each pulse. The first assessment of noise contribution from the cell-to-cell gain variation to the spectra collected with the peak or with the integral, was accomplished by reducing the recorded dataset to the subset corresponding to a single fired cell and comparing the σ of the 1-ph.e. peaks.

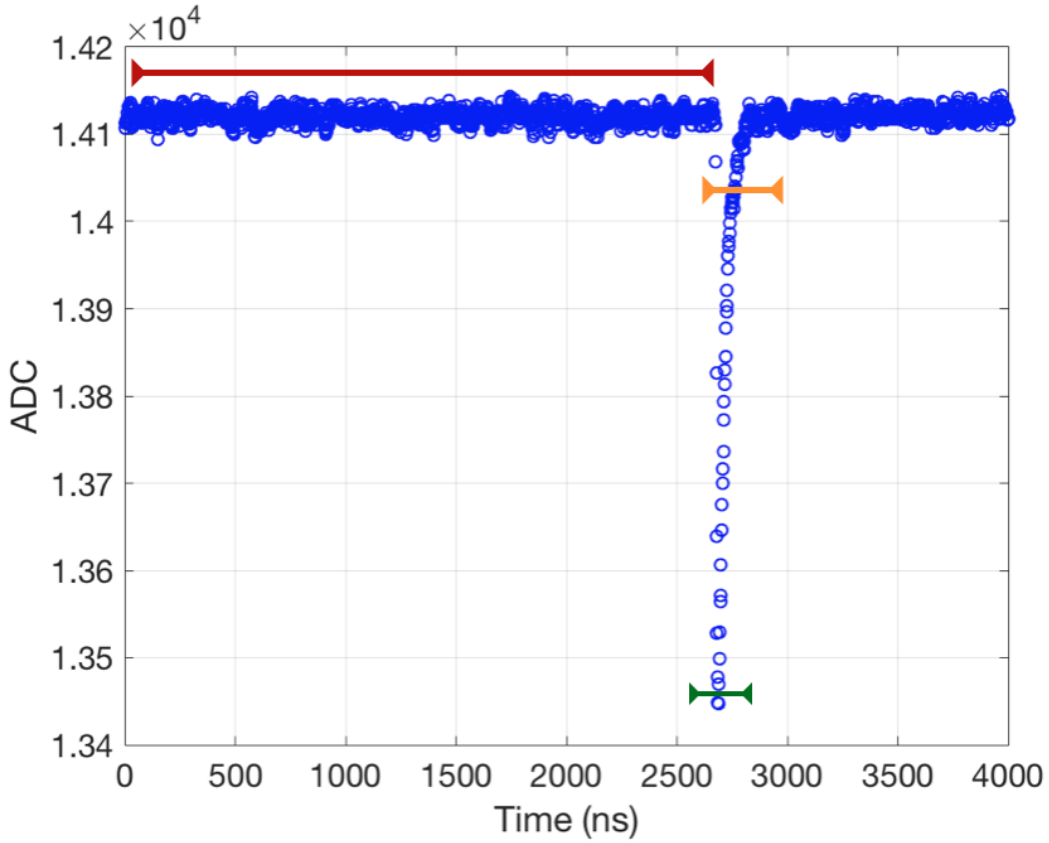

Fig. 5.2: Signal before the baseline subtraction. The red line shows search interval for the DCR in the pre-integration window. The orange one identifies the integration window of $124ns$ while the green one the peak search windows of $30ns$.

Digital charge integration signal window Δt was optimised to provide the maximum value of $integral/\sigma_{integral}(1p.e.)$ found to be $\Delta t = 124ns$. At this integration time, the relative error of the 1 photoelectron distribution signal-to-noise ratio is $6.6 \pm 0.6\%$.

The standard deviation of the distribution of the peak amplitude of the signals is influenced by two effects impacting in opposite directions: on the one hand, residual variations in the cell-to-cell multiplication process are expected to make it larger concerning the baseline fluctuations by the electronics noise; on the other hand, since the peak value is always retained, the order statistic applies, and fluctuations shall be reduced. The peak search window was reduced to 30ns interval, to correctly identify the peak getting rid of after-pulses and delayed cross-talks. The recorded data correspond to $\sigma_{peak}(1p.e.) = 9.4ADC$, to be compared to $\sigma_{baseline} = 6.6ADC$, indicating a prevailing effect due to the cell-to-cell gain variations. The signal-to-noise ration of $1p.e.$ distribution is $6.6 \pm 0.1\%$

In Figure 5.3, the two distribution of 0 and 1 photoelectron obtained with the two procedure is reported.

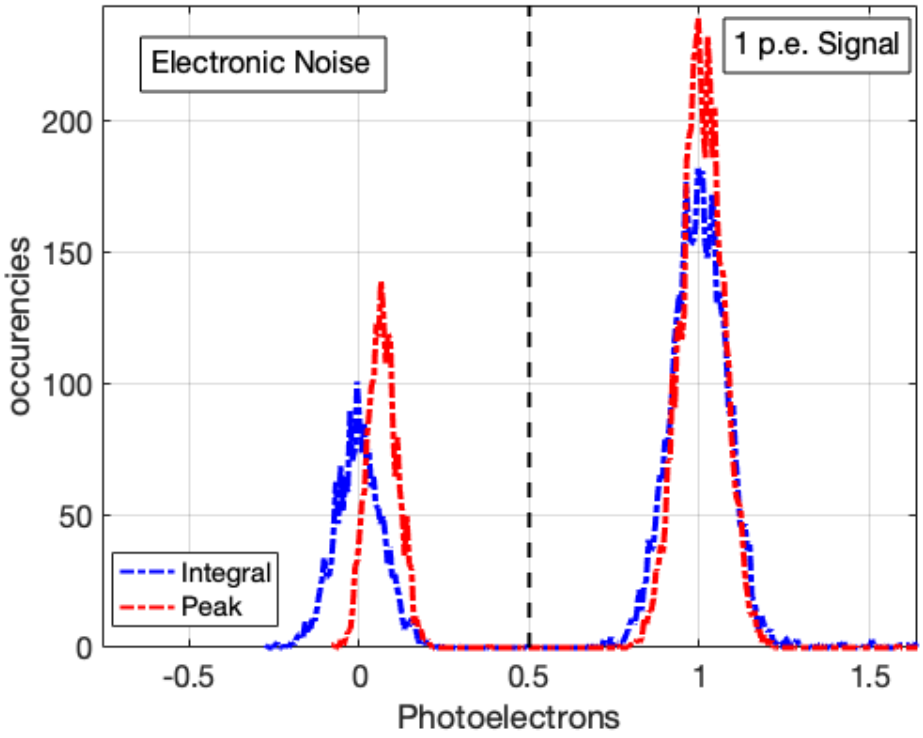

Fig. 5.3: distribution of the electronic noise and the one photoelectron signal. The noise in the peak amplitude is shifted with respect to the zero, and it is narrower since it follows a distribution given by the order statistics of the maxima as the maximum amplitude is always retained even in empty events.

As from those results, the performances of the two strategies are comparable, with a little bias towards the peak amplitude strategy.

5.2.1 Multi Photon Spectra comparison

Even if the performances on the single photoelectron signals are equal differences are evident in the quality of the multi-photon spectrum. Indeed the peak amplitude distribution is not affected by stochastic effects, namely delayed cross-talk and after-pulsing. In contrast, those effects contribute to the integral case spoiling the photon number resolution. The net result is a misidentification photoelectron number. A pile-up rejection method will not do it since the overall probability of having an event affected by a secondary avalanche increases with the number of primary avalanches. A rejection would then not be uniform with the number of photoelectrons resulting in an alteration of the photon statistics, and this may not always be the desidered outcome. In Figure **??**, the effect is shown: the left panel shows the overlaid spectra, while Figure 5.5 reports the scatter plots of the number of identified photons, event by event, using either the charge or the peak amplitude. The natural classification in a discrete number of fired cells is spoiled by random occurrences in the integration window, while the peak amplitude-based spectra show a better peak to valley ratio; it is expected a reduction of the maximum number of resolved peaks in the case of integral with respect to the peak amplitude since the events in between the peaks increase the RMS^2.

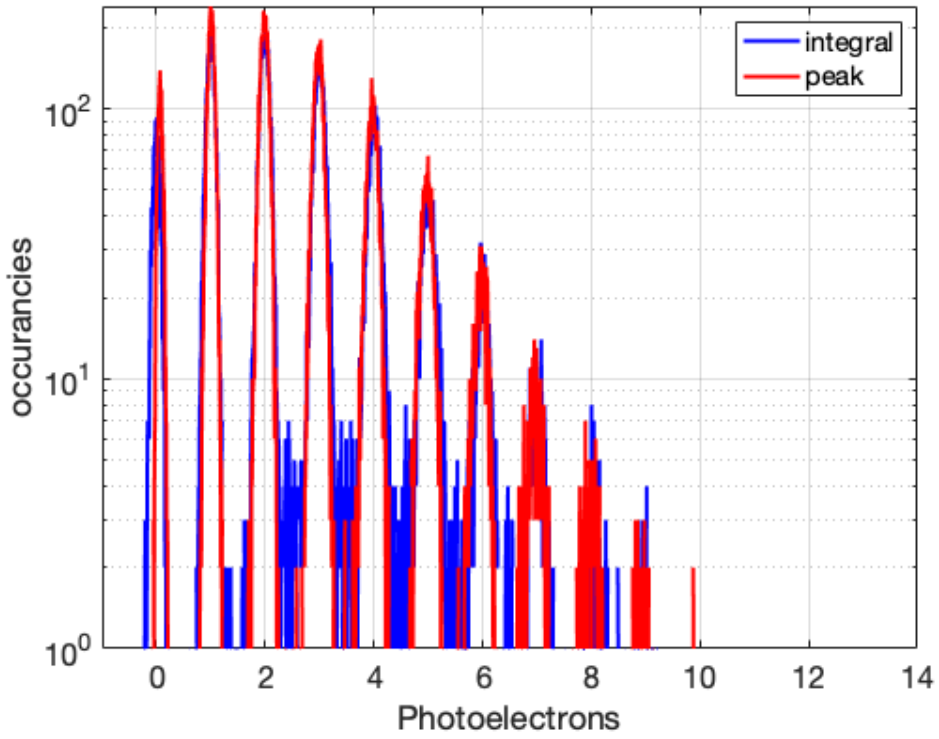

Fig. 5.4: Multiphoton spectra, considering the charge or the amplitude, in logarithmic scale.

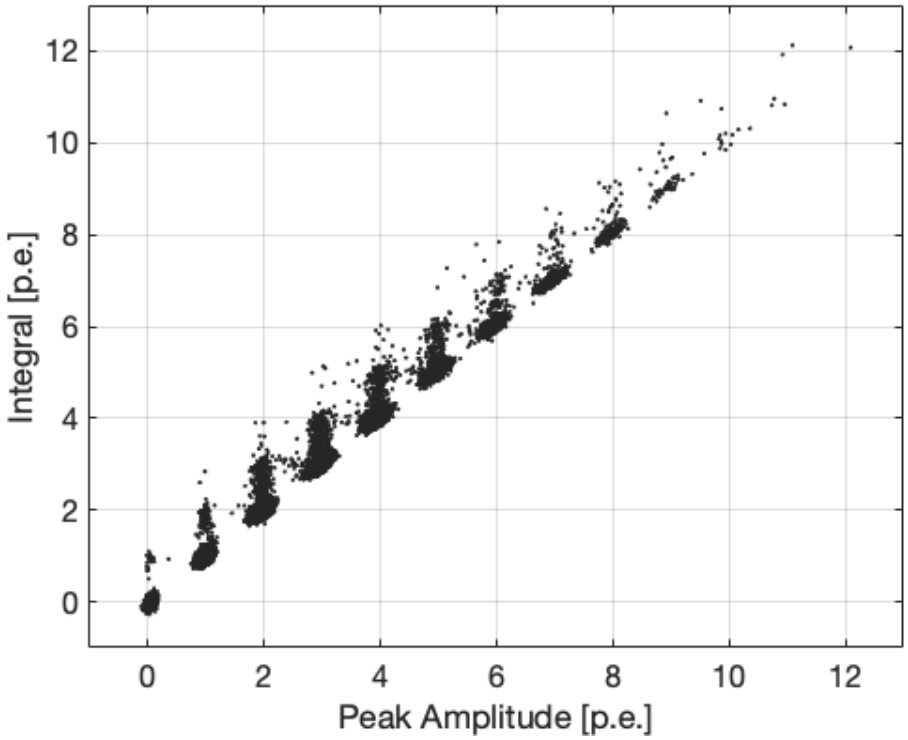

Fig. 5.5: Scatter plot of the number of p.e. measured with the integral or the peak amplitude.

With a slight modification to the Sparrow criterion (Equation (3.1)) the limit of two photoelectrons as no longer distinguishable is when the FWHM of the distribution is higher than 1.

$$FWMH \geq 1 \Rightarrow \text{No distinguishable photoelectrons} \tag{5.1}$$

σ^2 was measured as the variance of N^{th} photoelectron distribution considering asymmetric intervals that start at -3σ of the single Gaussian peak up to the next photoelectron (Figure 5.6).

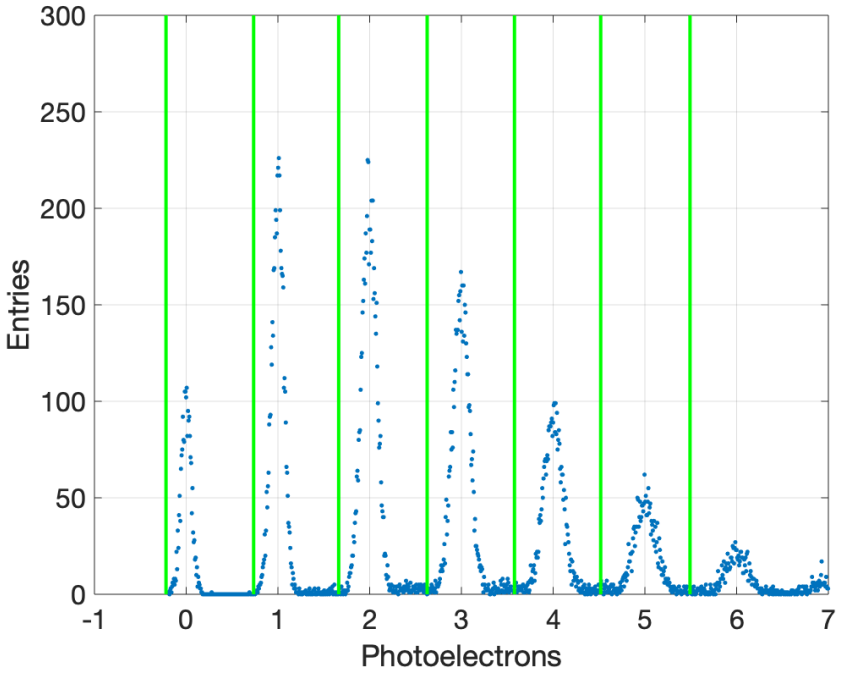

Fig. 5.6: Intervals to evaluate the σ of the N^{th} peak

$\sigma^2(N_{p.e.})$ is expected to increase linearly with the number of p.e. N, and when FWHM is equal to one (Equation 5.3) photoelectrons are considered too overlapped to be distinguishable. Solving Equations (5.2)- (5.7) it is possible to measure the maximum number N through a linear fit on $\sigma^2(N)$ data.

$$\sigma^2(N_{p.e.}) = \sigma_0^2 + N\sigma_{cell-to-cell}^2 \tag{5.2}$$

$$N : 1 \geq 2.355\sigma^2(N_{p.e.}) \tag{5.3}$$

$$\sigma^2(N) = mN + q \tag{5.4}$$

$$\sigma_0^2 = q \tag{5.5}$$

$$\sigma_{cell-to-cell}^2 = m \tag{5.6}$$

$$N = \frac{1}{\sigma_{cell-to-cell}^2} \cdot \left(\frac{1}{(2.355)^2} - \sigma_0^2 \right) \tag{5.7}$$

In equation 5.2 noise is given by electronic fluctuation σ_0, and the cell-to-cell gain variation $\sigma_{cell-to-cell}$. Electronic noise as a fraction of photoelectron can be either measured by q or by σ_0.

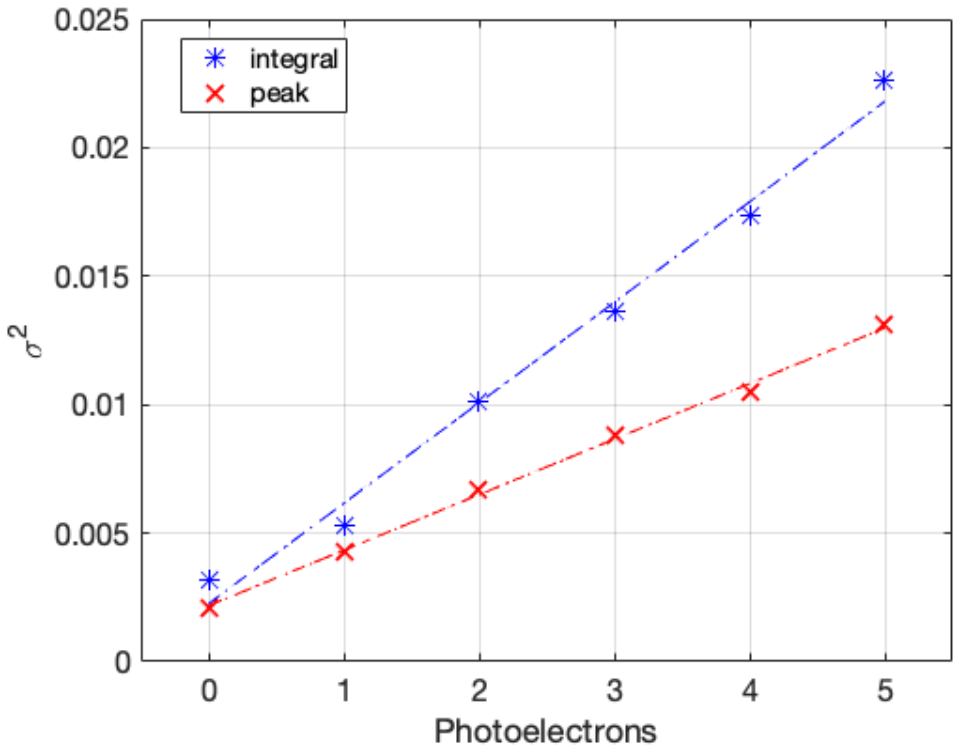

Fig. 5.7: $\sigma^2(p.e.)$ measured as the RMS of the distribution of photoelectrons for the integral and for the peak amplitude based measurement.

From this analysis, the number of resolved photons with digital charge integration is 45, while it is 82 for the peak amplitude. Those numbers were calculated by feeding fit results reported in Table 5.4 in Equation (5.7). Indeed, not only the peak amplitude allows to reconstruct the photon statistics in case of low light intensity, but also it allows to improve the photon-number resolution since it gets rid of

after-pulses and delayed cross-talk without altering the photon statistics as a pile-up rejection algorithm would do.

Parameter	Integral	Peak Amplitude
m	$0.00391 \pm 2.724 \cdot 10^{-4}$	$0.00216 \pm 7.398 \cdot 10^{-5}$
q	$0.00225 \pm 6.40 \cdot 10^{-4}$	$0.00217 \pm 2.398 \cdot 10^{-4}$
σ_0	0.0033	0.0020
N	45	82
Relative error	$6.6 \pm 0.6\%$	$6.6 \pm 0.1\%$

Tab. 5.2: Linear fit parameter of the $\sigma(N_{p.e.})$ for the peak amplitude and the integral expressed in photoelectrons at $V_{bias} = 53.5V$.

As additional qualifier Excess Noise Factor (Equation 5.8), as defined in [101], have been evaluated.

$$ENF = \mu_{ZP} \cdot \left(\frac{\mu_{MI}}{\sigma_{MI}}\right) \tag{5.8}$$

where μ_{ZP} is the mean value of the photoelectron distribution evaluated by the probability to detect zero photons (f_0) under the hypothesis of a Poissonian distribution ($\mu_{ZP} = -ln(f_0)$). μ_{MI}, σ_{MI} are the model-independent evaluation of mean value and variance of the photoelectron distribution. The ENF and maximum distinquishable peaks are evaluated at two bias: $53.5V (+2.5V_{OV})$ and at $55.5V (+4.5V_{OV})$, since at higher bias the PDE increases but also the amount of Cross-Talks and Afterpulses probability. The value are reported in Table 5.3 for the measurement performed at two different bias voltages.

	53.5	55.5
Peak	1.042 ± 0.002	1.036 ± 0.001
Integral	1.066 ± 0.002	1.093 ± 0.002

Tab. 5.3: EFN for the peak or the integral at two different bias voltage.

The number of distinguishable photoelectrons was evaluated at $V_{bias} = 55.5V$. According to the ENF analysis, a lower number of distinguishable photons is expected.

Parameter	Integral	Peak Amplitude
m	$0.0125 \pm 7.344 \cdot 10^{-4}$	$0.002895 \pm 1.66 \cdot 10^{-5}$
q	$0.00101 \pm 2.2 \cdot 10^{-4}$	$0.000289 \pm 5.33 \cdot 10^{-4}$
σ_0	0.0033	0.0020
N	15	63
Relative error	$9.7 \pm 0.1\%$	$5.0 \pm 0.\%1$

Tab. 5.4: Linear fit parameter of the $\sigma(N_{p.e.})$ for the peak amplitude and the integral expressed in photoelectrons at $V_{bias} = 55.5V$.

All the numerical figures chosen to compare the two approaches showed that peak amplitude would not only be equivalent to the use of the integral, but also it suffers less from the noise and stochastic effects, and better exploit the photon number resolution power of the SiPM.

5.3 Quality of γ spectra

A CsI(Tl) and LYSO scintillators with a volume of 6x6x15mm^3, produced by Hilger Crystals were exposed to a ^{137}Cs γ source to measure the quality when the peak amplitude or the integral are retained in a condition where lots of photons hit the sensor. Scintillators had all the sides polished and coated by a diffusive epoxy layer on the faces not interfaced to the sensor, whit their main characteristics reported in Table 5.5. The 6x6 mm^2 area SiPM, interfaced to LYSO and CsI(Tl) scintillators, recorded events and spectra were reconstructed by using the peak value or the integral of the signals. As a figure of merit, the resolution on the 662 keV photo-peak was retained. The 12 dB branch of the CR-RC amplifier had been used to avoid saturation due to the peak amplitude. It has been verified that the shaping time and the peak resolution of the 12 dB branch are equal to the 34dB one by collecting the spectrum of CsI(Tl) with the two branches since peak amplitude of CsI(Tl) signals lies below the saturation.

	CsI(Tl)	LYSO	
ρ	4.51	7.1	g/cm^2
λ_{peak}	550	420	nm
Light Yield	54000	40000	ph/MeV
τ	650/3500	37	ns

Tab. 5.5: Main Characteristics of CsI(Tl) and LYSO scintillators

The integration gate Δt for the light signal has been chosen as the one that maximises the resolution of the 662 keV photo-peak in the spectrum, being $\Delta t_{CsI(Tl)} = 10\mu s$ and $\Delta t_{LYSO} = 500ns$. The two spectra are reported in Figure 5.8 and Figure 5.9.

Spectra collected with the CsI(Tl) shows a worse resolution from peak amplitude with respect to one obtained the charge integral. Spectra reconstructed with the LYSO, on the other hand, show no appreciable difference between the two strategies.

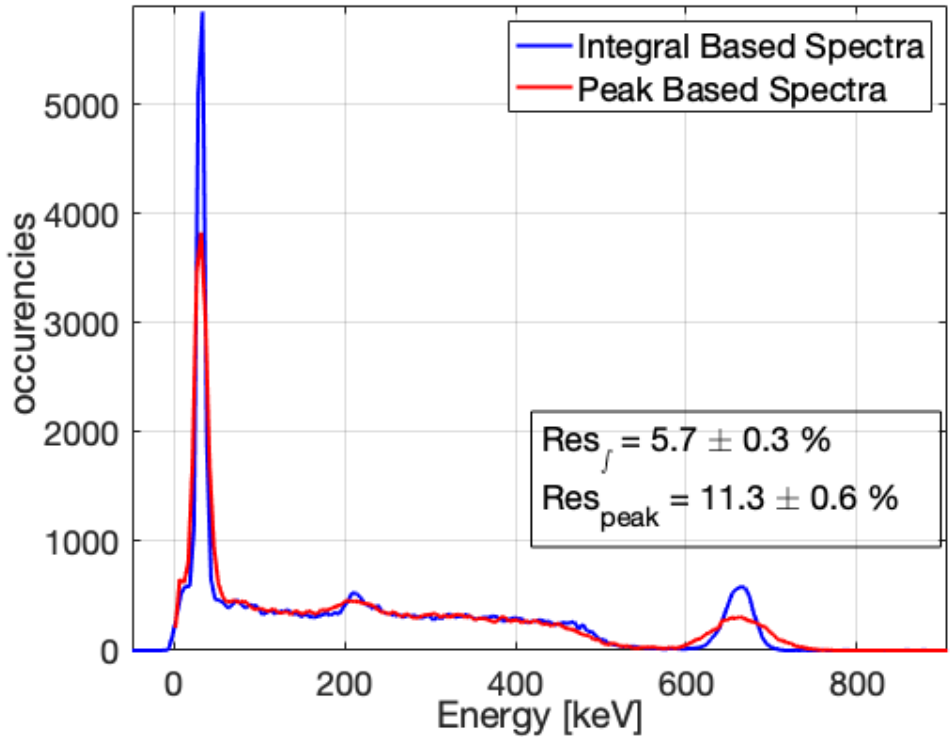

Fig. 5.8: Comparison of the spectrum obtained retaining the peak amplitude or the integral of the signal with the CsI(Tl) crystal

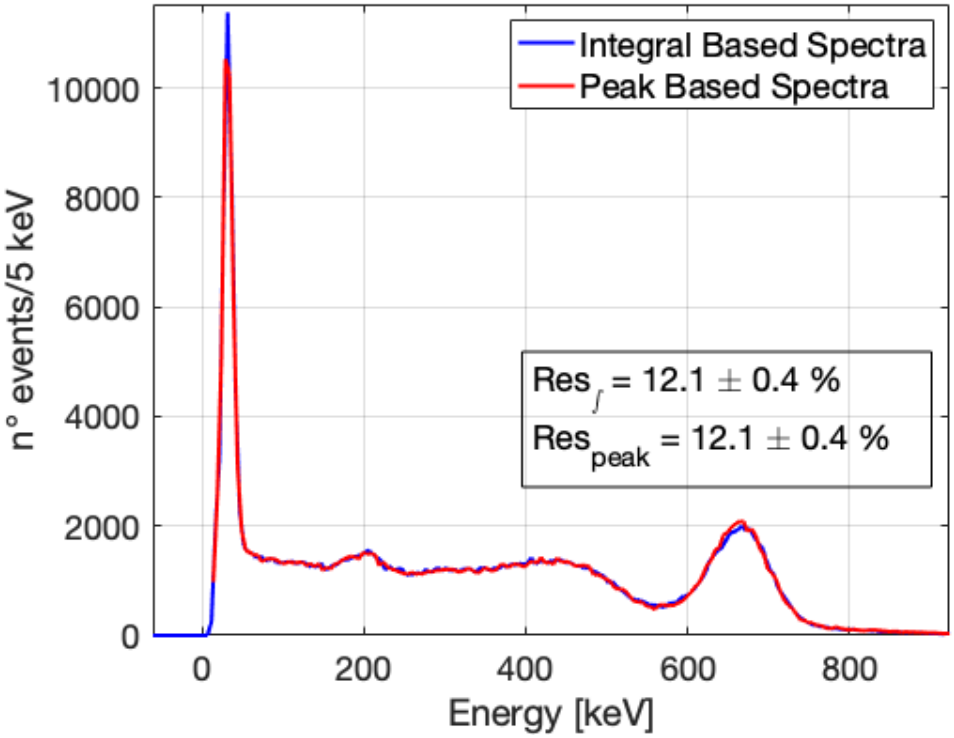

Fig. 5.9: Comparison of the spectrum obtained retaining the peak amplitude or the integral of the signal with the LYSO crystal

The result reflects the difference in the time development of the light from two scintillators, leading to a different number of photons that contributes to the peak build-up. This hypothesis was verified by means of a numerical simulation. The parameters used in the previous Chapter (Chapter 4) have been tuned to reproduce the scintillation profile of CsI(Tl) and LYSO crystals. In the two Figures, 5.10 and 5.11, the average signal is reported along with a single signal. 5400 photons, corresponding to a signal of $100keV$, was generated for the CsI(Tl), and distributed over two scintillating light component of $\tau_{prompt} = 600ns$ (80%) and $\tau_{long} = 3.5\mu s$ (20%). 4000 photons were generated with a $\tau_{LYSO} = 37ns$ to match the 100 keV energy in the LYSO simulation. The ratio of photons that contribute to the peak amplitude was evaluated by counting the number of detected photons at time $t < t_{peak}$.

In CsI(Tl) only $7.25 \pm 0.37\%$ of photons contributes to the peak while in the case of LYSO $69.5 \pm 1.3\%$ of photons contributes to peak, reducing the fluctuation and allowing for an estimation of the peak amplitude that better reflects the total amount of light produced.

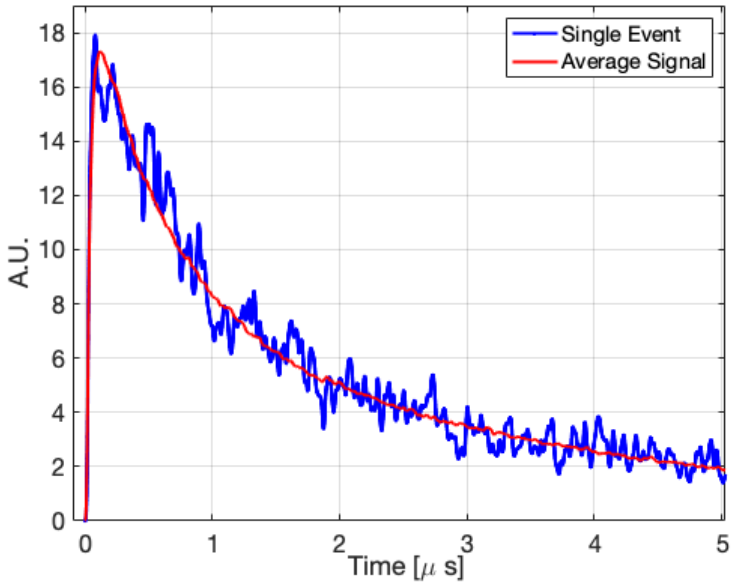

Fig. 5.10: Simulated CsI(Tl) signal.

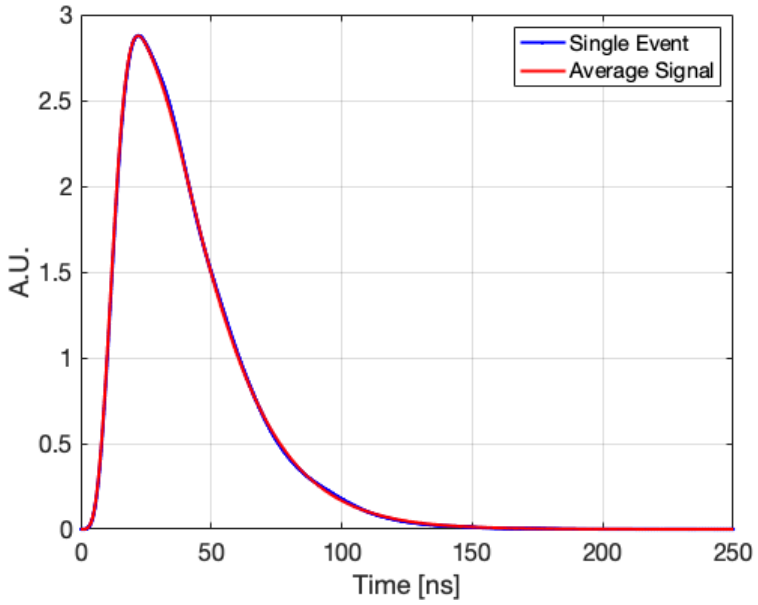

Fig. 5.11: Simulated LYSO signal.

5.4 The fast component in PSD scintillators

It is clear from the above-presented measurements and simulations that the peak amplitude is a proper measurement of the scintillation light when the components are such that a high fraction of the total light contributes to the peak built-up. In this sense, it can be verified with the same simulation if in the PSD scintillators the

prompt component contribute mostly to the build-up; It is easy to verify whether this is true or not in the simulation since it is possible to access to the arrival time of every photon.

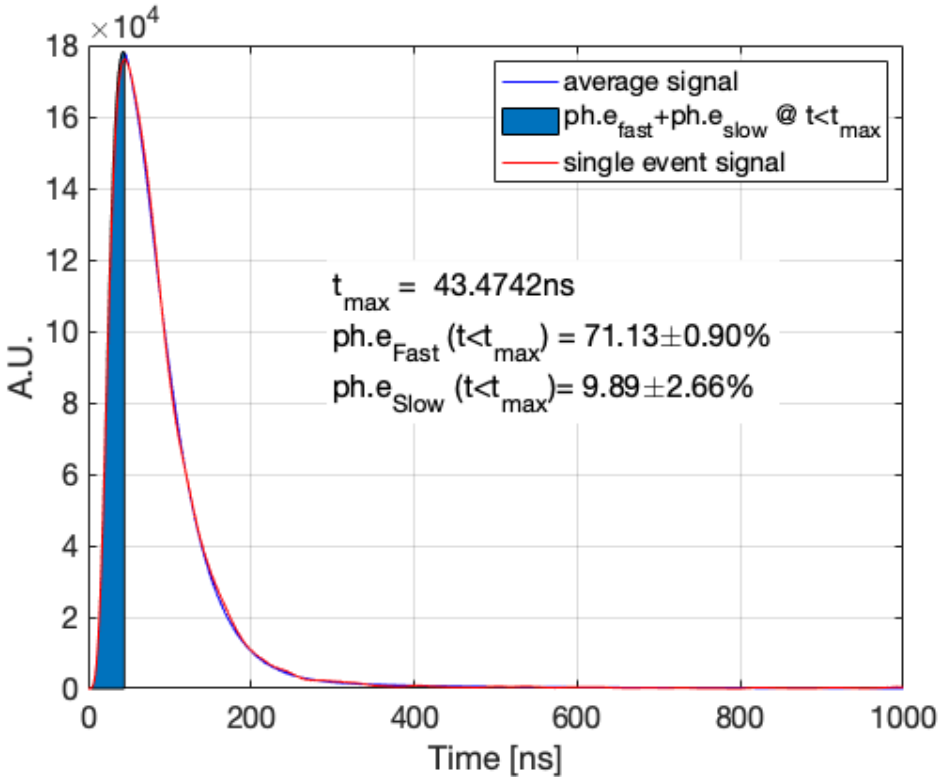

Fig. 5.12: Percentage of photons that arrive before the maximum when the prompt/delay proportion is 95/5.

As can be seen in Figures 5.12 and Figure 5.13 the peak is well defined when the fast component comprises the majority of the photons. On the other hand, when the long component prevails, the low statistics of photons increases the errors in the peak amplitude determination. These two conditions are similar to the one obtained with the simulation of the CsI(Tl) and LYSO scintillators, suggesting that the peak amplitude measurement better identifies the fast component.

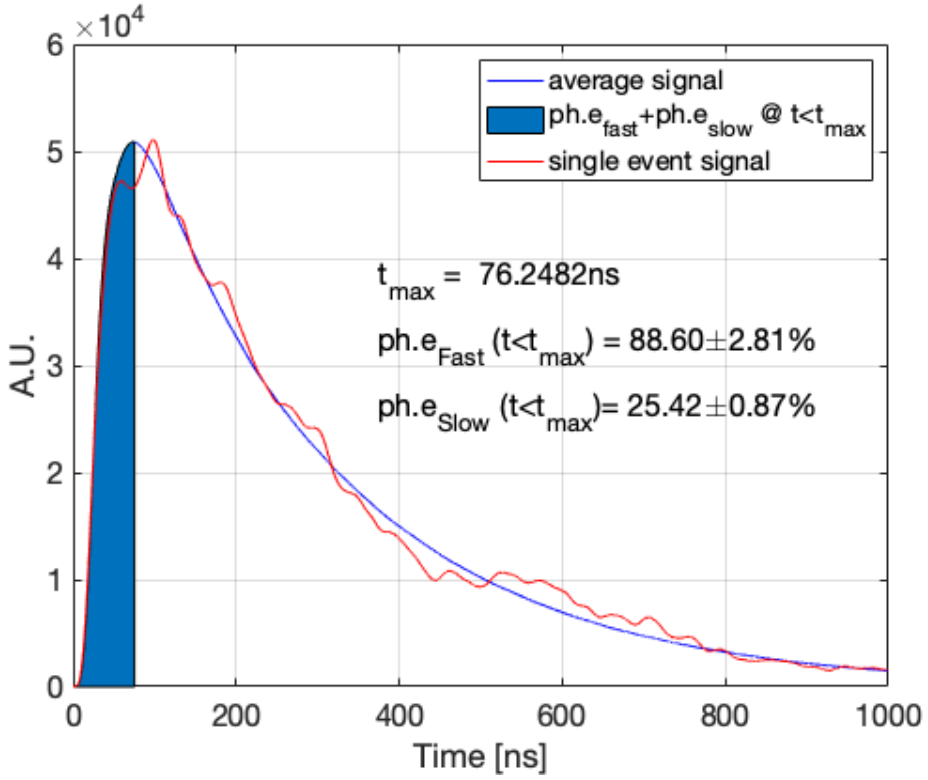

Fig. 5.13: Percentage of photons that arrive before the maximum when prompt/delay proportion is 5/95.

The ratio of the photons that arrive before the time of the peak is reported in Table 5.6, for prompt and long components at different simulated prompt/long ratio. Differences between $F.o.M.$for (2.7) and (2.8) are in favour of the peak normalisation when the prompt light is sensitively higher than the slow component in the prompt component. When the Fast/Total ratio becomes comparable to the Slow/Total ratio, the $F.o.M.$indicates that the total charge normalisation allows for achieving better results.

Component Ratio	Fast	Slow	Fast/total	Slow/total
95/5	$71.13 \pm 0.92\%$	$9.86 \pm 2.66\%$	$59.42 \pm 0.93\%$	$0.49 \pm 0.13\%$
80/20	$71.33 \pm 1.01\%$	$8.82 \pm 1.25\%$	$57.07 \pm 0.81\%$	$1.76 \pm 0.25\%$
50/50	$72.27 \pm 1.31\%$	$9.07 \pm 0.80\%$	$36.14 \pm 0.65\%$	$4.53 \pm 0.4\%$
20/80	$76.84 \pm 1.81\%$	$10.32 \pm 0.69\%$	$15.37 \pm 0.38\%$	8.26 ± 0.56
5/95	88.60 ± 2.81	25.42 ± 0.87	4.43 ± 0.71	24.15 ± 0.63

Tab. 5.6: Ratio of photons from fast ad slow components that contributes to the peak build up.

Peak height presents advantages in case of low light detection, while when it comes to the scintillation light is effective only if fluctuations of the peak are small. Indeed, the situation when the number of photons that contribute to the peak build-up is the

majority of the total generated photons. The physical meaning of peak-tail algorithm is then supported by the experimental results and simulations that showed how, through peak amplitude, a better estimation of fast components is achieved when the ratio of the components is in favour of the fast one.

6 Role of Light collection on PSD

In the last chapter, it was shown that light has a primary role in the performances of Pulse shape discrimination algorithm. In particular, the ratio of the prompt/delayed light was related to the performances of the different discrimination algorithms. The final step in the investigation of the parameters affecting the PSD performance is a study on the impact of the detected scintillating light intensity. The main goal of this chapter is to calibrate the detector response in photo-electrons, matching the $F.o.M.$with the amount of collected light instead of energy. In order to act on the detected scintillating light, it was changed the V_{bias}, and the PDE consequently. However, the incidence of stochastic effects changes with voltage, and it has an impact on the detected light, as shown in the previous chapter. It is still a matter of decoupling the effects, and to so, a small sensor area coupled to the LED pulsed light was used in order to use the MultiPhoton peak spectrum to measure the V_{bd}, the gain and the stochastic effects for different V_{ov}. It was then possible to retrieve the number of detected photons for different V_{ov}, accounting for the stochastics effect, by coupling the sensor to a PSD capable scintillator. The optimal parameters were found for each different bias voltage, and the $F.o.M.$has been evaluated in different energy windows. Notably, the minimum discrimination energy strongly dependent on the V_{ov}, and it corresponds to a fixed number of detected photo-electrons, independently with respect to the bias voltage. This results clarified the relation between the $F.o.M.$and the collected light.

6.1 Charaterisation of the SiPM

6.1.1 SiPM Gain

A 6x6mm^2 SiPM produced by HPK (s13360-6050c), whose main features are reported in Table 5.1, was used to perform this analysis. The sensor was illuminated by a blue light generated from a sub-ns LED driver PicoQuant PDL-800, as in Chapter 5, and signals were acquired synchronously. A three-stage inverting amplifier amplified siPM with gain that ranges from 1 to 50 dB, the SP5600 Power Supply and Amplification Unit (PSAU) by CAEN. The signal was then digitised via a CAEN DT5720 Desktop Digitiser, 250Msps, 2V input range and 12 Bit resolution (Figure 6.1) and integrated offline for $350ns$.

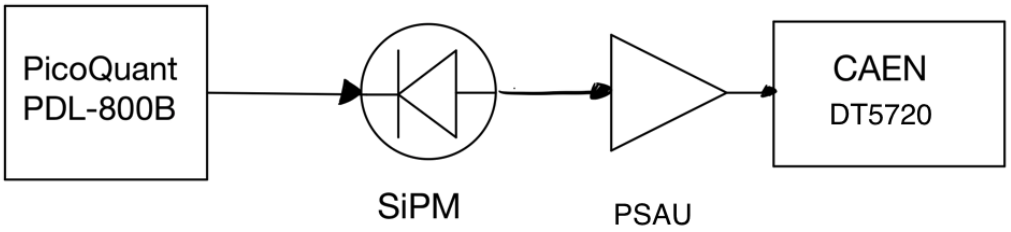

Fig. 6.1: Block scheme of the experimental set-up

An exemplary multi-photon spectrum is reported in Figure 6.2. The SiPM's gain is measured by the Δ_{pp}, namely the distance in ADC channels in the multi-photon spectrum, via Equation (6.1).

$$G = \frac{\Delta_{pp} \cdot ADC_{c.r.}}{q_e} \tag{6.1}$$

where $ADC_{c.r.}$ defined as in Equation (6.2):

$$ADC_{c.r.} = \frac{Coulomb}{ADC} = \frac{V_{pp} \cdot \Delta_t}{R_{in} \cdot 2^{N_{bit}} \cdot G_{PSAU}} \tag{6.2}$$

and

- V_{pp} is the dynamic range of the digitiser;
- R_{in} is the digitiser input impedance;
- N^{Bits} is the digitiser bit resolution;
- Δt is the digitiser sampling period $(1/250Mhz = 4ns)$;
- G_{Psau} is the gain of the PSAU;
- q_e is the elementary charge.

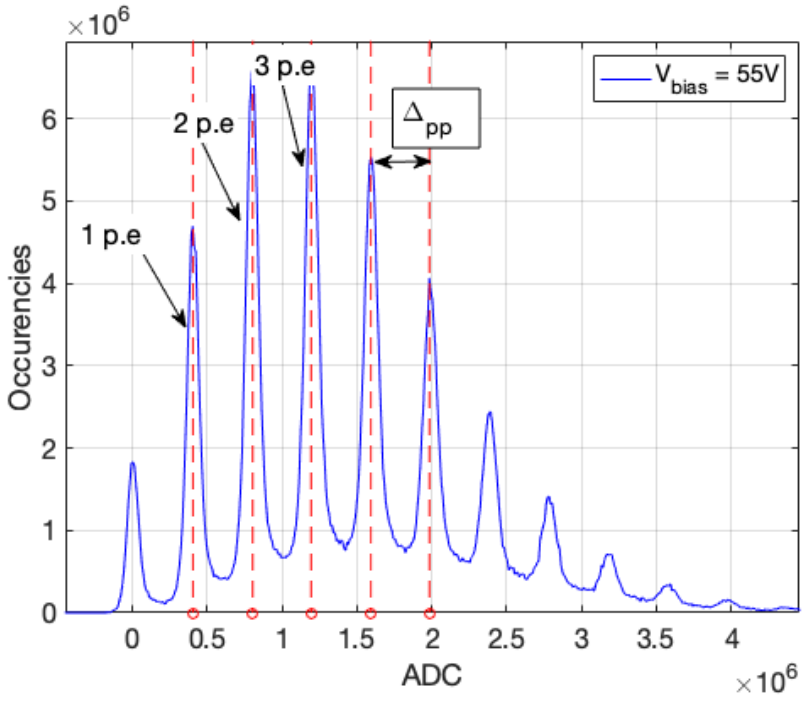

Fig. 6.2: Multi photon peak spectrum measured with G_{PSAU}=32, $V_{bias} = 55.5V$ integrating the light signal for $350ns$.

Equation (6.2) means that SiPM signal, that is in current, is read as a voltage drop across the input resistance R_{in} in the digitiser. Conversion factor $ADC_{c.r.}$ gauge the voltage step, of 1 ADC corresponding to the current through the R_{in} resistors in $Coulomb$.

6.1.2 BreakDown voltage

Δ_{pp} depends on the V_{ov} by its relation to gain expressed in Equation 6.1. The value of the V_{bd} was measured from the $\Delta_{pp}(V_{bias})$ curve, extrapolating the voltage for which the Δ_{pp} is equal to 0. The values of Δ_{pp} were measured with a $G_{PSAU} = 32dB$ and V_{bias} that ranges from 53.3 to $58.5V$ in steps of $0.5V$. The value of V_{bd} is then the intercept of linear regression reported in Figure 6.3 at $T = 20.1^o$. Its value is$V_{bd} = 52.25V \pm 0.02V$.

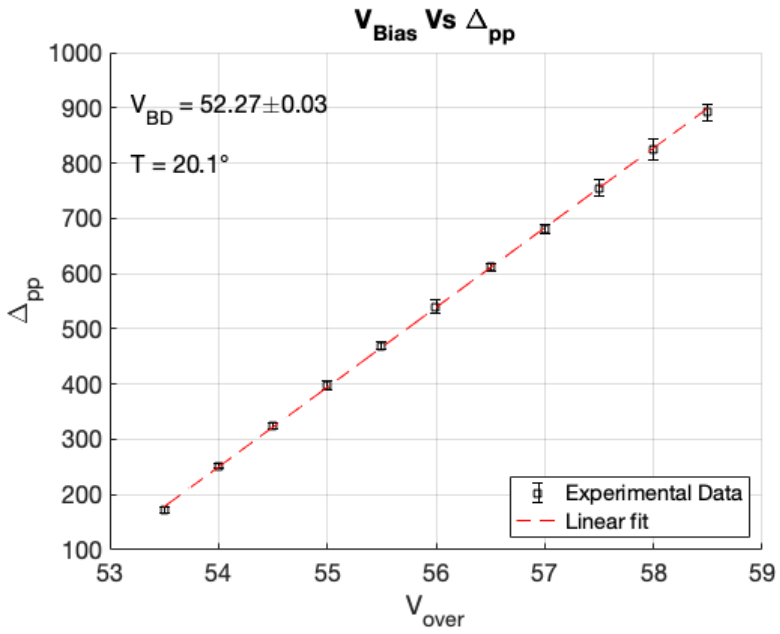

Fig. 6.3: Determination of the V_{bd} by looking at the V_{bias} that results in $\Delta_{pp} = 0$.

6.1.3 Effective cross-talk

To properly evaluate the PDE of the sensor, the number of primary events has to be measured. Even if it is not possible, event by event, to determine the number of primary fired cells, it is, however, possible to statistically correct the mean value of detected photo-electrons taking in account the cross-talk and afterpulses probability. Indeed, the net effect of cross-talk and after-pulses is to increase the mean value of the photon number distribution. Following this assumption, also expressed in [101] the stochastic effect impact can be measured as the excess of measured photo-electrons with respect to the real ones. The problem of measuring the number of primary fired cells can be solved if the light source follows a Poissonian distribution. In this case, the primary photo-electrons can be measured as in the Equation (3.15) as the probability to detect no photons.

Once the number of expected photons by a pure Poisson statistics and the measured ones are computed, it is possible to estimate than an "effective" cross-talk ϵ_{xt}^{eff} from Equation 6.3 and 6.4.

$$\mu_{MI} = \mu_{ZP}/ \cdot (1 - \epsilon_{xt}^{eff}) \tag{6.3}$$

$$\epsilon_{xt}^{eff} = 1 - \frac{\mu_{ZP}}{\mu_{MI}} \tag{6.4}$$

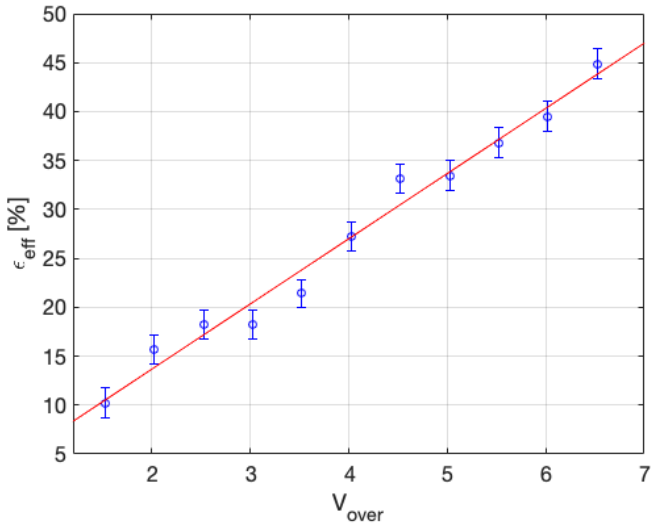

Fig. 6.4: ϵ_{xt}^{eff} as function of the V_{ov}.

6.1.4 Non amplified gain

Since it is not possible to obtain a multi-photon peak spectrum without amplifying the signal, a direct measurement of the Δ_{pp} is not possible. However, by the following procedure, it is possible to measure the $\Delta_{pp}(gain = 1)$ indirectly. In a first place, at the nominal voltage of $V_{ov} = +3V$, the Δ_{pp} has been evaluated for different gains ranging from 20 to 38 dB. Light pulses did non exceed ten photons per spill, while PSAU amplification range has not been fully exploited to avoid output saturation. By means of linear regression, the $\Delta_{pp}(gain)$ function can be evaluated and the $\Delta_{pp}(gain = 1)$ can be extrapolated.

A second method to measure the $\Delta_{pp}(gain = 1)$ is to increase the photon flux to hundreds of photons per spill, then measure the average number of photoelectrons when the gain is set for a value for which Δ_{pp} is known. It is possible to measure the number of photoelectrons $N_{phe^{hl}}$ utilizing Equation (6.5), profiting from the previous calibration:

$$N_{phe^{hl}} = \frac{< ADC_{hl} >}{\Delta_{pp}} \tag{6.5}$$

after the correction of the measured $< ADC_{hl} >$ value considering the stochastich effects term ϵ_{xt}^{eff}.

A gain = 1x results in a different Δ_{pp} and $< ADC_{hl} >$ values, but $N_{phe^{hl}}$ did not change. So far, it is possible to measure the $\Delta_{pp}(gain = 1)$ by inverting Equation (6.5)

The results of the two measurements are reported in Figure 6.5 and Figure 6.6. From those measurements, the value at gain = 1x can be extrapolated, and Table 6.1 reports the measured values.

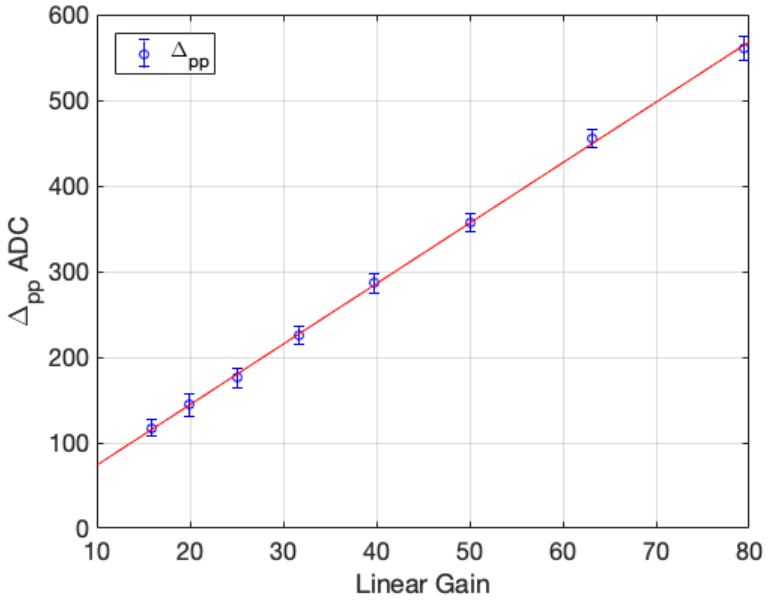

Fig. 6.5: Δ_{pp} as function of gain for $V_{ov} = +3V$ with low light intensity (<20 photons per spill) pulses and $G_{PSAU} \in [20; 38]dB$

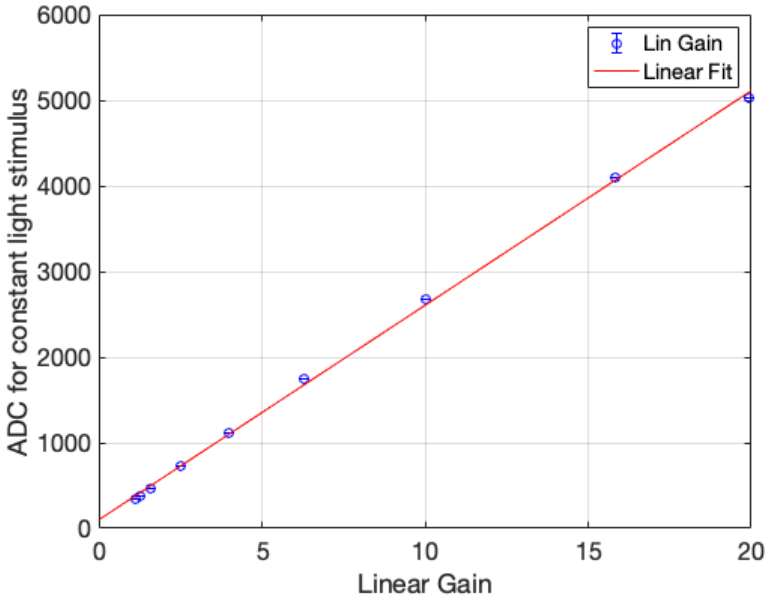

Fig. 6.6: Δ_{pp} as functiton of gain for $V_{ov} = +3V$ with high light intensity pulses ($\approx$ 100 photons per spill) and $G_{PSAU} \in [1; 20] dB$

Parameter	Low Light	High Light
m	7.06 ± 0.36	252.8 ± 7.2
q	3.01 ± 2.3	99.98 ± 8.51

Tab. 6.1: Parameter of the scan in Gain fit.

Given the Δ_{pp} at $Gain = 20dB$ it is possible to measure the primary photoelectrons number $N_{phe^{hl}} = 35$. Δ_{pp} from the high light measurement results to be 7.21 ± 0.35 that is comparable with the value obtained from the measurements at low light.

Since the PSAU is AC coupled, while the direct input of the digitiser is DC coupled, a gain conversion factor G_{CF} was measured to obtain the value of Δ_{pp}^{direct}. This conversion factor $k_{psau/digi}$ is measured by the ratio of $< ADC_{hl} >$ measured with direct signal and $< ADC_{hl} >$ measured after attenuating by 1db, via an HP desktop analogue attenuator, the PSAU signal with gain=1db.

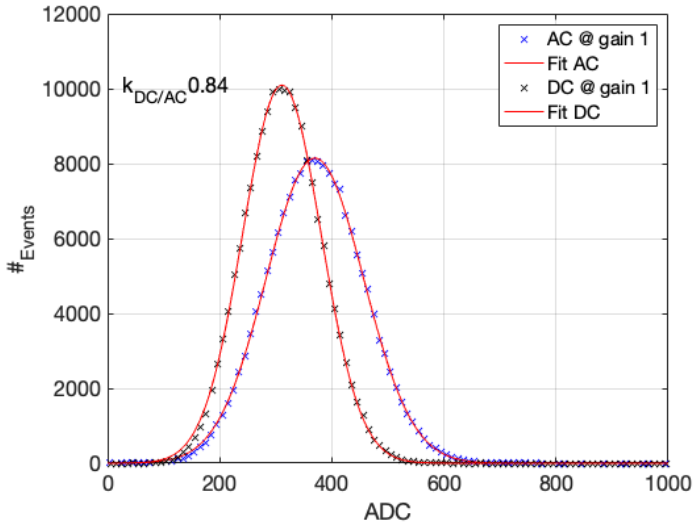

Fig. 6.7: Ratio of the two light distribution with no amplification collected with the DT5720 either directly or after the PSAU amplification stage at $1dB$ and an attenuator at $1dB$

Δ_{pp}^{direct} have been evaluated from Equation (6.6) under the hypothesis that a scale factor can model differences between AC and DC coupling.

$$\Delta_{pp}^{direct} = (\Delta_{pp}^{AC} \cdot G_{CF} \cdot k_{DC/AC}). \tag{6.6}$$

where the G_{CF} is the gain conversion factor and $k_{DC/AC}$ is the ratio between the AC/DC coupled $< ADC_{hl} >$ values

Once the Δ_{pp}^{direct} is measured for one value of V_{ov}, it is possible to evaluate $\Delta_{pp}^{rel}(V_{ov})$ recalling that relative Δ_{pp} variation are indipendent from the front end gain.

$$\Delta_{pp}^{rel}(V_{ov}) = \frac{\Delta_{pp}(V_{ov}) - \Delta_{pp}(3V_{ov})}{\Delta_{pp}(3V_{ov})} \tag{6.7}$$

A linear fit was then applied on the value of $\Delta_{pp}(V_{ov})$ for the low light measurement at different bias, ant the $\Delta_{pp}^{direct}(V_{ov})$ was obtained multiplying the $\Delta_{pp}(V_{ov} = +3V)$ for the $\Delta_{pp}^{rel}(V_{ov})$.

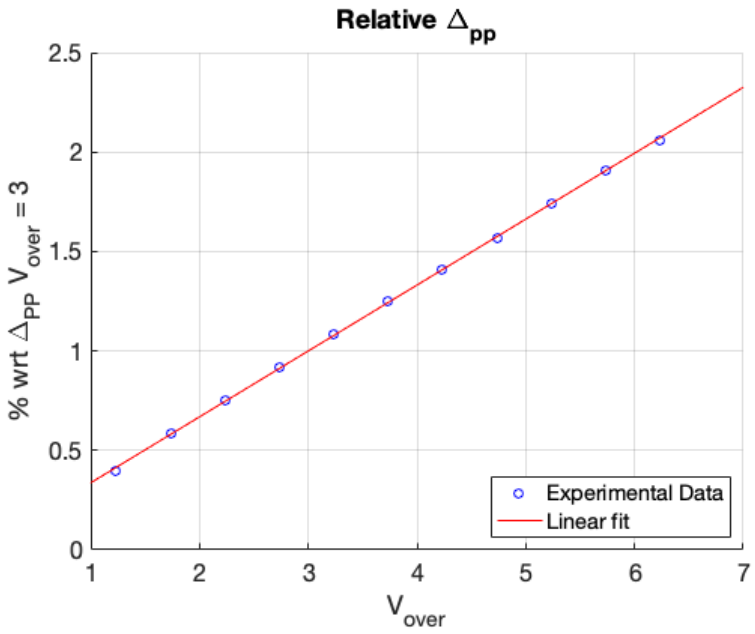

Fig. 6.8: Fit to the Equation 6.7 for the relative Δ_{pp} variation as function of V_{ov}

Parameter	Value
m	0.3333 ± 0.0016
q	0 ± 0.0066

Tab. 6.2: Parameter of the fit in Figure 6.8

The Δ_{pp}^{direct} as function of V_{ov} is reported in Figure 6.9, calculated as in Equation 6.8.

$$\Delta_{pp}^{direct}(V_{ov}) = \Delta_{pp}^{direct}(V_{ov} = 3) \cdot (V_{ov} m_{rel} + q_{rel}) \tag{6.8}$$

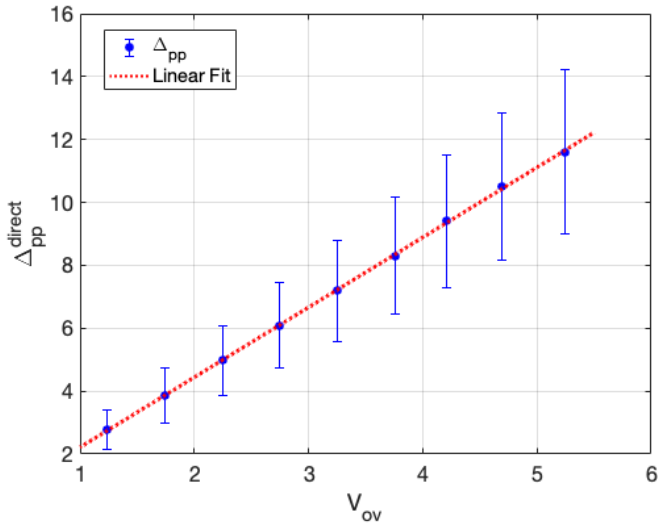

Fig. 6.9: Δ_{pp}^{direct} as function of V_{ov}.

6.1.5 PDE relative

The value of the Δ_{pp} was measured along with the impact of stochastic effects for all the V_{ov}. It is now possible to measure the relative PDE by measuring the difference in detected photons per each V_{ov} accounting for effects mentioned above. It can be measured in at least two ways measuring the PDE as variation in the number of photo-electrons under a constant light stimulus:

- given a fixed light intensity, $\approx$ 100 photons per spill, the $< ADC_{hl} >$ is measured and corrected for the ϵ_{xt}^{eff} for different V_{ov} and the relative PDE is evaluated as in Equation 6.9

$$PDE_{rel} = \frac{Obs(V_{ov})}{Obs(+3V_{ov})} \tag{6.9}$$

- at low light intensity, $\approx$ 20 photons per spill, the μ_{ZP} is evaluated as in Equation 3.15 and the relative PDE. evaluated as in Equation 6.9,

where the Obs is either $< ADC_{hl} >$ or μ_{ZP}. Both of the methods should give similar results, and in addition to the PDE measurement, the comparison qualifies the use of ϵ_{xt}^{eff} correction factor since the μ_{ZP} based method is not affected by any correction for stochastic effects. Figure 6.10 reports the value of the $< ADC_{hl} >$ before and after the correction for the ϵ_{xt}^{eff}. In Figure 6.11, the measurement of the PDE with

the two methods is reported. The results from the two methods are compatible when the correction for the stochastic effects is taken into account.

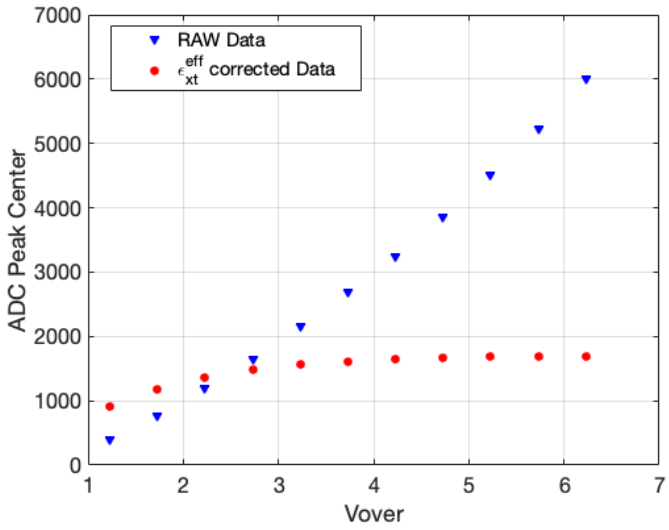

Fig. 6.10: The $< ADC_{hl} >$ mean value as function of V_{ov} before and after the ϵ_{xt}^{eff} correction.

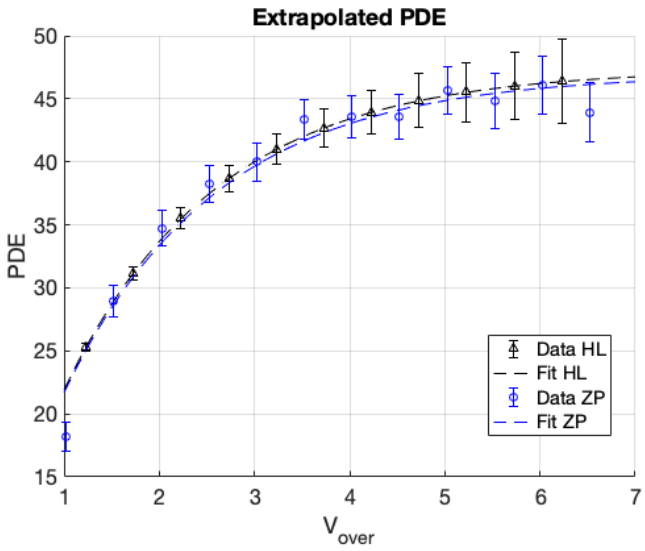

Fig. 6.11: PDE evaluated with the two above mentioned procedures.

6.2 Light - Energy Calibration

Once the ADC/Photoelectron conversion factor is known, namely the Δ_{pp}, it is possible to proceed to measure the conversion factor Photo-electrons/Energy in the EJ-276 scintillator for the different V_{ov}. The scintillator used in this measurement is a sample of 8x8x15mm^3 volume wrapped with a reflective coating (Figure 6.12). It

was interfaced to the SiPM through optical grease and the signal form the SiPM was directly digitised by the DT5720 CAEN digitiser. The EJ-276 has the same temporal characteristics of the EJ-299/34, but it results in improved mechanical robustness and optical stability in time. After the energy calibration γ sources for each V_{ov}, it will be possible to convert the ADC channel to photo-electrons (via ADC-Photons calibration factor Δ_{pp}^{direct}) and so far the energy in photo-electrons, to measure the number of photo-electrons per keVee for any tested V_{ov}.

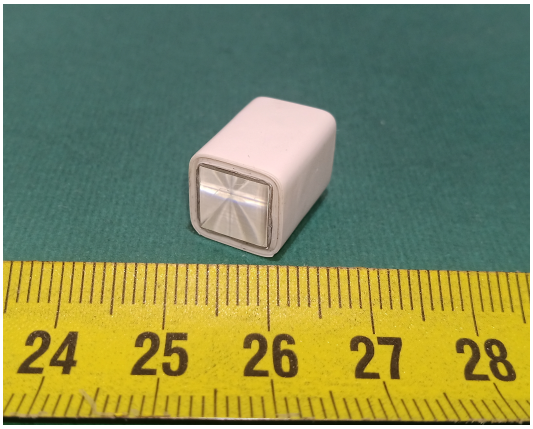

Fig. 6.12: The EJ-276 8x8x15mm^3 volume wrapped with reflective coating used for the measurement.

Different γ sources were employed: ^{137}Cs, ^{22}Na and a ^{60}Co spectra were collected integrating offline the signal digitised with DT5720 digitiser. The integration gate was set to $800ns$ in order to collect 95% of the light for a γ pulse.

An exemplary spectra obtained with the ^{137}Cs source is reported in Figure 6.13, while in Figure 6.14 the calibration curves ADC-keV and Photoelectrons-keV are reported for different V_{ov}.

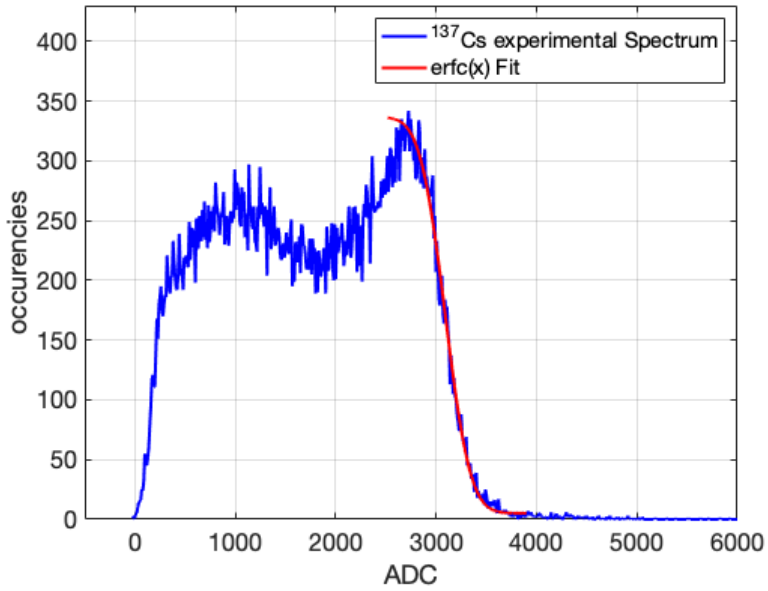

Fig. 6.13: Spectrum of ^{137}Cs source collected integrating for $800ns$ a the EJ-276 light read by the SiPM biased at $+3V_{ov}$

The calibration curves were measured for all the overvoltages ranging from $+1V_{ov}$ to $+5.5V_{ov}$.

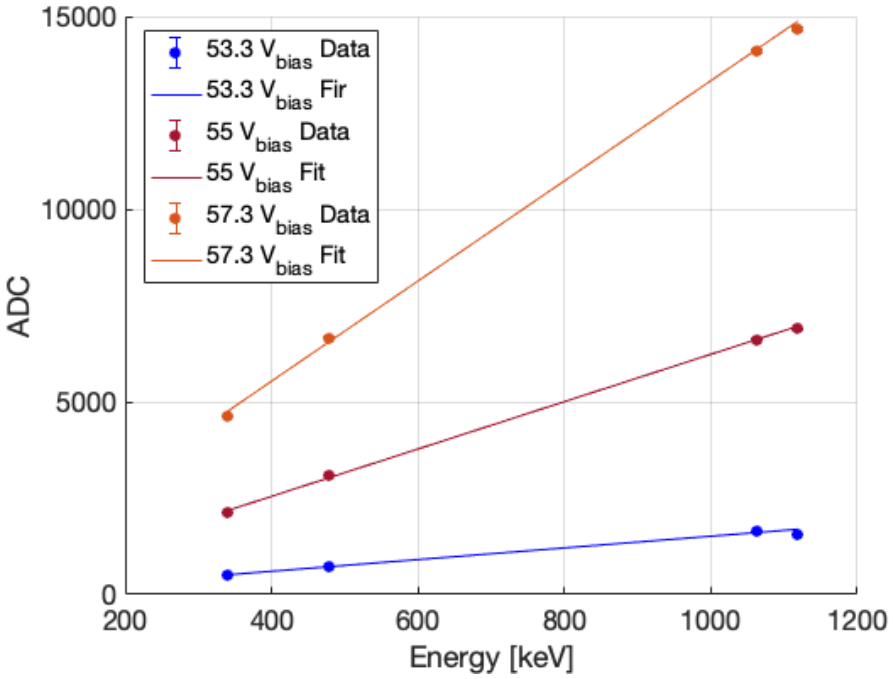

(a)

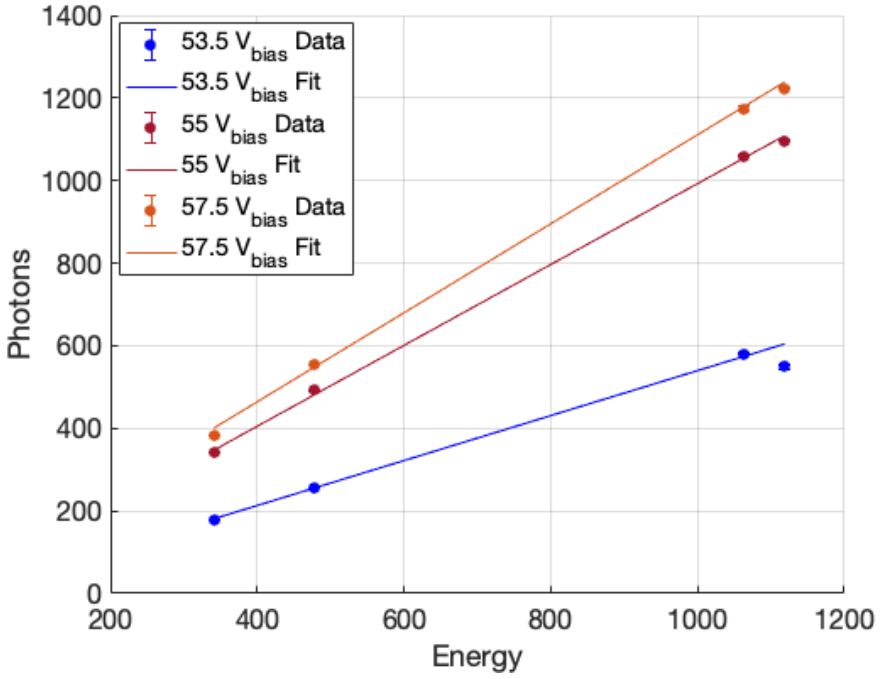

(b)

Fig. 6.14: Calibration curves measured with a linear curve when the Compton edge position is evaluated in ADC channels (a) or in photo electrons (b) after the correction for ϵ_{xt}^{eff}.

6.3 $F.o.M.$as function of detected light

$F.o.M.(E)$could be now related to the number of photo-electrons in order to measure the influence of detected light intensity.

6.3.1 FOM as function of Energy

The distribution of PSD discriminating variable as function of energy, biasing the sensor at $V_{ov} = +3V$, is reported in Figure 6.15, and the PSD distribution evaluated for pulses with $E \in [200; 300] keVee$ and in $E \in [1; 1.5] MeVee$ are reported in Figure 6.16 as example. The optimal integration windows have been evaluated through the optimisation procedure presented in Chapter 4.

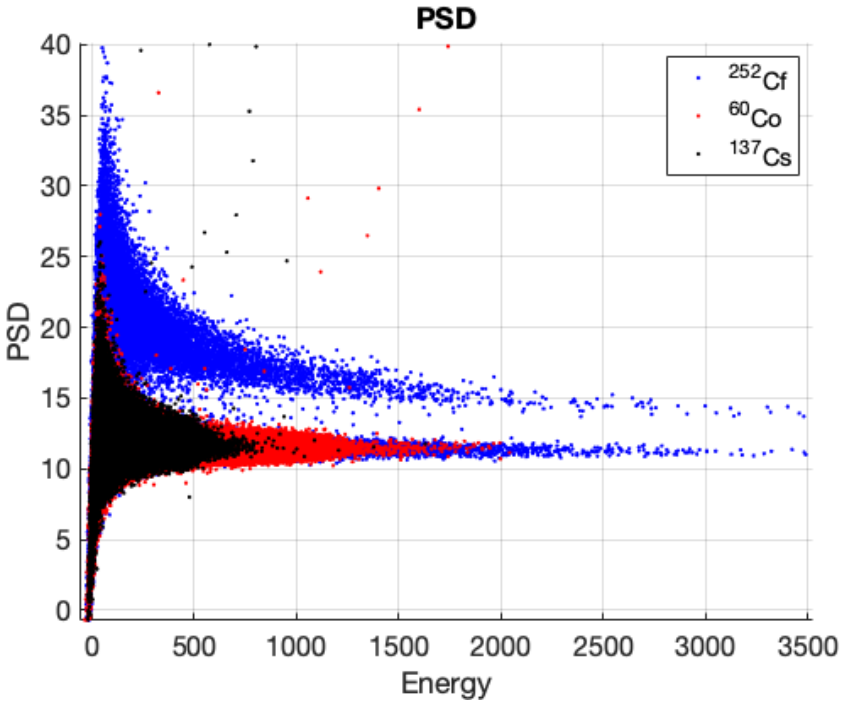

Fig. 6.15: PSD vs Energy Scatter Plot for the dataset at $V_{ov} = +3V$

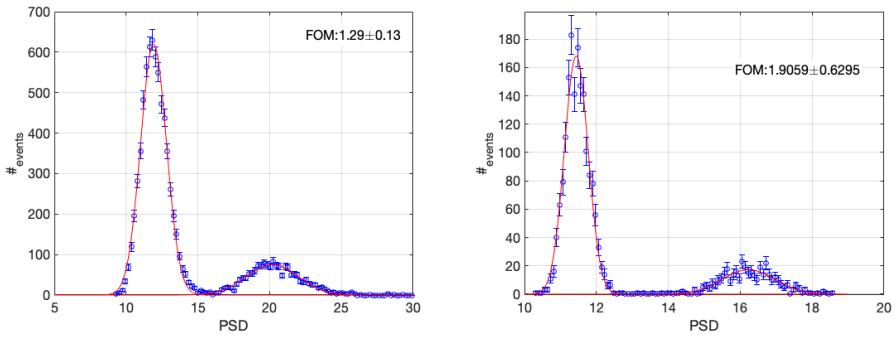

(a) (b)

Fig. 6.16: PSD distribution in the energy bins $[200; 300]keVee$ (a) and $[1; 1.5]MeVee$ (b)

To measure the minimum discrimination energy avoiding the arbitrary choice of the energy threshold, the $F.o.M.(E)$was evaluated in energy bins of 100 keVee from 50 to 950 keV. For signal higher than that the energy interval was doubled every step to compensate for the loss of statistics; moreover the curves are relatively flat in that region. In Figure 6.17 two curves $F.o.M.(E)$are reported for $V_{ov} = +2V$ and $V_{ov} = +5V$. The $F.o.M.(E)$curve was fitted with the Equation 6.10.

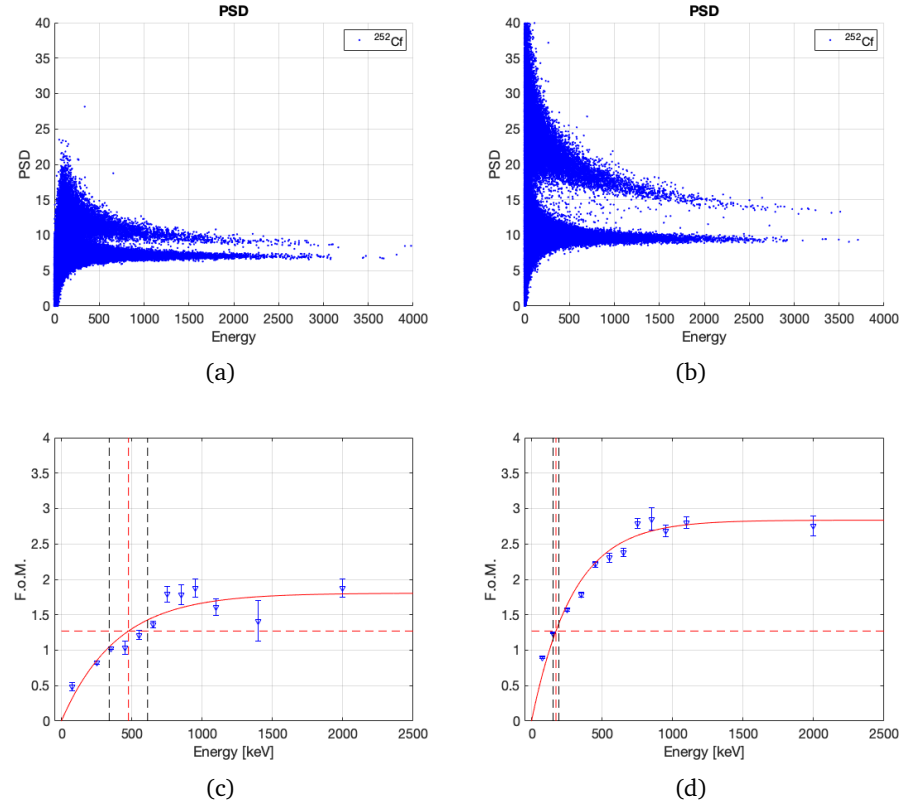

(a) (b)

(c) (d)

Fig. 6.17: Upper row shows the PSD distribution for $V_{ov} = +2V$ (a) and for $V_{ov} = +5.5V$ (b), while the bottom row show the respective $F.o.M.(E)$at $V_{ov} = +2V$ (c), and $V_{ov} = +5.5V$ (d)

$$F.o.M.(E) = \alpha \cdot \left(1 - e^{E/\beta})\right) \tag{6.10}$$

By inverting the Equation 6.10 we obtain the $E(F.o.M.)$ as in Equation 6.11.

$$E(F.o.M.) = -\beta \cdot \left(ln\left(1 - \frac{F.o.M.}{\alpha}\right)\right) \tag{6.11}$$

6.3.2 Number of photons corresponding to the E_{min}

The effect of a different $F.o.M$.with different bias voltages, so far with different PDE, is reflected in the minimum discrimination energy that is not constant with the bias. It is possible to evaluate the number of photons corresponding to $E_{min}V_{ov}$, as reported in Figure 6.18, utilising calibration curve Figure 6.14(b).

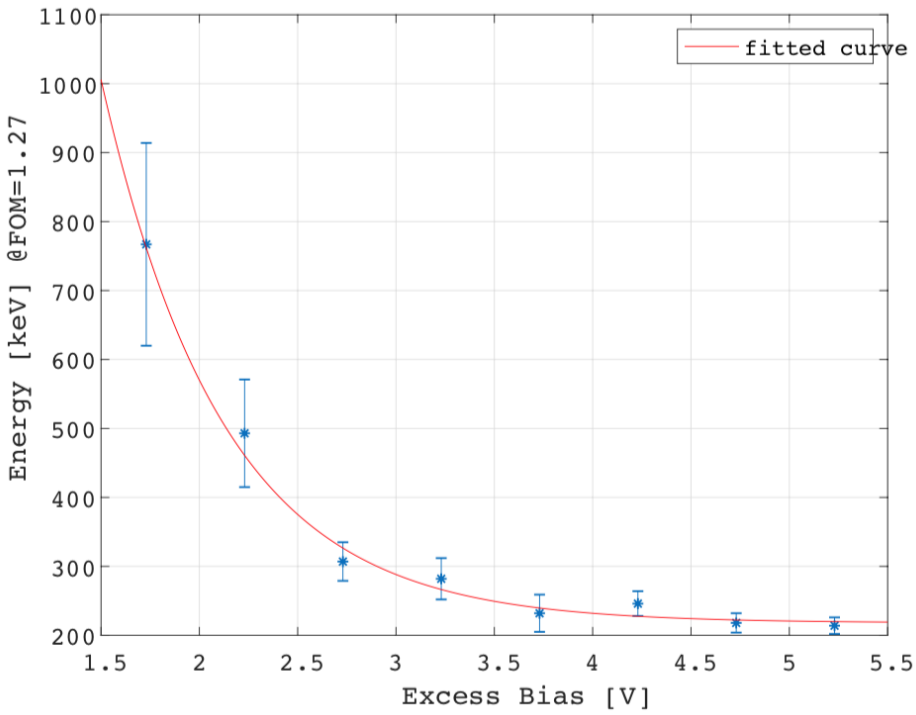

Fig. 6.18: Minimim energy for a $F.o.M.(E) \geq 1.27$ as function of V_{ov}

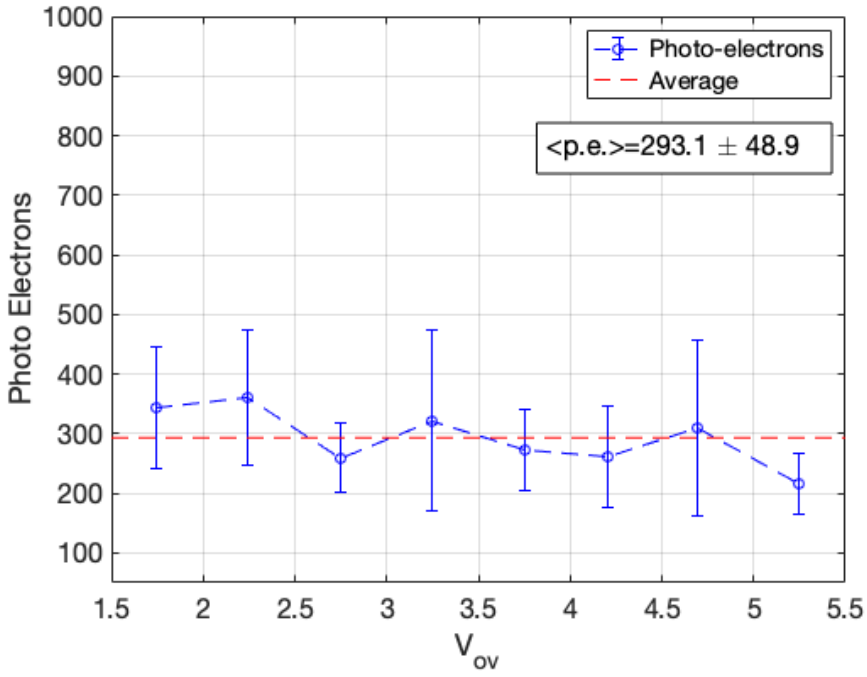

Fig. 6.19: Number of photoelectrons that correspond to the E_{min} for all the datasets (from $V_{ov} = +1.25$ to $V_{ov} = +5.25$)

The number of minimum photo-electrons appears to be constant irrespectively from the V_{ov}, as reported in Figure 6.19, confirming that the light collection efficiency affects the PSD more than the stochastic effects of the SiPM. Moreover, the initial hypothesis for the degradation of the information related to lower collected light was measured to be consistent. This result explains the reason why the $F.o.M.$depends on the deposited energy, and it shows a procedure to define the minimum number of a photon necessary to discriminate among the impinging particles, producing a physical model underneath the lower limit E_{min} in pulse shape discrimination.

7 Digital Signal Processing

In this chapter, the focus is about the performances of a digital-based acquisition method. In the first set of measurements, the signal from EJ-276 scintillator whose light has been collected with an array of SiPM was digitised for offline analysis. Worth noting that the EJ-276 is the latest release by Eljen technologies, replacing the EJ-299-34 material with improved mechanical properties and optical stability Digital processing follows the signal sampling, and the impact of the rate and the number of bits for every sample was investigated. Minimal requirements steered the development of a customised, mobile, hand-held system, an evolution of the I-Spector by Nuclear Instruments. The qualification of the device, designed in cooperation with AWE, is reported in the final sections of the chapter.

7.1 Influence of signal shaping in PSD

Signals generated by a SiPM array (s133360-3050C), made out of 16 channels, 3x3mm^3 each, arranged in a square) biased at 55 V ($\approx 4V_{ov}$) were shaped with different Front End Electronics (Figure 7.1). The signal was recorded using the DT5720 module by CAEN, the same used in the previous chapters.

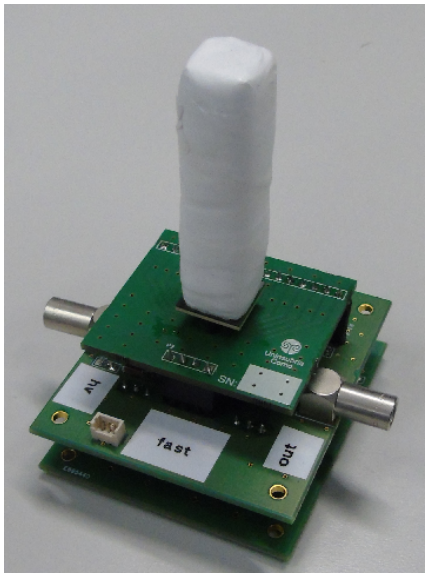

Fig. 7.1: Experimental Set up used to test different FEE. The scintillator is coupled to the SiPM mounted on a first-tier with connectors to adapt the SiPM input/output to a different board. The tear in the middle comprises the FEE and gives the output, while the bottom tier is the one embedding a small HV USB-controlled unit (cXXX by Hamamatsu) to bias the sensor.

The two schematics considered are sketched in Figure 7.2. Option A is quite simple but allows no control on the signal shape which depends on the SiPM parameters (e.g. the quenching resistor and the sensor capacitance). Besides, if more SiPM are connected in parallel, it may be expected that:

1. the output becomes longer due to the increased capacitance, scaling with the number of SiPM;

2. differences among the single sensor electrical parameters may unbalance the different branches;

3. the output is influenced by external load resistors used to read out the signal.

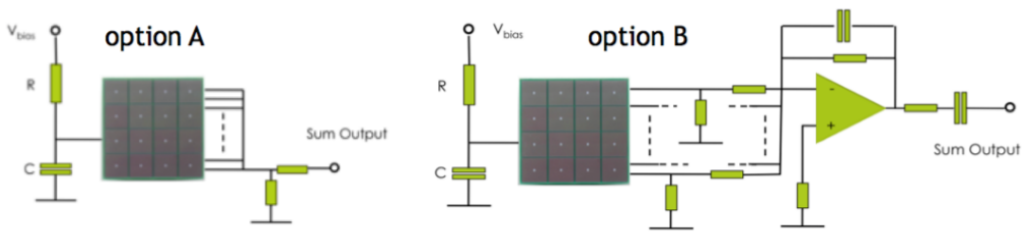

Fig. 7.2: The two Front End schematics implemented to study the impact of the signal shaping on the Pulse Shape Discrimination

For this reason, a different design was also considered, more robust and possibly providing equally good performance, here shown as Option B. This scheme uses a voltage divider connecting the output of each SiPM to the virtual ground of the amplifier to match the dynamic range and stabilise each branch independently. At the same time, the feedback loop acts on the shape of the summed signal. A Cadence simulation implementing a standard electrical circuit for SiPM as reported in Chapter 3 was used to optimise the values of the circuit components. According to the simulation, it was decided to explore two setting options that allow getting a fast and slow response.

The response to a light burst has measured for different set-up and time signal development, defined as the time in which signal goes for 95% to 5% of the peak amplitude, was measured.

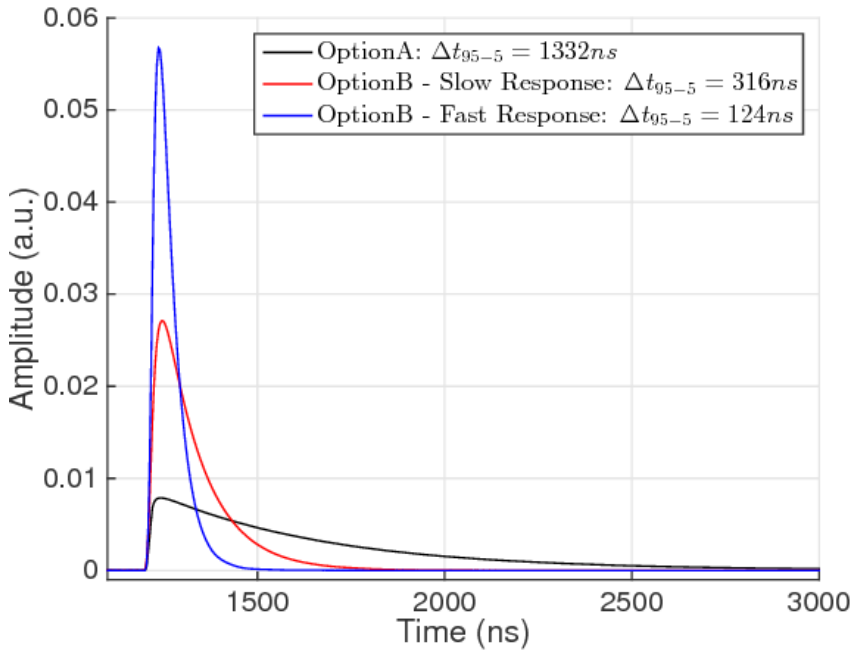

Fig. 7.3: Average of the response of SiPM with different FEE to a sub ns light pulse [109].

As an additional qualifier, the spectra of ^{137}Cs source were collected by a CsI(Tl), 10x10x15mm^3 volume. The spectra collected with Option B, slow configuration, is reported in Figure 7.4. After the energy calibration, the noise of the tree front end was evaluated as the variance of empty signals converted in keV, and it is reported in Table 7.1 along with the conversion parameter ADC/keV.

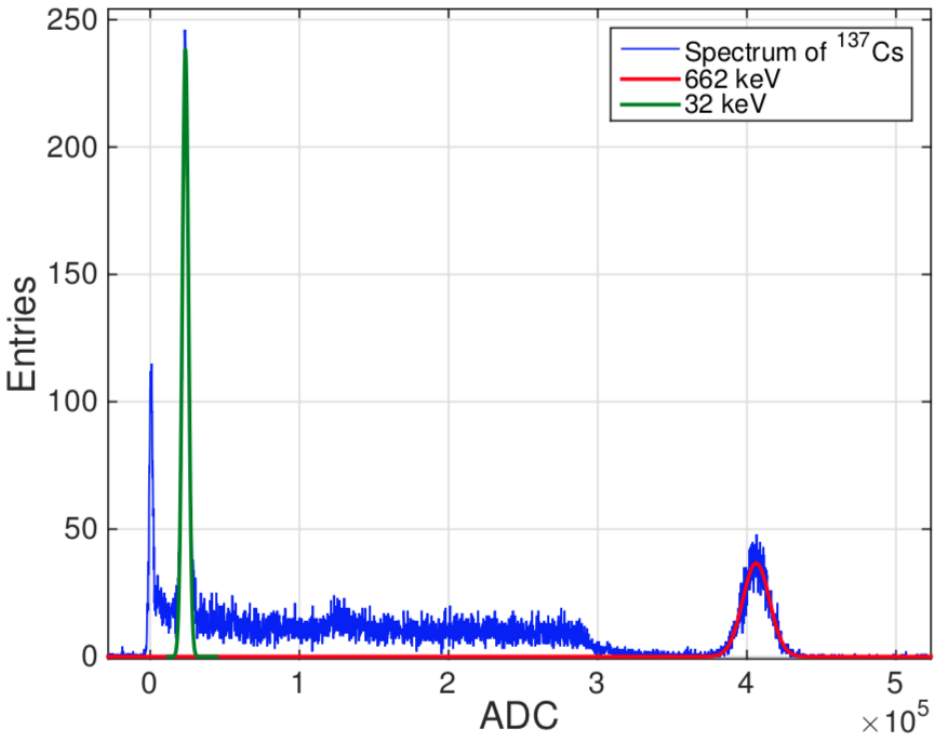

Fig. 7.4: Spectrum of a ^{137}Cs γ source collected with a CsI(Tl) crystal 10 x 10 x 15 mm^3 interfaced to the array of SiPM and readout by the FEE board OptionB in slow configuration

	Option A	Slow	Fast
ADC/keV	336 ± 12	588 ± 15	165 ± 7
σ (keV)	1.42 ± 0.05	1.53 ± 0.05	4.9 ± 0.2
$\Delta E/E$ %	5.11 ± 0.03	5.01 ± 0.03	5.72 ± 0.04

Tab. 7.1: Energy calibration measured with the CsI(Tl) 10x10x15 mm^3, system noise and energy resolution at 662 keV.

A PSD vs energy plot is reported in Figure 7.5 for the Option B with the slower shaping time, while the $F.o.M.$in 1-1.5 MeV energy range are reported in Table 7.2.

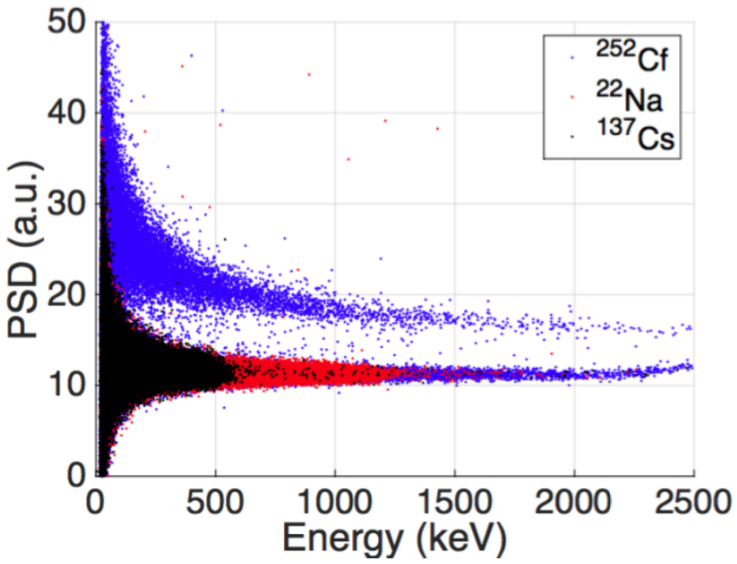

Fig. 7.5: PSD vs Energy measured with an EJ-299/34 coupled with a SiPM read out by a FEE in Configuration B/Slow [109]

It was observed that the signal shaping has a non-negligible impact on the Pulse Shape discrimination as outlined from the comparison of the $F.o.M.(E)(E \in [1; 1.5]MeVee)$ shown Table 7.2.

Configuration	A	B/Slow	B/Fast
$F.o.M.$	2.47 ± 0.1	2.61 ± 0.1	2.28 ± 0.1

Tab. 7.2: $F.o.M.(E)$with E in $1 - 1.5MeV$ for the tree tested FEE configuration [109].

7.2 Digitiser performances influence on PSD

To show the impact of the digitiser performances on the deliverable device, the Option A schematic is used hereafter as front end electronics since, as demonstrated by the end of the chapter, it provides the best results; the signal from the 16 channel array coupled to the EJ-276 scintillator was digitised by a DT5730 CAEN module, a 500Msps, 14Bit resolution 2V input range digitiser.

The detailed response to a light burst is reported in Figure 7.6 after the sensor was biased at 55.5V and illuminated by a blue light generated by the PicoQuant-PDL800 LED driver, conveyed on the sensor with an optical fibre.

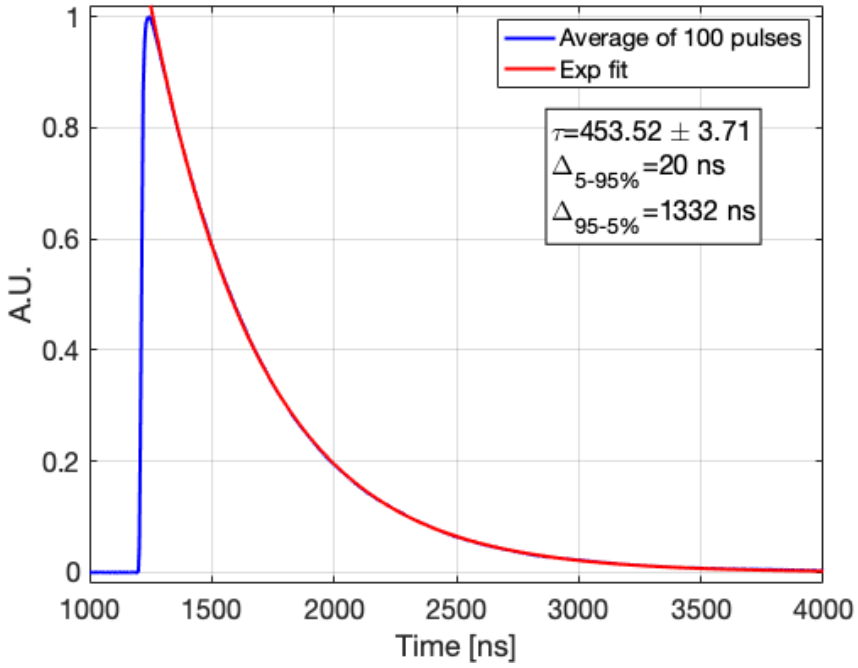

Fig. 7.6: SiPM array response to a light stimulus.

Concerning the measurements with the single sensor presented in the previous chapter, the longer decay time, given by the higher capacitance of the whole sensor, is expected to spoil the signal degrading the PSD. In contrast, the larger area sensor collects more light, and this is expected to increase the $F.o.M.$. It is not trivial to determine which effect matter the most, and if the $F.o.M.$is retained as a figure of full system capability, it is clear that collecting more light has a more significant impact.

7.2.1 Pulse Shape Discrimination

The EJ-276 was coupled to the array, and it was exposed to γ sources to provide the energy calibration. A ^{252}Cf source, as shown in Figure 7.7, was used as a mixed γ-neutron source. The sensor was based at $55.5V$, and the signal was digitised collecting more than 10^5 events per each source.

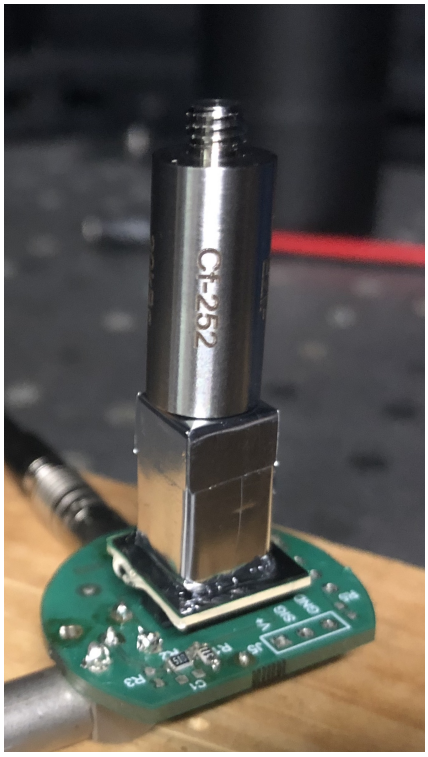

Fig. 7.7: EJ 276 scintillators is coupled to the SiPM array and exposed to a ^{252}Cf source

The Spectra of ^{137}Cs is reported in Figure 7.8, along with the calibration curve whose parameters are reported in Table 7.3.

$ADC = kev \cdot m + q$	
m	185.5 ± 0.41
q	4706.8 ± 45.94

Tab. 7.3: Fit parameters of the calibration curve in Figure 7.8

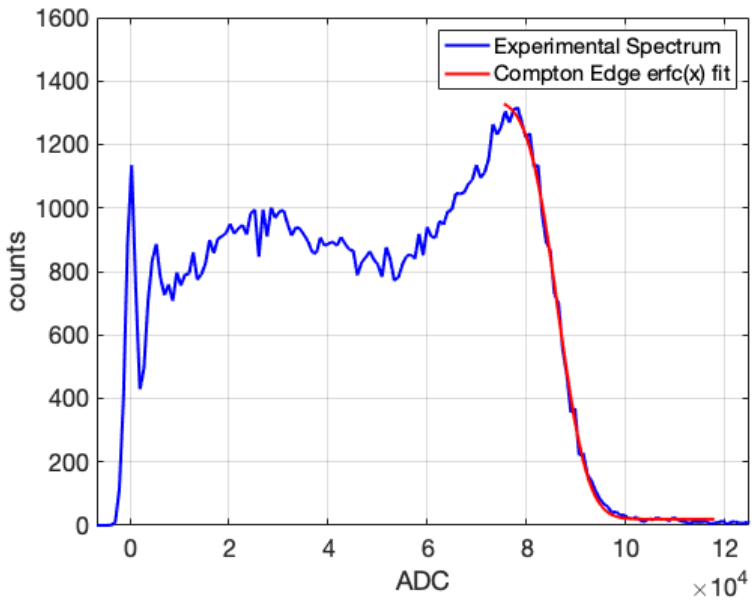

(a)

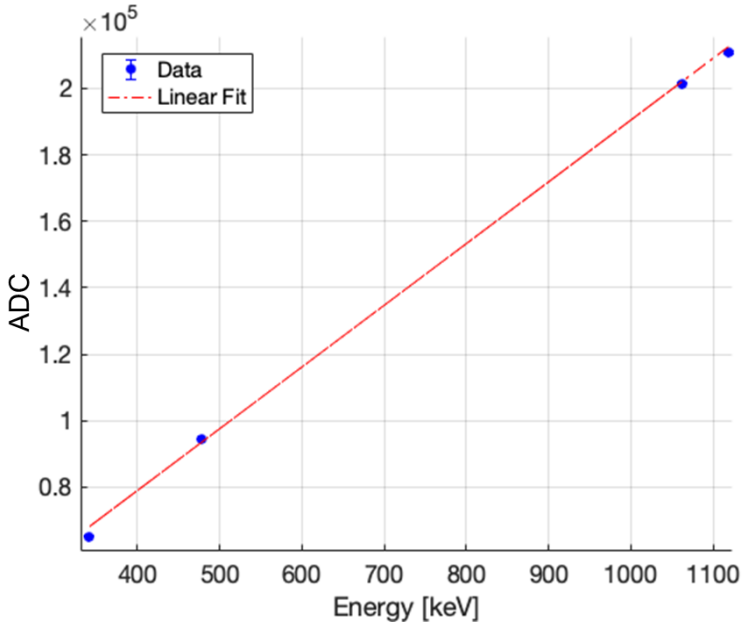

(b)

Fig. 7.8: Experimental spectrum of ^{137}Cs source collected with the EJ-276 scintillators (a) and the calibration curve for the same set-up.

Following the optimisation procedure applied in the Section 4.2.2, whose output is shown in Figure 7.9, the optimal parameters for the integration windows are $t_{delay} = 600ns$ and $t_{int} = 3\mu s$. These integration gates reflect the longer signal shaping, showing that there is a predominance of the SiPM response concerning the scintillator natural decay time.

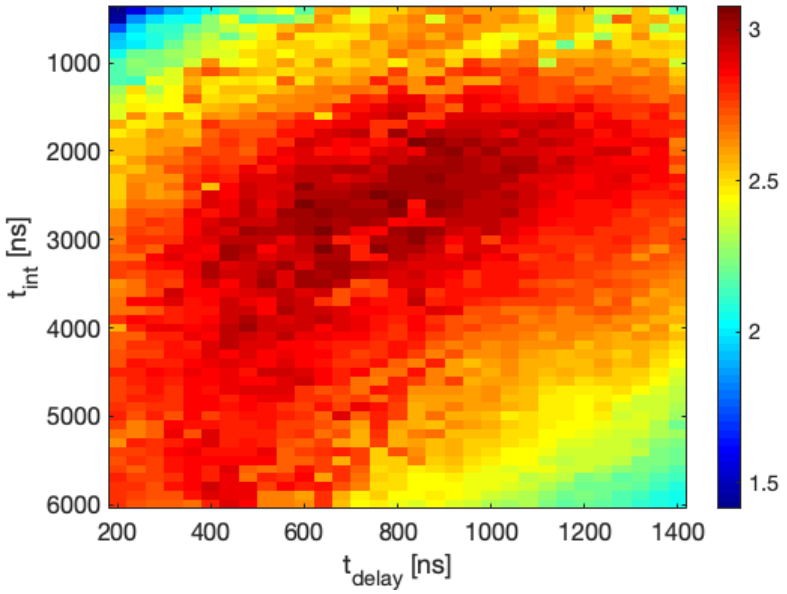

Fig. 7.9: Heat Map of the $F.o.M.$as function of different gate integration boundaries

The PSD vs Energy in this condition is reported in Figure 7.10(a), and from that distribution it is possible measure a $F.o.M.(E = \infty)$ equal to 3.47 ± 0.41 as reported in Figure 7.10(b) and an $E_{min} = 186.5 \pm 25.3 keVe$.

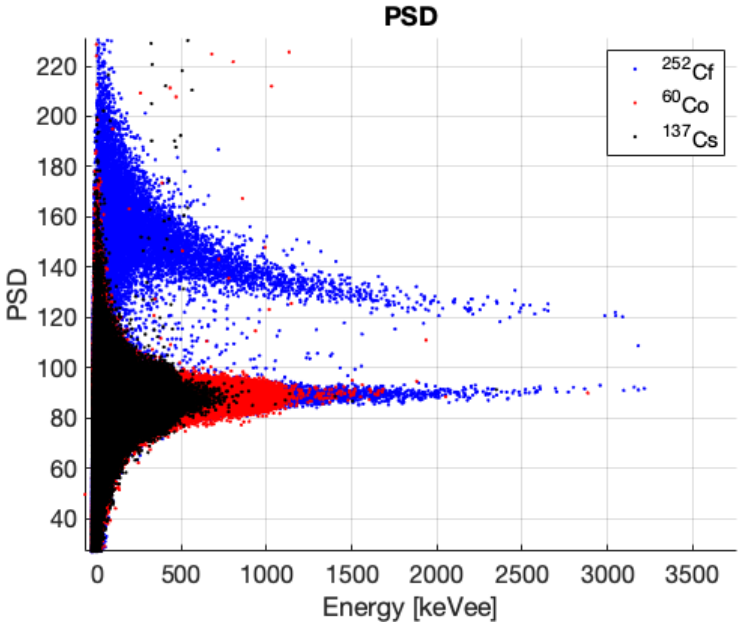

(a)

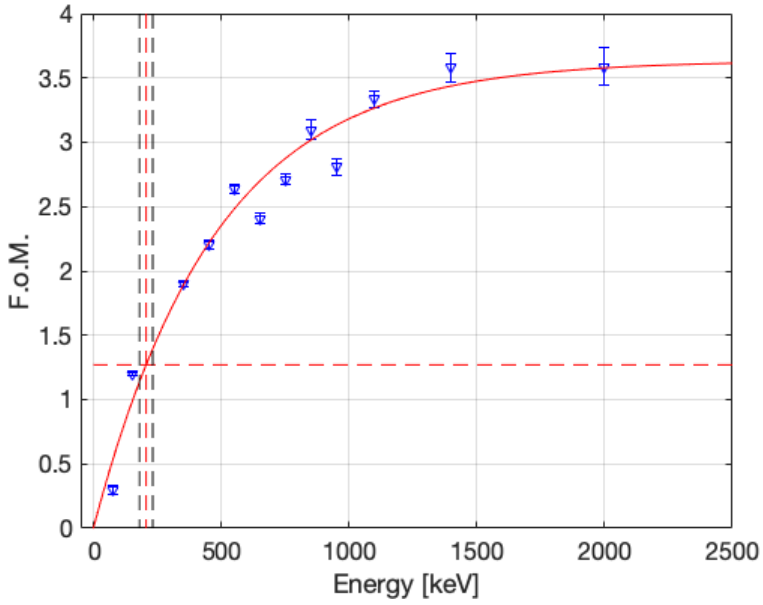

(b)

Fig. 7.10: The PSD parameter distribution as function of Energy (a) and the $F.o.M.(E)$(b)

7.2.2 Sampling Frequency effect

The impact of sampling rate was assessed sub-sampling offline the original waveform (500msps) to 250 and 100 Msps. The optimisation procedure identified the same time limits for the tail integration gate, $t_{delay} = 600ns$ and $t_{int} = 3\mu s$ irrespectively from the sampling rate.

The three datasets give excellent and similar results as all of the measured $F.o.M.(E)$at $E = \infty$ are statistically compatible.

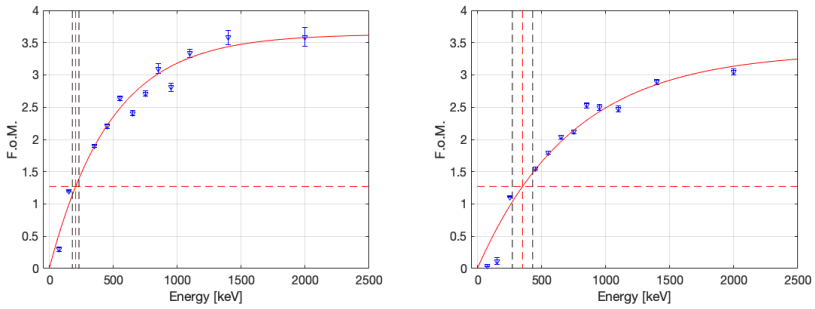

(a) (b)

Fig. 7.11: $F.o.M.(E)$for the 500 (a) and 50 (b) Msps set-up. The sampling rate does affect the $F.o.M.$and the E_{min} when the sampling rate is reduced by a factor 10.

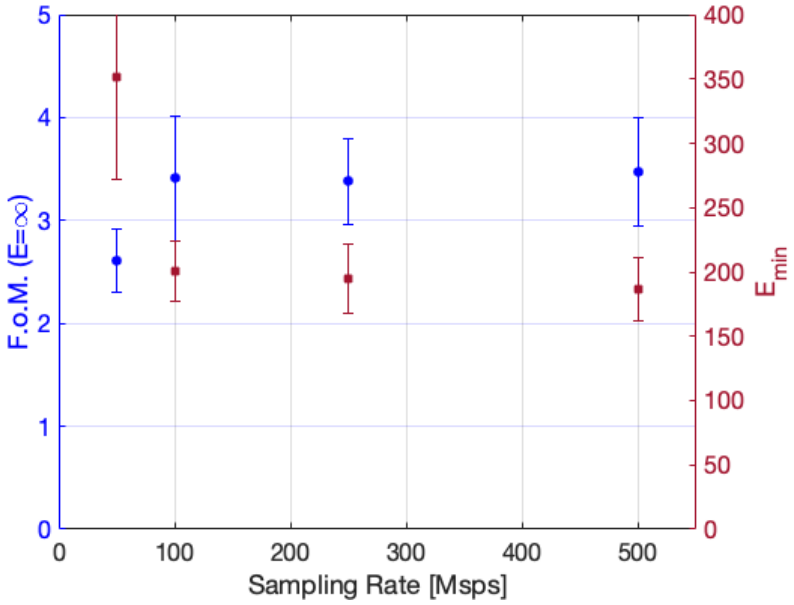

Fig. 7.12: Comparison between the $F.o.M.(E = \infty)$ and the E_{min} for different sampling rate

7.2.3 Bit Resolution Effect

The impact of the bit resolution was measured applying a bit-shift of 2 or 4 bits to the original dataset sampled at 500 Msps and 14-bit resolution.

In this case, the $F.o.M.(E)$and E_{min} from dataset at 14 and 12 bits resolution are compatible, while the degradation of the information when the dataset is reduced

to a resolution of 10 bits is non-negligible. Indeed in this case the $E_{min} = 482.88 \pm 68.24 keVee$ ad the $F.o.M.(E)$for $E = \infty$ is 2.09 ± 0.16.

The dataset was de-sampled at 100Msps and ten-bit resolution. It was found that, irrespectively from the sampling rate, the $F.o.M.(E)$at $E > 1MeVee$ is lower than 2.1 as reported in Figure 7.13.

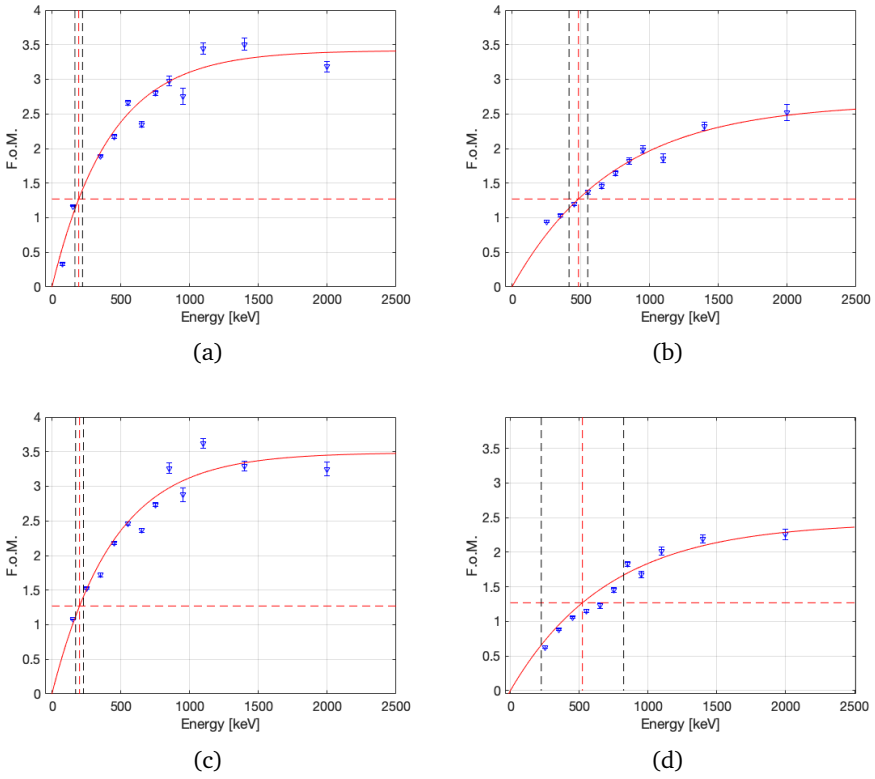

Fig. 7.13: The four panels shows the different $F.o.M.(E)$for different sampling-resolution combination: (a) 500Msps / 12 bit (b) 500 Msps / 10 bit (c) 100Msps/14 Bit (d) 100 Msps / 10 bits.

Figure 7.14 reports the values of the $F.o.M.(E)$for $E = \infty$, and the E_{min} for the different bit resolution. In the plot the qualifiers values obtained at 10 bits and 500 Msps is reported, to be comparable with the 12 and 14 bits datasets.

From those set of measurements, the bit resolution as an impact on the Pulse Shape Discrimination. In fact, since the noise RMS^2 is about $5mV$, and the least significant bit introduce an error of 0.12 or 0.48 mV, for the 14 and 12 bits respectively, when the bit resolution is 10 bits least significant bit corresponds to $1.9mV$.

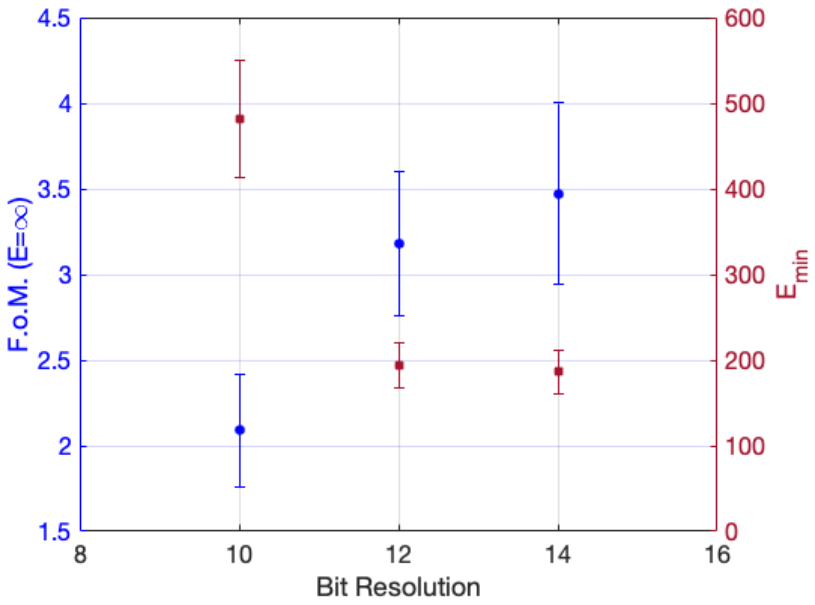

Fig. 7.14: Results of $F.o.M.(E)$and E_{min} in the bit scan

7.3 A system prototype based on a fully digital approach

The requirements for a custom re-design of a pre-existing device (I-Spector, commercialised by CAEN spa and designed by Nuclear Instruments SRL [110]) were set after the results obtained in the previous section. The customisation consists in the replacement of an MCA used for the γ spectroscopy with a digitiser. The on-line Pulse Shape Discrimination was implemented in FPGA with the Peak-Tail algorithm (Equation 2.8). This instrument is going to be a light-weight detector for neutron/γ discrimination in real-time for diffuse monitor applications. There are nonetheless fundamental differences in the instrument concerning the laboratory system presented in the first half of this chapter.

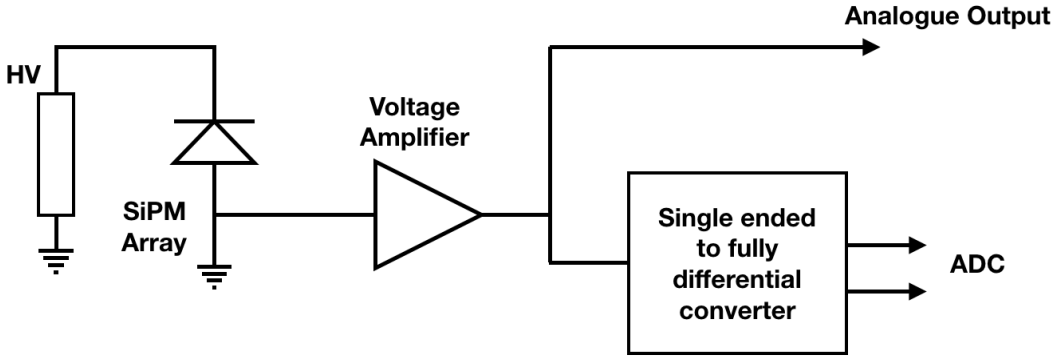

Fig. 7.15: Electrical scheme of the I-Spector Front End

First of all, the I-Spector embeds 4 SiPM 6x6mm^2 each arranged in a two by two square matrix, that belongs to the s14161-6050HS series, whose main features are reported in Table 7.4. The scheme of front end electronics is reported in Figure 7.15. The analogue output allows us to read the signal and to process it offline for further qualification. The digitiser has 12 bits resolution over 2V input range with a sampling rate of 250Msps. As shown in previous section 12 bits were required to collect enough information to perform PSD, while in principle 100Msps would have been sufficient. The choice to have 250Msps was driven by practical consideration on the design; in fact, the chosen ADC family used has the same pinout for the 250 or the 100 Msps, and the power dissipation of the device would have been, in both cases, below $\approx 3.5W$.

s14161-6050HS		
Number of SiPM	4	
Single SiPM Size	6 x x	mm^2
Pixel Pitch	50 μm	
V_{bd}	39.5	V
V_{op}	$V_{bd} + 2V$	V
Gain	$2.5 \cdot 10^6$	
DCR	2.5	μA
Cross-Talk	7	%
PDE_{max}	50	%
Fill Factor	74	%

Tab. 7.4: Main characteristics of the sensors mounted on the I-Spector

In the deliverable for AWE, the chosen scintillator was a sample of EJ-276 with 10x10x50mm^3 volume wrapped with Teflon, as shown in Figure 7.16.

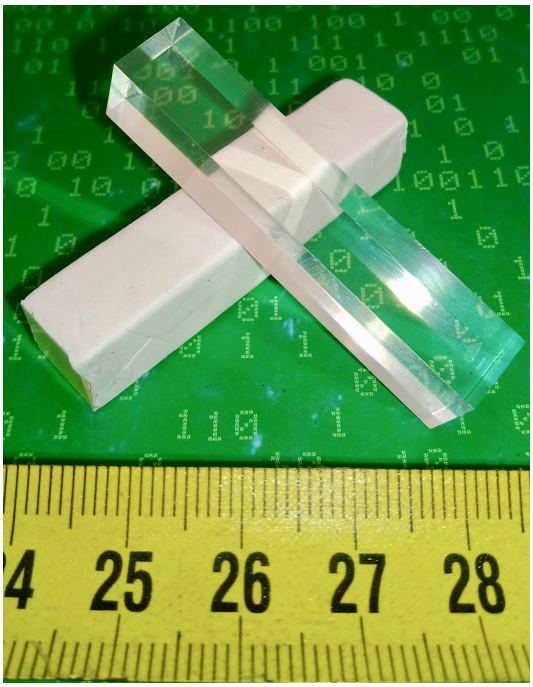

Fig. 7.16: The EJ-276 sample with dimension 10x10x50mm^3.

The I-Spector embeds a micro-controller:

- processes data from the FPGA;
- hosts the web-server for the communication with the instrument;
- manages the ethernet communication and the HV module.

Moreover, it embeds a LORA antenna for remote long-range data transmission. The Instrument in Figure 7.17 is 11cm long with a diameter of 5cm, and it weighs 300g. An FPGA apply the Pulse Shape Discrimination to digitised waveforms. Via software alarms can be set when different levels of radiation are measured, and the alert can be sent via embedded antenna for LORA protocol-based communications or the entire spectra. Alarm history can be stored into a cloud via ethernet connection.

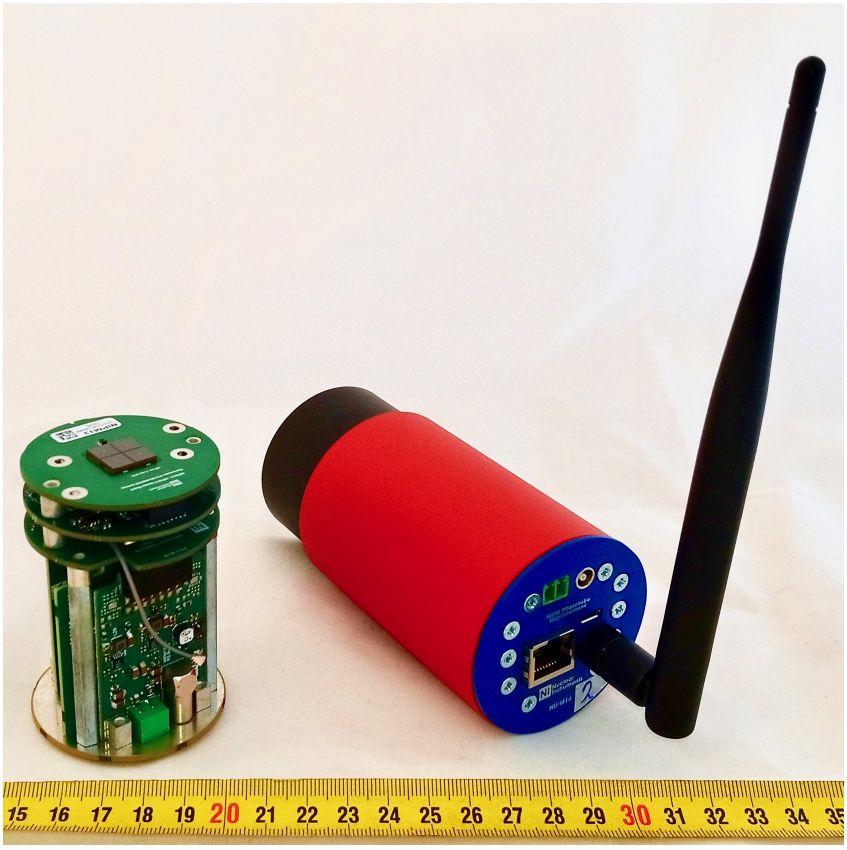

Fig. 7.17: The customised I-Spector device.

It is then necessary to qualify this system against the reference results obtained in Section 7.2.1 to evaluate the impact of the different front end on the PSD. In the first place, instrument response to a light signal, collected by illuminating the sensor with a PicoQuant PDL-800, was measured and the results reported in the dedicated following sub-section. The performances of the bigger scintillator coupled to the I-Spector were measured by externally digitising the signal with the CAEN DT5730. The experimental set-up realisation is shown in Figure 7.18 where the I-Spector were placed in a light-tight box, and it was possible to illuminate it with a light burst to measure the time development of the signal, and then to be coupled with the EJ-276 scintillator for the γ/neutron discrimination measurements.

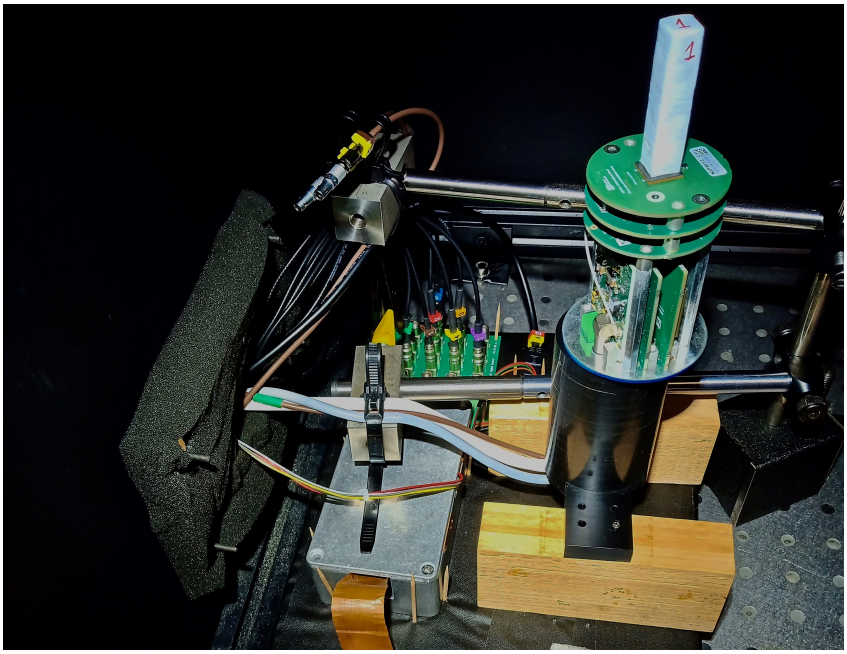

Fig. 7.18: The I-Spector mounted in a light-tight box for the measurements with light and with the EJ-276.

7.3.1 I-Spector Off-line Qualification

7.3.2 response to a light signal

Light from PicoQuant PDL-800 is conveyed to the SiPM, biased at $41.4V, V_{ov} = +2V$, surface with an optical fibre. The fibre is half a centimetre away from the centre of the surface to equally illuminates the 4 SiPMs. In Figure 7.19 the response to the light burst is shown, where the temporal development is shorter than the one from the electronic used in the previous section. The capacitance of those SiPM is higher than the S13 series, so far a shaping circuit is required to shorten the signals (Table 7.5) This is the reason why both the τ and the $\Delta_{95-5\%}$ are shorter than the ones presented in Section 7.2.1 even if the total capacitance of the s13361-3050CS is lower with respect to the s14161-6050HS one (Figure 7.19).

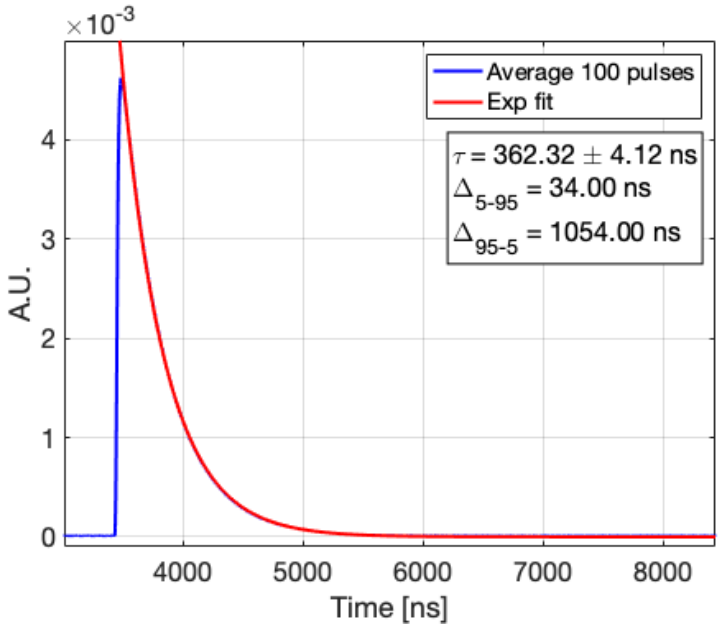

Fig. 7.19: I-Spector response to light burst

	s13360	**I-Spector**
τ	453.52 ± 3.71ns	1332 ns
Δ_{95-5}	$4.12362.32\pm$ ns	1054 ns

Tab. 7.5: Comparison of the time development of the signal for the two arrays

7.3.3 Pulse Shape Discrimination

The energy calibration has been performed integrating offline the signals for $2\mu s$, and the calibration curve is reported in Figure 7.20.

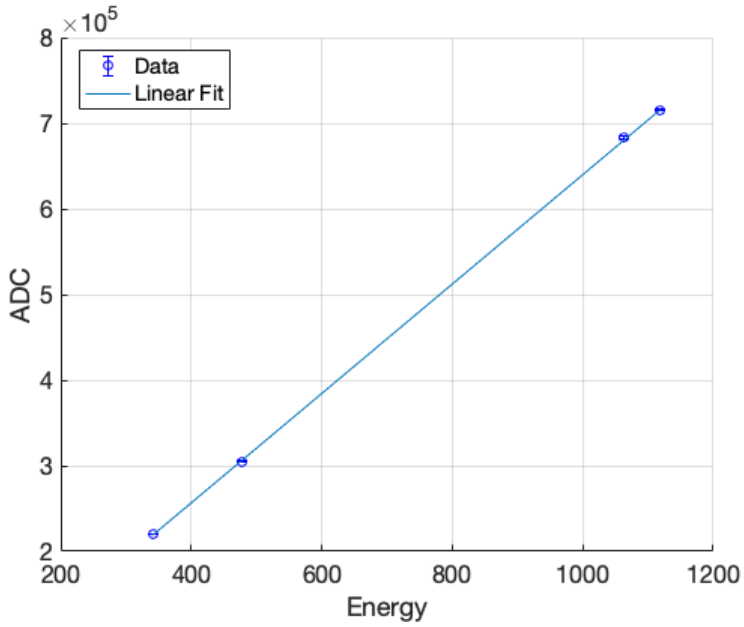

Fig. 7.20: The calibration curve obtained with a ^{137}Cs,^{22}Na and a ^{60}Co sources

Then the system was exposed to the ^{252}Cf and optimisation procedure was applied; the output is shown in Figure 7.21.

In order to compare the I-Spector front end electronics performance, analogue output was digitised with the DT5730, and the optimisation procedure defined the integration time boundaries that would then have been set on the I-Spector for the on-line analysis.

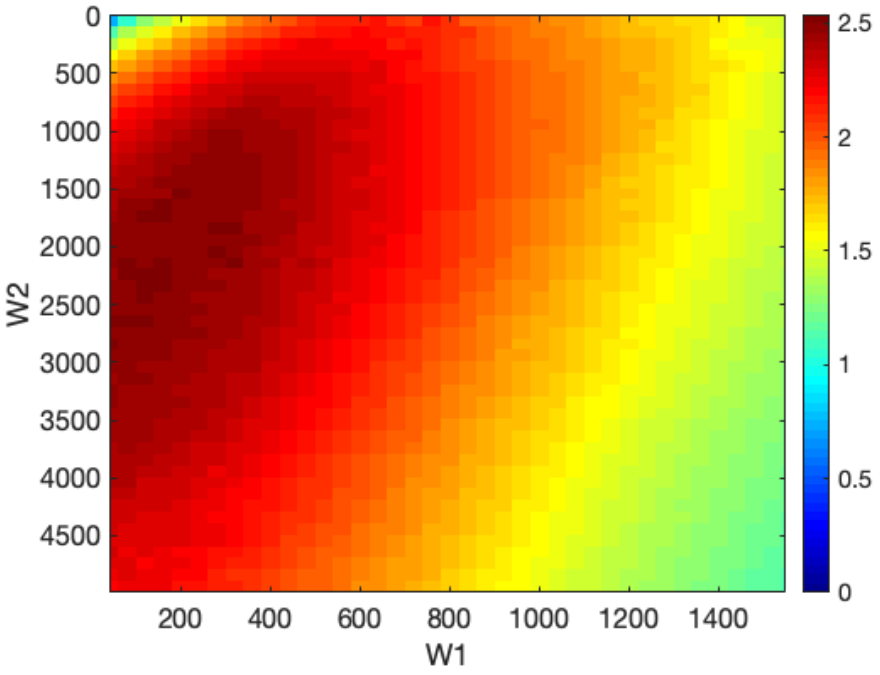

Fig. 7.21: Heat-Map as result of the optimisation procedure on the analogue output of the I-Spector.

The PSD vs Energy plot, where the PSD_{PT} was obtained with the integration boundaries found by the optimisation procedure, $t_{delay} = 300ns$ and $t_{int} = 1.5\mu s$,is reported in Figure 7.22 and the $F.o.M.(E)$shown in Figure 7.23.

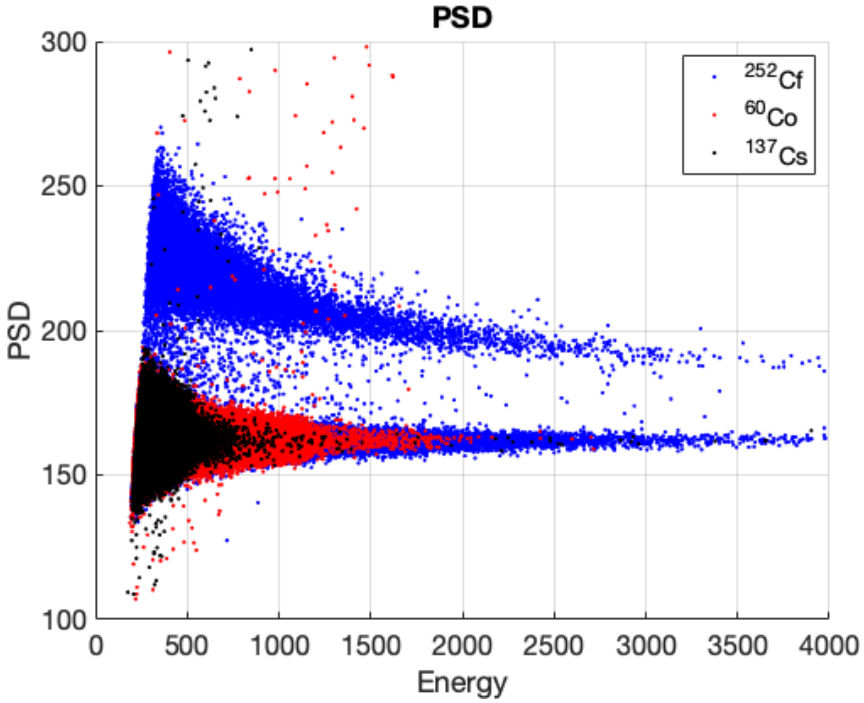

Fig. 7.22: PSD vs Energy scatter plot

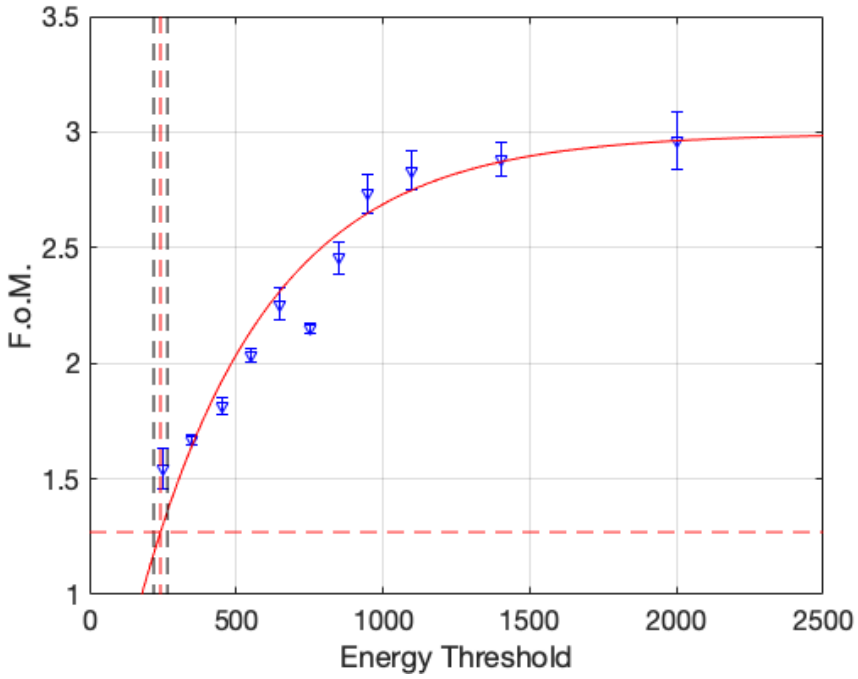

Fig. 7.23: $F.o.M.(E)$shows both a lower $E(F.o.M. = 1.27)$ and $E(F.o.M. = \infty)$

7.3.4 I-Spector On-line analysis qualification

The I-Spector host a web server that can be reached via ethernet connection, and from a web-page based software it is possible to access to the system configuration and settings and to perform the γ/neutron measurements. The configuration tab allows setting HV and the parameters for the temperature compensation (Figure 7.24(a)). A Log page shows the time series of HV, temperature and current of the sensor. The MCA tab shows the spectra and allows to perform the energy calibration fitting either the peak value with a gaussian function, and the Compton Edges with a complementary erf (Figure 7.24(b)). PSD tab shows both the PSD vs Energy plot as a 2D histogram allowing to evaluate the $F.o.M.$within user-defined energy boundaries (Figure 7.25(a)). The software saves the spectra, the PSD vs Energy 2D histogram for offline analysis and it also allows to dump on file the digitised waveforms for further offline analysis and data validation. Moreover, from the same software interface, it is possible to set Regions Of Interest (ROI) for the alarms, either related γ or neutron pulses(Figure 7.25(b)).

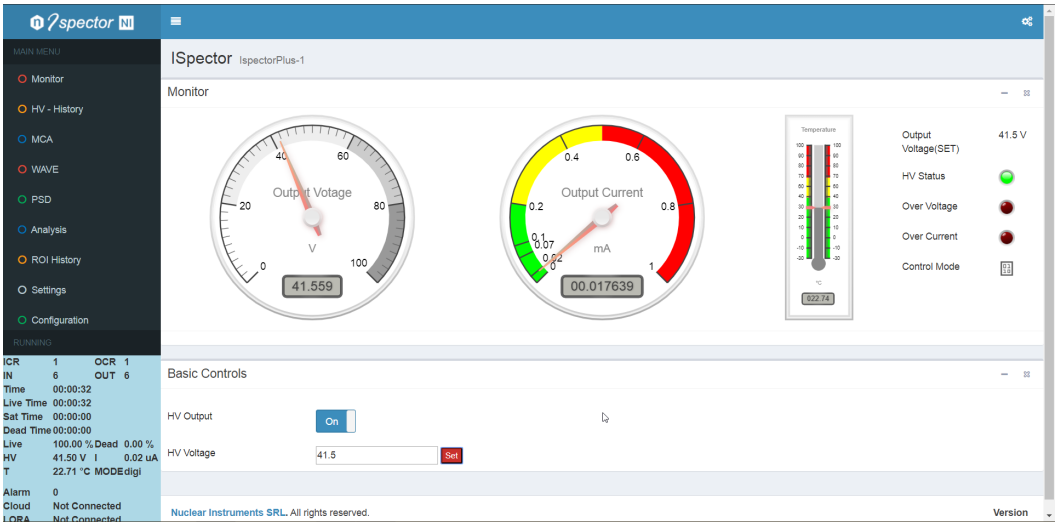

(a) I-Spector Monitor tab

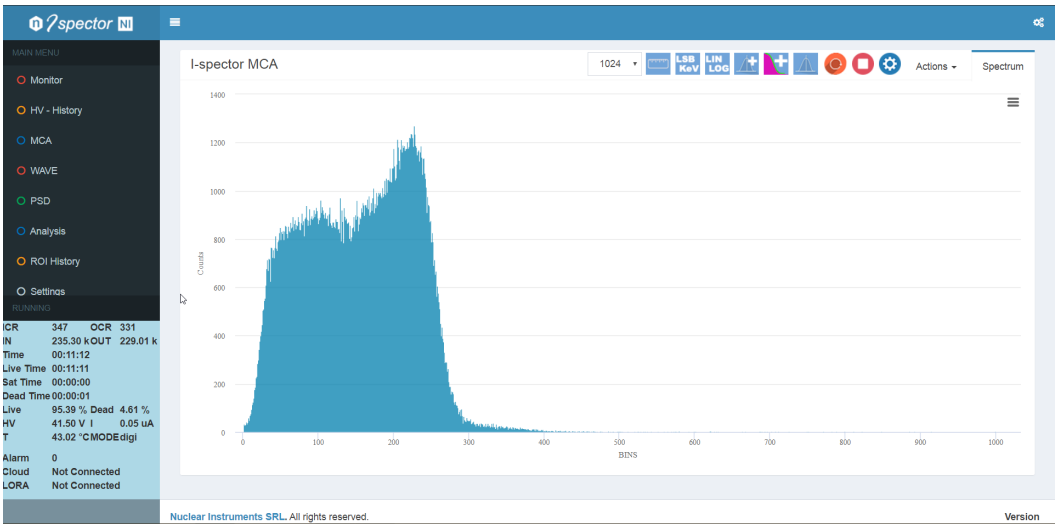

(b) MCA tab from where it is possible to calibrate the system

Fig. 7.24: Some screenshot of the I-Spector custom software for the on-line PSD analysis.

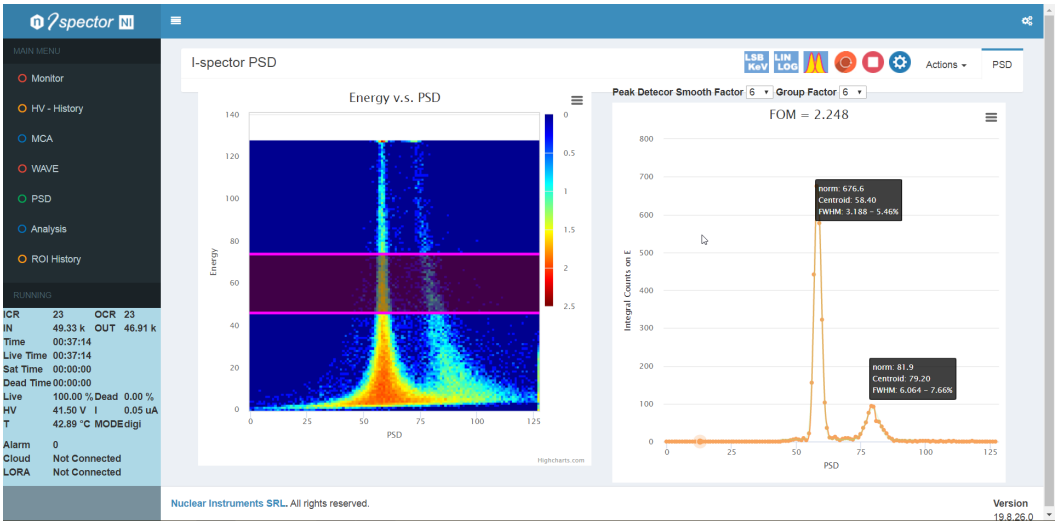

(a) PSD and $F.o.M.$tab

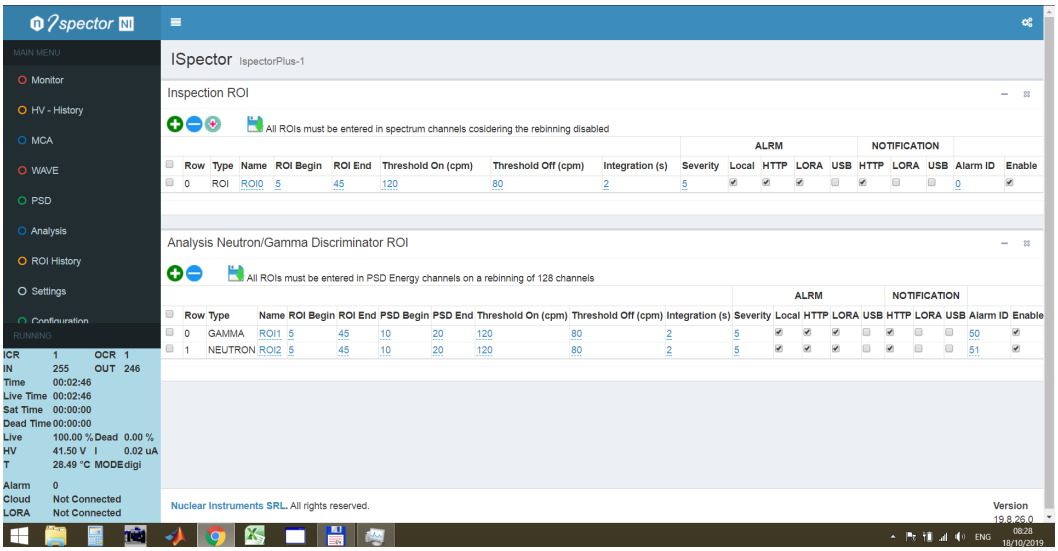

(b) ROI and alarm setting tab

Fig. 7.25: Some screenshot of the I-Spector custom software for the on-line PSD analysis.

7.3.5 On-Line PSD Software

The On-line calibration curve was verified by analysing offline the spectra and values within the error was found for the two curve parameters, as reported in Table 7.6

$ADC = kev \cdot m + q$	
m	0.37 ± 0.02
q	23.13 ± 7.24

Tab. 7.6: Calibratio of the I-Spector with EJ-276 scintillator.

An analysis of the collected data was performed offline to validate the results of the on-line procedure, a. It results worst concerning the one obtained by digitising the analogue output since the $E_{min} = 445.98 \pm 86.69$ and the $F.o.M.(E \in [1.5; 2]MeV) = 2.6$. The reason for the worst performances is related to the bin resolution in the FPGA when the PSD values are binned in the 2D histogram. Due to the limited memory, the binning produces PSD distribution to be mapped in no more than 5/6 bins, affecting the quality of the gaussian fit and resulting in higher errors. So far, the $F.o.M.(E)$plot is not entirely reliable, even if it gives a good indication and allows for sufficient discrimination in the reference energy window.

The I-Spector showed very satisfactory performances, allowing to achieve a rejection rate at the level 10^{-6} due to statistical fluctuation since the FOM is measured as 2.2 in $E \in [1; 1.5]MeV$. Moreover, it embeds advanced functionalities, from the on-line $F.o.M.$evaluation to the on-line calibration, the possibility to set alarms according to the measured rate in a given energy or PSD range, and to send alarms via LORA protocol. To conclude, a cloud service allows to remotely collect data from the I-Spector, even in a multi-device installation when they are configured in geo-tagged smart grids.

8 Analogue Signal Processing

Pulse Shape Discrimination performed with fully analogue systems is the last step in this works. The measurements rely on an ASIC designed by Kromek Group p.l.c and called APOLLO. Indeed, the ASIC is a multi-purpose platform, highly configurable, that is suitable for both low light measurement with SiPM, γ spectroscopy and Pulse Shape discrimination. For each of its 16 channels, it is possible to either integrate the signal (within a user-defined integration gate) or measure the peak amplitude.- The ASIC was just delivered from the production, so far the first half of the chapter presents a description of the instruments and the electronic characterisation. A set of measurements were performed to define its operational parameter. γ spectroscopy measurements were also performed to complete the qualification. Two crystals were used for the study on Pulse Shape Discrimination: the organic scintillator EJ-276 readout with the Front End presented in the previous chapters and the CLLB-C crystal in a configuration delivered by Kromek with dedicated SiPM and electronics.

8.1 The Apollo ASIC

The Apollo ASIC has 16 analogue input channels and a single digital output on an SPI port. For each channel, the analogue block (Figure 8.1) comprises a pre-amplifier, a shaping amplifier, a leading-edge threshold comparator, an analogue integrator and a peak detector. Analogue integrator and peak detector amplitude are digitised inside the ASIC over 12 bits sent over an SPI protocol to an external micro-controller. Operational parameters of the channels, e.g. the threshold level, the gain, the peaking time of the shaping amplifier, the integration time window and the peak detector track and hold window, are software-defined by the user. The main functionalities that the Apollo ASIC embeds are:

- **pre-amplifier:** voltage amplifier with a variable gain that can be set to 3,6,9,12,24 and 32x;

- **Semi-Gaussian Shaper:** this shaping circuit is a standard CR-RC shaper with a single τ that can be set ranging from 0.5 to 15 μs, resulting in a peaking time that ranges from 1 to 32 μs. It should be bypassed (with a proper ASIC configuration) to preserve the native signal shape for PSD application;

- **Threshold comparator:** a leading-edge discriminator logic that produces both the trigger for the readout and a timestamp for each triggered event with 8ns granularity;

- **Analogue integrator:** integration gate ranges from 100ns to 10μs with a step of 8 ns. It also has an internal amplification that adapts the input signal to the internal circuits to explore all the available output dynamic range at different integration gates.

- **Peak detector:** peak and hold circuits that can hold the peak up to 32 μs to cope with the longest peaking time of the Semi-Gaussian Shaper.

- **Digital and Communication block:** a 12-bit digitiser is embedded in the ASIC and read either the Analogue Integrator or the Peak Detector. An SPI port may transfer the digitised information and time stamp to the processing unit that, could be either an external device or a microprocessor embedded in an instrument for the analysis.

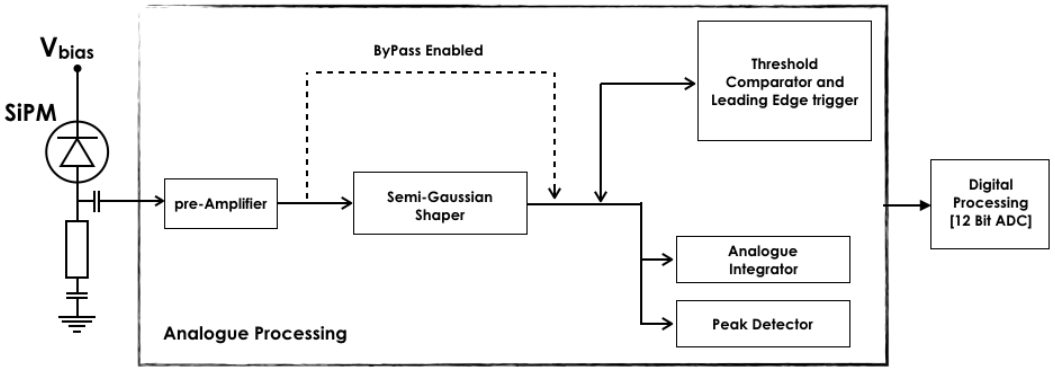

Fig. 8.1: APOLLO ASIC logic blocks

The 16 channel are grouped in groups of 4 that can share a common trigger. The trigger can be shared from one of the four channels to the other three by a leading-edge discriminator. Different channels and trigger scheme have been used to fit the measurements need, namely:

- Measurements with a light pulse: Channel 0 was used as a trigger, and the SiPM signal was recorded on Channel 1.

- γ Spectroscopy and PSD: Channel 0 was configured to trigger on the leading edge of the signal. Channels 1 and 2 were used as the analogue integrator/peak detector since the PSD_{PT} algorithm das been chosen.

8.1.1 Functionality characterisation

The range of the threshold comparator, the analogue integrator and the peak detector was measured, then the transfer function of the pre-amplifier and the Semi-Gaussian Shaper have been evaluated since, as it has been shown in Chapter 4 shaping has a non-negligible influence on PSD.

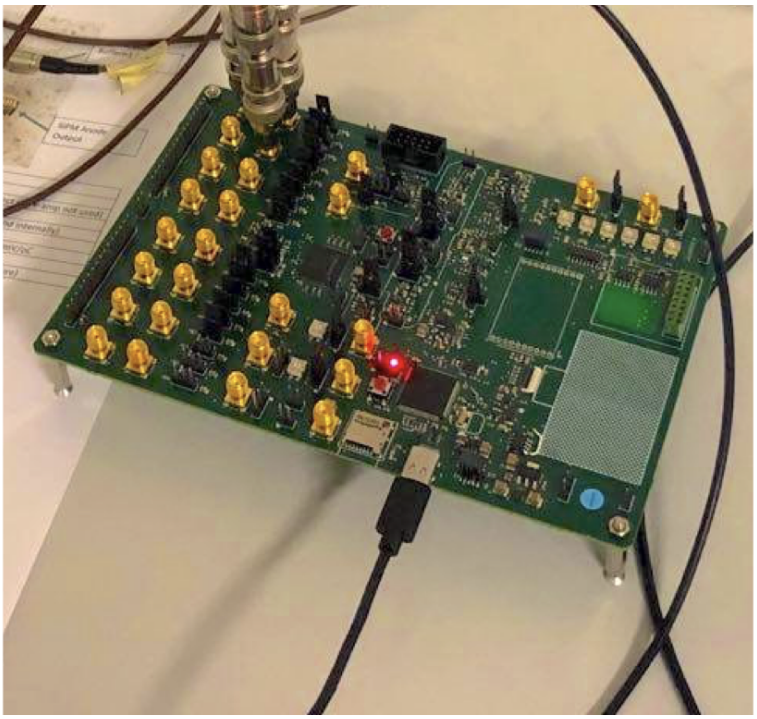

Fig. 8.2: APOLLO ASIC test board

The characterisation was carried out using the test board for the APOLLO ASIC developed by Kromek Group plc, (Figure 8.2 - a). The board individually address inputs channels of the ASIC, and it embeds a microcontroller that reads the SPI port, a USB-C port for the configuration and the readout of the ASIC digital output by dedicated software, an HV module for the SiPM biasing and a pulse generator for functionalities testing. The initial tests were carried out configuring the ASIC with the lowest gain of the pre-amplifier (3x) and bypassing the Semi-Gaussian Shaper. An external signal generator was used to generate different signal level, and signal length for the qualification of the ASIC working range measuring amplitude directly and signal length.

8.1.2 Threshold calibration

The threshold level can be set individually for each channel with a maximum excursion of +25mV above a common threshold value equal for all the channels. On the ASIC the common threshold value is set in steps of 25mV, while the individual chan-

nel setting has a granularity of 0.1 mV. a A squared signal high level was increased from a minimum of 5 to a maximum of 200 mV in steps of 0.1mV to calibrate the threshold and evaluate its linearity range. For each value, the corresponding ADC value set on the ASIC that guarantee at least 50% of pulses to generate a trigger was identified as the value in ADC of the threshold corresponding to the squared signal amplitude. The threshold comparator is downstream to the pre-amplifier, so far, the voltage range in which the Threshold Calibration was performed was 15-800 mV.

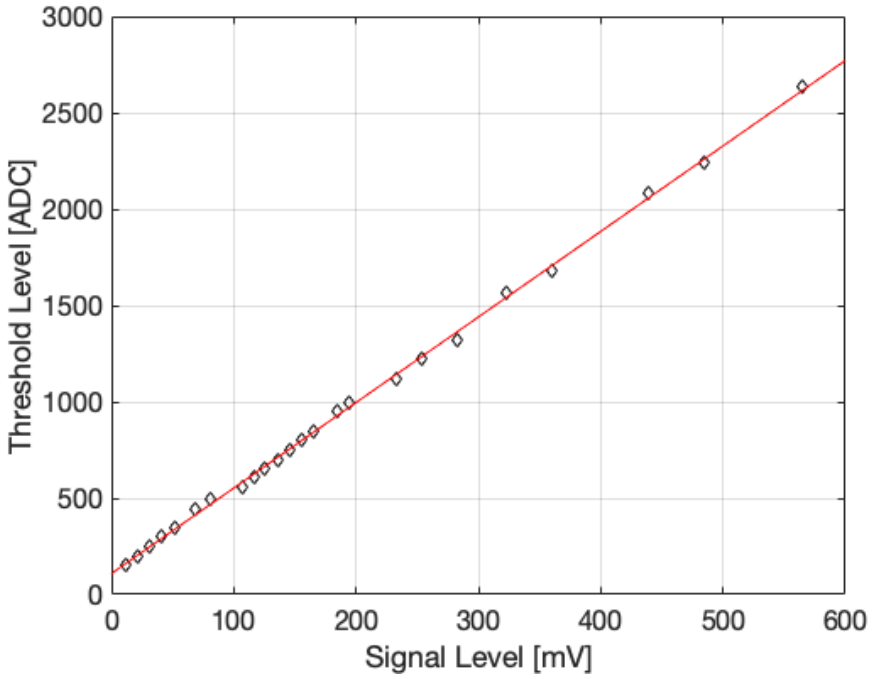

Fig. 8.3: Calibration curve for the threshold comparator.

The response of the threshold comparator is linear, with a residual non-linearity below 8%, where the maximum discrepancy occurs at the coarse steps changes of the shared value, as shown in Figure 8.3.

8.1.3 Peak Detector

A trapezoidal signal (50ns long high level and 20ns rise time) was increased between 5 mV and 800mV, to qualify the Peak Detector, namely 15-2400 mV taking into account the 3x gain by the Pre-Amplifier. The response of the peak detector is linear was measured to be linear up to 700mV with a residual non-linearity below 0.2%. For signals higher than 700mV, it deviates from linearity up to the saturation point at 2V, as shown in Figure 8.4.

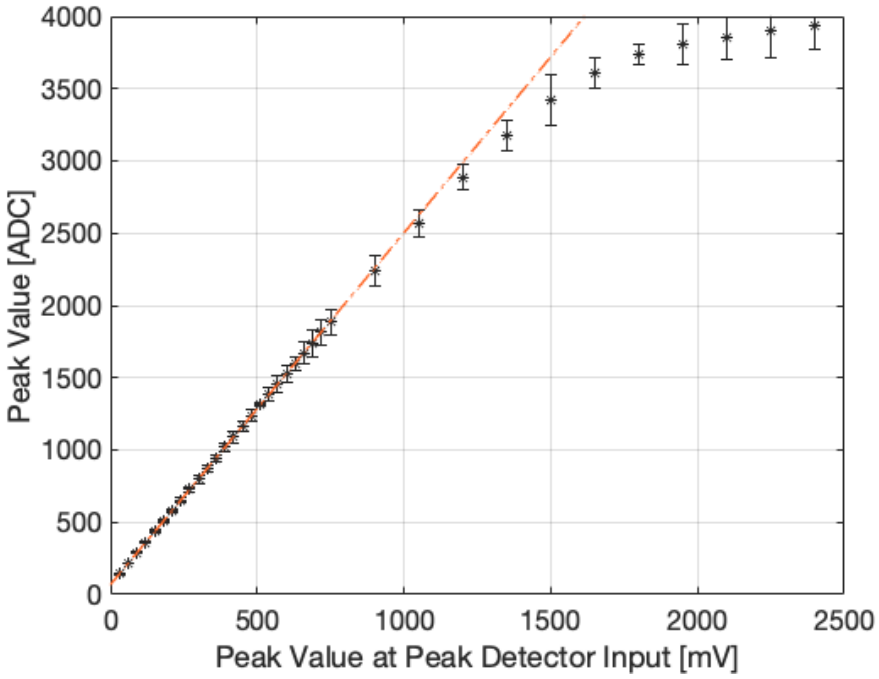

Fig. 8.4: Response of the Peak Detector

8.1.4 Analogue Integrator

The linearity of the integrator has been measured with respect to the variation of the input level and the signal duration. In particular, the difference in time duration will assess the linearity of the integration circuit, while the amplitude variation will test the response of the internal amplification stage. The first step was performed with a fixed integration gate of 10μs, and the different signal durations ranged from 200ns to 10 μs. The measurement was repeated with three signal of 150, 450 and 750 mV. As shown in Figure 8.5, the response is linear in the whole tested range, with a residual non-linearity below 0.5%. In Figure 8.5 the x-axes report the area under the signal, proportional to the charge collected by the integrator, corrected by the internal gain of the analogue integrator.

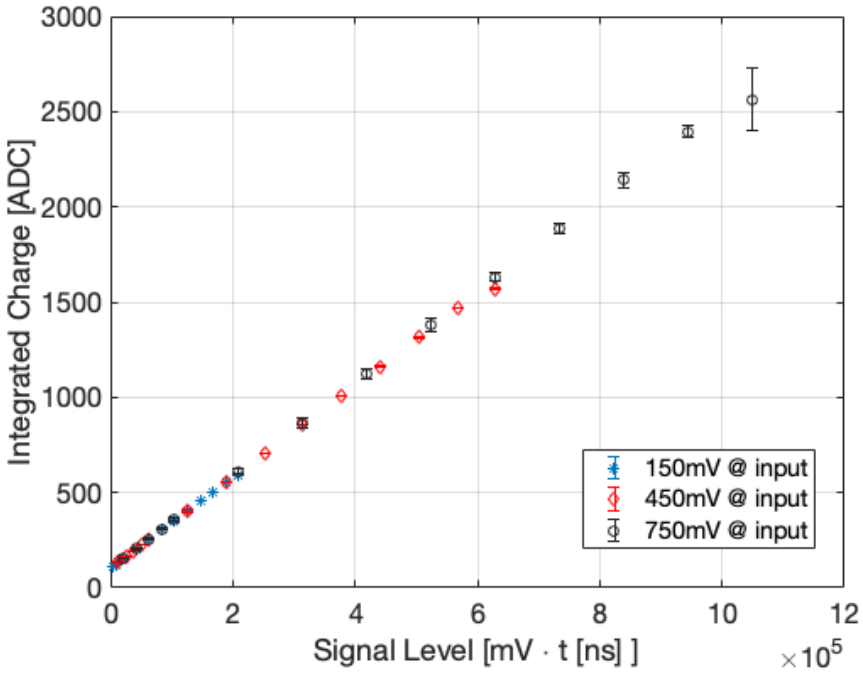

Fig. 8.5: Response of the analogue integrator to a time-varying signal

On the other hand, the response of the analogue integrator to a varying amplitude signal was investigated with a signal that covers in amplitude the same dynamic range used for the Peak Detector. Indeed, to collect the same amount of charge for the time linearity measurement, the signal length was set to 500ns and the integration gate to 2μs.

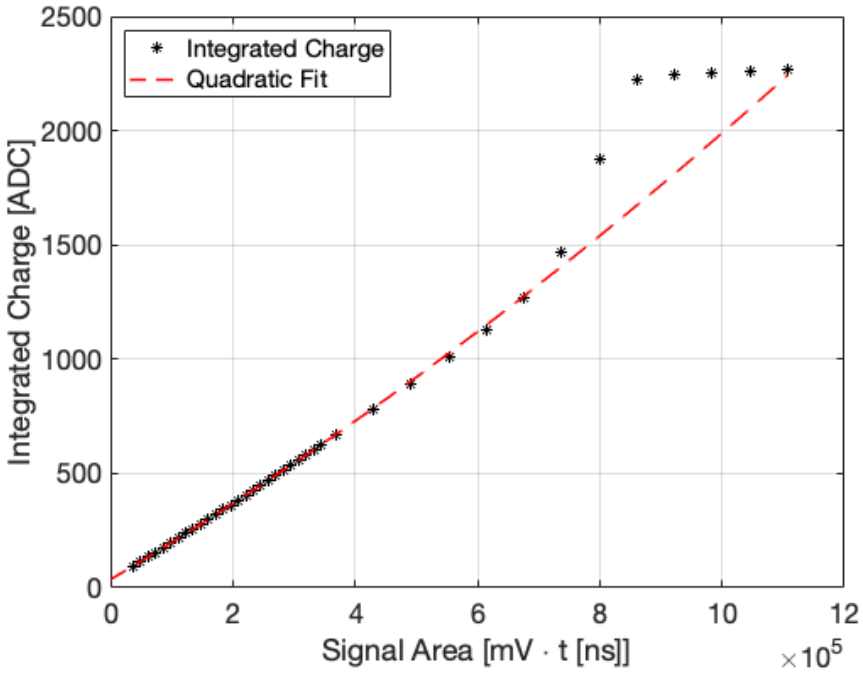

Fig. 8.6: Response of the analogue integrator to a signal-level varying signal

As shown in Figure 8.3, a quadratic curve well fits the up to 5 $mv \cdot t[ns]$, that corresponds to about 1V signal amplitude at analogue integrator input (to be corrected for the 0.88x internal gain), with residuals that non exceed 0.5%, showing a non-linearity of the internal amplification stage. For signal up to 7 $mv \cdot t[ns]$ ($\approx 1.5V$) the deviation from the ideal curve is, as expected, negative. Then the signal became comparable with analogue integrator power rails causing a drastic change in component behaviour resulting in the excess respect to the quadratic curve.

8.1.5 Transfer Function

The light generated by the LED Driver PicoQuant PDL800 is conveyed on the HPK SiPM array (s13360-3050C), and the signal shape was retrieved with the following procedure: the signal was integrated at different time windows, measuring $Q(t)$, the collected charge as a function of time as reported in Figure 8.7; the numerical derivative of $Q(t)$ was calculated, and it returned the signal shape at the input of the integrator, as shown in Equation (8.1).

$$Q(t) = \int_0^t S(\tau)d\tau \rightarrow \frac{dQ(t)}{dt} = S(t) \tag{8.1}$$

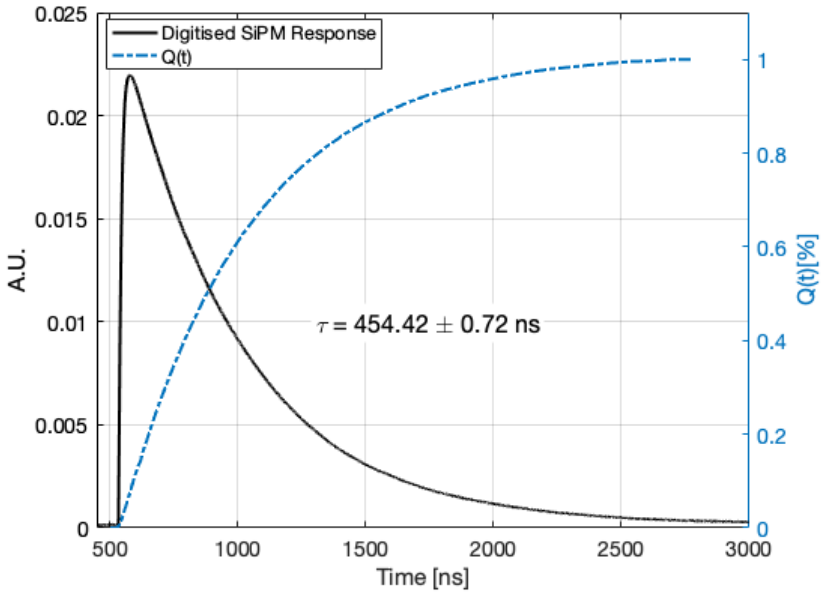

Fig. 8.7: SiPM response to an ultra-fast light pulse with superimposed $Q(t)$

The signal shape after the pre-amplification, shown in Figure 8.8, present a decay time of 458.15ns ±0.85ns, reasonably similar to the actual response of the SiPM array (454.42ns ± 0.72ns) obtained by directly digitising the SiPM array output with an Oscilloscope. The pre-amplifier thus does not affect the signal shape, so far good pulse shape discrimination results are expected.

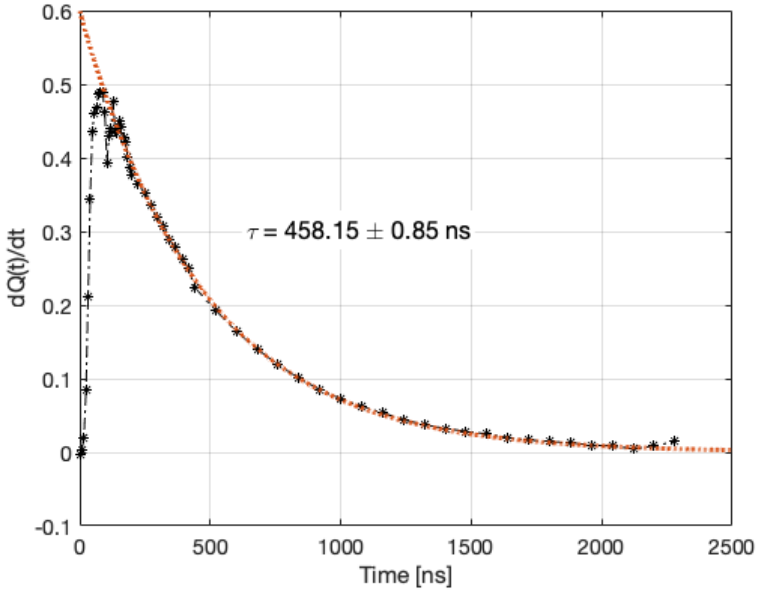

Fig. 8.8: Plot of the numerical derivative of $Q(t)$, representing the average signal after the pre-amplification stage

The same procedure was applied to measure the response of the Semi-Gaussian Shaper, that can be used in γ spectroscopy. In Figure 8.9 signal shapes after the shaping with $1\mu s$ and $2\mu s$ peaking time are reported. Moreover, the area under the two curves, proportional to the signal integral, is the same, confirming that the Semi-Gaussian Shaper does not affect the total collected charge from signals.

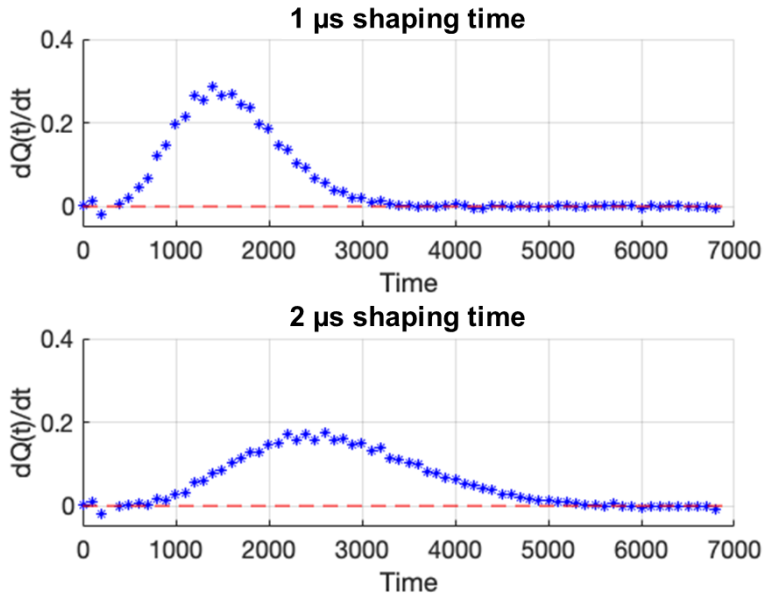

Fig. 8.9: The numerical derivative of $Q(t)$ after the Semi Gaussian Shaper for two different peaking time.

8.2 γ spectroscopy qualification

The qualification of the ASIC spectroscopic performance was achieved acquiring γ spectra with CsI(Tl) crystal (10x10x15mm^3) coupled to the SiPM array. The signal was either integrated for $10\mu s$ or shaped with 16 μs peaking time and the peak value captured by the peak detector. As expected from the electronics characterisation, the energy calibration curve for the analogue integrator is quadratic, with the main parameter of the fit shown in Figure 8.10(a) that are reported in Table 8.1. In contrast, the calibration curve for the peak detector is linear, as shown in Figure 8.10(b), and fit parameter are also reported in Table 8.1.

Parameter	Integrator	Semi-Gaussian
Quadratic Term	$-9.83 \cdot 10^{-5} \pm 0.78 \cdot 10^{-5}$	N.A.
Linear Term	1.31 ± 0.012	0.94 ± 0.07
Offset	116.9 ± 3.8	164.5 ± 17.5

Tab. 8.1: Calibration curves fitting parameters

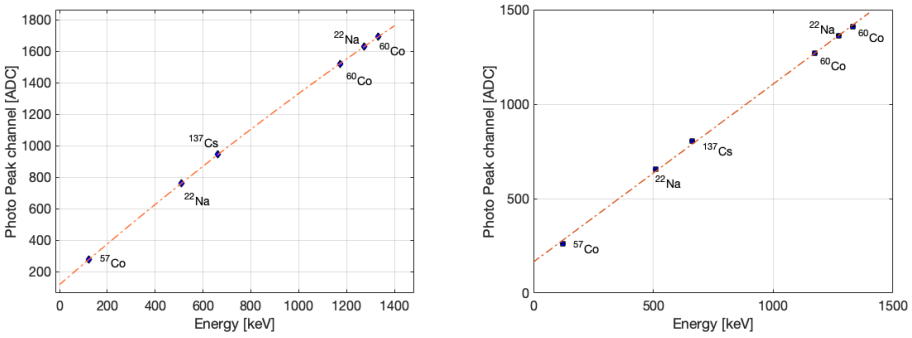

(a) (b)

Fig. 8.10: Calibration curve for the Analogue Integrator (a) and for the Peak Detector after the Semi-Gaussian Shaper (b).

In Figure 8.11 ^{137}Cs spectra acquired with the two approaches are shown, and in Table 8.2 the resolutions of the 662 keV peak are reported. The resolution obtained with the integral based spectrum is 5.71%, close to the intrinsic resolution of the crystal ($\approx 5\%$)

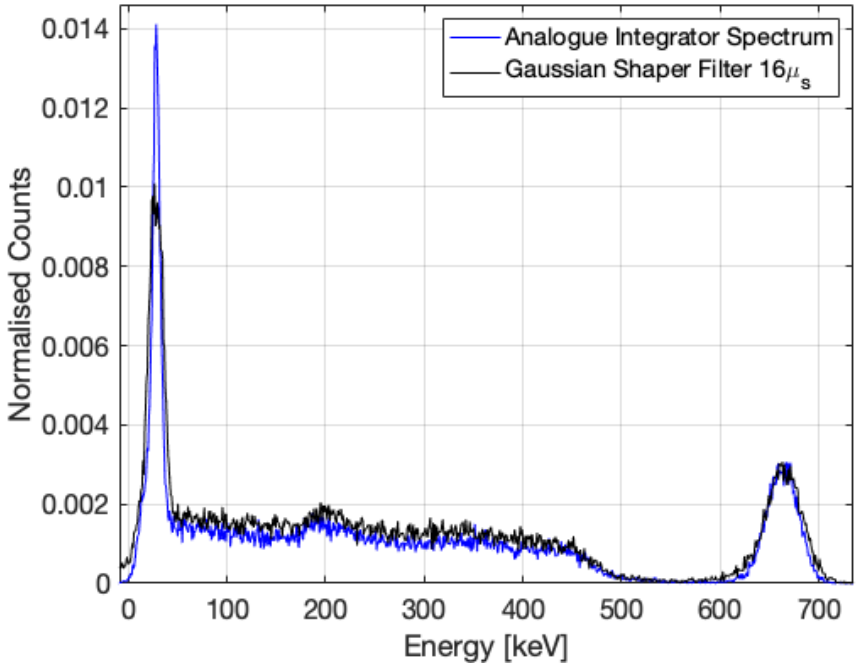

Fig. 8.11: Spectra of a ^{137}Cs source collected with the APOLLO ASIC with either retaining the integral or the peak amplitude after the Semi-Gaussian Shaper

It is sensible that the ballistic deficit could be non-negligible because the shaping time of the Semi-Gaussian Shaper is comparable with the signal length [47], so far this explains the worst resolution of the measurements performed with the

Semi-Gaussian shaper in respect to the one obtained with the integral. In this configuration, the consideration from Chapter 5 does not hold since the peaking time is long enough to collect all photons from the scintillator.

It is then worth to measure the γ spectra with the peak detector without any shaping. The results are shown in Figure 8.12, where the ^{137} spectrum obtained with the analogue integrator is shown superimposed to the one obtained retaining the peak amplitude. As expected, the resolution worsens, being $5.71 \pm 0.02\%$ for the integral while it is only $8.35 \pm 0.02\%$. This result is consistent with what was measured in Chapter 5: retaining the peak amplitude form signal generated by a scintillator with a long decay time is not the optimal solution to measure γ spectra.

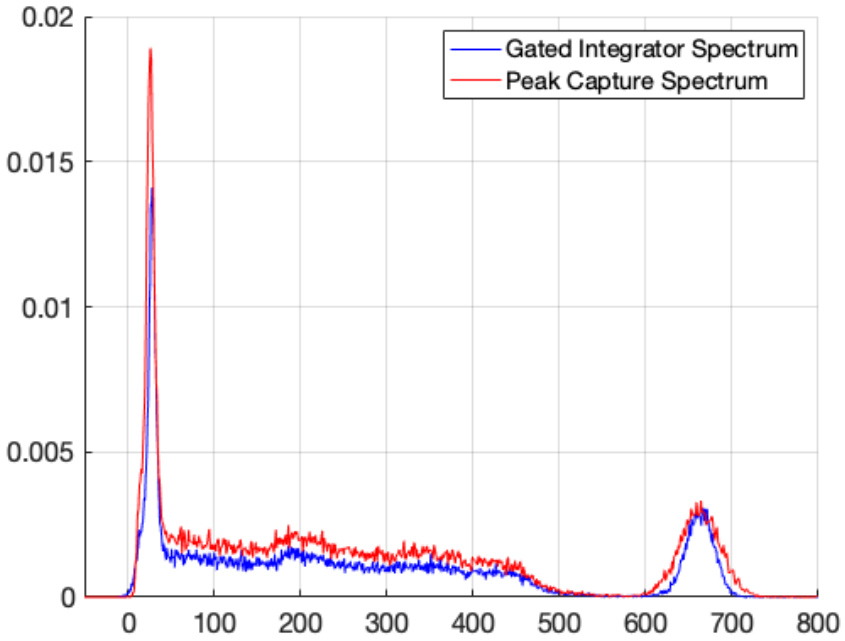

Fig. 8.12: Spectra of a ^{137}Cs source collected with the APOLLO ASIC with either retaining the integral or the peak amplitude with no signal shaping.

Tab. 8.2: Resolutions of the 662 keV peak of a ^{137}Cs, collected with tree different configurations

$\Delta E/E$ ^{137}**Cs**	
Analogue Integrator	$5.71\% \pm 0.02\%$
Semi-Gaussian Shaper	$6.82\% \pm 0.03\%$
Peak Amplitude	8.35 ± 0.02

8.3 γ-neutron discrimination with Apollo ASIC

The qualification of the ASIC for γ-neutron discrimination application was made either using the EJ-276 scintillator (8x8x15mm^3 volume) or the CLLB-C organic scintillator (2 inches diameter cylinder, 10cm height) coupled to the SiPM Array exposed to a ^{252}Cf source and several γ calibration sources.

8.3.1 EJ-276

8.3.2 Energy Calibration

Due to the low Z of the scintillating material, the energy calibration relied on the use of the Compton Edge position of the spectra, acquired integrating for 4μs signals from the γ calibration sources (^{137}Cs, ^{22}Na and ^{60}Co). The Compton edge positions were determined after a fit with a complementary error function ($erfc(x)$) on the Compton's shoulder, as shown in Figure 8.13, where the fit is superimposed to ^{137}Cs spectra [111].

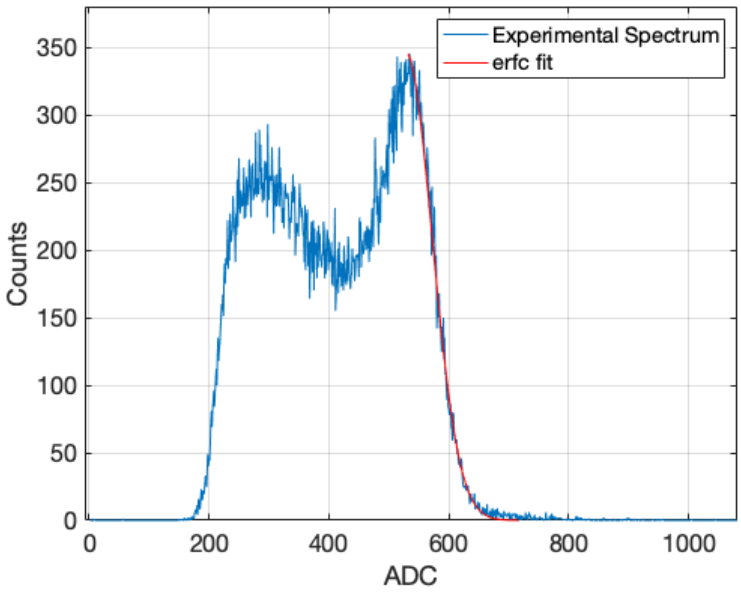

Fig. 8.13: The spectra of ^{137}Cs source obtained with the EJ-276 coupled with the SiPM array whose signal was processed by the APOLLO ASIC

The calibration curve is shown in Figure 8.14, where a quadratic function, whose parameters are reported in Table 8.3, was again used to account for integrator non-linearity.

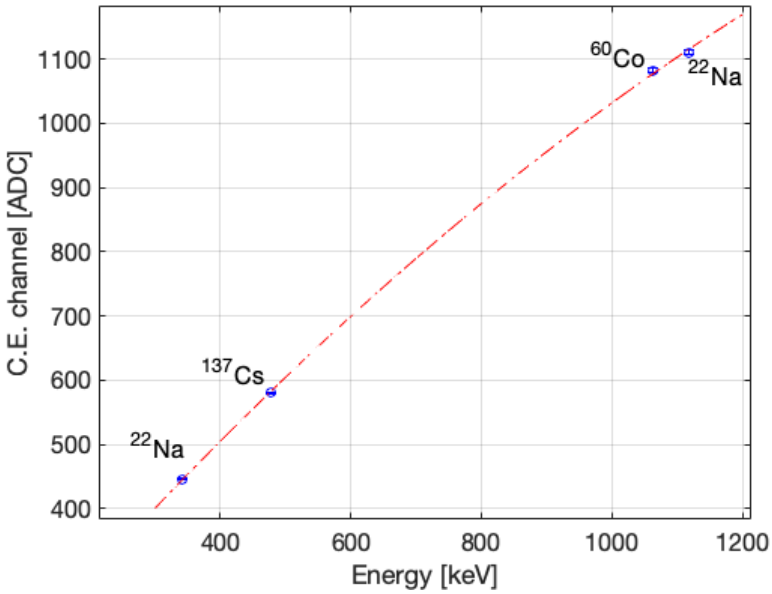

Fig. 8.14: Calibration Curve of the system. A second order polynomial was used to fit the data in order to account for the analogue integrator non linearity

Tab. 8.3: Calibration Curve fitting parameters

EJ-276 Energy Calibration

Quadratic term	$(3.1 \pm 0.5) \cdot 10^{-4}$
Linear Term	0.67 ± 0.3
Offset	-18.5 ± 38.3

8.3.3 Pulse Shape Discrimination

In order to evaluate the PSD discriminating variable according to the Equation 2.8, the signal was simultaneously connected to 3 channels of the ASIC: the first one used to retain the energy information integrating the signal for 4μs and propagate the trigger, the second channel was configured to retain the peak amplitude, and the third one integrates the tail of the signal. The integration limits were the one found in the optimisation procedure with the digital set-up presented in Chapter 7 ($t_{delay} = 600ns$,$t_{int} = 3000ns$).

In Figure 8.15 the PSD parameter is plotted versus the energy for the ^{252}Cf neutron source (6 kBq) and for the ^{60}Co and ^{137}Cs γ sources.

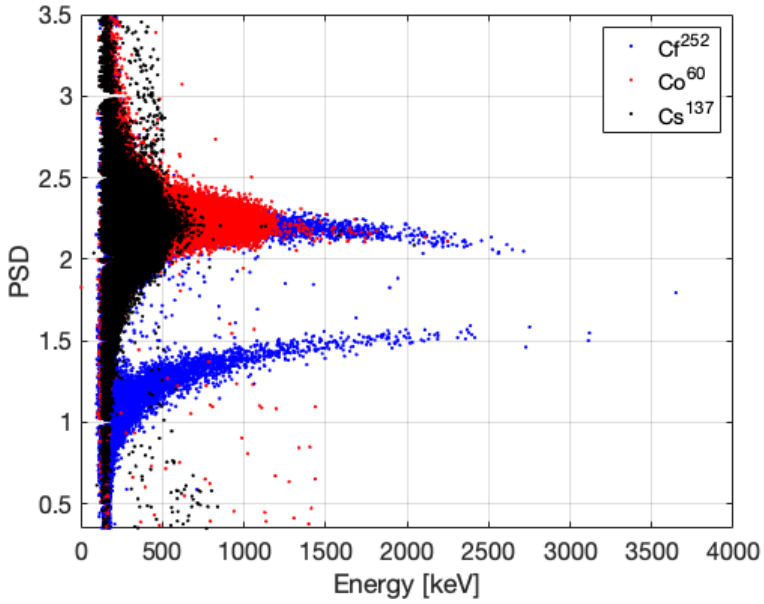

Fig. 8.15: PSD parameter vs Energy deposited in the scintillator in units of electron equivalent keV.

In Figure 8.16 is reported the distribution for the energy windows between 1 and 1.5 MeV where the $F.o.M.$was measured to be 3.76 ± 0.34. The centroids and the FWHM were obtained again with a double Gaussian fit on the PSD distribution.

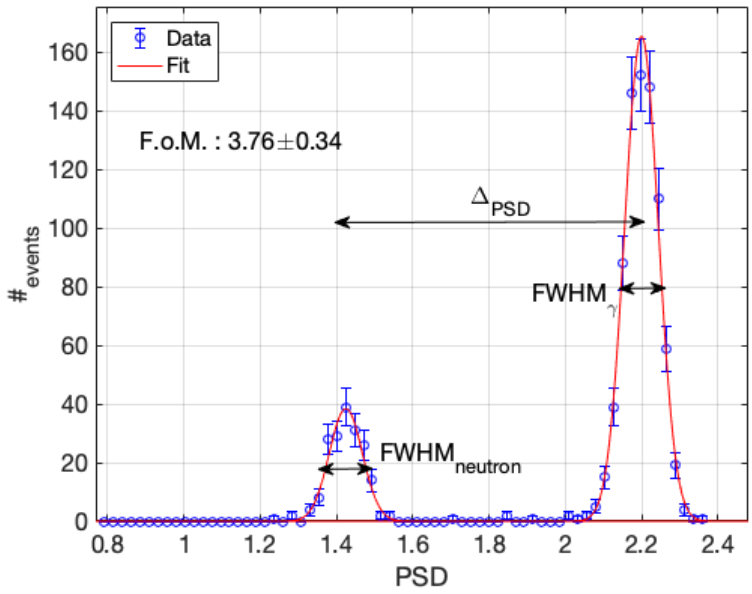

Fig. 8.16: F.o.M. from the PSD distribution in the energy slice 1-1.5 MeV

In Figure 8.17 the $F.o.M.(E)$is shown. It was evaluated for non-overlapping energy bins (100 keV) from 50 keV to 1 MeV plus one more bin for energies between 1 and 2.2 MeV.

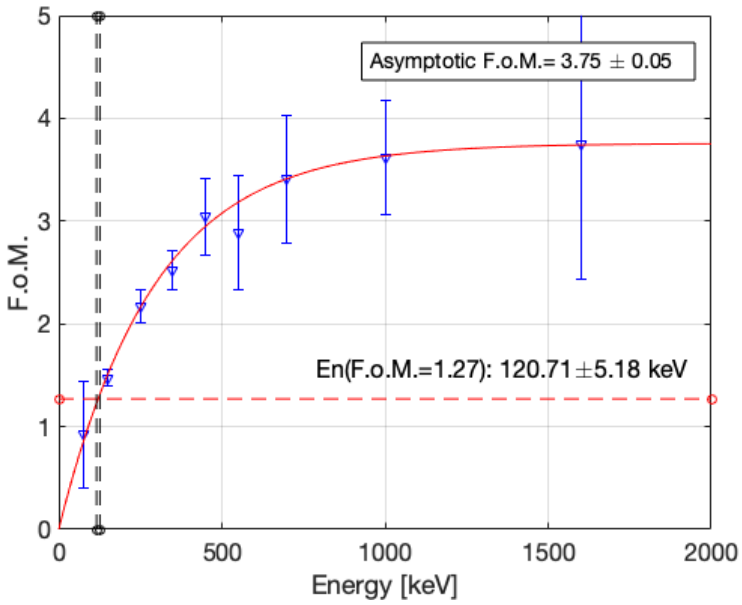

Fig. 8.17: F.o.M. as function of energy.

ASIC results to be better concerning the digital system a $F.o.M.(E = \infty)$, is equal to 3.75±0.05 should be compared with 3.47±0.04, and a slightly better E_{min}, equal to $120.71 \pm 5.18keV$ with the ASIC, to be compared with $186.5 \pm 25.3keV$.

8.3.4 CLLB-C

The high Z of the CLLB-C scintillator allows getting an energy calibration curve relying on the photo-peak positions. The excellent γ spectroscopy capability of this crystal was confirmed by the high quality γ spectra, for example, the ^{137}Cs shown in Figure 8.18. The $\Delta E/E$ for the 662 keV photo-peak is 4.2% ± 0.2%, with an intrinsic resolution of 3.5%.

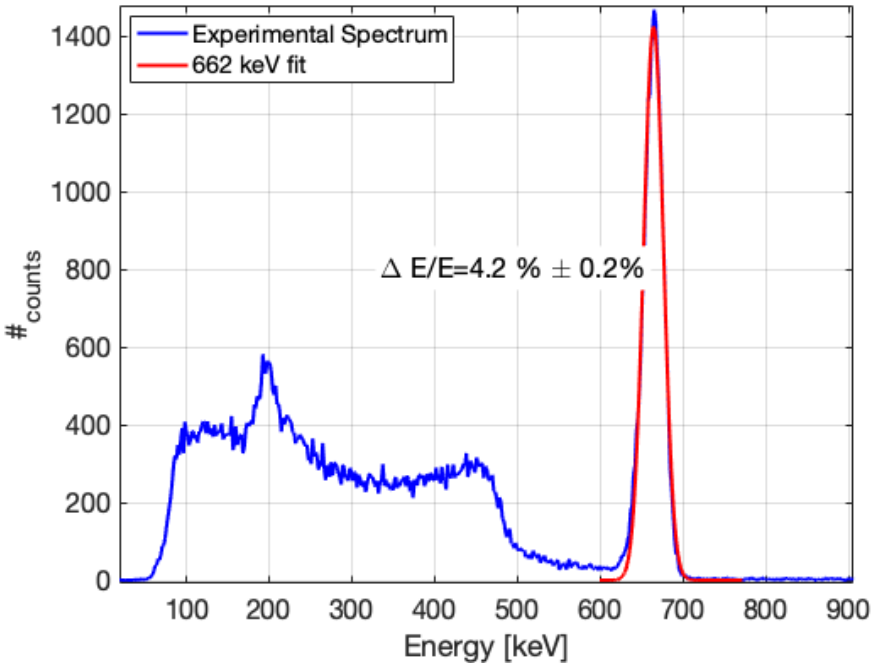

Fig. 8.18: ^{137}Cs spectra collected with the CLLB-C crystal

Thermal neutrons used in PSD capability assessment with the CLLB-C were obtained shielding a ^{252}Cf source with a cylinder of PVT with 10cm of diameter. PSD_{PT} parameter was evaluated, and event by event value vs pulse energy is plotted in Figure 8.19.

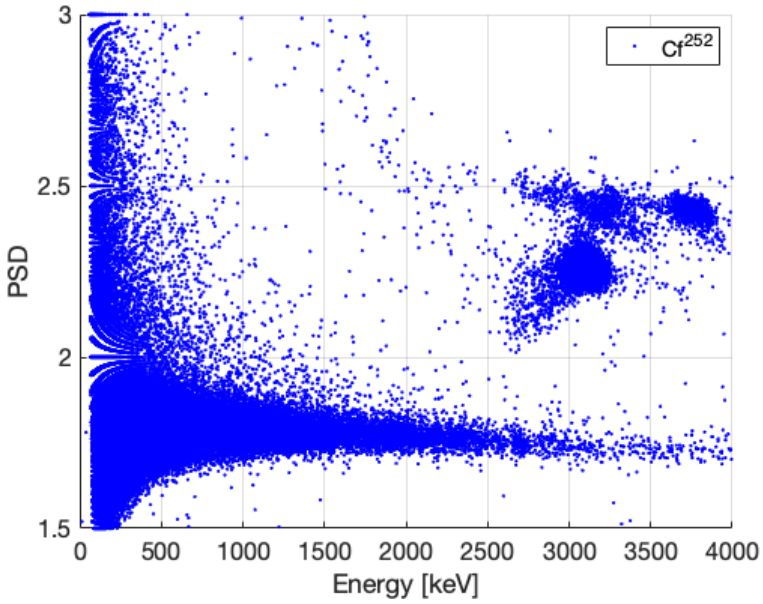

(a) PSD parameter vs Energy for the ^{252}Cf source obtained with the CLLB-C crystal

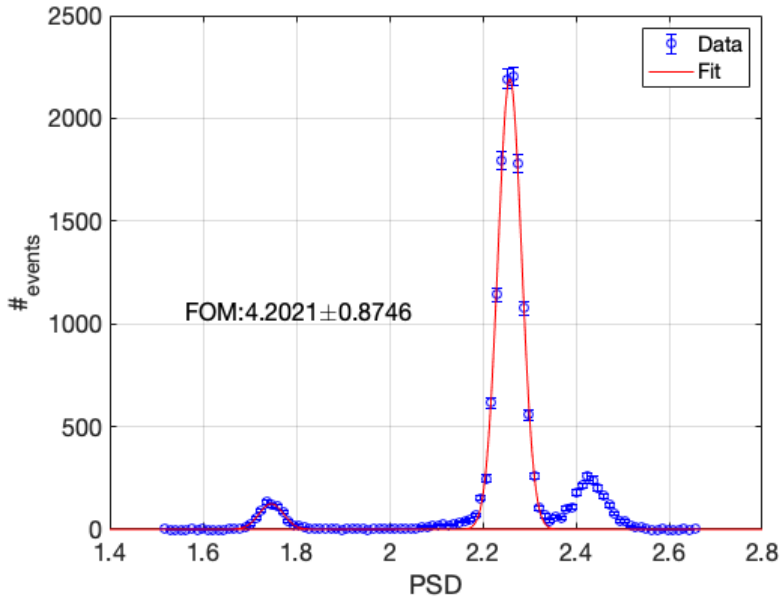

(b) $F.o.M.$ shows a good separation between γ and neutrons, even though the self activity of the CLLB-C is quite evident

Fig. 8.19

In Figure 8.19(a) the discrete structures in the low energy region of the scatter plot are due to the digitisation of the peak amplitude and the integral tail spectrum in 4096 channels.

γ-neutron separation is excellent, with a $F.o.M.$ of 4.29 $\pm$ 0.87 in the energy window between 2.5 and 4 MeV, but in fact, the contamination from the α particle from self-activity is quite evident, and it increases the false positive rate.

The background has been evaluated collecting data for 35 min (Figure 8.20) measuring a self-activity rate of 0.57Hz, 0.014 Hz of which are underneath the neutron blob.

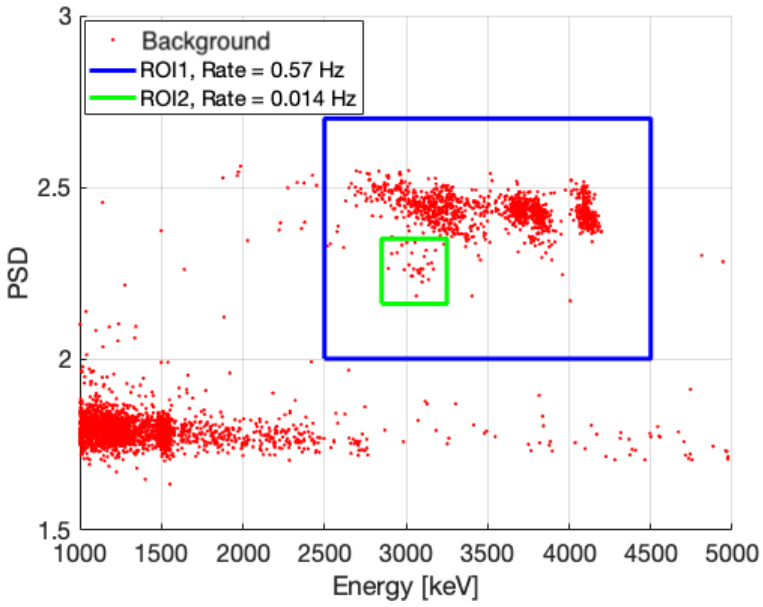

Fig. 8.20: Self activity and background in the CLLB-C crystal measurement. The Background was acquired for 35 min in the same condition as for the Figure 8.19

For any neutron measurement, especially for nuclear security, it is mandatory to properly evaluate this background because it can induce a false alarm rate that would prevent this crystal from being used successfully in an instrument.

9 Conclusions and Outlooks

The goal of the research activity described in this thesis was the developing of a new algorithm for Pulse Shape Discrimination applied to SiPMs coupled to PSD Capable Scintillators. In addition to that, the impact of the acquisition chain in Pulse Shape Discrimination had been studied, and its understanding allowed to implement this algorithm in two near-real time systems based on an ASIC and a FPGA. The peak amplitude normalisation measurements proposed in this work are an innovative approach to the PSD that has been studied, and the motivation for its excellent performances have been investigated. Indeed to understand the physical meaning of the peak amplitude a better knowledge in measurements with SiPM as light detector either from a source like a laser or a LED suggested that it may be possible to push the use of SiPMs in applications where a large number of photons need to be resolved, for example, in some quantum optics applications[105, 104].

After the definition of a robust and straightforward algorithm, the impact of the light collection efficiency was measured. The results highlighter how light collection efficiency plays a fundamental role in PSD since the same number of detected photons corresponds to the same $F.o.M.$. The use of a SiPM array allowed to collect all the light from the EJ-276 and produced a larger $F.o.M.$even if signal shaping is not negligible due to the considerably increased array capacitance. Then the measurement of the impact of digital acquisition chain for signal processing was performed. The gathered results allowed to build an instrument, based on an FPGA, that was capable of on-line Pulse Shape Discrimination. One of the main results obtained in this thesis was, indeed, the full commissioning of the custom version of the I-Spector prototype. This instrument, highly configurable, equipped with a LORA communication system, can be used in a diffuse monitoring system to remotely control a large area, receiving alarms for a specific energy region of interest, either neutron or γ related.

It was also shown that with proper electronics, it is possible to obtain good discrimination even if the latest generation of the Hamamatsu SiPM has an even larger capacitance, so a more substantial impact on the signal shape concerning the s13360 series. That is another proof that the factor with the higher impact on the $F.o.M.$is the light collection efficiency.

Concerning the research project, it was customised an instrument for on-line γ/neutron detection and discrimination. The instrument was fully qualified, commissioned and delivered to AWE. The instrument is a full-working product with dedicated software that allows controlling the unit remotely, to calibrate the detector, set ROI for alarms separately for neutron and γ, and with the possibility do send those alarms via LORA protocol due to the integrated LORA antenna. The on-line pulse shape discrimination allows to obtain separation down to $E_{min} = 400keV$ and with a $F.o.M.(E = [1; 1.5MeV]) = 2.2 \pm 39$).

The APOLLO ASIC developed by Kromek Group plc has been qualified for the Pulse Shape Discrimination application. The working range of the blocks comprised in the analogue part of the APOLLO ASIC have been tested, and the results showed, in the first place, high-grade γ spectroscopy performances, with a 662 keV peak resolution from a ^{137}Cs source close to the intrinsic resolution of the CsI(Tl) crystal.

Fast neutron detection via Pulse Shape Discrimination with $F.o.M. \geq 2$ for deposited energy more than 350 keV was obtained, and a maximum of $F.o.M.$ of 3.75 ± 0.05 was measured. Moreover, the low energy discrimination limit was found at $120.71keV \pm 5.18keV$.

In addition to that, APOLLO was qualified for the use with inorganic scintillator doped with ^{6}Li; in this scenario, the APOLLO showed itself as a useful tool, even thermal neutron detection. Discrimination power, qualified by a $F.o.M. = 4.20 \pm$ 0.87 is spoiled by the self-activity of the crystal, measured to be at sub-Hertz level, possibly limiting the use of CLLB-C crystal in the field. The results obtained in this thesis and the algorithm developed for γ-neutron discrimination based on peak-tail algorithm are the core of the D5 RIID produced and presented to the market by Kromek in late 2020.

In conclusion, it is possible to build a portable detector for diffuse monitoring applications based on a single scintillator read out by a SiPM using either an analogue or a digital approach, when all the acquisition chain blocks are accurately optimised.

A deep understanding of factors contributing to discrimination has been achieved, but integration gates boundary origin failed to be modelled yet. In particular further study shall indicate how those boundaries depend on noise band of electronics circuits and the convolution of the scintillator and SiPM signal time development. Moreover, the impact of temperature variation on the discrimination has to be investigated to guarantee better in-field operation performances. Additionally, the response of the scintillators, and the $F.o.M.$at different temperatures, should be investigated in order to disentangle the effect of changes in light yield and in the ratio of characteristic scintillating light time development. It seems that it is not

possible, however, neither in literature nor in the results reported in this thesis, to obtain acceptable discrimination below 100 keV, and it was proven that this limit is related to the minimum amount of light necessary to differentiate the pulse shape statistically.

Bibliography

[1] IAEA. « Nucear Security: Global directions for the future, Proceeding of the International Conference, London ». In: (2005) (cit. on pp. 1, 13).

[2] Sakari Ihantola et al. *European Reference Network for Critical Infrastructure Protection: Novel detection technologies for nuclear security*. Ed. by ERNCIP Thematic Group from JRC. May 2008 (cit. on pp. 1, 28, 30, 31, 39).

[3] Barak Obama. *National Security Strategy of the United States*. 2010 (cit. on p. 4).

[4] Francis Henry Williams. *The Röntgen rays in medicine and surgery*. Ed. by New York The McMillan Company. 1902 (cit. on p. 4).

[5] P. W. Allen. « Report of cases treated with Röntgen rays, JAMA **XXXVIII**,-15, 911-919 ». In: (1902). DOI: 10.1001/jama.1902.62480150001001. URL: https://doi.org/10.1001/jama.1902.62480150001001 (cit. on p. 5).

[6] M.Curie P. Curie. « Sur une nouvelle substance fortement radio-active, contenue dans la pechblende, Comptes rendus de l'Acadèmie des Sciences 127, 1215-1217 ». In: (1898) (cit. on p. 5).

[7] D. Walsh. « Deep Tissue Traumatism from Röntgen Ray Exposure., Br Med J. **1909**-2, 272273 ». In: (1897). DOI: 10.1136/bmj.2.1909.272 (cit. on p. 5).

[8] M.Curie P. Curie. « Über den Einfluss der Röntgenstrahlen auf epitheliale Gewebe, insbesondere auf das Carcinom. in von Langenbecks Archiv für klinische Chirurgie 71, 9551000 ». In: (1903) (cit. on p. 5).

[9] 1/08/2019. URL: http://lowdose.energy.gov/timeline.aspx (cit. on p. 5).

[10] Robert Serb. *The Los Alamos Primer - The first Lecture on how to build an atomic bomb*. Ed. by University of California Berkley. 1992 (cit. on pp. 6, 7).

[11] 1/08/2019. URL: https://www.un.org/disarmament/wmd/nuclear/npt/text/ (cit. on p. 6).

[12] IAEA. *IAEA Annual Report 2017*. 2017 (cit. on p. 6).

[13] C.D. Ferguson et al. *Commercial Radioactive Sources: Surveying the Security Risks*. Ed. by J.M. Center for Nonproliferation Study Middelbury Institute of International Study at Mnterey. 2003 (cit. on pp. 6, 7, 14).

[14] IAEA. « IAEA INCIDENT AND TRAFFICKING DATABASE (ITDB) Factsheet ». In: (2019). URL: https://www.iaea.org/sites/default/files/19/04/itdb-factsheet-2019.pdf (cit. on pp. 7, 9–12).

[15] IAEA. *Combatting Illicit Trafficking in Nuclear and Other Radioactive Material - Reference Manual. IAEA Nuclear Security Series N^o 6*. Ed. by Europool Interpool WCO IAEA. 2007 (cit. on pp. 7, 10, 11, 14, 16, 20–22).

[16] Fetter S et al. « Detecting Nuclear Warhear ». In: *The Technical Basis for Arms Control, Disarmament, and Nonproliferation Initiatives, 13/4, 225:253* (1990). DOI: 10.1080/08929889008426333 (cit. on p. 7).

[17] IAEA. *Categorization of Radioactive Sources, Safety Guide No. RS-G-1.9*. Ed. by Vienna IAEA. 2005 (cit. on p. 8).

[18] 1/08/2019. URL: https://www.arpalombardia.it/sites/DocumentCenter/Documents/RADIOATTIVITÀ/radioactivity.pdf (cit. on p. 12).

[19] 1/08/2019. URL: http://www.johnstonsarchive.net/ (cit. on p. 13).

[20] URL: https://thebulletin.org (cit. on p. 13).

[21] Carlton Stoiber, Alec Baer, Norbert Pelzer, and Wolfram Tonhauser. *Physical Protection of Nuclear Material and Nuclear Facilities against Sabotage*. Ed. by Vienna IAEA. 2018 (cit. on p. 14).

[22] IAEA. *Handbook on Nuclear Law. IAEA Nuclear Security Series*. Ed. by Vienna IAEA. 2003 (cit. on p. 15).

[23] *Treaty on the Non-Proliferation of NuclearWeapons, IAEA, INFCIRC/140, IAEA, Vienna (1970)*. (Cit. on p. 15).

[24] *Communication Received from Members Regarding the Export of Nuclear Material and of Certain Categories of Equipment and other Material, Guidelines for Nuclear Transfers, INFCIRC/209, IAEA, Vienna (1974)*. (Cit. on p. 15).

[25] *Nuclear Suppliers Group Guidelines, INFCIRC/254, IAEA, Vienna (1978)*. (Cit. on p. 15).

[26] *Treaty on the Prohibition of Nuclear Weapons in Latin America and the Caribbean (Tlatelolco Treaty), GOV/INF/179, IAEA, Vienna (1967)*. (Cit. on p. 15).

[27] *South Pacific Nuclear Weapon Free Zone Treaty (Rarotonga Treaty), INFCIRC/ 331/Add.1, Vienna (1987)*. (Cit. on p. 15).

[28] *INTERNATIONAL ATOMIC ENERGY AGENCY, Southeast Asia Nuclear Weapon Free Zone Treaty (Bangkok Treaty), INFCIRC/548, Vienna (1998)*. (Cit. on p. 15).

[29] *INTERNATIONAL ATOMIC ENERGY AGENCY, The African Nuclear Free Zone Treaty (Pelindaba Treaty), INFCIRC/512, Vienna (1996)*. (Cit. on p. 15).

[30] *The Structure and Content of Agreements Between the IAEA and States required in Connection with the Treaty on the Non-Proliferation of Nuclear Weapons INFCIRC/153 (Corrected), IAEA, Vienna (1972)*. (Cit. on p. 15).

[31] *Model Protocol Additional to the Agreement(s) between State(s) and the Inter- national Atomic Energy Agency for the Application of Safeguards, INFCIRC/540 (Corrected), IAEA, Vienna (1997)*. (Cit. on p. 15).

[32] *Convention on the Physical Protection of Nuclear Material, INFCIRC/274/Rev. 1, IAEA, Vienna (1980)*. (Cit. on p. 15).

[33] *Nuclear Security Measures to Protect against Nuclear Terrorism, Amendment to the Convention on the Physical Protection of Nuclear Material, Report by the Director General, GOV/INF/2005/10GC(49)/INF/6, IAEA, Vienna (2005)*. (Cit. on p. 15).

[34] *Convention on Early Notification of a Nuclear Accident, INFCIRC/355, IAEA, Vienna (1986)*. (Cit. on p. 15).

[35] *Europol Convention, Office for Official Publications of the European Communi- ties, Luxembourg (2004)*. (Cit. on p. 15).

[36] *International Convention for the Suppression of Acts of Nuclear Terrorism, A/59/ 766, United Nations, New York (2005)*. (Cit. on p. 15).

[37]*INTERNATIONAL ATOMIC ENERGY AGENCY, Code of Conduct on the Safety and Security of Radioactive Sources, IAEA, Vienna (2004)*. (Cit. on p. 15).

[38]*Measures to Strengthen International Cooperation in Nuclear, Radiation, Transport Safety and Waste Management, Code of Conduct on the Safety and Security of Radioactive Sources: Guidance on the Import and Export of Radio- active Sources, GOV/2004/62GC (48)/13, IAEA, Vienna (2004)*. (Cit. on p. 15).

[39]*Non-proliferation of Weapons of Mass Destruction, Security Council S/RES/ 1540, United Nations, New York (2004)*. (Cit. on p. 15).

[40]*Threats to International Peace and Security Caused by Terrorist Acts, Security Council Resolution 1373, United Nations, New York (2001)*. (Cit. on p. 15).

[41]IAEA. *IAEA-TechDoc 1312*. Tech. rep. 2002 (cit. on pp. 16, 17, 19, 20).

[42]*Technical and Functional Specifications for Border Monitoring Equipment*. Nuclear Security Series 1. Vienna: INTERNATIONAL ATOMIC ENERGY AGENCY (cit. on pp. 16, 17, 20).

[43]U.S department of Energy. *Neutron detectors Gamma Insensitivity Criteria, PNNL-18903*. 2009 (cit. on pp. 17, 29).

[44]*Nuclear Security Systems and Measures for Major Public Events*. Nuclear Security Series 18. Vienna: INTERNATIONAL ATOMIC ENERGY AGENCY, 2012 (cit. on p. 23).

[45]1/08/2019. URL: https://www.kromek.com/product/d3s-net/ (cit. on pp. 23–25).

[46]1(08/2019. URL: https://www.kromek.com/detectors-on-drones/ (cit. on p. 24).

[47]*Radiation Detection and Measurement*. 4^{th}. Wiley, 1955 (cit. on pp. 27–29, 31–34, 36, 68, 149).

[48]Hoshor C. B. et al. « A Portable and Wide Energy Range Semiconductor-Based Neutron Spectrometer ». In: *Nuclear Inst. and Methods in Physics Research, A **803**, 68-81* (2015). DOI: 10.1016/j.nima.2015.08.077 (cit. on p. 28).

[49]Caruso A. N. et al. « The Physics of Solid-State Neutron Detector Materials and Geometries ». In: *Journal of Physics. Condensed Matter,**22**(44), 443201* (2010). DOI: 10.1088/0953-8984/22/44/443201 (cit. on p. 28).

[50]Van Eijk et al. « Inorganic Scintillators for Thermal Neutron Detection ». In: *IEEE Transactions on Nuclear Science **59**(5):337-342* (2004). DOI: 10.1016/j.radmeas.2004.02.004 (cit. on pp. 30, 31).

[51]1/08/2019. URL: https://eljentechnology.com/21-products/neutron-detectors (cit. on p. 30).

[52]1/08/2019. URL: https://www.crystals.saint-gobain.com/products/zns-and-lif-based-neutron-detectors (cit. on p. 30).

[53]1/08/2019. URL: https://scintacor.com/products/6-lithium-glass/ (cit. on p. 30).

[54]1/08/2019. URL: https://www.bridgeportinstruments.com/products/neutron.html (cit. on p. 30).

[55] Paweczak I. A. et al. « Boron-Loaded Plastic Scintillator with Neutron- Pulse Shape Discrimination Capability ». In: *Nuclear Inst. and Methods in Physics Research, A* ***751****, 62-69* (2014). DOI: 10.1016/j.nima.2014.03.027 (cit. on p. 30).

[56] Zaitseva N. et al. « Pulse Shape Discrimination with Lithium-Containing Organic Scintillators ». In: *Nuclear Inst. and Methods in Physics Research, A* ***729****, 747754* (2013). DOI: 10.1016/j.nima.2013.08.048 (cit. on p. 30).

[57] 1/08/2019. URL: https://www.arktis-detectors.com/products/neutron-detectors/ (cit. on p. 31).

[58] J.B. Marion and F.C. Young. *Nuclear Reaction Analysis: Graphs and Tables*. North-Holland, 1968. URL: https://books.google.it/books?id=jSBRAAAAMAAJ (cit. on p. 32).

[59] « Evaluation of spectral unfolding techniques for neutron spectroscopy ». In: *AIP Conference Proceedings* ***988****, 315* (2008). DOI: 10.1063/1.2905089 (cit. on p. 33).

[60] Whilem K. et al. « Development and Operation of a 6 LiF:ZnS(Ag) scintillating Plastic Capture-Gated Detector ». In: *Nuclear Inst. and Methods in Physics Research, A* ***842*** *54-61* (2017). DOI: 10.1016/j.nima.2016.10.042 (cit. on p. 35).

[61] Doty F. P. et al. « Elpasolite Scintillators ». In: *Sandia Report* (2012). URL: https://prod-ng.sandia.gov/techlib-noauth/access-control.cgi/2012/129951.pdf (cit. on p. 35).

[62] Shirwadkar U. et al. « Scintillation Properties of Cs2LiLaBr6 (CLLB) Crystals with Varying Ce3 Concentration ». In: *Nuclear Inst. and Methods in Physics Research, A* ***652*** *268270* (2011). DOI: 10.1016/j.nima.2010.08.050 (cit. on pp. 35, 36).

[63] Kan Yang and PeterR. Menge. « Pulse shape discrimination of $Cs_2LiYCl_6 : Ce_3^+$ scintillator from 30 řC to 180 řC ». In: *Nuclear Inst. and Methods in Physics Research, A* ***784*** *794-79* (2015). DOI: 10.1016/j.nima.2014.08.031 (cit. on p. 35).

[64] Dinar N. et al. « Characterization of CLYC scintillator coupled with photomultipliers and a large SiPM array ». In: *Radiat. Prot. Dosimetry,* ***180****(1-4) : 399-402* (2018). DOI: 10.1093/rpd/ncx203 (cit. on p. 35).

[65] Glodo J. et al. « Selected Properties of Cs2LiYCl6, Cs2LiLaCl6, and Cs2LiLaBr6 Scintillators ». In: *IEEE Transactions on Nuclear Science* ***581****:333338* (2011). DOI: 10.1109/TNS.2010.2098045 (cit. on p. 35).

[66] Glodo J. et al. « Pulse Shape Discrimination With Selected Elpasolite Crystals ». In: *IEEE NSS/MIC* ***595****:23282333* (2011). DOI: 10.1109/NSSMIC.2012.6551125 (cit. on p. 35).

[67] Bourne M. M. et al. « Characterization of the CLYC Detector for Neutron and Photon Detection ». In: *Nuclear Inst. and Methods in Physics Research, A* ***736*** *124127* (2014). DOI: 10.1016/j.nima.2013.10.030 (cit. on p. 35).

[68] Bessiere A. et al. « Luminescence and scintillation properties of $Cs_2LiYCl_6 : Ce^+$ for gamma and neutron detection ». In: *Nuclear Inst. and Methods in Physics Research, A* ***537*** *242-246* (2005). DOI: 10.1016/j.nima.2004.08.018 (cit. on p. 35).

[69] Yang K. et al. « Scintillation properties and temperature responses of Cs 2LiLaBr6:Ce3+ ». In: *IEEE Nuclear Science Symposium conference record. Nuclear Science Symposium* (2013). DOI: 10.1109/NSSMIC.2013.6829676 (cit. on p. 36).

[70] Giaz A. et al. « Fast Neutron Measurements with 7Li and 6Li Enriched CLYC Scintillators ». In: *Nuclear Inst. and Methods in Physics Research, A **825** 51-61* (2016). DOI: 10.1016/j.nima.2016.03.090 (cit. on p. 35).

[71] Zaitseva N.P. et al. « Recent developments in plastic scintillators with pulse shape discrimination ». In: *Nuclear Inst. and Methods in Physics Research, A **889** 97-104* (2018). DOI: 10.1016/j.nima.2018.01.093 (cit. on pp. 36–38).

[72] 1/08/2019. URL: https://neutrinos.llnl.gov/content/assets/docs/workshops/2018/AAP2018-LLNLMaterials-Mabe.pdf (cit. on p. 36).

[73] Jan. 2020. URL: https://www.crystals.saint-gobain.com/sites/imdf.crystals.com/files/documents/cllb-material-data-sheet.pdf (cit. on p. 38).

[74] Jan. 2020. URL: https://cdn.dynasil.com//assets/CLYC-Gamma-Neutron-Scintillator-Properties.pdf (cit. on p. 38).

[75] Jan. 2020. URL: https://inradoptics.com/pdfs/datasheets/InradOptics_Datasheet_Stilbene_Final.pdf (cit. on p. 38).

[76] Jan. 2020. URL: https://eljentechnology.com/products/plastic-scintillators/ej-276 (cit. on p. 38).

[77] G.W. McBeth, J.E. Lutkin, and R.A. Winyard. « A simple zero crossing pulse shape discrimination system ». In: *Nuclear Instruments and Methods* 93.1 (1971), pp. 99 –102. DOI: 10.1016/0029-554X(71)90144-3 (cit. on p. 39).

[78] F.D. Brooks. « A scintillation counter with neutron and gamma-ray discriminators ». In: *Nuclear Instruments and Methods* 4.3 (1959), pp. 151 –163. DOI: 10.1016/0029-554X(59)90067-9 (cit. on p. 39).

[79] T. Szcze Smak et al. « Digital neutron-gamma discrimination methods: Charge comparison versus zero-crossing ». In: *IEEE Nuclear Science Symposium and Medical Imaging Conference. NSS-MIC, pp. 1-4* (2014). DOI: 10.1109/NSSMIC.2014.7431222 (cit. on p. 40).

[80] S. D. Jastaniah and P. J. Sellin. « Digital pulse-shape algorithms for scintillation-based neutron detectors ». In: *IEEE Transactions on Nuclear Science* 49.4 (2002), pp. 1824–1828. DOI: 10.1109/TNS.2002.801674 (cit. on p. 40).

[81] S. Yousefi, L. Lucchese, and M. D. Aspinall. « A novel wavelet-based method for neutron/gamma discrimination in liquid scintillators ». In: (2008), pp. 2387–2391. DOI: 10.1109/NSSMIC.2008.4774836 (cit. on p. 40).

[82] Kim Geehyun Kim Chanho Yeom Jung-Yeol. « Digital n- Pulse Shape Discrimination in Organic Scintillators with a High-Speed Digitizer ». In: *J Radiat Prot Res* 44.2 (2019), pp. 53–63. DOI: 10.14407/jrpr.2019.44.2.53. eprint: http://jrpr.org/journal/view.php?number=1030. URL: http://jrpr.org/journal/view.php?number=1030 (cit. on p. 40).

[83] Marc Lavi Ruch, Marek Flaska, and Sara A Pozzi. « Pulse shape discrimination performance of stilbene coupled to low-noise silicon photomultipliers ». In: *Nuclear Instruments and Methods in Physics Research Section A: Accelerators, Spectrometers, Detectors and Associated Equipment* 793 (2015), pp. 1 –5. DOI: 10.1016/j.nima.2015.04.053 (cit. on pp. 43–45, 47).

[84] 1/09/2019. URL: https://www.onsemi.com/pub/Collateral/MICROC-SERIES-D.PDF (cit. on p. 43).

[85] R. M. Preston, J. E. Eberhardt, and J. R. Tickner. « Neutron-Gamma Pulse Shape Discrimination Using Organic Scintillators With Silicon Photomultiplier Readout ». In: *IEEE Transactions on Nuclear Science* 61.4 (2014), pp. 2410–2418. DOI: 10.1109/TNS.2014.2335208 (cit. on pp. 43, 45, 47).

[86] Brent S. Budden et al. « Analysis of Cs2LiYC16:Ce3+ (CLYC) Waveforms as Read Out By Solid State Photomultipliers ». In: *IEEE Nuclear Science Symposium and Medical Imaging Conference Record (NSS/MIC)* (2012) (cit. on p. 46).

[87] Kan Yang and Peter R. Menge. « Pulse shape discrimination of Cs2LiYCl6:Ce3+ scintillator from 30řC to 180řC ». In: *Nuclear Instruments and Methods in Physics Research Section A: Accelerators, Spectrometers, Detectors and Associated Equipment* 784 (2015). Symposium on Radiation Measurements and Applications 2014 (SORMA XV), pp. 74–79. DOI: 10.1016/j.nima.2014.08.031 (cit. on pp. 46, 47).

[88] P. Buzhan, B. Dolgoshein, L. Filatov, et al. « Silicon photomultiplier and its possible applications ». In: *Nuclear Instruments and Methods in Physics Research Section A: Accelerators, Spectrometers, Detectors and Associated Equipment* 504.1 (2003), pp. 48–52. DOI: https://doi.org/10.1016/S0168-9002(03)00749-6 (cit. on p. 48).

[89] A. Gola C. Piemonte. « Overview on the main parameters and technology of modern Silicon Photomultipliers ». In: *Nuclear Inst. and Methods in Physics Research, A* ***926*** *2-15* (2019). DOI: 10.1016/j.nima.2018.11.119 (cit. on pp. 49–51, 53).

[90] Robert Klanner. « Charachterisation of SiPM ». In: *Nuclear Inst. and Methods in Physics Research, A* ***926*** *129-147* (2019). DOI: 10.1016/j.nima.2018.11.083 (cit. on pp. 49, 58).

[91] B. Dolgoshein et al. « Status report on silicon photomultiplier development and its applications ». In: *Nuclear Inst. and Methods in Physics Research, A* ***563*** *368-376* (2006) (cit. on pp. 49, 58).

[92] D. Renker. « Geiger-mode avalanche photodiodes, history, proprieties and problems ». In: *Nuclear Inst. and Methods in Physics Research, A* ***567*** *48-56* (2006) (cit. on p. 49).

[93] Valentina Arosio. « Development of a silicon photomultiplier based innovative and low cost positron emission tomography scanner. » 2017. URL: http://hdl.handle.net/10277/753 (cit. on pp. 51, 56, 60, 73).

[94] A. Vacheret et al. « Characterization and simulation of the response of Multi- Pixel Photon Counters to low light levels ». In: *Nuclear Inst. and Methods in Physics Research, A* ***656*** *69* (2011) (cit. on p. 51).

[95] C. M. Sparrow. « On spectroscopic resolving power ». In: *Astrophys. J., 44;7686* (1916) (cit. on p. 51).

[96] F. Acerbi and S. Gundacker. « standing and simulating SiPMs ». In: *Nuclear Inst. and Methods in Physics Research, A* ***926*** *16-35* (2019). DOI: 10.1016/j.nima.2018.11.118 (cit. on pp. 51–54, 57–60).

[97] Claudio Piemonte. « A new Silicon Photomultiplier structure for blue light detection ». In: *Nuclear Inst. and Methods in Physics Research, A* ***568*** *224-232* (2006). DOI: 10.1016/j.nima.2006.07.018 (cit. on p. 51).

[98] S. Seifert et al. « Simulation of Silicon Photomultiplier Signals ». In: *IEEE TRANSACTIONS ON NUCLEAR SCIENCE, 56-6* (2009) (cit. on pp. 51, 58).

[99] S. Sze. *Physics of Semiconductor Device*. Ed. by New York Wiley. 1981 (cit. on pp. 53, 59).

[100] N.Serra and et al. « Experimental and TCAD Study of Breakdown Voltage Temperature Behaviour in n+/p SiPMs ». In: *IEEE Transactions on Nuclear Science, **58** 1233-1240* (2011). DOI: 10.1109/TNS.2011.2123919 (cit. on p. 53).

[101] R. Klanner et al. « On the characterisation of SiPMs from pulse-height spectra ». In: *Nuclear Instruments and Methods in Physics Research A **854**:7081* (2017). DOI: 10.1016/j.nima.2017.02.049 (cit. on pp. 59, 64, 90, 101).

[102] G. Vincent, A. Chantre, and D. Bois. « Electric field effect on the thermal emission of traps in semiconductor junctions ». In: *J. Appl. Phys. **50** 54845487* (1979). DOI: 10.1063/1.326601 (cit. on p. 59).

[103] S.Cova, M. Gioni, and et al. « Large-area low-jitter silicon single photon avalanche diodes ». In: *Proc of SPIE Integrated Optoelectronic Devices, Quantum Sensing and Nanophotonic Devices V, **6900**, 69001D* (2008). DOI: 10.1117/12.761578 (cit. on p. 59).

[104] L.Malinverno et al. « optimizing silicon photomultipliers for Quantum optics ». In: *Scientific Reports, 9:7433* (2019). DOI: 10.1038/s41598-019-43742-1 (cit. on pp. 60, 158).

[105] L.Malinverno et al. « Measuring nonclassicality with silicon photomultipliers. » In: *Optical Letters, **44**(6),1371-1374* (2019). DOI: 10.1364/OL.44.001371 (cit. on pp. 60, 158).

[106] R. Klanner. « Characterisation of SiPMs ». In: *arXiv:1809.04346v2* (2018) (cit. on p. 62).

[107] M.Caccia et al. « A simple and robust method to study after-pulses in Silicon Photomultipliers ». In: *Journal of Instrumentation, **9** T10004* (2014). DOI: 10.1088/1748-0221/9/10/T10004 (cit. on p. 64).

[108] V. Arosio M. Beretta et al. « A robust and semi-automatic procedure for Silicon Photomultipliers characterisation ». In: *Journal of Instrumentation, **12** C03030* (2017). DOI: 10.1088/1748-0221/12/03/c03030 (cit. on pp. 64, 73).

[109] Romualdo Santoro, Massimo Caccia, Luca Malinverno, et al. « Qualification and performance of a neutron detector system with enhanced gamma discrimination, based on Silicon Photomultiplier arrays coupled to an EJ-29934 scintillator ». In: *2017 IEEE Nuclear Science Symposium and Medical Imaging Conference (NSS/MIC)* (2017), pp. 1–5 (cit. on pp. 118, 120).

[110] Sept. 2019. URL: http://www.nuclearinstruments.eu/nipm14.html (cit. on p. 129).

[111] Luca Malinverno. « An optimisation procedure for pulse shape discrimination algorithms tailored for hand-held nuclear security instruments ». In: *Nuovo Cimento C, **3** 123* (2018). DOI: 10.1393/ncc/i2018-18123-7 (cit. on p. 151).

List of Figures

List of Tables